Maastricht University

A modeled approach to absolute velocity detection with ultrasound

Citation for published version (APA):

Ledoux, L. A. F. (1999). *A modeled approach to absolute velocity detection with ultrasound*. [Doctoral Thesis, Maastricht University]. Universiteit Maastricht. https://doi.org/10.26481/dis.19991007ll

Document status and date:
Published: 01/01/1999

DOI:
10.26481/dis.19991007ll

Document Version:
Publisher's PDF, also known as Version of record

Please check the document version of this publication:

• A submitted manuscript is the version of the article upon submission and before peer-review. There can be important differences between the submitted version and the official published version of record. People interested in the research are advised to contact the author for the final version of the publication, or visit the DOI to the publisher's website.
• The final author version and the galley proof are versions of the publication after peer review.
• The final published version features the final layout of the paper including the volume, issue and page numbers.

Link to publication

General rights
Copyright and moral rights for the publications made accessible in the public portal are retained by the authors and/or other copyright owners and it is a condition of accessing publications that users recognise and abide by the legal requirements associated with these rights.

• Users may download and print one copy of any publication from the public portal for the purpose of private study or research.
• You may not further distribute the material or use it for any profit-making activity or commercial gain
• You may freely distribute the URL identifying the publication in the public portal.

If the publication is distributed under the terms of Article 25fa of the Dutch Copyright Act, indicated by the “Taverne” license above, please follow below link for the End User Agreement:

www.umlib.nl/taverne-license

Take down policy
If you believe that this document breaches copyright please contact us at:

repository@maastrichtuniversity.nl

providing details and we will investigate your claim.

Download date: 10 May. 2024

A modeled approach to absolute velocity detection with ultrasound

© Ledoux, Léon Armand Franciscus

The scientific work presented in the current thesis was performed at the Department of Biophysics of the Maastricht University, The Netherlands.

Part of the scientific work was financially supported by the Dutch Department of Economic Affairs (IBV 96.001).

Cover illustration:
Typical shape of the modulus of the correlation function of analytic radiofrequency signals received along a single line of observation from scratterers that moved through the ultrasound beam at an oblique angle (i.e., there is an axial as well as a lateral motion component).

A modeled approach to absolute velocity detection with ultrasound

PROEFSCHRIFT

ter verkrijging van de graad van doctor
aan de Universiteit Maastricht,
op gezag van de Rector Magnificus,
Prof. dr. A.C. Nieuwenhuijzen Kruseman,
volgens het besluit van het College van Decanen,
in het openbaar te verdedigen op
donderdag 7 oktober 1999 om 14.00 uur

door

Léon Armand Franciscus Ledoux

geboren op 1 mei 1971 te Heerlen.

Promotor:

Prof. dr. ir. A.P.G. Hoeks

Beoordelingscommissie:

Prof. dr.	R.S. Reneman	(voorzitter)
Prof. dr. ir.	T. Arts	
Prof. dr. ir.	N. Bom	(Erasmus Universiteit Rotterdam)
Prof. dr. ir.	A. Hasman	
Dr. ir.	J.M. Thijssen	(Katholieke Universiteit Nijmegen)

Financial support by Pie Medical Equipment BV (Maastricht, The Netherlands) for the publication of this thesis is gratefully acknowledged.

Aan:

Jolanda, mijn ouders en schoonouders.

Promotor:

Prof. dr. ir. A.P.G. Hoeks

Beoordelingscommissie:

Prof. dr.	R.S. Reneman	(voorzitter)
Prof. dr. ir.	T. Arts	
Prof. dr. ir.	N. Bom	(Erasmus Universiteit Rotterdam)
Prof. dr. ir.	A. Hasman	
Dr. ir.	J.M. Thijssen	(Katholieke Universiteit Nijmegen)

Financial support by Pie Medical Equipment BV (Maastricht, The Netherlands) for the publication of this thesis is gratefully acknowledged.

Aan:

Jolanda, mijn ouders en schoonouders.

Contents

Chapter 1

General introduction

General introduction

1.1 Introduction

Only a century ago, the instruments to get noninvasively useful information about normal and abnormal conditions inside the body of a patient were very limited. Besides the anamnesis, the main instruments to find internal abnormalities were palpation and the stethoscope. Palpation, which is the examination of the body by means of touch, can be used to search for superficial abnormalities in human tissues. The stethoscope, which is an instrument for auscultation, can be employed to find abnormalities in the sounds produced in the abdomen, chest, and heart. With the discovery of the X-rays at the end of the nineteenth century, the clinicians got a powerful noninvasive imaging technique that enabled the detection of organic disorders even at deeply located sites inside the human body. Benefiting from the giant investments in space and war technology in the twentieth century, the noninvasive medical imaging techniques were extended with ultrasonic echographic imaging and Magnetic Resonance Imaging (MRI). All medical imaging techniques provide specific information, not attainable with the other techniques, or give similar information in an easier, cheaper or safer way. Nowadays, ultrasonic echographic imaging is one of the main imaging techniques for fast (preliminary) diagnoses, because the real time images provide functional and morphological information in a relatively cheap way that is above all harmless for the patient.

At first, medical imaging techniques were only qualitative tools that were, for example, able to visualize abnormalities or the rhythmic motion of organs. As technique improved, it became possible to obtain quantitative functional information based on, for example, the analysis of frame-to-frame images. One of the main quantitative parameters, that can be assessed, is velocity. Conventional techniques to determine the magnitude and direction of the velocity of structures moving within the imaging plane are based on tracking of clearly visible reference points within the images. These reference points can be default present characteristic parts of the acquired images, but they can also be markers attached to the moving organs. Default present markers are for example the boundaries of anatomic structures (Chan 1993). Physical attachment of markers to the structures inside the body provides good motion information (Ingels et al. 1975; Ingels et al. 1980; Prinzen et al. 1986), but it is no option for medical screening of patients. Markers that can be used for medical screening are, for example, (bolus) injections op contrast agents and Röntgen-markers, but the application of those markers is a heavy burden for the patients. The current state of the art in MRI is able to place markers inside the body in a patient friendly way with a technique called tagging (McVeigh 1996). The

tags are made electromagnetically in the tissue and remain no longer than a few hundreds of milliseconds. A disadvantage of MRI is that it often requires averaging in which case real time images can not be provided. Averaging is only possible if the motions or deformations to be measured are rhythmic and reproducible (Azhari et al. 1993). To avoid the problem of nonsimultaneous physiologic events to appear simultaneous in the averaged images, e.g., motion artifacts, MRI often uses ECG-triggering and/or the breath-hold method.

Ultrasonic echography has, besides the already mentioned advantages, the advantage that it does not require the addition of any type of markers, because the speckled appearance of the echographic images can be used as markers (Bohs and Trahey 1991; Mailloux et al. 1987). Velocity analysis based on the speckle variation in the echographic images is possible if the contrast is high enough, the speckle distribution is random and the local velocity is coherent (Walker and Trahey 1994).

Echographic systems acquire their data with the use of a beam of ultrasonic waves. Nowadays, a lot of methods are available to measure the velocity in the direction of the sound beam, i.e., the axial velocity (Bonnefous and Pesqué 1986; de Jong et al. 1990; Hoeks et al. 1993; Loupas et al. 1995). One of the most widely applied applications of ultrasound velocity measurements is color flow imaging, which provides velocity information at precise locations. The velocity information is color encoded and superimposed on the conventional grayscale echographic image (Cape and Yoganathan 1991). Color flow imaging is nowadays an important method for the selection of patients for cardiac surgery (D'Cruz 1991).

The absolute velocity, i.e., the magnitude of the actual velocity, can be derived from the axial velocity based on simple goniometry if the angle between the velocity direction and the ultrasound beam is known. Currently, the only medical application where this angle approximately is known is for (laminar) blood flow velocity measurements in straight vessels. The desired angle is estimated from the corresponding image of the longitudinal cross-section of the blood vessel.

The angle-dependency of echographic velocity measurement methods is a severe limitation. In a lot of cases, the angle between the velocity direction and the sound beam is not known like, for example, during the measurement of tissue motion or the evaluation of cardiac hemodynamics. So far, one of the most promising methods to circumvent the angle-dependency of ultrasound based velocity

measurements is tracking of the speckle in frame-to-frame images (Trahey et al. 1988). This technique is not only computational intensive with relatively low axial, temporal and velocity resolutions, but it only provides the magnitude and direction of the velocity component in the plane of the images. The velocity component perpendicular to the image plane is ignored.

1.2 Aim of the thesis

Current ultrasound based velocity measurement methods are limited because of their angle-dependency. Removal of this angle-dependency will have a substantial positive spin-off, because it would be no longer necessary to estimate the angle between the local velocity direction and the direction of the sound beam. Hence, it would be sufficient to aim the sound beam in the direction of interest and the absolute velocity would directly be provided. This would enable the measurement of tissue motion with ultrasound. The measurement of tissue motion and the corresponding deformation behavior provides information about the local mechanical stiffness of tissue, for example, as a consequence of muscle contraction or the presence of tumors (de Korte et al. 1997; Gao et al. 1996; Ophir et al. 1991). The detection of abnormal mechanical behavior as a consequence of local stiffness inhomogeneities contributes to improved clinical diagnoses of, for example, the liver (Lerner et al. 1990). Another important application is the quantification of the contractility of the heart wall and the detection of local inhomogeneities in the deformation behavior of the heart wall (Aelen et al. 1997; Delhaas et al. 1993). Regions with decreased contractility, due to ischemia or a disturbed electrical activation, can be evaluated with respect to their inhomogeneities in their deformation behavior from which the size and location of the infarcted region can be derived.

In the current thesis, a model-based method is presented for the angle-independent measurement of the absolute velocity with ultrasound. To circumvent the angle-dependency, the proposed method determines, besides the axial velocity component, also the lateral velocity component, i.e., the velocity component in the plane perpendicular to the sound beam. Combination of the axial and lateral velocity components results in the absolute velocity (not its complete three-dimensional direction). Specifically, the following aims will be addressed to arrive at a feasible approach for absolute velocity detection:

1. Ideally, the method should be applicable for the measurement of blood flow velocities as well as for the measurement of tissue motion. This does not only enable the detection of tissue deformation, but it also enables the assessment of blood flow velocities near bifurcations, junctions and in curves of blood vessels.

2. The axial resolution of the absolute velocity estimates should be high. Preferably, it should be equal to the axial resolution obtained with conventional (axial) velocity estimators. These estimators have in the ideal situation an axial resolution equal to the applied pulse length, which in most cases is equal to one or a few times the wavelength of the emitted ultrasonic waves. In human tissue, the wavelength of sound waves with a frequency of 5 MHz is approximately 300 μm.

3. The temporal resolution should be high to be able to measure fast velocity fluctuations. For blood flow velocity measurements, a temporal resolution window of 10 ms is in most cases sufficient. The temporal velocity fluctuations of tissue motion are normally less than those occurring in the blood flow. Therefore, the temporal resolution window for tissue motion measurements might even be larger than 10 ms to be still acceptable.

4. The velocity resolution should be high such that no additional (velocity) interpolation is required.

5. And finally, the computational load of the method should be as small as possible to allow for real-time velocity assessment.

1.3 Outline of the thesis

The next chapter gives a short summary of the main principles of medical ultrasonic echography. Special attention is paid to some properties of the ultrasound beam, because it plays an important role in the measurement of lateral velocities. An extensive description of the concept of the angle-independent velocity measurement method is presented in chapter 3. Based on the phenomena observed and described in that chapter, a model is derived that predicts the observed phenomena. The derivation and (phantom) evaluation of the model is

presented in chapter 4. The model includes, amongst others, the axial and lateral motion components and characteristics of the ultrasound beam. In chapter 5, a computational efficient method is presented for the measurement of the local absolute velocity based on the aforementioned model.

To measure blood flow velocity, in most cases a clutter filter is required that rejects the echoes from stationary or slowly moving tissue (clutter), e.g., originating from vessel or heart walls, that mask the low amplitude blood signals. Mostly, clutter filters are high-pass filters with a cut-off frequency that determines which frequencies are suppressed. Increasing the cut-off frequency removes more clutter, but it eliminates also signals from blood with low velocity. Furthermore, most high-pass filters have a settling time. In chapter 6, a clutter filter is presented based on the Singular Value Decomposition (SVD). This filter is not based on frequency characteristics of the echo signals and it has no settling time. The concept of the filter is roughly that the strongest common signal is searched for in a set of echo signals. Once this signal is found, it is subtracted from all signals after which the next strongest common signal is searched for. The strongest common signals are caused by clutter and have to be removed in all echo signals.

Finally, before the general discussion and conclusions (chapter 8), a few preliminary in-vivo results obtained with the methods described in the current thesis are shown in chapter 7.

1.4 References

Aelen FWL, Arts T, Sanders DGM, Thelissen GRP, Muijtjens AMM, Prinzen FW, Reneman RS. Relation between torsion and cross-sectional area change in the human left ventricle. J Biomechanics. 1997;30:207-212.

Azhari H, Weiss JL, Rogers WJ, Siu CO, Zerhouni EA, Shapiro EP. Noninvasive quantification of principal strains in normal canine hearts using tagged MRI images in 3-D. Am J Physiol. 1993;264:H205-H216.

Bohs LN, Trahey GE. A novel method for angle independent ultrasonic imaging of blood flow and tissue motion. IEEE Trans Biomed Eng. 1991;38:280-286.

Bonnefous O, Pesqué P. Time domain formulation of pulse-Doppler ultrasound and blood velocity estimation by cross correlation. Ultrason Imaging. 1986;8:73-85.

Cape EG, Yoganathan AP. Basic principles of ultrasound. In: Pohost GM, O'Rourke RA, ed. Principles and practice of cardiovascular imaging. Boston: Little, Brown Co, 1991.

Chan KL. Two approaches to motion analysis of the ultrasound image sequence of carotid atheromatous plaque. Ultrasonics. 1993;31:117-123.

D'Cruz IA. M-mode and two-dimensional echocardiography. In: Pohost GM, O'Rourke RA, ed. Principles and practice of cardiovascular imaging. Boston: Little, Brown Co, 1991.

de Jong PGM, Arts T, Hoeks APG, Reneman RS. Determination of tissue motion velocity by correlation interpolation of pulsed ultrasonic echo signals. Ultrason Imaging. 1990;12:84-98.

de Korte CL, Céspedes EI, van der Steen AFW, Lancée CT. Intravascular elasticity imaging using ultrasound: feasibility studies in phantoms. Ultrasound Med Biol. 1997;23:735-746.

Delhaas T, Arts T, Prinzen FW, Reneman RS. Relation between regional electrical activation time and subepicardial fiber strain in the canine left ventricle. Pflügers Arch (Eur J Phys). 1993;423:78-87.

Gao L, Parker KJ, Lerner RM, Levinson SF. Imaging of the elastic properties of tissue - a review. Ultrasound Med Biol. 1996;22:959-977.

Hoeks APG, Arts TGJ, Brands PJ, Reneman RS. Comparison of the performance of the RF cross correlation and Doppler autocorrelation technique to estimate the mean velocity of simulated ultrasound signals. Ultrasound Med Biol. 1993;19:727-740.

Ingels NB, Daughters GT, Stinson EB, Alderman EL. Measurement of midwall myocardial dynamics in intact man by radiography of surgically implanted markers. Circulation. 1975;52:859-867.

Ingels NB, Daughters GT, Stinson EB, Alderman EL. Evaluation of methods for quantitating left ventricular segmental wall motion in man using myocardial markers as a standard. Circulation. 1980;61:966-972.

Lerner RM, Huang SR, Parker KJ. "Sonoelasticity" images derived from ultrasound signals in mechanically vibrated tissues. Ultrasound Med Biol. 1990;16:231-239.

Loupas T, Powers JT, Gill RW. An axial velocity estimator for ultrasound blood flow imaging, based on a full evaluation of the Doppler equation by means of a two-dimensional autocorrelation approach. IEEE Trans Ultrason Ferroel Freq Contr. 1995;42:672-688.

Mailloux GE, Bleau A, Bertrand M, Petitclerc R. Computer analysis of heart motion from two-dimensional echocardiograms. IEEE Trans Biomed Eng. 1987;BME-34:356-364.

McVeigh ER. MRI of myocardial function: motion tracking techniques. Magn Reson Imag. 1996;14:137-150.

Ophir J, Céspedes I, Ponnekanti H, Yazdi Y, Li X. Elastography: a quantitative method for imaging the elasticity of biological tissues. Ultrason Imaging. 1991;13:111-134.

Prinzen TT, Arts T, Prinzen FW, Reneman RS. Mapping of epicardial deformation using a video processing technique. J Biomechanics. 1986;19:263-273.

Trahey GE, Hubbard SM, von Ramm OT. Angle independent ultrasonic blood flow detection by frame-to-frame correlation of B-mode images. Ultrasonics. 1988;26:271-276.

Walker WF, Trahey GE. A fundamental limit on the performance of correlation based phase correction and flow estimation techniques. IEEE Trans Ultrason Ferroel Freq Contr. 1994;41:644-654.

Chapter 2

Ultrasonic echography

Ultrasonic echography

2.1 Basic concepts of sound propagation

Since the early fifties of the twentieth century, ultrasonic echography is in use for making noninvasive images of internal structures of the living human body and later on for the measurement of the blood flow velocity. Ultrasonic echography, which is based on sound wave propagation, has under normal clinical conditions no harmful effects. The principle of ultrasonic echography is that a pulse of ultrasonic waves is generated and emitted into the human body. Parts of the emitted waves are reflected and/or scattered (echoed) as the waves impinge on internal structures. The echoed waves are used to generate images of the internal body or to measure the motion of blood or tissue. The time between emission and reception is converted to distance under the assumption that the propagation velocity is known and that it is independent of the tissue encountered.

Sound, which is acoustic energy, is the resultant of the vibration of a material. A material is able to vibrate as it has mass and elasticity, i.e., the ability to recover from distortion. All natural materials contain both properties (Speaks 1992). A vibrating material generates longitudinal sound waves that propagate in the oscillation direction of the material. Sound waves consist of alternating regions of compression (higher pressure) and rarefaction (lower pressure). The particles of the material through which the sound waves are traveling, i.e., the transmission material, are not displaced over any appreciable distance, but they are only moved back and forth in the propagation direction of the sound waves. The rate of the alternations determines the frequency of the sound waves. The most common sound frequencies are those within the audible range, which for a young person ranges from approximately 20 Hz till 20 kHz (Vander et al. 1990). Ultrasonic echography commonly uses sound waves with frequencies ranging from 1 MHz till 20 MHz which is far outside the audible range.

The speed at which sound waves propagate depends on the material they are travelling through (Feynman et al. 1977). Soft human tissue behaves like a liquid for ultrasound. The speed of sound c [m/s] is for a liquid given by

$$c = \sqrt{B/\rho} \tag{2-1}$$

where ρ [kg/m^3] is the density of the material and B [N/m^2] is the bulk modulus (elasticity) of the material, which is defined as the pressure change divided by the

corresponding fractional volume change (Young and Freedman 1996). Generally, the less compressible a material is, the higher the speed of sound will be. The sound velocities in most kinds of soft tissue are close to 1540 m/s (Goss et al. 1978).

The wavelength λ [m] of sound waves is related to the carrier frequency f_C [Hz] of the waves and the sound velocity c [m/s] in the transmission material conform

$$\lambda = \frac{c}{f_C} \tag{2-2}$$

Sound waves impinging on structures smaller than the wavelength are scattered in many directions (backscatter). Red blood cells and structures inside tissue are examples of sources of scattering within the human body. Collision of sound waves at a relatively smooth boundary between materials with different acoustic properties results in specular reflection of a part of the incident waves and transmission of the remaining part. The acoustic property of a material is given by the acoustic impedance Z [kg/m^{2}s] or [Rayl] that is equal to

$$Z = \rho c \tag{2-3}$$

where ρ [kg/m^3] is the density of the material and c [m/s] the sound velocity of the material. For human tissue, the acoustic impedance ranges from 1.3 to 1.9 MRayl (Evans et al. 1989).

In the case of specular reflection, the angle α_R [°] (with the normal to the boundary) of the reflected sound waves is equal to the angle α_I [°] (with the normal to the boundary) of the incident sound waves conforming to the law of reflection (Fig. 2-1). The incident waves, the normal to the boundary and the reflected waves all lie in the same plane (Hudson and Nelson 1990; Young and Freedman 1996). Snell's law (law of refraction) states that the angle (with the normal to the boundary) of the transmitted waves α_T [°] depends on the ratio of the sound velocities in both materials and the angle of the incident waves as is given by

$$\frac{\sin(\alpha_I)}{\sin(\alpha_T)} = \frac{c_1}{c_2} \tag{2-4}$$

where c_1 and c_2 are the sound velocities before and after the boundary, respectively (Young and Freedman 1996). The refraction of the propagation direction is negligible for ultrasonic waves traveling through the human body, because, as is mentioned before, the sound velocity variations of the different types of human tissue are very small (Goss et al. 1978). The transmitted p_T [Pa] and reflected p_R [Pa] wave pressures at a boundary are given by

$$p_R = \frac{Z_2 \cos(\alpha_I) - Z_1 \cos(\alpha_T)}{Z_2 \cos(\alpha_I) + Z_1 \cos(\alpha_T)} p_I$$

$$p_T = \frac{2Z_2 \cos(\alpha_I)}{Z_2 \cos(\alpha_I) + Z_1 \cos(\alpha_T)} p_I \qquad (2\text{-}5)$$

where p_I [Pa] is the incident wave pressure and Z_1 and Z_2 are the acoustic impedances of the material before and after the boundary, respectively (Fig. 2-1) (Jensen 1996; Wells 1977). The acoustic impedances of different kinds of soft human tissue are approximately equal, i.e., $Z_1 \approx Z_2$. Hence, the transmitted pressure is almost equal to the incident pressure ($p_T \approx p_I$) for sound waves impinging almost perpendicularly on the boundary between two different kinds, i.e., $\alpha_I \approx 0^o$.

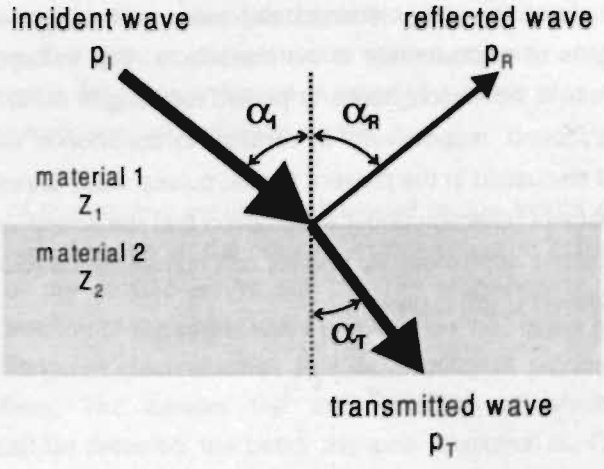

Fig. 2-1 Schematic representation of an incident sound wave at the boundary between two materials with different acoustic properties and the corresponding transmitted and reflected waves.

Due to scattering, reflection and radial spread of the wave front, the acoustic energy of the propagating sound waves is attenuated. Furthermore, absorption (conversion of wave motion energy into heat) causes an additional decrease of the acoustic energy (Kandath and Nanda 1991). Attenuation due to absorption increases rapidly with increased ultrasound frequency and traveled distance in tissue. Therefore, the possible depth of penetration decreases with increasing frequency of the ultrasonic waves (Evans et al. 1989; Wells 1969).

2.2 The ultrasound beam

A piezoelectric crystal (e.g., Lead-Zirconate-Titanate (PZT) or PolyVinylidene DiFluoride (PVDF)) placed in the tip of a probe, is the vibrating material in an ultrasonic echographic system. The piezoelectric crystal converts electric energy into acoustic energy and vice versa for which reason it is called a transducer. Ultrasonic waves impinging on the surface of the transducer deform the crystal and produce electric signals. These electric signals are called radiofrequency (RF) signals referring to their carrier frequency which is located in the range used for radio transmission.

The amount of acoustic energy emitted depends on the applied voltage that governs the degree of displacement of the transducer. The voltage applied to the piezoelectric crystal is either continuous or pulsed resulting in continuous wave and pulsed wave ultrasound, respectively. In contrast to continuous wave ultrasound, which will not be discussed in the present thesis, pulsed wave ultrasound is able to determine the place of reflection under assumption that the sound velocity is known and constant, which is approximately true for soft human tissue (Goss et al. 1978). The place of reflection d [m] is given by

$$d = \frac{c\, t_d}{2} \tag{2-6}$$

where c [m/s] is the sound velocity in the transmission material and t_d [s] is the time that sound waves require to travel to axial distance d and back. The factor 2 compensates for the round trip of the sound waves.

The resonance (or fundamental) frequency f_{res} [Hz] of the waves that are excited in the piezoelectric crystal is a function of the length (thickness) l [m] of the ceramic and is given by

$$f_{res} = \frac{c_{crystal}}{2l} \tag{2-7}$$

where $c_{crystal}$ [m/s] is the sound velocity in the crystal (Kinsler and Frey 1962; Wells 1977). In case of pulse activation, a transducer is not able to produce "mono-frequent" ultrasonic waves, but it generates waves with a certain bandwidth (often symmetrically) located around the resonance frequency. The frequency with maximum amplitude in the frequency spectrum denotes the center frequency f_c [Hz]. A very short unipolar spike activation (a few nano-seconds) gives an approximation of the impulse response of the transducer, revealing the maximal obtainable bandwidth of the generated ultrasonic waves. The attenuation that sound waves experience while travelling through a material influences the bandwidth of the generated sound waves since higher frequencies are more strongly attenuated.

To generate enough acoustic energy with a short activation pulse (a few nanoseconds), the magnitude of the activation voltage should be considerably high (e.g., 100-200V). Because of safety considerations, the instantaneous amount of acoustic energy emitted into the body should be kept as small as possible. A high dose of acoustic energy may cause heating of the body due to absorption resulting in tissue damage. The dose of instantaneous emitted acoustic energy can be kept as small as possible by using a limited number of periods of a square wave at (near) resonance frequency as activation signal.

The bandwidth of the emitted waves is influenced by the length of the activation pulse (Gabor 1946). The longer the duration of the activation pulse is, the smaller the bandwidth of the emitted waves will be. The resolution of an echographic scanner in the direction of the sound wave propagation, i.e., in the axial direction, is the ability to distinguish discontinuities that lie in different planes parallel to the transducer surface. The smaller the axial distance at which distinct axial discontinuities can be detected, the better the axial resolution is. The optimal axial resolution is obtained as the (axial) length of the emitted acoustic waves is as short as possible. Therefore, the activation pulse should be as short as possible. An increased pulse length is at the expense of a decreased axial resolution, but the

activation voltage can be considerably lower. For higher frequencies, the same number of periods results in a shorter pulse length than for lower frequencies. Hence, higher frequencies result in a better axial resolution, but at the expense of a lower penetration depth because of the depth dependent attenuation.

The axial resolution is improved by tempering the ringing of the transducer. Therefore, the transducer has a highly attenuative backing that controls the duration of the transducer vibration by absorbing the energy radiating from the back. For optimal absorption, the acoustic impedance of the backing should be equal to that of the transducer. Highly damped transducers generate ultrasonic waves with a wider bandwidth than mildly damped transducer. To avoid unnecessarily high energy losses, a matching layer is placed in front of the transducer that serves as an intermediate between the high acoustic impedance of the transducer and the lower acoustic impedance of the human tissue. The matching layer is often called "quarter lambda" layer, which refers to the thickness of the layer that is equal to a quart of the wavelength of the resonance frequency of the transducer. This thickness enables constructive interference such that the emitted sound waves are in phase with the waves reverberated in the matching layer.

The three dimensional shape of the ultrasonic pressure waves generated by the transducer after a pulse activation denotes the sensitivity function of the transducer. The local shape and the path followed by the sensitivity function describe the shape of what is called the ultrasound beam. The resolution of the echographic system in the direction perpendicular to the propagation direction of the sound waves, i.e., the lateral resolution, is the ability to distinguish discontinuities which lie in different planes perpendicular to the transducer surface. The smaller the lateral distance at which distinct lateral discontinuities can be detected, the better the lateral resolution is. The lateral resolution depends on the width of the ultrasound beam which is often characterized by the local half maximum width (-6 dB) of the lateral round trip power distribution (Sung 1989). Smaller ultrasound beams have a better lateral resolution, but the amount of acoustic energy emitted is generally less.

An ideal homogeneous ultrasound beam would be obtained if the transducer generated plane waves, i.e., waves with equal phase in any plane perpendicular to the propagation direction of the sound waves (Angelsen 1975). In practice, the surface of a transducer can be assumed to consist of point sources transmitting mono-frequent diverging spherical waves concentric with their point sources. The mono-frequent beam shape can be constructed by summing the contributions of

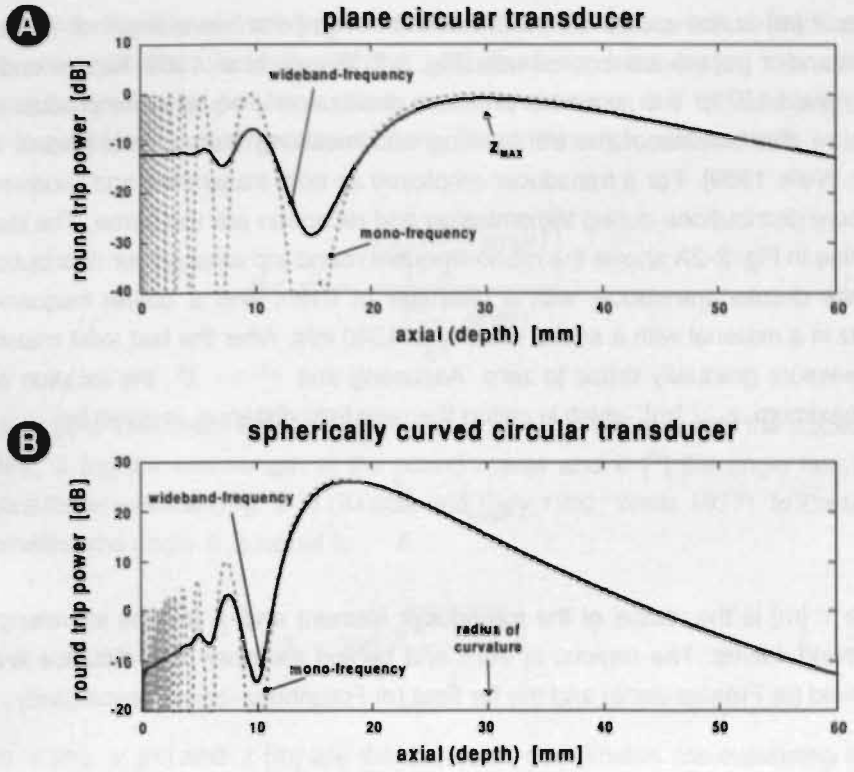

Fig. 2-2 (A) Theoretical round trip axial power distribution for a plane circular transducer with a diameter of 6 mm and a center frequency of 5 MHz in a material with a sound velocity of 1540 m/s. The gray dashed line shows the distribution for mono-frequent waves and the solid black line for wideband waves (Gaussian power spectrum with equivalent bandwidth of 2 MHz). (B) Idem (A), but the transducer surface is spherical concave with a radius of curvature of 30 mm.

each of the point sources conform the Huygens' principle (Wells 1969; Young and Freedman 1996). Consequently, the pressure of the sound waves goes through a series of maxima and minima in the region directly in front of the transducer. The mono-frequent single trip pressure distribution along the axial axis $p(z)$ [Pa] for a plane circular transducer is proportional with

$$p(z) \propto \sin^2\left(\frac{\pi}{\lambda}\left(\sqrt{r^2 + z^2} - z\right)\right) \tag{2-8}$$

where r [m] is the radius of the transducer, λ [m] the wavelength of the sound waves and z [m] the axial coordinate (Fig. 2-3) (Evans et al. 1989; Kinsler and Frey 1962; Wells 1977). The round trip pressure distribution is equal to the product of the pressure distributions of the transmitting and receiving transducers (Evans et al. 1989; Wells 1969). For a transducer employed as both transmitter and receiver, the pressure distributions during transmission and reception are the same. The dashed gray line in Fig. 2-2A shows the mono-frequent round trip axial power distribution for a plane circular transducer with a diameter of 6 mm and a center frequency of 5 MHz in a material with a sound velocity of 1540 m/s. After the last axial maximum, the pressure gradually drops to zero. Assuming that $r^2 >> \lambda^2$, the location of the last maximum z_{MAX} [m], which is called the near field distance, is given by

$$z_{MAX} = \frac{r^2}{\lambda} \tag{2-9}$$

where r [m] is the radius of the transducer element and λ [m] the wavelength of the sound waves. The regions in front and behind the near field distance are the near field (or Fresnel-zone) and the far field (or Fraunhofer-zone), respectively.

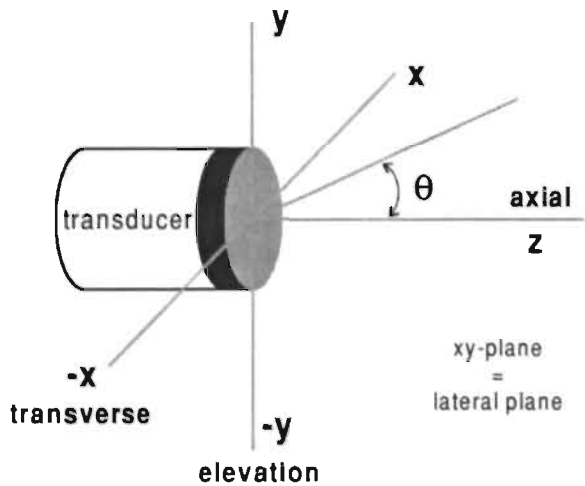

Fig. 2-3 Schematic representation of the orientation of the coordinate axes for a circular transducer.

In the lateral direction of the ultrasound beam, there are also pressure fluctuations. In the near field the calculation of the lateral pressure distribution can only be performed numerically, but for a plane circular transducer, the far field single trip mono-frequent lateral pressure distribution $p(x, y)$ [Pa] is proportional with

$$p(x, y) \propto \frac{2J_1\left(\frac{2\pi r}{\lambda}\sin(\theta)\right)}{\frac{2\pi r}{\lambda}\sin(\theta)} \tag{2-10}$$

where J_1 [-] is the Bessel function of the first kind, r [m] the radius of the transducer element, λ [m] the wavelength of the sound waves and θ [°] the angle normal to the transducer surface (Fig. 2-3) (Kinsler and Frey 1962; Wells 1977). In Cartesian coordinates, the angle θ is equal to

$$\theta = \tan\left(\frac{\sqrt{x^2 + y^2}}{z}\right) \tag{2-11}$$

where x [m], y [m] and z [m] are the Cartesian coordinates corresponding to the transverse, the elevation and the axial direction, respectively (Fig. 2-3). The dashed gray line in Fig. 2-4 shows the mono-frequent round trip lateral power distribution at an axial distance of 30 mm for a plane circular transducer with a diameter of 6 mm and a center frequency of 5 MHz in a material with a sound velocity of 1540 m/s.

The lateral pressure fluctuations are more rapid in the near field than in the far field. In the near field, the transmitted energy is often considered to be confined within a cylinder of radius r. In the far field, the main part of the acoustic energy is constricted to a narrow beam that is called the main lobe. The main lobe reduces to zero as the angle θ is equal to

$$\theta_0 = \arcsin\left[\frac{0.61\lambda}{r}\right] \tag{2-12}$$

where r [m] the radius of the transducer element, λ [m] the wavelength of the sound waves and θ_0 is equal to the angle of divergence (Kinsler and Frey 1962; Wells 1977). Eq. (2-12) shows that the width of the main lobe decreases as the

frequency of the sound waves increases. Combining Eqs. (2-11) and (2-12) shows that in the far field the width of the main lobe increases with increasing depth resulting in the spherical divergence of the sound waves (Kinsler and Frey 1962). Besides the main lobe, there is a skirt of ultrasound energy located in side lobes (Sung 1989). The energy in the side lobes is much lower than that in the main lobe. The maximum power level of the first side lobe is in single trip more than 17 dB down and in round trip more than 35 dB down (Fig. 2-4) (Kinsler and Frey 1962). The subsequent lobes are even more deciBells down.

The ultrasound beam of a plane rectangular transducer element behaves almost the same as a circular transducer, only the pressure fluctuations in the near field are somewhat less (Wells 1977). The ultrasound beam of a circular transducer is cylindrical such that the beam is symmetric about the axial axis (z-axis), where as a rectangular transducer generates at some distance an elliptic ultrasound beam such that the lateral beam shape is not uniform across any cross section of the beam.

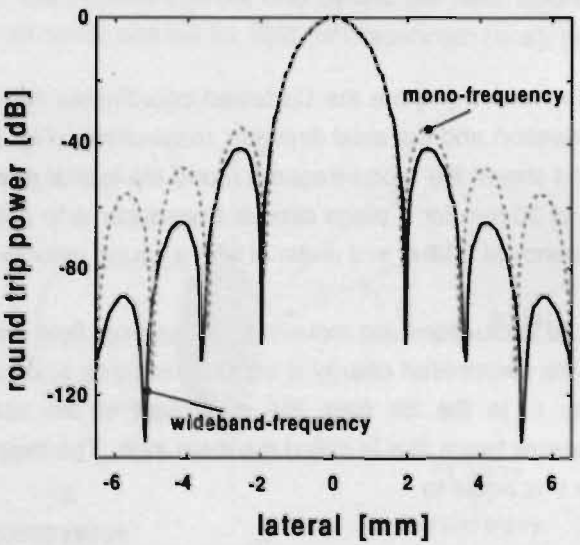

Fig. 2-4 Theoretical round trip lateral power distribution at an axial distance of 30 mm for a plane circular transducer with a diameter of 6 mm and a center frequency of 5 MHz in a material with a sound velocity of 1540 m/s. The gray dashed line shows the distribution for mono-frequent waves and the solid black line for wideband waves (Gaussian power spectrum with equivalent bandwidth of 2 MHz).

The lateral resolution can be influenced by focussing of the sound waves. Focussing at a fixed range is possible by placing an acoustic lens in front of the transducer or using a concave piezoelectric crystal (Evans et al. 1989). The focus, which is the location with maximum pressure, is always located in the near field (Angelsen 1975; Kossoff 1979). At the focus, the lateral resolution is improved (minimally obtainable lateral beam width is in the order of the wavelength), but in the far field the lateral divergence of the sound beam is larger than that of the unfocussed beam and thus the lateral resolution will deteriorate faster with increasing axial distance. For a spherically curved circular transducer, the mono-frequent single trip pressure distribution along the axial axis $p(z)$ [Pa] is proportional with

$$p(z) \propto \left(\frac{A}{A - z} \sin\left[\frac{(A - z)\pi r^2}{2\lambda z A} \right] \right)^2 \qquad (2\text{-}13)$$

where r [m] the radius of the transducer element, λ [m] the wavelength of the sound waves, z [m] the axial coordinate and A [m] the radius of curvature of the lens surface (Kossoff 1979). The focus of a spherical concave transducer lies slightly in front of the center of curvature (Wells 1977). The dashed gray line in Fig. 2-2B shows the mono-frequent round trip axial power distribution for a spherical concave circular transducer with a diameter of 6 mm, a center frequency of 5 MHz and a radius of curvature of 30 mm in a material with a sound velocity of 1540 m/s. Normally, the larger the transducer surface, the better the center of curvature will be approximated.

The focus of spherical or cylindrical acoustic lenses z_{lens} [m] is given by

$$z_{lens} = \frac{c_{load}}{c_{load} - c_{lens}} A \qquad (2\text{-}14)$$

where A [m] is the radius of curvature of the lens surface and c_{lens} [m/s] and c_{load} [m/s] are the sound velocities in the acoustic lens and in the load in front of the transducer, respectively (Angelsen 1975; Wells 1969). A negative radius of curvature of the acoustic lens means that the surface of the lens is concave. The material of the acoustic lens should be chosen such that the absorption of acoustic energy within the lens is as small as possible. Maximum transmission of acoustic energy through the lens occurs on those places where the lens has a thickness that is equal to an integral number of half wavelengths (Wells 1969).

In case of mono-frequent sound waves, the axial and lateral pressure fluctuations are very sharp. In pulsed ultrasound systems, the sound waves have a certain bandwidth which causes the pressure fluctuations to be less sharp, because the pressure distribution is the resultant of the summation of the pressure distributions of a number of frequencies, each with their corresponding weighting factors. The black solid lines in Figs. 2-2 and 2-4 show the corresponding wideband (Gaussian spectrum with (equivalent) bandwidth of 2 MHz) axial and lateral power distributions. Fig. 2-2 shows that the axial power fluctuations in the near field are indeed less pronounced for wideband ultrasonic waves. Fig. 2-4 shows that the power of the side-lobes in the lateral direction is suppressed for the considered wideband waves, but they are still reasonably sharp. Only for larger bandwidths (approximately equal to the center frequency) the side-lobes get smoother, but such large bandwidths are normally not encountered in practical situations.

Besides single element transducers, nowadays a wide range of transducers is available consisting of a number of elements, e.g., annular arrays (number of concentric circular elements) and array transducers (a number of mostly rectangular elements in a row). An advantage of these types of transducers is that they during emission can be focussed electrically by controlling the activation delays of neighboring elements. The sound beam of an electrically focussed transducer has the same behavior as a mechanically focussed sound beam. During reception of the echoes, the RF-signals of neighboring transducer elements are summed. Controlling the delays of these RF-signals before summation results in a dynamical changeable focus.

2.3 Echographic velocity measurement: a short historical overview

The "simplest" and historically the earliest application of pulsed ultrasound is the amplitude (A-mode) scan, which is a one-dimensional image showing the amplitude of the envelope of the recorded radiofrequency (RF) signals. An extension of A-mode is motion mode (M-mode) in which a number of consecutive RF-signals are acquired along the same line of observation and sequentially displayed in gray-scale showing the temporal influence of motion on the amplitude of the RF-signals (Cape and Yoganathan 1991; D'Cruz 1991). As techniques improved and transducers became able to move their sound beam in a scan plane, it became possible to generate real-time two-dimensional images with a framerate of

appriximately 25 frames per second. The envelopes of the RF-signals recorded at a number of places within the scan plane are two dimensionally imaged in brightness mode (B-mode), i.e., high amplitudes are white and low amplitudes are black. Nowadays, B-mode imaging is still in common use for the evaluation of anatomical relationships. Echographic images have a characteristic pattern called speckle, which is the consequence of the constructive and destructive interference of the reflected and scattered sound waves.

Besides for imaging, pulsed ultrasound can also be applied to measure the velocity of structures passing through the sound beam. Already in the nineteenth century, it was known that the frequency of sound waves increases as the observer moves towards the source of the waves, while the frequency decreases as the observer moves away from the source. The first (not completely correct) theoretically description of this phenomenon in the case of light waves was given by Doppler in 1843 (White 1982). Assuming that the sound waves are moving in the same direction as the observer, Doppler derived that the frequency shift of the observed waves f_{dop} [Hz] is equal to

$$f_{dop} = \frac{v_{observer} - v_{source}}{c + v_{source}} f_C \qquad (2\text{-}15)$$

where f_C [Hz] is the frequency of the original waves, c [m/s] the sound velocity in the transmission material, and $v_{observer}$ [m/s] and v_{source} [m/s] the speeds of the observer and of the source, respectively (Hudson and Nelson 1990; Jensen 1996).

In 1845, Buys Ballot tried to proof experimentally that the theory of Doppler was not correct. Buys Ballot used for his famous experiments sound waves instead of light waves. The propagation speed of sound is much lower than that of light such that the Doppler shift is larger for any given difference in relative velocity between source and observer. The concept of his experiments was that a musician generated a pure tone on a horn while another musician located at a considerable distance registered the received tone (Jonkman 1980). To get the largest possible Doppler shift, one of both musicians was placed on a fast moving vehicle. In those days, the fastest way of transportation were the railroads, which moved with a speed of approximately 20 m/s resulting in a Doppler shift of approximately 6% (c_{AIR} = 333 m/s). The first experiments had to be stopped because of a hail storm, but the results showed, unlike Buys Ballot expected, that the Doppler shift indeed

occurred. The results of his first experiments were published already a month later in a Dutch journal for music lovers (Buys Ballot 1845b). A few months later, Buys Ballot repeated his experiments more thoroughly finding the same results which he published in a German physics periodical (Buys Ballot 1845a).

Transducers generate sound waves that travel in a specific direction, which in the case of a single element transducer is the axial direction. Therefore, only the axial velocity component of a structure passing through the ultrasound beam will contribute to the measured Doppler shift. If the angle between the propagation direction of the structure and the ultrasound beam is known, i.e., the transducer-to-motion angle α [°], then the actual velocity v [m/s] can be determined by using goniometry resulting in the following extended Doppler equation (assuming $v << c$)

$$v = \frac{c}{2\cos(\alpha)} \frac{f_{dop}}{f_c} \tag{2-16}$$

where f_c [Hz] is the (center) frequency of the sound waves and c [m/s] the sound velocity of the propagation material. The factor 2 compensates for the round trip of the sound waves. An overview of velocity measurement methods based on this equation is given by Brands (Brands 1996).

A severe limitation of those velocity measurement methods is that they require the transducer-to-motion angle (and the center frequency has to be known) to determine the absolute velocity, i.e., the magnitude of the actual velocity. It should be noted that, even if the transducer-to-motion angle is known, the direction of the actual velocity is not known, because the direction of the velocity component in the lateral plane, i.e., in the xy-plane (Fig. 2-3), is not known. In most commercial echographic scanners, the transducer-to-motion angle is estimated from the B-mode image. This is feasible for laminar blood flow measurements in straight vessels where the transducer-to-motion angle can be estimated from the longitudinal cross-sectional image of the vessel under the assumption that the blood flow velocity direction is the same as the direction of the axis of the vessel. Application of this strategy near curves and bifurcations in the vessel may lead to incorrect velocity estimates, because in those regions the blood flow is generally not parallel to the vessel wall (Kandath and Nanda 1991; Phillips et al. 1989; Reneman et al. 1989). For tissue motion, it is almost impossible to make assumptions about the direction of the motion. Hence, it is almost impossible to determine the transducer-to-motion angle from the B-mode image.

To circumvent the angle-dependency of the Doppler equation, a wide range of strategies have been proposed, but so far not one of these methods has been incorporated in a commercially available scanner, because all methods have their limitations. The first angle-independent velocity measurement methods were based on the application of two or more transducers with crossing beams. Because the angle between the beams is known, the magnitude of the actual velocity can be derived from the combination of the axial velocity estimates determined with the individual transducers. An overview of some of these multiple transducer methods is given by Evans (Evans et al. 1989). The best results are obtained as the angle between the transducers is large, but this has the consequence that only meaningful absolute velocity estimates can be obtained at the junction of the beams (Jensen 1996).

Other angle-independent velocity measurement methods are based on speckle tracking (Bohs et al. 1995; Trahey et al. 1987). These methods try to determine the interframe movement of the speckle pattern in consecutive B-mode images by means of correlation. Speckle tracking, which requires a considerable computational load, results in the magnitude and direction of the velocity component in the plane of the B-mode image ignoring the motion component perpendicular to the image plane. The inter-pixel distance in the B-mode image influences the precision of velocity estimates. Generally, the technique works best for small motion components (with respect to the speckle size) and high frame rates.

2.4 Absolute velocity measurement: a conceptual approach

Goniometry shows that the absolute velocity v [m/s] also can be determined in an angle-independent way as

$$v = \sqrt{v_{AX}^2 + v_{LAT}^2} \tag{2-17}$$

where v_{AX} [m/s] and v_{LAT} [m/s] are the axial and lateral velocity components, respectively. Therefore, angle-independent absolute velocity measurement is possible as the axial and lateral velocity components can be measured.

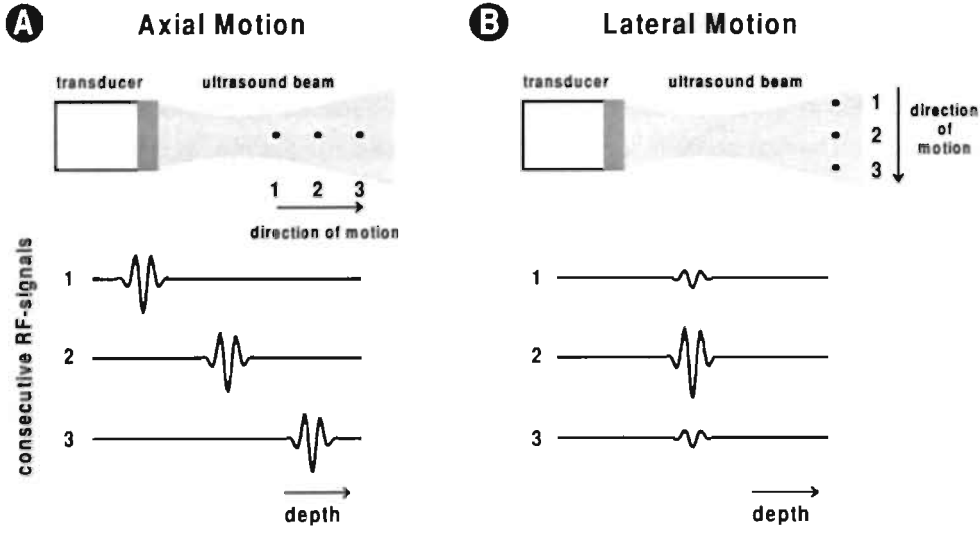

Fig. 2-5 Schematic representation of the influence of axial and lateral motion on the recorded RF-signals. (A) shows the effect of axial motion on the shape of the RF-signals and (B) of lateral motion.

Axial and lateral velocities both influence the shape of the recorded RF-signals in a characteristic way. In M-mode, an axially moving structure results in a shift of the corresponding echo in the consecutive RF-signals. The axial velocity is linearly related to the degree of the shift. Figure 2-5A gives a schematic representation of a structure moving axially away from the transducer. The RF-signals corresponding to three axial positions of the structure are presented. The position of the echo in the RF-signals increases as the distance between the transducer and the structure increases, which is conform Eq. (2-6). In clinical practice, the pulse repetition frequency (PRF) is chosen such that the maximum displacement of a structure during the acquisition of two consecutive RF-signals is maximally a fraction of the wavelength. Eqs. (2-8) and (2-13) show that in the far field the axial pressure fluctuations over such a short distance is almost negligible. Hence, the amplitude of the shifted echo in the consecutive RF-signals will almost be the same.

Structures passing through the sound beam in a lateral direction cause an amplitude modulation of the consecutive RF-signals acquired in M-mode (Atkinson and Berry 1974). This is caused by the inhomogeneity of the sound beam in lateral direction (Eq. (2-10)). The amplitude of the echo corresponding to a structure

passing through the sound beam in lateral direction depends on the lateral place of the structure within the sound beam. Figure 2-5B gives a schematic representation of a structure moving through the sound beam in lateral direction. The RF-signals corresponding to three lateral positions of the structure are presented. The amplitude of the corresponding echoes is the largest as the structure is located near the central axial axis of the transducer. The amplitude of the echo decreases as the distance to the central axis is increased. If the shape of the ultrasound beam is known, the lateral velocity can be derived from the rate at which the amplitude of the consecutive RF-signals changes.

To illustrate that axial and lateral motion components indeed affect RF-signals, Fig. 2-6 shows brightness mode images of the envelope of consecutive RF-signals acquired in a phantom setup in M-mode of a scattering object moving at three different velocities. Figures 2-6A and 2-6B show that the length of the speckle depends on the lateral motion. It can be seen that fast lateral motion results in short speckle. Figure 2-6C shows that axial motion results in an axial (depth) shift of the speckle.

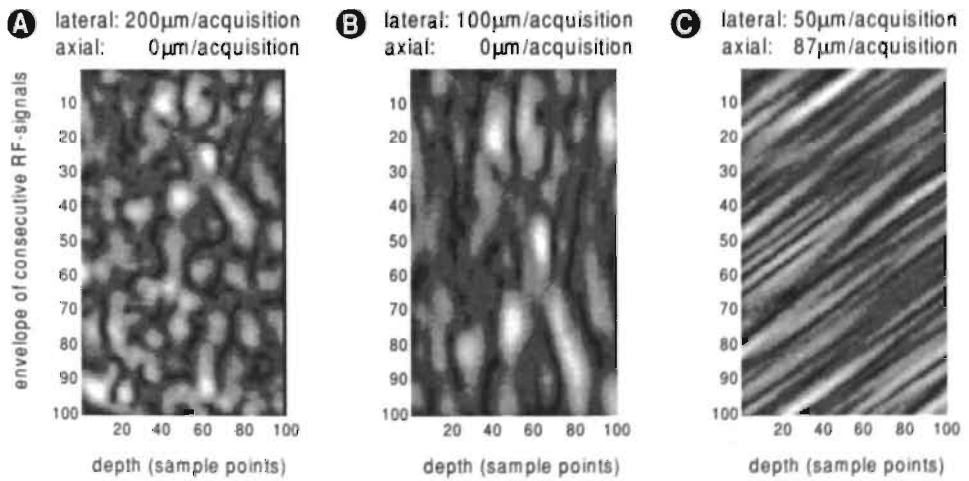

Fig. 2-6 Brightness mode images of the envelope of consecutive RF-signals acquired in a phantom setup in M-mode of a scattering object moving with a displacement between acquisitions of (A) 200 μm pure laterally, (B) 100 μm pure laterally and (C) 50 μm laterally and 87 μm axially.

Because of the phenomena described above, it is possible to determine the axial (Brands et al. 1997; Loupas et al. 1995) and lateral velocity (Dotti and Lombardi 1996; Li et al. 1997) components by means of correlation of consecutive RF-signals. In the current thesis, a completely automatic velocity measurement method with high axial, temporal and velocity resolution is presented for the measurement of the axial and lateral velocity components. Substitution of these velocity components in Eq. (2-17) results in the absolute velocity, i.e., the magnitude of the actual velocity. The direction of the actual velocity in the *xy*-plane (Fig. 2-3) remains unclear, because the direction of the lateral component can not be determined.

2.5 References

Angelsen BAJ. Transcutaneous measurement of aortic blood velocity by ultrasound: a theoretical and experimental approach. PhD Thesis University of Trondheim, 1975.

Atkinson P, Berry MV. Random noise in ultrasonic echoes diffracted by blood. J Phys A: Math Nucl Gen. 1974;7:1293-1302.

Bohs LN, Friemel BH, Trahey GE. Experimental velocity profiles and volumetric flow via two-dimensional speckle tracking. Ultrasound Med Biol. 1995;21:885-898.

Brands PJ. Non-invasive methods for the assessment of wall shear rate and arterial impedance. PhD Thesis, Maastricht University, 1996.

Brands PJ, Hoeks APG, Ledoux LAF, Reneman RS. A radio frequency domain complex cross-correlation model to estimate blood flow velocity and tissue motion by means of ultrasound. Ultrasound Med Biol. 1997;23:911-920.

Buys Ballot CHD. Akustische Versuche auf der Niederländischen Eisenbahn, nebst gelegentlichen Bemerkungen zur Theorie des Hrn. Prof. Doppler. Annalen der Physik und Chemie. 1845a;LXVI:321-351.

Buys Ballot CHD. Bedrog van het gehoororgaan in het bepalen van de hoogte van eenen waargenomen toon. Ceacilia Algemeen Muzikaal Tijdschrift van Nederland. 1845b;2:79-81.

Cape EG, Yoganathan AP. Basic principles of ultrasound. In: Pohost GM, O'Rourke RA, ed. Principles and practice of cardiovascular imaging. Boston: Little, Brown Co, 1991.

D'Cruz IA. M-mode and two-dimensional echocardiography. In: Pohost GM, O'Rourke RA, ed. Principles and practice of cardiovascular imaging. Boston: Little, Brown Co, 1991.

Dotti D, Lombardi R. Estimation of the angle between ultrasound beam and velocity through correlation functions. IEEE Trans Ultrason Ferroel Freq Contr. 1996;43:864-869.

Evans DH, McDicken WN, Skidmore R, Woodcock JP. Doppler ultrasound: Physics, instrumentation, and clinical applications. Chichester: John Wiley & Sons, 1989.

Feynman RP, Leighton RB, Sands M. The Feynman lectures on physics. Reading: Addison-Wesley Publishing Co, 1977.

Gabor D. Theory of communication. Journal of IEEE. 1946;9:429-457.

Goss SA, Johnston RL, Dunn F. Comprehensive compilation of empirical ultrasonic properties of mammalian tissues. J Acoust Soc Am. 1978;64:423-457.

Hudson A, Nelson R. University physics. Philadelphia: Saunders College Publishing, 1990.

Jensen JA. Estimation of blood velocities using ultrasound: a signal processing approach. Cambridge: University Press, 1996.

Jonkman EJ. A historical note: Doppler research in the nineteenth century. Ultrasound Med Biol. 1980;6:1-5.

Kandath D, Nanda NC. Conventional Doppler echocardiography. In: Pohost GM, O'Rourke RA, ed. Principles and practice of cardiovascular imaging. Boston: Little, Brown Co, 1991.

Kinsler LE, Frey AR. Fundamentals of acoustics. New York: John Wiley & Sons, 1962.

Kossoff G. Analysis of focusing action of spherically curved transducers. Ultrasound Med Biol. 1979;5:359-365.

Li W, Carlier S, Céspedes I, Mastik F, van der Steen AFW, Verdouw PD, Born N. Quantification of blood volume flow by decorrelation analysis of radio-frequency intravascular echo signals. Comp Card. 1997;24:1-4.

Loupas T, Powers JT, Gill RW. An axial velocity estimator for ultrasound blood flow imaging, based on a full evaluation of the Doppler equation by means of a two-dimensional autocorrelation approach. IEEE Trans Ultrason Ferroel Freq Contr. 1995;42:672-688.

Phillips DJ, Beach KW, Primozich J, Strandness Jr DE. Should results of ultrasound Doppler studies be reported in units of frequency or velocity? Ultrasound Med Biol. 1989;15:205-212.

Reneman RS, van Merode T, Smeets FAM, Hoeks APG. Geschwindigkeitsmuster in und Wandeigenschaften vom Bulbus der Arteria carotis beim Menschen die Beziehung zur Atherogenese. Hämostaseologie. 1989;9:44-52.

Speaks CE. Introduction to sound: Acoustics for the hearing and speech sciences. San Diego: Singular Publ Group, 1992.

Sung SH. Acoustic wave-field analysis of ultrasonic transducers. J Acoust Soc Am. 1989;86:1595-1601.

Trahey GE, Allison JW, von Ramm OT. Angle independent ultrasonic detection of blood flow. IEEE Trans Biomed Eng. 1987;34:965-967.

Vander AJ, Sherman JH, Luciano DS. Human physiology: the mechanisms of body function. New York: McGraw-Hill Publishing Company, 1990.

Wells PNT. Physical principles of ultrasonic diagnosis. London: Academic Press, 1969.

Wells PNT. Biomedical Ultrasonics. London: Academic Press, 1977.

White DN. Johann Christian Doppler and his effect: a brief history. Ultrasound Med Biol. 1982;8:583-591.

Young HD, Freedman RA. University physics. Reading: Addison-Wesley publishing company, 1996.

Chapter 3

Experimental verification of the correlation behavior of analytic ultrasound radiofrequency signals received from moving structures

L.A.F. Ledoux, J.M. Willigers, P.J. Brands, A.P.G. Hoeks

Ultrasound in Medicine and Biology, 24 (9): 1383-1396; 1998.

Experimental verification of the correlation behavior of analytic ultrasound radiofrequency signals received from moving structures

3.1 Abstract

Conventional pulsed ultrasound systems are only able to detect motion along the ultrasound beam (i.e., axial motion). If the angle between the actual motion direction and the ultrasound beam is known, then the magnitude of the actual motion can be derived. This technique can be applied for laminar blood flow measurements in straight vessels, but for tissue motion it is inadequate because the local tissue motion direction is unknown and may be position-dependent. Assessment of both the axial motion and the lateral motion (i.e., in the direction perpendicular to the ultrasound beam) makes angle-independent assessment of the magnitude of the actual motion feasible. Information about the axial and lateral motion is available in a set of radiofrequency (RF) signals obtained along the same line of observation (M-mode). The experiments described in the present chapter show that axial and lateral motion can be estimated from the shape of the envelope of the 2-D (spatial and temporal) correlation function of analytic M-mode RF-signals. Furthermore, it is demonstrated that the shape is also affected by the bandwidth of the received RF-signals, signal-to-noise ratio, and local amplitude and phase characteristics of the ultrasound beam.

3.2 Introduction

Pulsed ultrasound can be used to assess tissue motion, blood flow velocity or tissue elasticity, which all depend on motion detection. Conventional pulsed ultrasound systems are only able to detect motion of scatterers and/or reflecting structures along the ultrasound beam (i.e., in the axial direction) (Fig. 3-1).

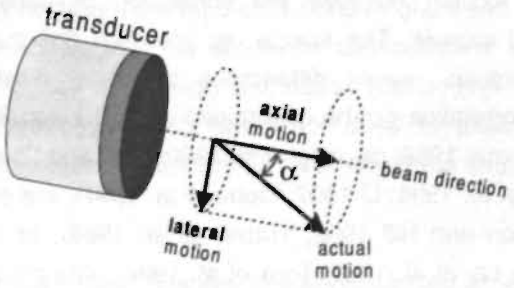

Fig. 3-1 Actual motion component decomposed in an axial and a lateral motion component.

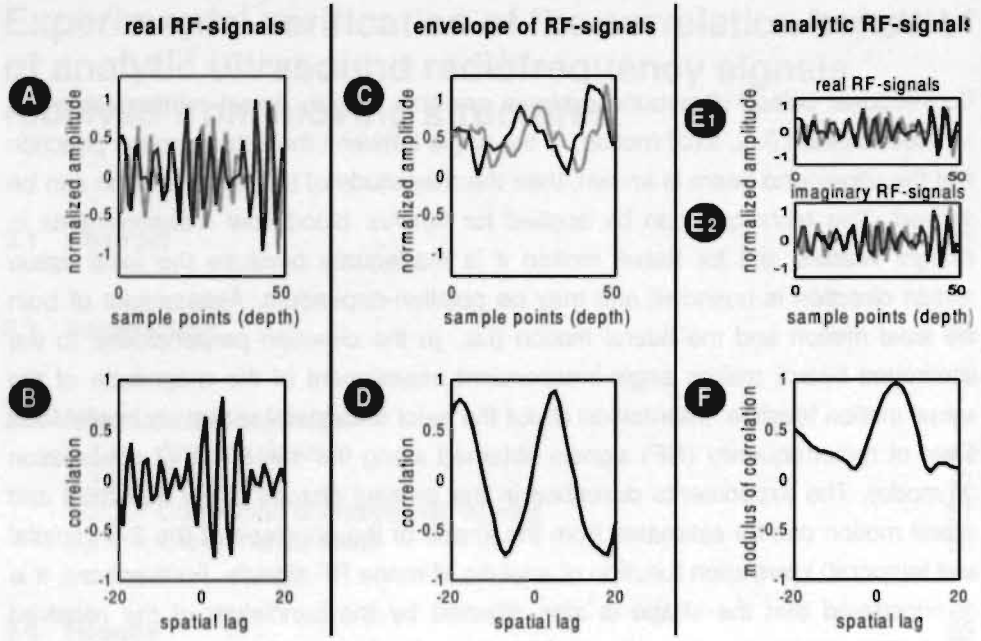

Fig. 3-2 The (spatial) correlation function of two real RF-signals (A) is shown in (B). (D) shows the (spatial) correlation function of the envelope of the same two RF-signals (C). Summation of the real RF-signals of (E_1) and the imaginary RF-signals (Hilbert transform of the real RF-signals) of (E_2) results in analytic RF-signals. The modulus of the (spatial) correlation function of these analytic RF-signals is shown in (F).

One of the techniques to estimate the axial motion between observations with a pulsed ultrasound system employs the correlation of consecutively received radiofrequency (RF) signals. The spatial lag at which the maximum correlation between two RF-signals occurs determines the axial displacement between observations. The correlation can be determined using the acquired real RF-signals (Bonnefous and Pesqué 1986; de Jong et al. 1990; Dotti and Lombardi 1996; Foster et al. 1990; Hoeks et al. 1994; Li 1997; Ophir et al. 1991), the envelope of the real RF-signals (Dickinson and Hill 1982; Trahey et al. 1986), or analytic RF-signals (Brands et al. 1997; Lai et al. 1997; Torp et al. 1994). The characteristic shape of the spatial correlation function using the Pearson product-moment correlation, see Eq. (3-4), of two real RF-signals (Fig. 3-2A) is shown in Fig. 3-2B. The center

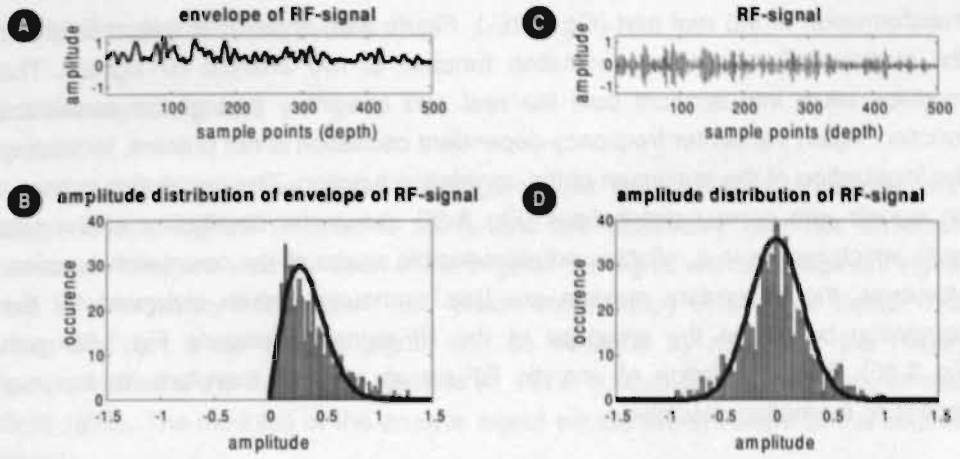

Fig. 3-3 (B) shows a typical histogram of the amplitude distribution of the envelope of an RF-signal (A), which is more or less Rayleigh distributed (solid line). (D) shows a typical histogram of the amplitude distribution of an RF-signal (C), which is almost normal distributed (solid line).

frequency-dependent oscillation of this spatial correlation function complicates the location of the position of the maximum. The characteristic shape of the spatial correlation function of the envelopes of both RF-signals (Fig. 3-2C) is shown in Fig. 3-2D. The center frequency-dependent oscillation is not present, facilitating the location of the maximum of the correlation, albeit that secondary maxima may attain values close to the main maximum.

In general, the Pearson product-moment correlation should be applied only to data with symmetrical (preferably normal) distributions (Ingram and Bloch 1984; Siegel 1956). Figure 3-3B shows that the amplitude distribution of the envelope of an RF-signal (Fig. 3-3A) has a Rayleigh distribution (Burckhardt 1978), which is not symmetrical. The asymmetry of this distribution does not affect the location of the maximum of the correlation function, but it does affect the shape of the correlation function.

The modulus of the correlation function of analytic signals exhibits, in addition to a clearly identifiable location of the maximum also a reliable and reproducible shape. The imaginary part of an analytic signal (Fig. 3-2E_2) is obtained by means of Hilbert

transformation of the real part (Fig. 3-2E_1). Figure 3-2F shows the typical shape of the modulus of the spatial correlation function of two analytic RF-signals. The modulus takes into account both the real and imaginary part of the correlation function. Again the center frequency-dependent oscillation is not present, facilitating the localization of the maximum of the correlation function. The correlation is based on signals with normal distributions (Fig. 3-3D shows the distribution of the real part), which results in a reliable and reproducible shape of the correlation function. Moreover, the secondary maxima are less pronounced than observed for the correlation based on the envelope of the RF-signals (compare Fig. 3-2D with Fig. 3-2F). The correlation of analytic RF-signals seems, therefore, to be very promising for motion detection.

The magnitude of the actual motion follows from the axial motion in combination with the angle between the ultrasound beam and the actual motion direction (angle α [°] in Fig. 3-1). In conventional pulsed ultrasound systems, the angle between the ultrasound beam and the actual motion direction is estimated from the two-dimensional (2-D) brightness (B-mode) image. This can be done quite accurately for laminar blood flow in a straight vessel shown in a longitudinal cross-section. For tissue motion and turbulent blood flow, it is impossible to estimate the position dependent motion direction from the B-mode image.

The magnitude of the actual motion also follows from the axial motion in combination with the motion in the lateral direction (i.e., in the direction perpendicular to the ultrasound beam) (Fig. 3-1). The lateral motion can also be detected by means of correlation of RF-signals, because scatterers or reflecting structures passing through the ultrasound beam in a lateral direction cause an amplitude modulation of consecutive RF-signals obtained along the same line of observation (M-mode) (Atkinson and Berry 1974), affecting the correlation in the temporal direction.

The present chapter demonstrates, with measurements, the correlation behavior of analytic M-mode RF-signals and its applicability for lateral and axial motion detection. The correlation behavior has been examined for various motions, transmitter settings, transducer characteristics and sizes of scatterers. This allows for a detailed analysis of the correlation behavior, not only as function of axial and lateral motion, but also as function of the bandwidth of the received RF-signals, local amplitude and phase characteristics of the ultrasound beam and the signal-to-noise ratio.

3.3 Materials and methods

3.3.1 Analytic signals

Analytic signals describe, without ambiguity, the instantaneous amplitude and phase of real signals (Picinbono 1997), and are commonly used for envelope detection. They are a combination of the original real signal with an imaginary signal that is a frequency-independent -90^{o} phase-shifted copy of the real signal. The imaginary part of an analytic signal can be obtained by means of the Hilbert transformation of the real signal (Gold et al. 1972; Loupas et al. 1995; Rabiner and Gold 1975). The modulus of the analytic signal equals the envelope of the original signal.

The easiest way to transform a real signal into an analytic signal is performed in the frequency domain (Picinbono 1997; Wilson and Robinson 1982). If $S(f)$ is the frequency spectrum of a real signal, then the corresponding analytic frequency spectrum $A(f)$ can be determined as follows:

$$A(f) = \begin{cases} 2S(f) & f > 0 \\ S(f) & f = 0 \\ 0 & f < 0 \end{cases} \qquad (3\text{-}1)$$

Transformation of the frequency spectrum $A(f)$ to the time-domain results in the analytic signal. It is also possible to obtain analytic RF-signals directly in the time-domain (Brands et al. 1997).

3.3.2 Correlation

RF-signals received in pulsed mode along a single line of observation (M-mode) are stored in a matrix structure (RF-matrix) in such a way that the rows of the matrix contain the consecutive RF-signals (Ledoux et al. 1997). The t-th RF-signal can then be described as $RF(t)$ and the z-th sample point of the t-th RF-signal as $RF(t, z)$, with t and z the time and depth indices, respectively. Before processing, the RF-signals are made analytic.

The variance (VAR) of an RF-signal is a measure for the fluctuations in the amplitude of the signal around its mean. The variance of the t-th RF-signal can be determined as:

$$VAR(RF(t)) = \frac{1}{N_z} \sum_{z=1}^{N_z} \left(RF(t,z) - \overline{RF(t)}\right)^* \left(RF(t,z) - \overline{RF(t)}\right) \tag{3-2}$$

where N_z is the number of sample points in the RF-signal, $\overline{RF(t)}$ is the mean of the t-th RF-signal, and $*$ denotes the complex conjugate.

The variance between two different RF-signals is called the covariance (COV), and is a measure of the difference in amplitude behavior of signals. The covariance between the t_1-th and the t_2-nd RF-signal is:

$$COV(RF(t_1), RF(t_2)) = \frac{1}{N_z} \sum_{z=1}^{N_z} \left(RF(t_1,z) - \overline{RF(t_1)}\right)^* \left(RF(t_2,z) - \overline{RF(t_2)}\right) \tag{3-3}$$

The covariance is sensitive to the variance of both signals. Normalization of the covariance reduces the influence of this variance. The normalized covariance is called *correlation* or *correlation coefficient* (R). The term correlation (junction of the words "co" and "relation") was first used by Galton in 1886-1888 and coefficient of correlation by Edgeworth in 1892 (Kendall and Stuart 1979). The (Pearson product-moment) correlation of two RF-signals can be calculated as follows:

$$R(RF(t_1), RF(t_2)) = \frac{COV(RF(t_1), RF(t_2))}{\sqrt{VAR(RF(t_1))VAR(RF(t_2))}} \tag{3-4}$$

Because of the normalization, the value of the correlation will be in the range of -1 to 1.

Because the correlation is determined from sampled RF-signals with a finite length, the number of sample points influences the accuracy of the correlation estimation. The large sample (> 500) variance of the correlation is given by (Kendall and Stuart 1977):

$$VAR(R) = \frac{(1 - \rho^2)^2}{N} \tag{3-5}$$

where R is the estimated correlation, ρ is the expected correlation and N is the number of sample points. Usually, the expected correlation ρ is not known. Its influence can be removed by applying the Fisher z-transform, which is defined as:

$$z = 0.5 \ln\left[\frac{1 + R}{1 - R}\right] \tag{3-6}$$

The variable z has a normal distribution and its variance can be approximated by

$$VAR(z) = \frac{1}{N - 3} \tag{3-7}$$

The 95% confidence limits of the correlation coefficient are subsequently given by:

$$R_{\text{limits}\pm} = \frac{\exp\left[2\left(z \pm 1.96\sqrt{VAR(z)}\right)\right] - 1}{\exp\left[2\left(z \pm 1.96\sqrt{VAR(z)}\right)\right] + 1} \tag{3-8}$$

These confidence limits are only a function of the estimated correlation coefficient (see Eq. (3-6)) and the number of sample points (see Eq. (3-7)). The more (independent) sample points are available, the smaller the confidence interval will be.

If the correlation of RF-signals is used to assess local tissue or blood motion, then spatial and temporal resolution are of importance. Subdivision of the RF-signals into smaller parts increases the spatial resolution, but the accuracy of the correlation estimates decreases because the number of sample points per segment decreases, Eq. (3-8). Sampling of RF-signals with a frequency beyond the Nyquist criterion does not reduce the variance of the correlation, because the number of independent sample points does not increase. The accuracy of the correlation estimates can be increased by determining the correlation of the same segment over a number of consecutive RF-signals (averaging in time) but, as a consequence, the temporal resolution will decrease. Therefore, there is always a trade-off between spatial and temporal resolutions and accuracy of the correlation coefficients.

The sample points from which the local correlation is determined are located in the RF-matrix within a data window with N_Z sample points in the spatial direction and N_T analytic RF-signals in the temporal direction. The correlation for temporal lag T and spatial lag Z between the sample points within a selected data window is:

$$R(T,Z)=\frac{\sum_{t=1}^{N_T-|T|}\sum_{z=1}^{N_Z-|Z|} W_1^* W_2}{\sqrt{\sum_{t=1}^{N_T-|T|}\sum_{z=1}^{N_Z-|Z|} W_1^* W_1 \sum_{t=1}^{N_T-|T|}\sum_{z=1}^{N_Z-|Z|} W_2^* W_2}}$$

$$W_i = w(t-T_i, z-Z_i) - \sum_{\tau=1}^{N_T-|T|}\sum_{\zeta=1}^{N_Z-|Z|} w(\tau-T_i, \zeta-Z_i) \quad i=1 \text{ or } 2$$

$$|T| \le N_T - 1 \text{ and } |Z| \le N_Z - 1 \tag{3-9}$$

$$\text{if } T \ge 0 \text{ then } T_1 = 0 \text{ and } T_2 = -T \text{ else } T_1 = T \text{ and } T_2 = 0$$

$$\text{if } Z \ge 0 \text{ then } Z_1 = 0 \text{ and } Z_2 = -Z \text{ else } Z_1 = Z \text{ and } Z_2 = 0$$

where $w(t, z)$ is the z-th sample of the signal in the t-th row of the data window.

The estimation of the correlation conforming Eq. (3-9) considers only sample points within the selected data window (i.e., a static window). A disadvantage of this approach is that with increasing lag sizes, the number of contributing sample points decreases (solid dots in the illustrations on the left side of Fig. 3-4), which results in less reliable estimates (see Eq. (3-8)). For windows containing many sample points, the influence of the lag on the accuracy will be negligible for small lags.

Instead of using a static window, it is also possible to keep the number of terms that contribute to the estimation of the correlation coefficients constant for all lags. This can be achieved by determining the correlation between the sample points in the initial window (solid squares in the illustrations of the right side of Fig. 3-4) and the sample points in a window that has been shifted T sample points in the temporal direction and Z sample points in the spatial direction (dashed squares in the illustration on the right side of Fig. 3-4). The advantage of this approach is that the accuracy of the estimates is the same for all lags but, for each combination of lags, a different shifted window is considered.

Both approaches have a different spatial and temporal resolution. In case of a static window, the spatial and temporal resolutions are determined by the size of the data window. For shifted windows, the spatial and temporal resolutions are also determined by the size of the initial window, but they degrade as function of the lags considered (exchange of resolution for parameter variance).

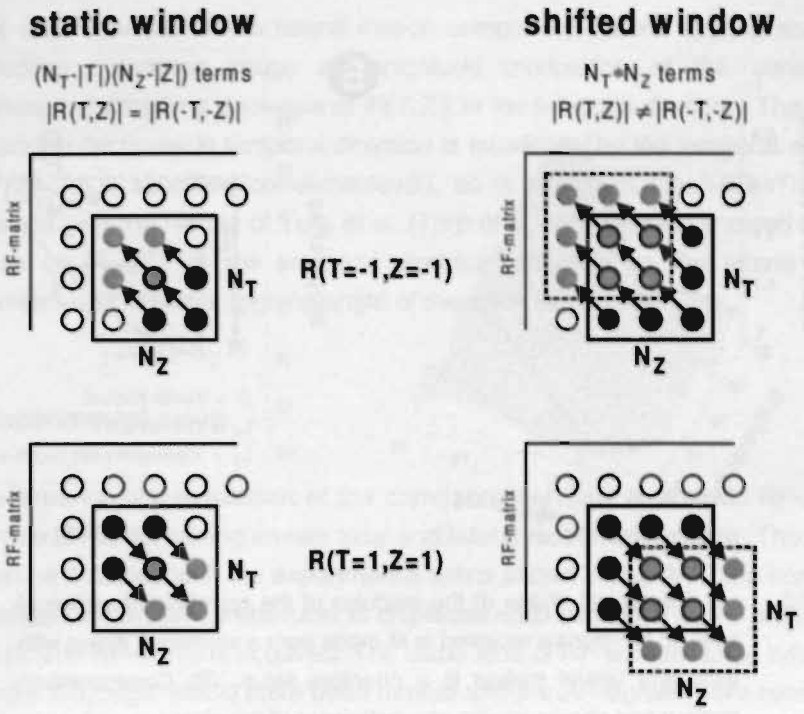

Fig. 3-4 Differences between the estimation of the correlation coefficient based on the sample points within a static window (left) and based on a shift of the initial window (right).

A basic difference between both approaches is that a static window results in a correlation function with a symmetric modulus (i.e., $|R(T,Z)| = |R(-T,-Z)|$). This is because opposite correlation coefficients are based on the same sample points (left side of Fig. 3-4). For a shifted data window, different sample points are considered dependent on the size and direction of the lag (right side of Fig. 3-4).

3.3.3 Correlation of analytic RF-signals

Figure 3-5A shows the typical shape of the modulus of the correlation function ($|R(T,Z)|$) of measured analytic RF-signals received in M-mode from scatterers with axial and lateral motion. A corresponding contour plot is shown in Fig. 3-5B, in which some of the characteristics of the shape are emphasized. The shape depends on a number of signal and system parameters.

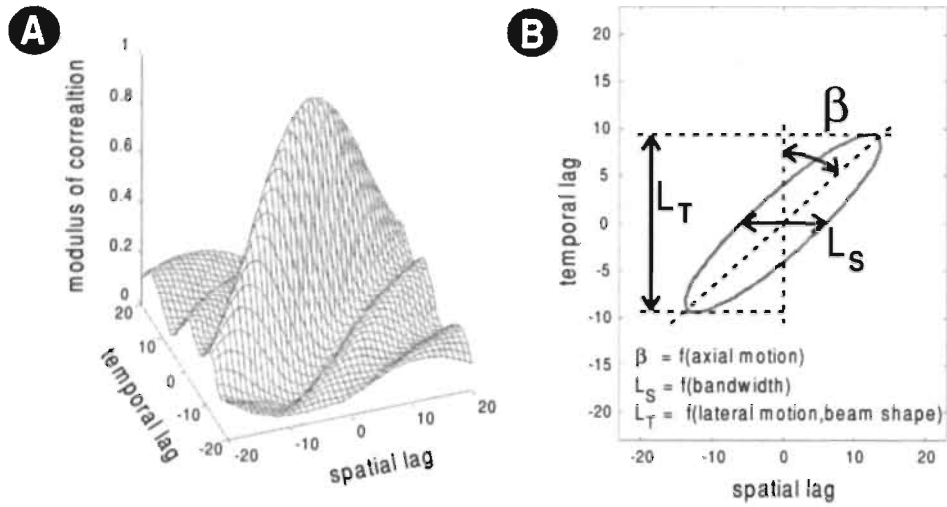

Fig. 3-5 (A) The typical shape of the modulus of the correlation function of analytic RF-signals received in M-mode from a scattering object with axial and lateral motion in a phantom setup. (B) Corresponding contour plot showing some characteristics of the shape.

Recently, Brands et al. (Brands et al. 1997) introduced a model for the correlation of analytic RF-signals based on a model for the spectral distribution of the received RF-signals. The parameters included in this model are: center frequency, spatial quality factor (i.e., center frequency divided by bandwidth), signal power, noise power and axial motion. In this model, the width of $|R(T,Z)|$ (at a specified correlation level) in spatial direction (L_S in Fig. 3-5B) is inversely dependent on the bandwidth of the received RF-signals. The noise influences $|R(T,Z)|$ only at temporal lag zero, because noise is not correlated in time. The model shows that, as a consequence of the axial motion, the spatial lag of maximum correlation increases with increasing time lag, which appears as a rotation of $|R(T,Z)|$ (angle β in Fig. 3-5B). The angle β [°] of rotation of $|R(T,Z)|$ is equal to

$$\beta = \arctan\left(\frac{2f_S S_{AX}}{c}\right) \tag{3-10}$$

where f_S [Hz] is the sample frequency, S_{AX} [m] the axial motion per acquisition, and c [m/s] the sound velocity.

$|R(T,Z)|$ also depends on the lateral motion component. Lateral moving scatterers or reflecting structures cause an amplitude modulation of the consecutive RF-signals, resulting in a decrease of $|R(T,Z)|$ in the temporal direction. The degree of correlation decrease in temporal direction is expressed by the temporal width L_T of $|R(T,Z)|$ (at a specified correlationlevel), as is shown in Fig. 3-5B. This is in accordance with the results of Torp et al. (Torp et al. 1994), which showed that the decrease of $|R(T,Z)|$ in the temporal direction depends on the lateral motion component and the beam opening angle of the transducer.

3.3.4 Experimental setup

For the experimental evaluation of the correlation behavior of analytic RF-signals, data are required containing known axial and lateral motion information. This kind of data can be obtained with the experimental setup shown in Fig. 3-6. The concept of the arrangement is that a transducer is displaced each second and, 0.7 s after each step, a pulsed RF-signal is acquired. The same kind of RF-signals would have been obtained if the target would have been moved and the RF-signals were recorded in M-mode. Acquisition is obtained after 0.7 s to eliminate settling effects. The transducer is moved by a stepper motor with a minimal step size S [m] of 100 µm. The axial S_{AX} [m] and lateral S_{LAT} [m] motions depend on the angle α [°] between the ultrasound beam and the motion direction:

$$\begin{aligned} S_{AX} &= S\cos(\alpha) \\ S_{LAT} &= S\sin(\alpha) \end{aligned} \qquad (3\text{-}11)$$

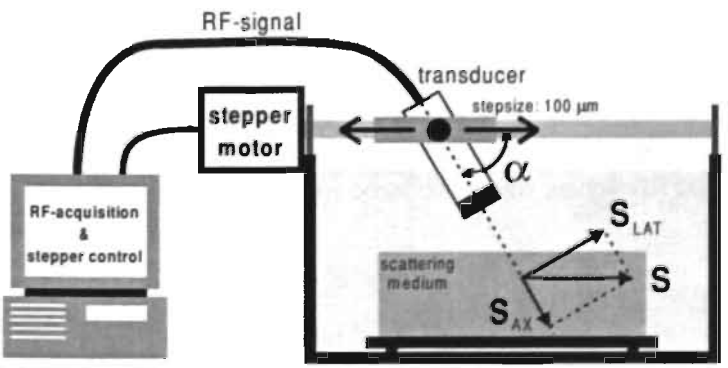

Fig. 3-6 Schematic representation of the experimental arrangement.

3.4 Results

The experiments described in this section show the influence of motion, beam shape, transmitter pulse and scattering material on the shape of the correlation function of measured analytic RF-signals recorded in M-mode.

3.4.1 Influence of motion on correlation

3.4.1.1 *Lateral motion* ($\alpha = 90^{o}$)

To examine the influence of lateral motion on $|R(T,Z)|$, the transducer beam axis has been placed perpendicular to the motion direction (i.e., $\alpha = 90^{o}$). The step size has been varied between 100 µm/acquisition and 1200 µm/acquisition. The temporal data window size was set at 100 RF-signals to maintain the data window within the 12 cm range of the stepper system for the large step size. Figure 3-7 shows the results of some of the measurements. The contour plots (contour level: $|R(T,Z)| = 0.7$) illustrate the influence of various lateral motions on $|R(T,Z)|$. It can be seen that lateral motion only influences the correlation in temporal direction. The smaller the step size is and, thus, the longer the same scatterers remain inside the ultrasound beam, the slower the temporal correlation decreases. The circles in the graph of Fig. 3-8 illustrate the relation between the temporal width (L_T) at $|R(T,Z)| = 0.7$ and the applied lateral motions. The figure shows an inverse proportional relation between the temporal width and the lateral motion.

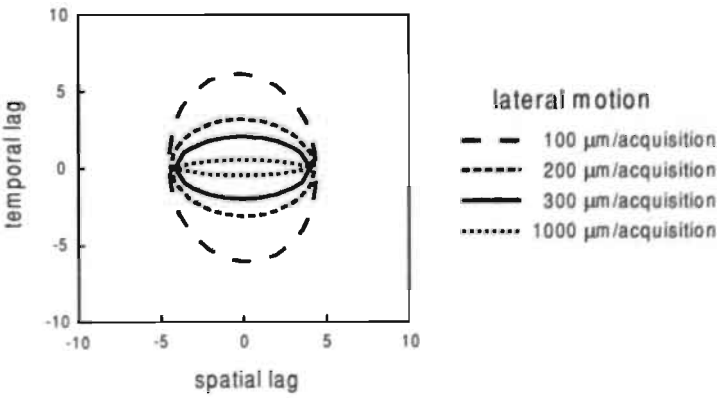

Fig. 3-7 Contour plots (contour level: $|R(T,Z)| = 0.7$) showing the influence of various lateral motions on $|R(T,Z)|$.

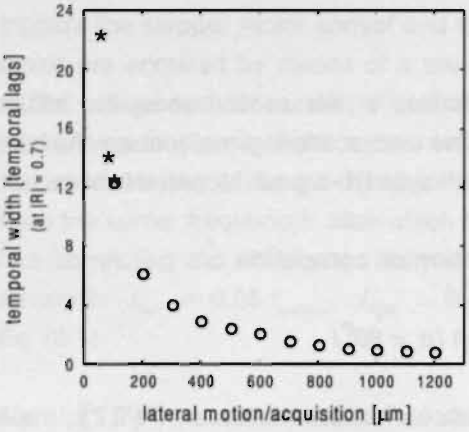

Fig. 3-8 Relation between the temporal width (L_T) of the correlation function and the applied lateral motions/acquisition. The circles are obtained from measured data with only lateral motion (see Fig. 3-7), and the stars are obtained from data with lateral as well as axial motion (see Fig. 3-9).

3.4.1.2 *Axial and lateral motion (α = variable)*

Rotation of the transducer beam within the plane defined by the beam and direction of motion results in a combination of an axial and a lateral motion component in the received RF-signals. The expected axial and lateral motions given by Eq. (3-11) and the expected angle of rotation of $|R(T,Z)|$ given by Eq. (3-10) for angles of 30°, 60°, 90°, 120° and 150° are listed in Table 3-1. Note that a negative axial motion is directed towards the transducer.

Figure 3-9 shows contour plots of the results of the above mentioned measurements (contour level: $|R(T,Z)| = 0.7$). The axial motion causes a rotation of the shape of $|R(T,Z)|$. The larger the axial motion is, the larger the angle of rotation will be. The direction of the axial motion determines the direction of the rotation. Axial motion away from the transducer results in a clockwise rotation (Fig. 3-9A), while axial motion towards the transducer results in a rotation in the opposite direction (Fig. 3-9B). The angle of rotation of the shape of $|R(T,Z)|$ can be estimated as follows

$$\hat{\beta} = \arctan\left(\frac{Z_{T,max}}{T}\right) \qquad (3\text{-}12)$$

Table 3-1. Expected axial and lateral motion components per acquisition and expected and estimated angles of rotation of $|R(T,Z)|$ corresponding to the angle of the transducer.

angle of measurement (α)	30°	60°	90°	120°	150°
expected lateral motion [µm/acquisition]	50	87	100	87	50
expected axial motion [µm/acquisition]	87	50	0	-50	-87
expected angle of rotation (β)	66.9°	53.3°	0.0°	-53.3°	-66.9°
estimated angle of rotation ($\hat{\beta}$)	66.5°	52.4°	0.0°	-50.2°	-66.5°

where $Z_{T,max}$ is the spatial lag of the largest correlation coefficient at temporal lag T. The angles of rotation, estimated by this equation for the considered measurements, are listed in Table 3-1.

The lateral motion governs the width of $|R(T,Z)|$ in temporal direction as is indicated in Fig. 3-5B. Again, the smaller the lateral motion is, the larger is the temporal width of $|R(T,Z)|$. The stars in Fig. 3-8 illustrate the relation between the temporal width (L_T) at $|R(T,Z)| = 0.7$ and the applied lateral motions.

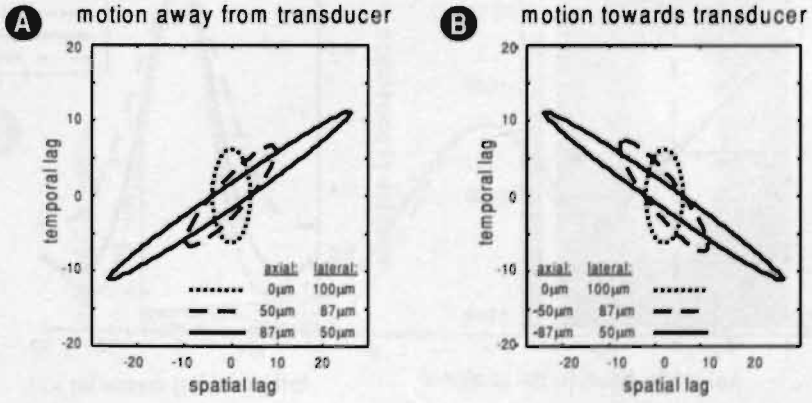

Fig. 3-9 Contour plots (contour level: $|R(T,Z)| = 0.7$) showing the influence of different combinations of axial and lateral motions on the shape of the correlation function. (A) Contour plot of the shape for axial motion away from the transducer, and (B) for axial motion toward the transducer.

3.4.2 Influence of beam shape on correlation

3.4.2.1 *Beam shape*

So far, it has been demonstrated that the temporal width of $|R(T,Z)|$ is related to the lateral step size. The size of the temporal width depends on the time the same scatterers remain inside the ultrasound beam. To examine the influence of the beam shape, a transducer with an almost elliptical beam shape has been employed (7.5 MHz linear array of a Scanner 350, Pie Medical, Maastricht, the Netherlands). The electrical focus was set at 60 mm, the transmit voltage was 10 V and the sample volume was located at 55 mm. The intensity plot of the round-trip beam profile of this transducer at a depth of 30 mm is shown in Fig. 3-10A. The transducer was placed perpendicular to the motion direction (i.e., $\alpha = 90^{o}$), and it was orientated in three different positions in such a way that the lateral motion was either along the short, oblique or long axis of the beam (see arrows in Fig. 3-10A). Figure 3-10B shows the corresponding behavior of $|R(T,0)|$. It can be seen that motion along the short axis results in the fastest decrease of $|R(T,0)|$, whereas the same motion along the long axis results in a slower decrease.

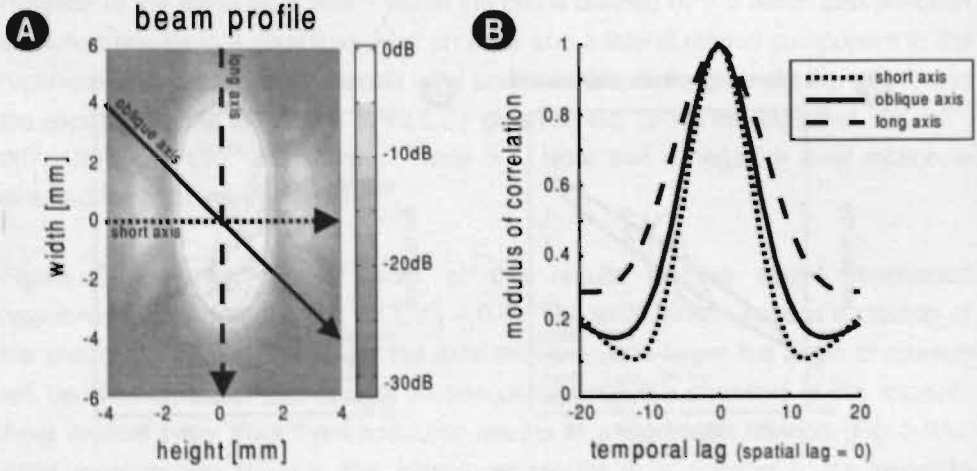

Fig. 3-10 (A) Intensity plot of the round-trip beam profile of a linear array transducer at a depth of 30 mm. The arrows indicate the directions of the lateral motion component. (B) Corresponding decreases of the correlation in temporal direction.

3.4.2.2 *Depth of measurement*

The beam width changes with depth. Figure 3-11A shows the contour plot of the round-trip beam profile (maximum of the reflection of a synthetic ball with 2 mm diameter at each position, normalized at each depth) of the focused circular KB-Aerotech transducer. Beyond the focus (> 20 mm), the width of the beam increases with depth. Therefore, the same lateral motion at a larger depth should result in a slower decrease of the correlation in temporal direction. $|R(T,0)|$ is considered at depths of 20 mm, 30 mm, 40 mm and 50 mm. The results are shown in Fig. 3-11B. The graph indicates that there is, indeed, a relation between depth (and, thus, beam width) and decrease of correlation in the temporal direction, but this relation is not as systematic as the increase in beam width.

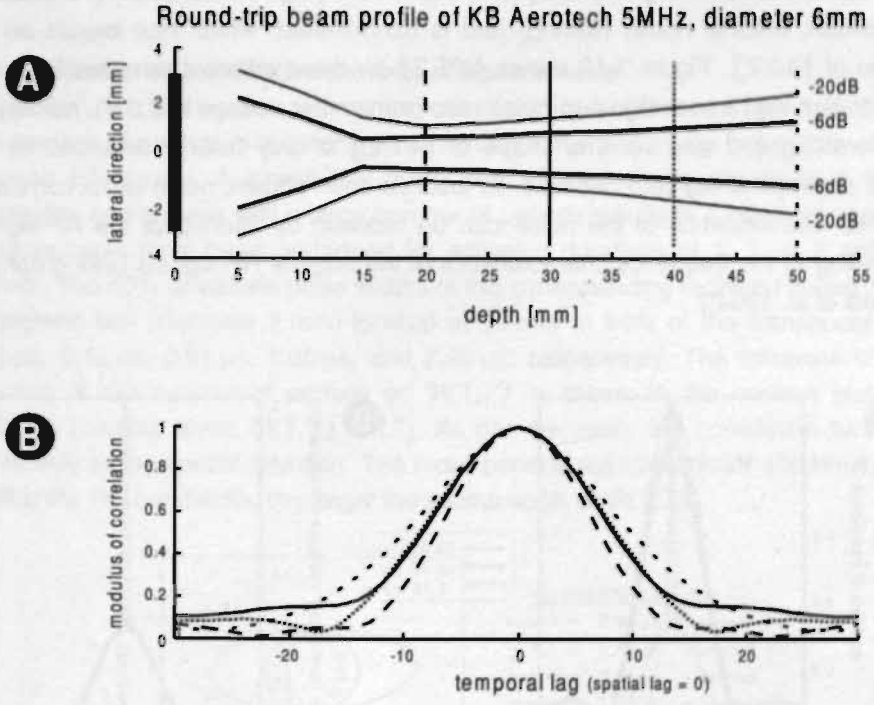

Fig. 3-11 (A) Contour plot of the round-trip beam profile of the focused circular KB-Aerotech transducer (diameter: 6 mm). (B) Correlation in the temporal direction of RF-samples corresponding to depths of 20 mm, 30 mm, 40 mm and 50 mm. (A) and (B) use the same encoding for position.

3.4.3 Influence of transmitter pulse on correlation

3.4.3.1 *Transmitter voltage*

Normally, a higher transmitter voltage results in a better signal-to-noise ratio *SNR* [dB]. The effect of transmitter voltages of 2.5 V (*SNR* = 5 dB), 5 V (*SNR* = 16 dB) and 10 V (*SNR* = 23 dB) on $|R(T,0)|$ is shown in Fig. 3-12A. A noise-dependent spike occurs at $|R(0,0)|$ and the values for all other lags are lower depending on the signal-to-noise ratio (*SNR*). The spike occurs because noise is not correlated in time. Normalization of the correlation for the noise can be reached by dividing each correlation coefficient by $|R(1,0)|$. After this "noise normalization", all three temporal correlation functions coincide (Fig. 3-12B).

The noise within RF-signals is system-dependent (e.g., influenced by transducer bandwidth, thermal noise, filtering) and is band-limited, which has impact on the shape of $|R(0,Z)|$. Figure 3-13 shows $|R(T,Z)|$ for three different temporal lags of a registration with a poor signal-to-noise ratio (transmitter voltage is 2.5 V), namely for temporal lag 0, 1 and 10. The shape of $|R(T,Z)|$ is only heavily disturbed by the noise at temporal lag zero because, as just has been shown, noise is not correlated in time. The influence of the noise can be reduced by filtering of the RF-signals according to the frequency characteristics of the original RF-signals (see graphs in (Hoeks et al. 1994)).

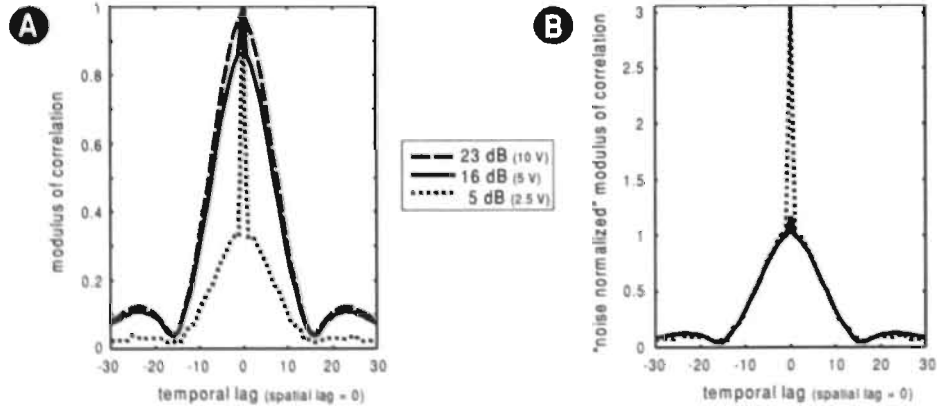

Fig. 3-12 (A) Influence of transmitter voltage on $|R(T,0)|$. (B) Corresponding "noise-normalized" correlation functions (i.e., each correlation function is divided by $|R(1,0)|$).

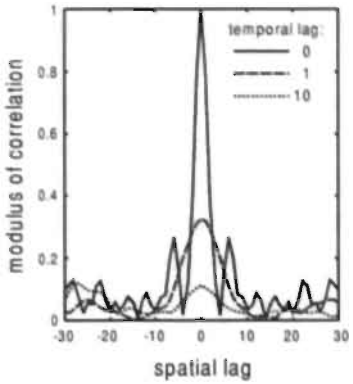

Fig. 3-13 Influence of noise on the correlation in spatial direction for a registration with a poor signal-to-noise ratio. The shape of the correlation function is disturbed only at temporal lag zero.

3.4.3.2 *Number of transmitted periods of square wave*

The number of periods of the transmitted square wave affects the bandwidth of the received RF-signals. A transmitter pulse with a few periods results in a large bandwidth, and a pulse with a large number of periods results in a small bandwidth. Measurements have been performed for emission durations of 1, 2, 4, 8 and 15 periods. The 50% amplitude pulse widths of the corresponding received pulses from a synthetic ball (diameter 2 mm) located at 30 mm in front of the transducer are 0.36 µs, 0.42 µs, 0.81 µs, 1.60 µs, and 2.99 µs, respectively. The influence of the variation of the number of periods on $|R(T,Z)|$ is shown in the contour plots of Fig. 3-14 (contour level: $|R(T,Z)| = 0.7$). As can be seen, the correlation function varies only in the spatial direction. The more periods are transmitted and, thus, the smaller the RF-bandwidth, the larger the spatial width of $|R(T,Z)|$.

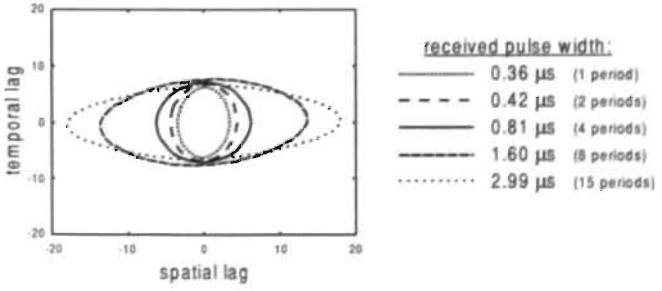

Fig. 3-14 Influence of number of periods of transmitted square wave on $|R(T,Z)|$ (contour level: $|R(T,Z)| = 0.7$).

3.4.4 Influence of scattering material on correlation

Finally, the influence of the scattering material on the shape of $|R(T,Z)|$ has been examined. Three different materials have been used. One medium was the standard Carborundum target. The particle size of Carborundum is approximately 5 µm and is much smaller than the wavelength of the transmitted ultrasound waves (≈ 300 µm). The second medium was made of 1% mass-concentration Sephadex G-200 (Pharmacia Fine Chemicals, Uppsala, Sweden) (de Jong et al. 1991) bound in Agorose (1% mass-concentration). The particle size of Sephadex is approximately 50 µm. The third medium was a synthetic sponge with a random distribution of its pores. Using a microscope, it can be seen that there are roughly 2 pores/mm. Measurements with these three materials resulted in the correlation plots shown in Fig. 3-15. The figure shows that the correlation is independent of the material under investigation both in the temporal and spatial direction.

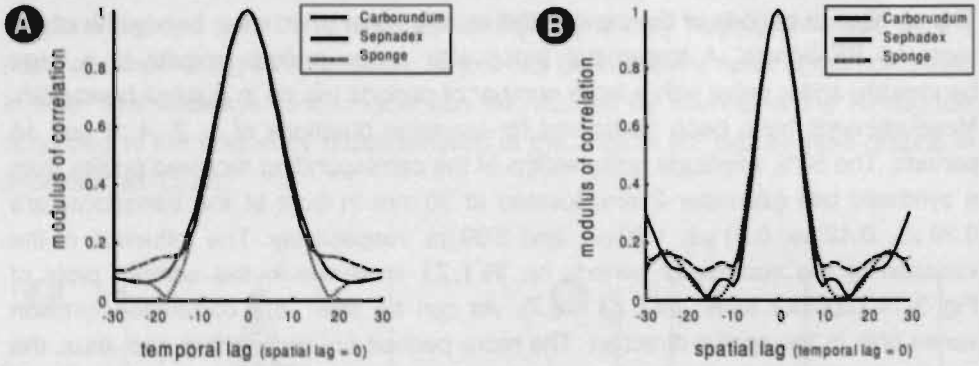

Fig. 3-15 The influence of different scattering materials on the shape of $|R(T,Z)|$ in the (A) temporal and in the (B) spatial direction. The materials are Carborundum (particle size: ≈ 5 µm, mass-concentration: 1%; 1% Agarose), Sephadex (particle size: ≈ 50 µm, mass concentration: 1%; 1% Agarose) and a synthetic sponge with a random distribution of pores (approximately 2 pores/mm).

3.5 Discussion

Figures 3-7 and 3-9 show that, at a given depth, the motion-dependent behavior of the correlation is as expected for all combinations of lateral and axial motion. Only results for a depth of 30 mm are shown, which is 10 mm beyond the focus of the employed transducer, but the systematic motion-dependent change of $|R(T,Z)|$ did also occur at other depths, both in the far field and in the near field of the transducer. The direction and magnitude of the axial motion can be derived from the direction and degree of rotation of the shape of the 2-D correlation function. Table 3-1 shows that there is a good agreement between the expected and estimated angles of rotation. Part of the difference between both angles is caused by the fact that the estimated angle of rotation is based on an integer value for the spatial lag of maximum correlation. The magnitude of the lateral motion component can be derived from the temporal width of $|R(T,Z)|$, but its direction remains unresolved. Figure 3-8 shows that the temporal width of $|R(T,Z)|$ is inverse proportional with the lateral motion. The magnitudes of the axial and lateral motion components are sufficient to determine the magnitude of the actual motion component.

The decrease of $|R(T,Z)|$ in the temporal direction of either RF-signals or the envelope of RF-signals, or analytic RF-signals, is based on the same phenomenon. Therefore, the way $|R(T,Z)|$ decreases in temporal direction should be the same for all these methods. Some reports assume a linear relation between temporal lag and decrease of $|R(T,Z)|$ in temporal direction (Dotti and Lombardi 1996; Li 1997), but others state that the relation is Gaussian (Kallel et al. 1997; Torp et al. 1994; Wagner et al. 1983). Our measurements indicate a non-linear relation both in the far field and in the near field (results not shown).

The maximum detectable lateral motion is dependent on the beam width. Lateral motion can be detected as long as a part of the scatterers that were present in the beam during the registration of the previous RF-signal are still present during the registration of the current RF-signal.

The Nyquist aliasing criterion does not apply for the measurement of the axial motion via the rotation of the shape of $|R(T,Z)|$. If there is only axial motion, then the maximal detectable axial motion depends on the size of the spatial data window. As long as the axial motion per observation is smaller than the spatial data window size, the spatial shift of the correlation maximum at temporal lag 1 can still be found.

contour plot corresponding to one period is in temporal direction slightly smaller than the others. This is because the noise downscales the correlation coefficients.

The graphs of Fig. 3-15 show that $|R(T,Z)|$ is not influenced by the kind of material under investigation. This indicates that the method is applicable for a large range of materials (e.g., blood and tissue).

3.6 Conclusions

It has experimentally been demonstrated that the shape of $|R(T,Z)|$ of analytic RF-signals recorded in M-mode is dependent on lateral and axial motion, bandwidth of the received RF-signals, signal-to-noise ratio, and local amplitude and phase-dependent characteristics of the ultrasound beam. The spatial width of the 2-D shape of $|R(T,Z)|$ has an inverse relation with the RF-bandwidth. The noise influences $|R(0,Z)|$. Axial motion causes a rotation of the shape. The direction of the rotation indicates whether the axial motion is toward or away from the transducer. The temporal width of $|R(T,Z)|$ is inverse proportional with the lateral motion. Combination of the axial and lateral motion components results in the same rotation and the same temporal width as would be obtained for the individual axial and lateral motion components.

If the depth-dependent phase and amplitude characteristics of the ultrasound beam are known, then it should be possible to obtain, with a good temporal and spatial resolution, the true magnitude of the actual motion via the modulus of the correlation of analytic RF-signals for any angle of observation. If the size of the data window and the pulse repetition frequency are chosen adequately, then larger motions can be resolved than would be possible with conventional pulsed ultrasound systems.

3.7 References

Atkinson P, Berry MV. Random noise in ultrasonic echoes diffracted by blood. J Phys A: Math Nucl Gen. 1974;7:1293-1302.

Bonnefous O, Pesqué P. Time domain formulation of pulse-Doppler ultrasound and blood velocity estimation by cross correlation. Ultrason Imaging. 1986;8:73-85.

Brands PJ, Hoeks APG, Ledoux LAF, Reneman RS. A radio frequency domain complex cross-correlation model to estimate blood flow velocity and tissue motion by means of ultrasound. Ultrasound Med Biol. 1997;23:911-920.

Burckhardt CB. Speckle in ultrasound B-mode scans. IEEE Trans Sonics Ultrasonics. 1978;SU-25:1-6.

de Jong PGM, Arts T, Hoeks APG, Reneman RS. Determination of tissue motion velocity by correlation interpolation of pulsed ultrasonic echo signals. Ultrason Imaging. 1990;12:84-98.

de Jong PGM, Arts T, Hoeks APG, Reneman RS. Experimental evaluation of the correlation interpolation technique to measure regional tissue velocity. Ultrason Imaging. 1991;13:145-161.

de Korte CL, Céspedes EI, van der Steen AFW, Lancée CT. Intravascular elasticity imaging using ultrasound: feasibility studies in phantoms. Ultrasound Med Biol. 1997;23:735-746.

Dickinson RJ, Hill CR. Measurement of soft tissue motion using correlation between A-scans. Ultrasound Med Biol. 1982;8:263-271.

Dotti D, Lombardi R. Estimation of the angle between ultrasound beam and velocity through correlation functions. IEEE Trans Ultrason Ferroel Freq Contr. 1996;43:864-869.

Foster SG, Embree PM, O'Brien WD. Flow velocity profile via time-domain correlation: error analysis and computer simulation. IEEE Trans Ultrason Ferroel Freq Contr. 1990;37:164-175.

Gold B, Oppenheim AV, Rader CM. Theory and implementation of the discrete Hilbert transform. In: Rabiner LR, Rader CM, ed. Digital Signal Processing. New York: IEEE Press, 1972: 94-109.

Hoeks APG, Arts TGJ, Brands PJ, Reneman RS. Processing scheme for velocity estimation using ultrasound RF cross correlation techniques. Eur J Ultrasound. 1994;1:171-182.

Ingram D, Bloch RF. Mathematical methods in medicine. Part 1: Statistical and analytical techniques. Chichester: John Wiley and sons, 1984.

Kallel F, Varghese T, Ophir J, Bilgen M. The nonstationary strain filter in elastography: Part II. Lateral and elevational decorrelation. Ultrasound Med Biol. 1997;23:1357-1369.

Kendall M, Stuart A. Distribution theory. London: Charles Griffin & Company, 1977.

Kendall M, Stuart A. Inference and relationship. London: Charles Griffin & Company, 1979.

Lai X, Torp H, Kristoffersen K. An extended autocorrelation method for estimation of blood velocity. IEEE Trans Ultrason Ferroel Freq Contr. 1997;44:1332-1342.

Ledoux LAF, Brands PJ, Hoeks APG. Reduction of the clutter component in Doppler ultrasound signals based on singular value decomposition: a simulation study. Ultrason Imaging. 1997;19:1-18.

Li W. Image and signal processing in intravascular ultrasound. PhD Thesis Erasmus University Rotterdam, 1997.

Loupas T, Peterson RB, Gill RW. Experimental evaluation of velocity and power estimation for ultrasound blood flow imaging, by means of a two-dimensional autocorrelation approach. IEEE Trans Ultrason Ferroel Freq Control. 1995;42:689-699.

Ophir J, Céspedes I, Ponnekanti H, Yazdi Y, Li X. Elastography: a quantitative method for imaging the elasticity of biological tissues. Ultrason Imaging. 1991;13:111-134.

Picinbono B. On instantaneous amplitude and phase of signals. IEEE Trans Sign Proc. 1997;45:552-560.

Rabiner LR, Gold B. Theory and application of digital signal processing. Englewoods Cliffs: Prentice-Hall, 1975.

Siegel S. Nonparametric statistics for the behavioral sciences. Tokyo: McGraw-Hill Kogakusha, 1956.

Torp H, Kristoffersen K, Angelsen BAJ. Autocorrelation techniques in color flow imaging: signal model and statistical properties of the autocorrelation estimates. IEEE Trans Ultrason Ferroel Freq Contr. 1994;41:604-612.

Trahey GE, Smith SW, von Ramm OT. Speckle pattern correlation with lateral aperture translation: experimental results and implications for spatial compounding. IEEE Trans Ultrason Ferroel Freq Contr. 1986;33:257-264.

Wagner RF, Smith SW, Sandrik JM, Lopez H. Statistics of speckle in ultrasound B-scans. IEEE Trans Sonics Ultrasonics. 1983;30:156-163.

Wilson LS, Robinson DE. Ultrasonic measurement of small displacements and deformations of tissue. Ultrason Imaging. 1982;4:71-82.

Chapter 4

Modeling of the correlation of analytic ultrasound radiofrequency signals for angle-independent motion detection

L.A.F. Ledoux, J.M. Willigers, P.J. Brands, A.P.G. Hoeks

Ultrasonic Imaging, accepted for publication (february 1999).

Modeling of the correlation of analytic ultrasound radiofrequency signals for angle-independent motion detection

4.1 Abstract

Conventional pulsed ultrasound systems are able to assess motion of scatterers in the direction of the ultrasound beam (i.e., axial motion) by determining the lag at which the maximum correlation occurs between consecutively-received radiofrequency (RF) signals. The accuracy, resolution, and processing time of this technique is improved by making use of a model for the correlation of RF-signals. All previously-described correlation models only include axial motion, but it is common knowledge that lateral motion (i.e., motion in the plane perpendicular to the beam axis) reduces the correlation of RF-signals in time. In the present chapter, a model for the correlation of analytic RF-signals in depth and time is derived and verified. It also includes, aside of some signal and transducer parameters, both axial and lateral motion. The influence of lateral motion on the correlation of (analytic) RF-signals is strongly related to local phase and amplitude characteristics of the ultrasound beam. It is shown how the correlation model, making use of an ultrasound transducer with a circular beam shape, can be applied to estimate, independent of angle, the magnitude of the actual motion. Furthermore, it is shown that the model can be applied to estimate the local signal-to-noise ratio and RF-bandwidth.

4.2 Introduction

In medicine, noninvasive imaging techniques are gaining more and more attention for reliable diagnoses and follow-up studies. One of these imaging techniques uses pulsed ultrasound, resulting in cross-sectional images (B-mode images). Pulsed ultrasound can also be employed to register the axial motion of scatterers or reflecting structures (i.e., motion in the direction of the ultrasound beam). Axial motion detection is essential for the determination of tissue motion (Chen et al. 1995; de Jong et al. 1990; Dickinson and Hill 1982; Wilson and Robinson 1982), blood flow velocity (Bonnefous and Pesqué 1986; Brandestini and Forster 1978; Foster et al. 1990; Hoeks et al. 1994; Loupas et al. 1995; Ramamurthy and Trahey 1991) or tissue elasticity (Céspedes et al. 1997; Gao et al. 1996; Ophir et al. 1991). The motion-dependent information (e.g., blood flow velocity) can be color encoded and superimposed on the B-mode image, enriching the information content of the image (Evans 1993; Ferrara and DeAngelis 1997).

Axial motion can be assessed by correlating consecutively-received radiofrequency (RF) signals. The spatial lag at which the maximum correlation between two RF-signals occurs determines the axial motion between observations. The technique of estimating axial motion by means of correlation has gradually evolved. The first algorithms only searched for the lag with maximum correlation (Bonnefous and Pesqué 1986; Embree and O'Brien 1990; Foster et al. 1990). The precision of these techniques depended on the sample frequency, which, in some cases, needed to be as high as 10 times the estimated carrier frequency. Further improvement of the precision was obtained by interpolation of the correlation function in the region near the maximum.

To search for the lag with maximum correlation, all the aforementioned techniques needed to determine correlation coefficients at a large number of lags. The number of correlation coefficients required can be reduced by modeling the shape of the correlation function, allowing at the same time, an RF-sample frequency in accordance with the Nyquist criterion. The model of the correlation function (correlation model) can be used to derive estimators for the parameters included in the model (axial motion among others). Each such parameter estimator needs only the calculation of a few correlation coefficients (Brands et al. 1997; de Jong et al. 1990; Hoeks et al. 1993; Loupas et al. 1995). An advantage of the model approach is that, aside of the axial motion, other characteristics of the RF-signals can also be determined. One of these is the local carrier frequency (i.e., the center frequency of the received signals). Inherently, axial motion estimates are corrected for the depth-dependent frequency attenuation of this center frequency.

De Jong et al. (de Jong et al. 1990) introduced a correlation model for real RF-signals with a rectangular and band-limited power spectral density distribution. Hoeks et al. (Hoeks et al. 1993) improved this model by using a more realistic Gaussian-shaped power spectral density distribution. Both models assumed band-limited RF-signals, resulting in velocity-dependent biased estimates as was also shown by Hoeks et al. (Hoeks et al. 1993). The bias is no problem in blood flow velocity measurements, but it is too large for the registration of small local differences in tissue motion. Brands et al. (Brands et al. 1997) showed that this bias can be strongly reduced by applying the same model to analytic RF-signals (obtained by means of Hilbert transformation). From the latter correlation model, based on analytic RF-signals, estimators are derived for the signal-to-noise ratio, the local center frequency and the local bandwidth of the RF-signals.

All aforementioned correlation models can only estimate the axial component of the actual motion. To derive the magnitude of the actual motion, it is assumed that the local angle between the axial motion component and the ultrasound beam is known. This angle is normally difficult to determine, especially for tissue motion. Therefore, the accuracy of most motion detection algorithms is only as accurate as the estimate of the angle of measurement. The angle of measurement is no longer needed if the estimation of the actual motion could be based on the axial and the lateral motion (i.e., the motion in the direction perpendicular to the ultrasound beam).

Scatterers or reflecting structures, passing through the ultrasound beam in a lateral direction, cause an amplitude modulation of consecutive RF-signals obtained along the same line of observation (M-mode) affecting the maximal obtainable correlation between the RF-signals (Atkinson and Berry 1974). The decrease of the maximal obtainable correlation as function of the time between the registrations is related to the lateral motion (Dickinson and Hill 1982; Dotti et al. 1992; Li 1997; Ramamurthy and Trahey 1991; Torp et al. 1994; Trahey et al. 1986). The experimental study of Ledoux et al. (chapter 3 or (Ledoux et al. 1998)) showed that the correlation of analytic RF-signals received in M-mode indeed revealed information about the lateral motion. Furthermore, it was shown that the decrease of correlation as function of the time between the registrations is not only influenced by lateral motion, but also by depth-dependent phase and amplitude characteristics of the ultrasound beam.

Estimators can only be developed for the lateral and actual motion components, based on the correlation of analytic RF-signals, if a model for the correlation is available that also includes the lateral motion component. In the present chapter, a model for the correlation of analytic M-mode RF-signals is derived, including axial and lateral motion and characteristics of the received RF-signals and of the ultrasound beam. Deriving the correlation model based on analytic RF-signals, which results in a complex model, has a number of advantages. First, the correlation model for real RF-signals can easily be derived from the one for analytic RF-signals by taking the real part of the latter correlation model. In the second place, the amplitude and phase behavior of the correlation function can easily be separated by taking the modulus and argument of the correlation model, respectively. This might be very helpful for the derivation of motion estimators based on the model. Thirdly, taking the modulus of the correlation function of analytic RF-signals results in a smooth shape of the correlation function (chapter 3

or (Ledoux et al. 1998)), whereas the shape of the correlation function of real RF-signals contains a periodic modulation that depends on the center frequency and the sample frequency of the RF-signals (Dotti and Lombardi 1996). For the latter function, it is difficult to find automatically the location of the main correlation lobe (Dotti and Lombardi 1996).

To verify the analytic correlation model, correlation coefficients obtained from measured RF-signals are fitted with model-based correlation coefficients. It is shown that the model can be applied to estimate the local bandwidth, center frequency and signal-to-noise ratio of the received RF-signals and the direction and magnitude of the axial motion without aliasing. Moreover, it is shown that for a transducer with a circular beam shape, the model can be applied to estimate the magnitude of the lateral motion. Combining the magnitudes of the axial and lateral motion components results in an estimate for the magnitude of the actual motion independent of the angle of insonification.

4.3 Theory: derivation analytic correlation model

4.3.1 Model for RF-signals

The first received RF-signal RF_0 of a registration along the same line of observation (M-mode) can, after being made analytic (by means of Hilbert-transformation), be described as (Dotti and Lombardi 1996)

$$RF_0(t) = \int\int\int f_t(x,y,z)\, g(x,y,z)\, dx\, dy\, dz \qquad (4\text{-}1)$$

where t [s] is the time after transmission, $g(\ )$ is the 3-D space distribution of the scatterers, and $f_t(\ )$ is the 3-D sensitivity function of the transducer describing the 3-D pressure wave volume contributing to the RF-sample at time t. For analytic RF-signals, the 3-D sensitivity function is complex. The x [m], y [m], and z [m] coordinates correspond to the transverse, the elevation, and the axial direction, respectively (Fig. 4-1).

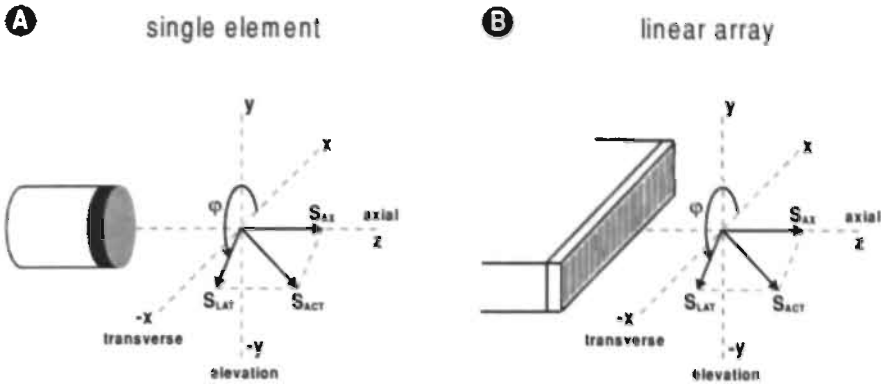

Fig. 4-1 Schematic representation of the orientation for a single-element transducer (A) and a linear array (B). The actual motion component (S_{ACT}) can be decomposed in an axial (S_{AX}) and a lateral (S_{LAT}) motion component.

The local distribution of the scatterers is assumed to be constant during the passage of the ultrasound pressure wave. This is a reasonable assumption because the duration of the passage is typically only a few tenths of a microsecond. The displacement of the scatterers is during such a small time interval less than 1 μm, even if the scatterers move at a relatively high velocity (> 1 m/s).

The distribution of scatterers or small structures within an organ (e.g., capillaries or muscle fibers) is stochastic, but their motion is coherent, because they are part of an organ. In brightness mode (B-mode) images, these distributions result in a textured pattern (speckle). The scatterer distribution, as well as the associated speckle pattern, is relatively stable while the target is translated over multiple wavelengths along any direction within the imaging plane (Trahey et al. 1988). The actual motion S_{ACT} [m] of the scatterers between observations has a transverse, elevation and axial component. The axial component is denoted by S_{AX} [m] and the transverse and elevation components are denoted by $S_{LAT}\cos(\varphi)$ and $S_{LAT}\sin(\varphi)$ respectively, where S_{LAT} [m] is the magnitude of the motion component in the lateral direction (i.e., in the xy-plane), and φ [°] is the counter clockwise angle between the positive x-axis and the direction of the lateral motion component (Fig. 4-1). Consequently, the T-th analytic RF-signal after RF_0 is given by

$$RF_T(t) = \int\int\int f_t(x,y,z)\, g(x - TS_{LAT}\cos(\varphi), y - TS_{LAT}\sin(\varphi), z - TS_{AX})\, dx\, dy\, dz \qquad (4\text{-}2)$$

4.3.2 Correlation of analytic RF-signals

The complex correlation between two analytic RF-signals is defined as (Press et al. 1986)

$$R(T, Z) = \left\langle RF_0^*(t)\, RF_T\left(t + \frac{Z}{f_S}\right)\right\rangle \tag{4-3}$$

where T [-] is temporal lag, Z [-] is axial lag, f_S [Hz] is sample frequency, $*$ denotes complex conjugated and $\langle\ \rangle$ denotes mathematical expectation. Substitution of Eqs. (4-1) and (4-2) for the RF-signals in Eq. (4-3) for the correlation function results in

$$\begin{aligned} R(T,Z) = \int\int\int\int\int\int\int \big\langle g(x,y,z)\, g(x'-TS_{LAT}\cos(\varphi), y'-TS_{LAT}\sin(\varphi), z'-TS_{AX})\big\rangle \\ \times\ f_t^*(x,y,z)\, f_{t+\frac{Z}{f_S}}(x',y',z')\, dx\,dy\,dz\,dx'\,dy'\,dz' \end{aligned} \tag{4-4}$$

Scatterers are considered to be numerous and δ-correlated in space (Angelsen 1980; Dotti and Lombardi 1996; Torp et al. 1994). For this case, the expectation of the space distribution of the displaced scatterers is equal to

$$\begin{aligned} &\big\langle g(x,y,z)\, g(x'-TS_{LAT}\cos(\varphi), y'-TS_{LAT}\sin(\varphi), z'-TS_{AX})\big\rangle = \\ &\big\langle g^2\big\rangle\, \delta(x-x'+TS_{LAT}\cos(\varphi), y-y'+TS_{LAT}\sin(\varphi), z-z'+TS_{AX}) \end{aligned} \tag{4-5}$$

where δ is the Dirac delta function and $\langle g^2\rangle$ is the mean-squared value of the space distribution of the scatterers. Making use of this δ-correlation, the correlation function of Eq. (4-4) can be simplified to

$$R(T,Z) = \big\langle g^2\big\rangle \int\int\int f_t^*(x,y,z)\, f_{t+\frac{Z}{f_S}}(x+TS_{LAT}\cos(\varphi), y+TS_{LAT}\sin(\varphi), z+TS_{AX})\, dx\,dy\,dz \tag{4-6}$$

The two sensitivity functions f_t and $f_{t+\frac{Z}{f_S}}$ are located at almost the same positions; therefore both sensitivity functions are considered to have the same shape and size.

4.3.3 3-D sensitivity function

The 3-D sensitivity function of the transducer is a 3-D pressure wave volume insonifying the scatterers that contribute to the value of the received RF-signal at a certain delay after transmission. The shape of the sensitivity function in the axial direction depends on the length of the transmitted ultrasound pulse. This pulse length is inversely related to the bandwidth of the received RF-signals. Therefore, the shape of the sensitivity function in the axial direction (z-axis) is related to the power spectral density distribution of the received RF-signal, while in the *xy*-plane the sensitivity function is dependent on local characteristics of the ultrasound beam. These contributions to the sensitivity function can be derived separately and can be combined retrospectively.

The power spectral density distribution of an RF-signal is approximately Gaussian-shaped (Hoeks et al. 1993). For analytic RF-signals, the distribution reduces to a single sideband distribution centered at the carrier frequency f_c [Hz] (Fig. 4-2A) and is in normalized form ($P(f_c) = 1$) given by (Gold et al. 1972):

$$P(f) = \exp\left[- \pi \left(\frac{f - f_c}{BW_{EQ}} \right)^2 \right] \tag{4-7}$$

where BW_{EQ} [Hz] is the equivalent power bandwidth. The equivalent power bandwidth is the width of a rectangular power spectral density distribution, which has the same area as the curve defined by the original power spectral density function, where the height of the equivalent function is equal to the height at f_c of the original function (Deutsch 1969). For a Gaussian distribution, the equivalent power bandwidth is related to the bandwidth at a specified level in decibels (with respect to the maximum) by

$$BW_{EQ} = \sqrt{- \frac{5\pi}{dB \ln[10]}}\, BW_{dB} \tag{4-8}$$

where dB is a negative value indicating the specified dB-level.

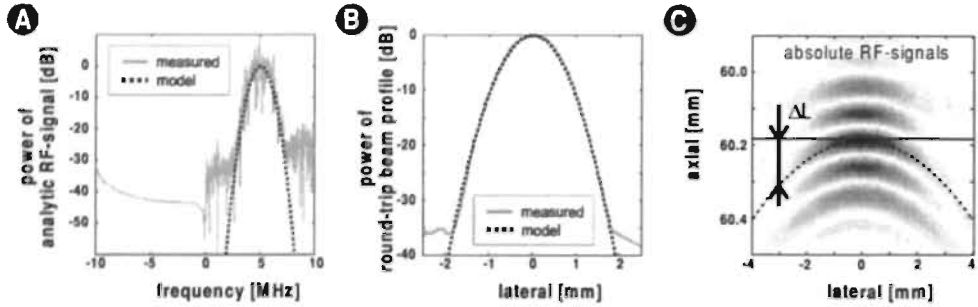

Fig. 4-2 Assumptions made for derivation of 3-D sensitivity function. The measured signals are acquired with a focused circular single element transducer (MLA 50 BS of KB-Aerotech) with a diameter of 6 mm and a center frequency of approximately 5 MHz. (A) shows the power spectral density distribution of an acquired analytic RF-signal (solid gray line) and its Gaussian approximation (dotted black line). (B) shows the (power) round-trip beam profile at 30 mm (solid gray line) and its Gaussian approximation (dotted black line). (C) shows the (round-trip) curvature of the wave front at 60 mm and its parabolic approximation (dotted black line).

The axial shape of the sensitivity function can easily be derived from an RF-signal originating from a single scatterer. Because of the linearity of the (inverse) Fourier transform and the assumption of a homogeneous contribution of all scatterers, the power spectral density distribution of a signal originating from a single scatterer has theoretically the same shape as the spectrum of a signal originating from multiple randomly-distributed scatterers. Therefore, it is possible to derive from the power spectral density distribution of a random signal an RF-signal originating from only one scatterer. Such an RF-signal for a scatterer located at an axial distance d $(= 0.5ct_d)$ and with a power spectral density distribution conforming Eq. (4-7), is in normalized form $(\max[|RF(t)|] = 1)$ equal to

$$RF(t) = \exp\left[-2\pi BW_{EQ}^2 (t-t_d)^2\right] \exp\left[j\{2\pi f_c (t-t_d)+\psi\}\right] \tag{4-9}$$

where ψ [rad] is a random initial phase.

To receive an RF-signal with the shape conforming Eq. (4-9), the axial sensitivity function corresponding to the RF sample at t seconds after transmission must be equal to (for convenience given in the space domain)

$$f_t(z) = \exp\left[C_Z (z_t - z)^2\right] \exp\left[j\{C_P (z_t - z) + \psi\}\right] \qquad (4\text{-}10)$$

$$\text{with} \quad C_Z = -\frac{8\pi BW_{EO}^2}{c^2} \quad \text{and} \quad C_P = \frac{4\pi f_C}{c}$$

where c [m/s] is the sound velocity in the medium under investigation and z_t $(= 0.5\, c\, t)$ [m] is the axial distance corresponding to t seconds after transmission.

The transverse and elevation beam widths contribute to the sensitivity function in the xy-plane. The sensitivity function corresponding to the RF-sample at t seconds after transmission in transverse direction $f_t(x)$ and in elevation direction $f_t(y)$ may be approximated by Gaussian functions (Fig. 4-2B) resulting in (Azimi and Kak 1985)

$$f_t(x) = \exp\left[C_X(z_t) x^2\right] \qquad \text{where} \qquad C_X(z_t) = \frac{dB \ln[10]}{5 wx_{dB}^2(z_t)} \qquad (4\text{-}11)$$

and

$$f_t(y) = \exp\left[C_Y(z_t) y^2\right] \qquad \text{where} \qquad C_Y(z_t) = \frac{dB \ln[10]}{5 wy_{dB}^2(z_t)} \qquad (4\text{-}12)$$

where $wx_{dB}(z_t)$ [m] and $wy_{dB}(z_t)$ [m] are, respectively, the transverse and elevation round-trip beam widths at axial distance z_t [m] at a specified power level (in dB) with respect to the peak value. It should be noted that dB is negative, because it expresses an attenuation.

The overall 3-D sensitivity function, contributing to the RF-sample at t seconds after transmission, is the product of the sensitivity functions of Eqs. (4-10), (4-11), and (4-12) resulting in

$$f_t(x, y, z) = \exp\left[C_X(z_t)\, x^2 + C_Y(z_t)\, y^2 + C_Z\, (z_t - z)^2\right] \exp\left[j\left\{C_P\, (z_t - z) + \psi\right\}\right] \qquad (4\text{-}13)$$

The 3-D sensitivity function of Eq. (4-13) is only valid for plane waves, for which all pressure waves in the xy-plane are in phase. Focused transducers do not transmit plane waves, but they transmit a curved wave front (e.g., by means of an acoustic lens or curvature of the transducer) such that most pressure waves arrive simultaneously in the focus (Huygens' principle). Figure 4-2C shows the absolute value of the RF-signals acquired by means of a lateral scan across a steel ball with a diameter of 2 mm located at approximately 60 mm. The resulting image shown in Fig. 4-2C has a close resemblance with the sensitivity function and shows that the wave front has some degree of curvature. The solid line shows the wave front for a plane wave, whereas the dashed line is a parabolic approximation of the actual wave front. The additional axial round-trip distance traveled by a curved wave front at position (x,y,z) compared to the corresponding plane wave front is expressed by $\Delta L(x,y,z)$ [m] (Fig. 4-2C). If the transverse additional distance $\Delta L(X,0,z)$ [m] and the elevation additional distance $\Delta L(0,Y,z)$ [m] are known, we can approximate the additional distance for each position in that xy-plane at axial distance z [m] with the following parabolic equation

$$\Delta L(x,y,z) = P_x(z)x^2 + P_y(z)y^2 \tag{4-14}$$

$$\text{where} \quad P_x(z) = \frac{\Delta L(X,0,z)}{X^2} \quad \text{and} \quad P_y(z) = \frac{\Delta L(0,Y,z)}{Y^2}$$

The overall 3-D sensitivity function of Eq. (4-13) must be corrected for the additional distance ΔL [m]. The correction can be omitted in the amplitude part, because the influence of the additional distance on the amplitude is very small (a small value quadratic in the exponent). Correcting the phase part of the overall 3-D sensitivity function results in the following modified 3-D sensitivity function

$$f_t'(x,y,z) = \exp\left[C_x(z_t)x^2 + C_y(z_t)y^2 + C_z(z_t - z)^2\right] \tag{4-15}$$

$$\times \exp\left[j\left[C_p(z_t - z - 0.5\Delta L(x,y,z_t)) + \psi\right]\right]$$

The modified 3-D sensitivity function can be split up in the following transverse $f_t'(x)$, elevation $f_t'(y)$ and axial $f_t'(z)$ parts

$$f_t'(x,y,z) = f_t'(x)\, f_t'(y)\, f_t'(z)$$

$$\text{with} \quad \begin{aligned} f_t'(x) &= \exp\left[C_X(z_t)x^2\right] \exp\left[-0.5jC_P P_X(z_t)x^2\right] \\ f_t'(y) &= \exp\left[C_Y(z_t)y^2\right] \exp\left[-0.5jC_P P_Y(z_t)y^2\right] \\ f_t'(z) &= \exp\left[C_Z(z_t - z)^2\right] \exp\left[j\{C_P(z_t - z) + \psi\}\right] \end{aligned} \tag{4-16}$$

4.3.4 Analytic correlation model

Substitution of the sensitivity functions of Eq. (4-16) in the correlation function of Eq. (4-6) results in

$$R(T,Z) = \langle g^2 \rangle\, R_X(T,Z)\, R_Y(T,Z)\, R_Z(T,Z) \tag{4-17}$$

where R_X [-], R_Y [-] and R_Z [-] are the transverse, the elevation and the axial part of the correlation functions, respectively.

In accordance with Eqs. (4-6) and (4-17), the transverse part of the correlation model is given by

$$R_X(T,Z) = \int_{-\infty}^{\infty} f_t'^{*}(x)\, f'_{t+\frac{Z}{f_s}}\left(x + T\, S_{LAT} \cos(\varphi)\right) dx \tag{4-18}$$

After substitution of the equation for the transverse part of the sensitivity function (Eq. (4-16)), Eq. (4-18) can be simplified to

$$R_X(T,Z) = \sqrt{\frac{\pi}{2C_X(z_t)}} \exp\left[T^2 C_{Bx}(z_t)\, S_{LAT}^2 \cos^2(\varphi)\right]$$

$$\text{with} \quad C_{Bx}(z_t) = \frac{C_X(z_t)}{2} + \frac{C_P^2 P_X^2(z_t)}{2C_X(z_t)} \tag{4-19}$$

$$= \frac{dB \ln[10]}{10 wx_{dB}^2(z_t)} + \frac{40\pi^2 f_C^2 wx_{dB}^2(z_t) \Delta L^2(X,0,z_t)}{c^2 X^4 dB \ln[10]}$$

where $C_{Bx}(z_t)$ [1/m^2] is a negative value that is a function of the characteristics of the ultrasound beam in transverse direction at depth z_t [m].

The elevation part of the correlation model can be derived in the same way resulting in

$$R_Y(T,Z) = \sqrt{-\frac{\pi}{2C_Y(z_t)}}\exp\left[T^2 C_{By}(z_t) S_{LAT}^2 \sin^2(\varphi)\right]$$

$$\text{with} \quad C_{By}(z_t) = \frac{C_Y(z_t)}{2} + \frac{C_P^2 P_Y^2(z_t)}{2C_Y(z_t)} \tag{4-20}$$

$$= \frac{dB\ln[10]}{10wy_{dB}^2(z_t)} + \frac{40\pi^2 f_C^2 wy_{dB}^2(z_t)\Delta L^2(0,Y,z_t)}{c^2 Y^4 dB\ln[10]}$$

where $C_{By}(z_t)$ [1/m^2] is a negative value that is a function of the characteristics of the ultrasound beam in elevation direction at depth z_t [m].

In accordance with Eqs. (4-6) and (4-17), the axial part of the correlation model is given by

$$R_Z(T,Z) = \int_{-\infty}^{\infty} f_t^*(z)\, f_{t+\frac{Z}{f_S}}(z + TS_{AX})\, dz \tag{4-21}$$

After substitution of the equation for the axial part of the sensitivity function (Eq. (4-16)), Eq. (4-21) can be simplified to

$$R_Z(T,Z) = \sqrt{-\frac{\pi}{2C_Z}}\exp\left[\frac{C_Z}{2}\left(\frac{Zc}{2f_S} - TS_{AX}\right)^2\right]\exp\left[jC_P\left(\frac{Zc}{2f_S} - TS_{AX}\right)\right] \tag{4-22}$$

It should be noted that this is the same equation as was derived by Brands et al. (Brands et al. 1997).

After expansion of Eq. (4-17) and normalization (i.e., $R(0,0)=1$), the normalized analytic correlation model is given by

$$R(T,Z)= \exp\left[T^2 C_B(z_t,\varphi) S_{LAT}^2 - \frac{4\pi BW_{EO}^2}{c^2}\left(\frac{Zc}{2f_S} - TS_{AX} \right)^2 \right] \times \exp\left[j\frac{4\pi f_C}{c}\left(\frac{Zc}{2f_S} - TS_{AX} \right) \right] \tag{4-23}$$

$$\text{with} \quad C_B(z_t,\varphi) = C_{Bx}(z_t)\cos^2(\varphi) + C_{By}(z_t)\sin^2(\varphi)$$

where $C_B(z_t,\varphi)$ [1/m^2] is a negative value that is a function of the characteristics of the ultrasound beam at depth z_t [m] and the direction of the lateral motion φ [rad].

Noise influences the behavior of the correlation of RF-signals. In the case of noisy RF-signals, the autocorrelation $R(0,0)$ is a measure for the sum of the normalized signal power P_S and the normalised noise power P_N of the RF-signals (i.e., $R(0,0) = P_S + P_N = 1$). Assuming that the noise within an RF-signal has the same Gaussian-shaped power spectral density distribution as the ultrasound signal and knowing that the noise between consecutive RF-signals is uncorrelated (chapter 3 or (Ledoux et al. 1998)), the correlation model for RF-signals with noise is given by

$$R(T,Z)= \left(P_S + P_{N_T}\right)\exp\left[T^2 C_B(z_t,\varphi) S_{LAT}^2 - \frac{4\pi BW_{EO}^2}{c^2}\left(\frac{Zc}{2f_S} - TS_{AX} \right)^2 \right] \times \exp\left[j\frac{4\pi f_C}{c}\left(\frac{Zc}{2f_S} - TS_{AX} \right) \right] \tag{4-24}$$

where $P_{N_{T=0}} = P_N$ and $P_{N_{T\neq 0}} = 0$.

4.4 Experimental setup

In the remaining sections, the modulus of the analytic correlation model of Eq. (4-24) will be evaluated with phantom measurements. The argument part of the correlation model is the same as described by for example Loupas et al. (Loupas et al. 1995) and Brands et al. (Brands et al. 1997) and therefore its evaluation will not be presented. The argument part of the model can be applied to estimate the local center frequency of the received RF-signals and to obtain unbiased estimates for the axial motion that are limited in accordance with the Nyquist-criterion.

To verify the modulus part of the analytic correlation model, RF-signals with known motion information are obtained with the arrangement shown in Fig. 4-3. A stepper motor displaces the transducer after which a pulsed RF-signal is acquired.

The transducer is a circular single-element transducer MLA 50 BS of KB-Aerotech (Lewistown, Pennsylvania, USA) with a diameter of 6 mm, a center frequency of approximately 5 MHz and its focus at approximately 15 mm (Fig. 4-5A). A circular single-element transducer has the advantage that at each depth $C_{Bx}(z)$ and $C_{By}(z)$ are the same, namely $C_B(z)$ (Eqs. (4-19) and (4-20)).

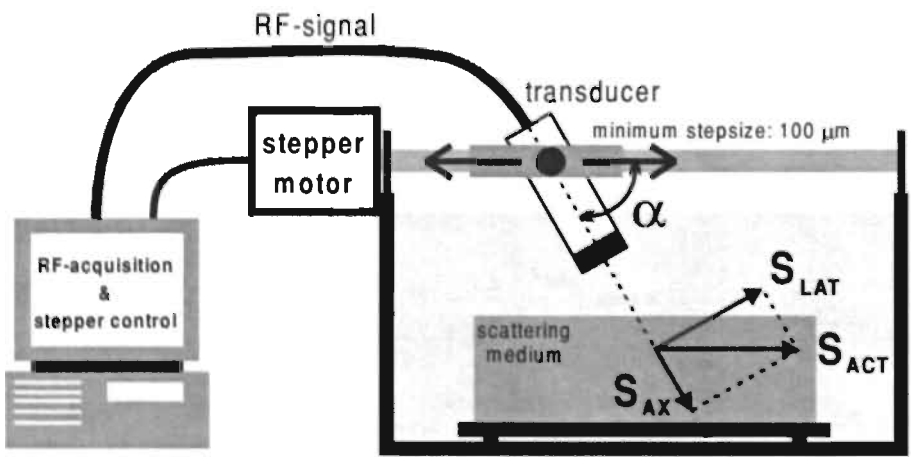

Fig. 4-3 Schematic representation of the experimental arrangement.

The target used was made of a 1% mass-concentration Agarose (Life Technologies, Paisley, Scotland) solution, to which 1% mass-concentration Carborundum particles (≈ 5 μm) are added. The sound velocity of the target is approximately 1490 m/s. The type of scattering medium is not critical for the shape of the correlation function (chapter 3 or (Ledoux et al. 1998)).

In the experimental setup, the axial S_{AX} [m] and lateral S_{LAT} [m] motion components depend on the angle α [°] between the ultrasound beam and the actual motion direction:

$$\begin{aligned} S_{AX} &= S_{ACT}\cos(\alpha) \\ S_{LAT} &= S_{ACT}\sin(\alpha) \end{aligned} \tag{4-25}$$

where S_{ACT} [m] is the actual step size. Unless otherwise mentioned, the step size is equal to 100 μm per acquisition and the angle is 90° (i.e., only lateral motion).

The stepper motor and the data acquisition is controlled by a personal computer. A transmit/receive board and a data acquisition board in the personal computer transmits/receives and digitizes the RF-signals, respectively. Unless otherwise mentioned, the transmitter will activate the transducer with 2 periods of a 5 MHz square wave with a peak-to-peak voltage of 30 V. The received RF-signals are digitized (dynamic range 12 bits, sample frequency f_S = 20 MHz, i.e., approximately four times the center frequency) and stored on the hard disk.

Before processing, the RF-signals are digitally band-pass filtered (2nd order Butterworth: $f_{low} = 0.05 f_S$ and $f_{high} = 0.45 f_S$) and are made analytic as follows (Gold et al. 1972). If $S(f)$ is the frequency spectrum of the RF-signal, then the corresponding analytic frequency spectrum $A(f)$ is equal to:

$$A(f) = \begin{cases} 2S(f) & f > 0 \\ S(f) & f = 0 \\ 0 & f < 0 \end{cases} \tag{4-26}$$

Transformation of the frequency spectrum $A(f)$ to the time-domain results in the analytic RF-signal.

To increase the precision of the calculated correlation coefficients, the correlation calculations will not be based on two RF-signals, but on the mean of a set of RF-signals using a data window. This data window is located arbitrarily in the RF-matrix and contains N_Z sample points in the axial direction and N_T points in the temporal direction. The dimensions of the data window specify the possible axial (depth) and temporal resolution. The normalized correlation coefficient for temporal lag T and spatial lag Z between the sample points within a selected data window is:

$$R(T,Z) = \frac{\sum_{t=1}^{N_T-|T|} \sum_{z=1}^{N_Z-|Z|} W_1^* W_2}{\sqrt{\sum_{t=1}^{N_T-|T|} \sum_{z=1}^{N_Z-|Z|} W_1^* W_1 \sum_{t=1}^{N_T-|T|} \sum_{z=1}^{N_Z-|Z|} W_2^* W_2}}$$

$$W_i = w(t - T_i, z - Z_i) - \frac{\sum_{\tau=1}^{N_T-|T|} \sum_{\zeta=1}^{N_Z-|Z|} w(\tau - T_i, \zeta - Z_i)}{(N_T - |T|)(N_Z - |Z|)} \qquad i = 1 \text{ or } 2$$

$$|T| \le N_T - 1 \quad \text{and} \quad |Z| \le N_Z - 1 \tag{4-27}$$

$$\text{if} \quad T \ge 0 \quad \text{then} \quad T_1 = 0 \quad \text{and} \quad T_2 = -T \quad \text{else} \quad T_1 = T \quad \text{and} \quad T_2 = 0$$

$$\text{if} \quad Z \ge 0 \quad \text{then} \quad Z_1 = 0 \quad \text{and} \quad Z_2 = -Z \quad \text{else} \quad Z_1 = Z \quad \text{and} \quad Z_2 = 0$$

where $w(t,z)$ is the z-th sample of the analytic RF-signal in the t-th row of the data window.

The derivation of the correlation model is based on a Gaussian beam profile, which is certainly the case in the far field, which starts for focused transducers at the focus (chapter 2). Therefore, the RF-data used for the evaluation of the correlation model should preferably not be located in front of the focus. Unless otherwise mentioned, the segments of the RF-signals that are located at 30 mm in front of the transducer (i.e., behind the focus) are considered for the calculation of the correlation coefficients. The axial size of the applied data window is 32 sample points (i.e., approximately 1.2 mm). The precision of the calculated correlation coefficients

increases with increasing size of the data window (chapter 3 or (Ledoux et al. 1998)). To exclude the effect of the size of the data window in the evaluation of the correlation model, a relatively large number of 100 RF signals is considered (temporal window size).

The model and the correlation of the observed RF-data are compared by means of a least-squares fit algorithm. The fit algorithm includes only correlation coefficients with a positive temporal lag greater than zero, because the modulus of the complex correlation function is symmetric (chapter 3 or (Ledoux et al. 1998)). Correlation coefficients at temporal lag zero are excluded in the fit to reduce the influence of noise. Furthermore, all correlation coefficients located near $|R(0,0)|$ greater than a certain threshold value are included in the fit algorithm. The threshold was set at 0.67, which is possible because of the good signal-to-noise ratio of the acquired RF-signals. The least-squares fit results in estimates for: (1) the normalized signal power P_S [-], (2) the equivalent bandwidth BW_{EQ} [Hz], (3) the axial motion per acquisition S_{AX} [m], and (4) $C_B(z)S_{LAT}^2$ [-] which is a combination of the depth dependent beam characteristic $C_B(z)$ [1/m^2] and the lateral motion per acquisition S_{LAT} [m]. Their initial values for the fit algorithm (Matlab function "fmins") are 1 (no noise), 2.5 MHz ($= 0.5 f_C$), 0 µm per acquisition and -0.01 ($C_B(z)S_{LAT}^2$ is negative), respectively. The results are listed as mean value plus/minus the standard deviation of a set of data windows with the same kind of signals.

4.5 Results

4.5.1 Measurement and model agreement

Figure 4-4 gives an overview of the agreement between the 2-D correlation function based on an assessed RF-data set and the corresponding model applying fitted parameters. The RF-data set had a high signal-to-noise ratio, an axial motion component of 50 µm per acquisition and a lateral motion component of 87 µm per acquisition. Near the center of the correlation function (i.e., where the correlation coefficients are relatively large) the agreement is excellent. At larger temporal and axial lags, small fluctuations in the observed correlation function occur, caused by incidental correlation between RF-signals. These incidental rises of the correlation are not included in the model.

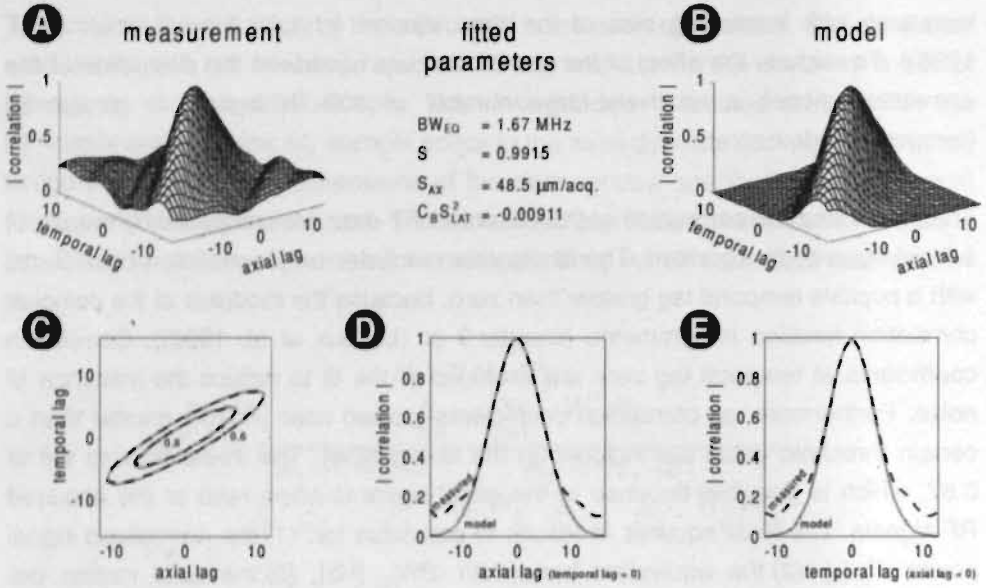

Fig. 4-4 Comparison between the 2-D correlation function based on a measured RF-data set (A) and on the analytic correlation model with least-squares fitted parameters (B). (C) Contour plots at correlation values of 0.6 and 0.8 showing only very little difference between model (solid lines) and measurement (dashed lines). (D) shows an axial cross-section of the correlation functions (temporal lag=0) and (E) shows a temporal cross-section (axial lag=0).

4.5.2 Beam characteristic $C_B(z)$

The fit algorithm results in an estimate for $C_B(z)S_{LAT}^2$. The analytic correlation model is not able to provide separate estimates for the beam characteristic $C_B(z)$ and the lateral motion per acquisition S_{LAT}. To obtain an estimate for the lateral motion, the beam characteristic $C_B(z)$ must be known. Eq. (4-23) shows that the depth-dependent beam characteristic $C_B(z)$ consists of a transverse and an elevation part. Therefore, it is dependent on the direction of the lateral motion.

Table 4-1 Fitted estimates ± standard deviation (n=5) for $C_B(z)S_{LAT}^2$ corresponding to measurements with an elliptic beam shape. The direction of the lateral motion was varied in steps of 45°.

angle	long axis		oblique axis				short axis	
n=5	0°	180°	45°	135°	225°	315°	90°	270°
$C_B(z)S_{LAT}^2$	-21.8	-23.6	-16.7	-15.5	-15.6	-16.1	-8.8	-9.2
$*10^{-3}$	±3.8	±3.5	±1.9	±3.7	±3.3	±3.2	±2.7	±3.5

To illustrate this effect, a transducer with an almost elliptic beam shape was applied (7.5 MHz linear array of a Scanner 350, Pie Medical, Maastricht, The Netherlands). The electrical focus was set at 60 mm and the transmit voltage was 10 V. Measurements were performed at a depth of 30 mm with only a lateral motion component. The angle of the lateral motion component with the positive x-axis (φ in Fig. 4-1) was varied with increments of 45° (short, oblique, and long axis of the beam cross-section). For each angle φ, the fit algorithm resulted in an estimate for $C_B(z)S_{LAT}^2$ (Table 4-1). Because the lateral motion increments were the same for each angle φ, the variations of $C_B(z)S_{LAT}^2$ must be caused by variation of the beam shape (i.e., variation of the beam characteristic $C_B(z)$). Table 4-1 shows that $C_B(z)S_{LAT}^2$ is almost the same for both long axis measurements, for the four oblique axis measurements, and for both short axis measurements, which indicates that the beam characteristic $C_B(z)$ is indeed dependent on the direction of the lateral motion.

The same measurements are performed with the single-element KB-Aerotech transducer, which has a circular beam shape. Table 4-2 shows that $C_B(z)S_{LAT}^2$ is almost the same for all angles of lateral motion. The magnitude of the lateral motion was the same for each direction; therefore, for a circular ultrasound beam $C_B(z)$ is independent of the direction of the lateral motion component. Hence, a depth-dependent calibration curve for the beam characteristic $C_B(z)$ would make it possible to estimate the magnitude (not the direction) of the lateral motion.

Table 4-2 Fitted estimations ± standard deviation (n=5) for $C_B(z)S_{LAT}^2$ corresponding to measurements with a circular beam shape. The direction of the lateral motion was varied in steps of 45°.

angle (n=5)	0°	45°	90°	135°	180°	225°	270°	315°
$C_B(z)S_{LAT}^2$ *10^{-3}	-9.5 ± 2.4	-9.7 ± 2.5	-10.6 ± 2.0	-9.6 ± 1.8	-8.3 ± 1.9	-8.5 ± 2.1	-9.1 ± 1.0	-8.7 ± 0.5

A depth-dependent calibration curve for the beam characteristic $C_B(z)$ can be obtained by substitution of the parameters in the equation for $C_B(z)$, but, in most situations, the depth-dependent beam widths and additional distances ΔL are not known. Figure 4-5B shows a depth-dependent calibration curve for the beam characteristic $C_B(z)$ of the circular KB-Aerotech transducer based on a data set with *known lateral motion. $C_B(z)S_{LAT}^2$ is estimated at a number of depths and the known* lateral motion is substituted resulting in the calibration curve for $C_B(z)$. At each depth, five measurements were performed. The calibration curve of Fig. 4-5B is based on measurements with only lateral motion and the target at three different depths. One measurement was performed with the target very close to the transducer (region I in Fig. 4-5B), the second with the target near the focus of the transducer (region II in Fig. 4-5B), and the last with the target in the far field (region III in Fig. 4-5B). The positions of the target were chosen in such a way that regions were partially overlapping. For each target position, estimates are performed at a number of depths within the target.

Figure 4-5C shows the corresponding curve for the additional distance ΔL. For a transducer with a circular beam shape, the additional distance ΔL can be obtained by rearranging the equation for $C_B(z)$, resulting in

$$\Delta L(x,y,z) = \frac{c\left(x^2+y^2\right)}{2\pi f_C}\sqrt{\frac{dB\ln[10]}{10\,w_{dB}^2(z)}\left(C_B(z)-\frac{dB\ln[10]}{10\,w_{dB}^2(z)}\right)} \qquad (4\text{-}28)$$

where $\sqrt{x^2+y^2}$ (= 1 mm applied for Fig. 4-5C) is the lateral position where ΔL is considered, f_C (= 5 MHz) is the center frequency of the received RF-signals, $C_B(z)$ is the depth-dependent beam characteristic (Fig. 4-5B) and $w_{dB}(z)$ is the depth-dependent beam width (Fig. 4-5A).

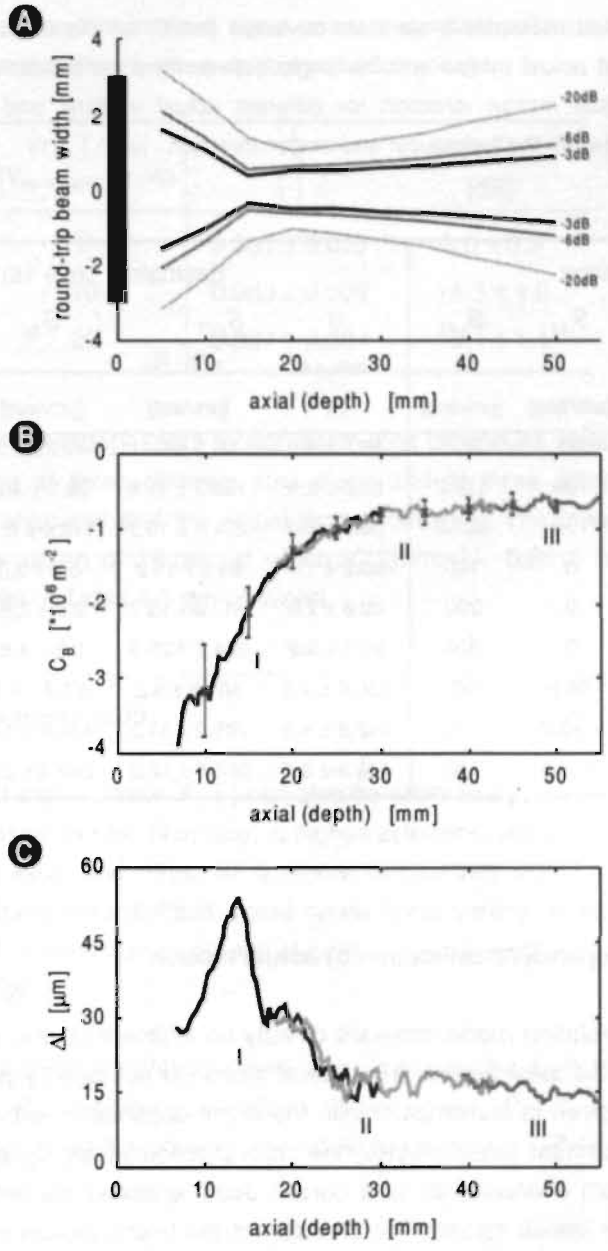

Fig. 4-5 (A) Contour plot of the round-trip beam profile (normalized at each depth) of the focused circular (6 mm) KB-Aerotech transducer. (B) Corresponding calibration-curve for the depth-dependent beam characteristic $C_B(z)$. (C) Corresponding curve for the depth-dependent additional distance ΔL.

Table 4-3 Fitted estimates ± standard deviation (n=16) for the axial, lateral, and actual motion and the angle between the transducer and the actual motion direction for different actual motions and angles between the transducer and motion direction.

Settings				Estimates (n = 16)			
α	S_{ACT}	S_{AX}	S_{LAT}	α $= \arccos(S_{AX}/S_{ACT})$	S_{ACT} $= \sqrt{S_{AX}^2 + S_{LAT}^2}$	S_{AX}	S_{LAT} $= C_B(z)S_{LAT}^2 / C_B$
[°]	[µm/acq]	[µm/acq]	[µm/acq]	[°]	[µm/acq]	[µm/acq]	[µm/acq]
60	100	50	86.6	58.5 ± 4.6	96.3 ± 8.1	49.7 ± 2.7	82.2 ± 10.5
60	200	100	173.2	59.9 ± 2.1	198.3 ± 11.8	99.2 ± 4.2	171.6 ± 13.2
60	300	150	259.8	58.5 ± 2.0	284.0 ± 15.3	148.0 ± 5.1	242.2 ± 17.5
90	100	0	100	90.2 ± 1.4	98.9 ± 15.2	-0.3 ± 2.3	98.9 ± 15.2
90	200	0	200	89.9 ± 1.0	203.9 ± 13.7	0.2 ± 3.6	203.8 ± 13.7
90	300	0	300	90.0 ± 0.9	304.7 ± 23.3	0.2 ± 4.6	304.6 ± 23.3
150	100	-86.6	50	150.0 ± 4.0	101.2 ± 5.2	-87.3 ± 1.5	50.7 ± 8.8
150	200	-173.2	100	148.8 ± 4.0	205.3 ± 11.2	-174.8 ± 1.8	106.7 ± 18.8
150	300	-259.8	150	149.3 ± 3.0	305.8 ± 10.2	-262.3 ± 2.0	156.4 ± 19.2

4.5.3 Angle-independent estimation of actual motion

The analytic correlation model provides directly an estimate for the magnitude and the direction of the axial motion. The lateral motion is not directly provided by the model, but it is given in combination with the depth-dependent beam characteristic $C_B(z)S_{LAT}^2$. For circular beam shapes, the calibration curve for $C_B(z)$ provides the value of the beam characteristic at a certain depth enabling the estimation of the magnitude of the lateral motion. The direction of the lateral motion component can not be determined, but the magnitudes of the axial and the lateral motion components are sufficient to determine the magnitude of the actual motion in an angle-independent way, because

$$S_{ACT} = \sqrt{S_{AX}^2 + S_{LAT}^2} \tag{4-29}$$

Table 4-4 Estimated normalized signal power ± standard deviation (n=5) for measurements with a variable activation voltage.

VOLTAGE [$V_{peak\text{-}peak}$] (n=5)	P_S [-]	SNR [dB]
5	0.861 ± 0.023	8.0 ± 0.9
10	0.963 ± 0.009	14.3 ± 1.0
20	0.987 ± 0.004	19.1 ± 1.1

To verify this angle-independent motion estimation procedure, measurements have been performed at three different step sizes and at three different angles (α) between the transducer and the actual motion direction. The measurements were performed at a depth of 30 mm at which $C_B(30mm) = -0.8518\ mm^{-2}$. Using this value, the results of Table 4-3 are obtained.

4.5.4 Signal-to-noise ratio

The normalized signal power P_S [-] can also be estimated using the modulus of the analytic correlation model. Normally, a higher activation voltage results in a better signal-to-noise ratio and, thus, in a higher normalized signal power. Table 4-4 shows the estimated normalized signal power for a variety of activation voltages. The estimated normalized local signal power increases indeed with increasing activation voltage.

Because the analytic correlation model is normalized, the sum of the normalized signal power P_S and the normalized noise power P_N is equal to 1 (i.e., $P_S + P_N = 1$). Using this equality, the signal-to-noise ratio (SNR) in decibels is:

$$SNR = 10\ ^{10}\log\left(\frac{P_S}{P_N}\right) = 10\ ^{10}\log\left(\frac{P_S}{1 - P_S}\right) \qquad (4\text{-}30)$$

Table 4-4 shows also the signal-to-noise ratios corresponding to the estimated normalized signal powers.

4.5.5 Equivalent RF-bandwidth

The bandwidth of the received RF-signals can be modified by changing the number of periods of the activation pulse. The more periods are transmitted, the smaller the bandwidth of the received RF-signals. The modulus of the analytic correlation model also provides an estimate for the equivalent local bandwidth of the RF-signals. Table 4-5 shows the estimated equivalent RF-bandwidths for the measurements where the number of periods of the transducer activation was varied. The estimated bandwidths indeed decrease with increasing number of transmitted periods of the activation pulse. The table also shows the estimated equivalent bandwidths based on a fit of an ideal Gaussian power spectral density distribution (PSD) (Eq. (4-7)) with the observed one. The data window (temporal 100 sample points, spatial 32 sample points) for the model fit was located at 30 mm. The PSD-based estimates used the mean PSD of 100 RF-signals (segments from 20 mm to 40 mm, i.e., approximately 500 sample points).

Table 4-5 Estimated equivalent RF-bandwidths ± standard deviation (n=5) for measurements with a variable number of transmitted periods of a square wave.

Number of periods of transducer activation (n = 5)	BW_{EQ} model (z=30 mm) [MHz]	BW_{EQ} PSD (z=20..40 mm) [MHz]
1	1.91 ± 0.14	1.85 ± 0.03
2	1.49 ± 0.08	1.47 ± 0.03
4	1.01 ± 0.10	0.99 ± 0.03
8	0.48 ± 0.07	0.50 ± 0.02
15	0.34 ± 0.11	0.29 ± 0.01

4.6 Discussion

Figure 4-4 showed that the agreement between the analytic correlation model and the experimental correlation based on measured RF-signals was excellent. It is shown that the modulus of the analytic correlation model is a function of the normalized signal power (P_S), equivalent RF-bandwidth (BW_{EQ}), axial motion per acquisition (S_{AX}) and $C_B(z)S_{LAT}^2$. The latter is a combination of a depth-dependent beam characteristic and the lateral motion per acquisition. Table 4-1 confirms that $C_B(z)S_{LAT}^2$ for elliptic ultrasound beams depends on the direction of the lateral motion, while for circular ultrasound beams, $C_B(z)S_{LAT}^2$ is independent of that direction (Table 4-2). For the latter case, a calibration curve can be made for the depth-dependent beam characteristic $C_B(z)$ (Fig. 4-5B). Figure 4-5B shows that the standard deviation of this calibration curve is smaller in the region behind the focus (= far field) than in the region before (= near field). This is caused by the fact that the sound field in the near field is not Gaussian shaped, as is assumed in the model, but it contains local maxima and minima. The deviation of the calibration curve is an indication for the possible precision of the motion estimates as function of the depth, indicating that near field estimations will be less precise as compared with the far field estimates.

The depth-dependent beam characteristic $C_B(z)$ is a function of the local beam width and the shape of the local phase front (Eq. (4-19) or Eq. (4-20)). The local beam width (normalized at each depth) of the applied circular single-element transducer is shown in Fig. 4-5A. The local phase front can be characterized by the additional travel distance ΔL. Substitution of the beam width curve of Fig. 4-5A and the $C_B(z)$ calibration curve of Fig. 4-5B into Eq. (4-28) resulted in the curve for ΔL of Fig. 4-5C. The graph shows that ΔL (at a lateral position of 1 mm from the center of the beam axis) is only a fraction of the wavelength (which is approximately 300 μm) and that it is maximal near the focus. This is as expected, because near the focus the curvature of the phase front is at largest; it decreases with increasing distance to the focus where the wave front gets wider, but also locally flatter.

The results of Table 4-3 illustrate that it is possible with use of a calibration curve for $C_B(z)$ to estimate the magnitude of the actual motion in an angle-independent way.

All estimated parameters are in good agreement with the settings. The small discrepancy between the settings and the estimates may be caused by inaccurate positioning of the transducer. Larger structures in the target cause the scatterers not to be δ-correlated in space, which also contributes to the observed deviation. Furthermore, deviation may be caused by the accuracy of the stepper motor. Finally, discrepancies in the assumptions made in the derivation of the model cause some deviation (e.g., Fig. 4-2). It should be noted, that in the case of severe phase aberrations, the accuracy and precision of the lateral motion estimates will decrease, because phase aberrations influence the beam shape causing a discrepancy between the actual value for $C_B(z)$ and the value estimated from the calibration curve.

The maximum detectable lateral motion is limited by the beam width. To be detectable by means of correlation of consecutive RF-signals, the lateral motion of the scatterers between registrations must be smaller than the beam width. The maximum detectable axial motion depends on the axial size of the data window and is considerably higher than would be possible with algorithms that are limited by the Nyquist-criterion ($S_{NYQUIST} = \frac{c}{4f_c} = 75\mu m$), see Table 4-3.

The model provides also estimates for the signal-to-noise ratio (Table 4-4) that can serve as a display threshold for (power) Doppler imaging. Assuming a linear relation between transmitter voltage and signal-to-noise ratio, a doubling of the transmitter voltage should result in an increase in signal-to-noise ratio of 6 dB. Table 4-4 shows that the estimated signal-to-noise ratio indeed increases with approximately 6 dB as the transmitter voltage is doubled.

Table 4-5 shows the comparison of the model based estimated equivalent bandwidths with those obtained based on the power spectral density distribution. The agreement between both is good, only the model based estimates have a slightly larger fluctuation. This might be caused by the fact that the model based estimates are local estimates (axial window 32 points), whereas the power spectral density based estimates are based on a larger segment of the RF-signal (approx. 500 points).

Comparison between motion detection techniques based on speckle tracking using conventional ultrasound scanners (e.g. (Bohs et al. 1995)) and the currently proposed technique shows that both techniques have different applications. Speckle tracking results in the magnitude and direction of the motion component in the plane of the corresponding image. It ignores the motion component perpendicular to the image plane. The current technique results in the magnitude of the actual motion and the direction of the axial motion component. It omits the direction of the lateral motion component. Furthermore, speckle tracking is based on images, whereas the current technique is based on M-mode signals. Consecutive M-mode signals can be acquired faster than consecutive images, so the current technique should be able to measure larger motions. Another difference is that the inter-pixel distance of an image influences the precision of the speckle tracking based motion estimates. The sampling does not influence the current method, because the model is able to predict inter-pixel values.

The current technique closely resembles the motion estimation technique presented by Dotti et al. (Dotti and Lombardi 1996). The main difference between both approaches is that the latter method uses the correlation of real RF-signals, whereas the current method is based on the modulus of the correlation of analytic RF-signals. The method based on the correlation of real RF-signals requires the detection of the main lobe of the correlation function, so correlation coefficients for a large number of lags have to be calculated. Once the main lobe has been found, the correlation coefficient with half the value at the origin has to be found on this main lobe. For small lateral motions, in which case the correlation only reduces very slowly, a lot of correlation coefficients have to be calculated. This process can only partially be automated in the method presented by Dotti et al. (Dotti and Lombardi 1996). With the current technique, this localization is not required, because comparison between a few calculated correlation coefficients and the correlation model reveals the shape and location of the entire correlation function. Furthermore, the current technique provides also local information of the RF-signals (center frequency, bandwidth, signal-to-noise ratio), which is not provided by most other motion estimators.

4.7 Conclusions

In the present chapter, a model is derived for the correlation of analytic RF-signals received in M-mode. The modulus of this model can be applied to obtain local estimates for the signal-to-noise ratio, the equivalent RF-bandwidth, and the magnitude and direction of the axial motion per acquisition. The maximal detectable axial motion depends on the axial size of the data window and is not limited by the Nyquist criterion. If a transducer is employed with a circular beam shape, it is possible to estimate the magnitude of the lateral motion, but then a calibration curve for the depth-dependent beam characteristic $C_B(z)$ is required. Combination of the axial and lateral motion components results in angle-independent estimates for the magnitude of the actual motion per acquisition interval.

4.8 References

Angelsen BAJ. A theoretical study of the scattering of ultrasound from blood. IEEE Trans Biomed Eng. 1980;27:61-67.

Atkinson P, Berry MV. Random noise in ultrasonic echoes diffracted by blood. J Phys A: Math Nucl Gen. 1974;7:1293-1302.

Azimi M, Kak AC. An analytic study of Doppler ultrasound systems. Ultrason Imaging. 1985;7:1-48.

Bohs LN, Friemel BH, Trahey GE. Experimental velocity profiles and volumetric flow via two-dimensional speckle tracking. Ultrasound Med Biol. 1995;21:885-898.

Bonnefous O, Pesqué P. Time domain formulation of pulse-Doppler ultrasound and blood velocity estimation by cross correlation. Ultrason Imaging. 1986;8:73-85.

Brandestini MA, Forster FK. Blood flow imaging using a discrete-time frequency meter. 1978 Ultrasonics Symposium Proceedings. 1978;348-352.

Brands PJ, Hoeks APG, Ledoux LAF, Reneman RS. A radio frequency domain complex cross-correlation model to estimate blood flow velocity and tissue motion by means of ultrasound. Ultrasound Med Biol. 1997;23:911-920.

Céspedes EI, de Korte CL, van der Steen AFW, von Birgelen C, Lancée CT. Intravascular elastography: principles and potentials. Semin Intervent Cardiol. 1997;2:55-62.

Chen EJ, Adler RS, Carson PL, Jenkins WK, O'Brien Jr. WD. Ultrasound tissue displacement imaging with application to breast cancer. Ultrasound Med Biol. 1995;21:1153-1162.

de Jong PGM, Arts T, Hoeks APG, Reneman RS. Determination of tissue motion velocity by correlation interpolation of pulsed ultrasonic echo signals. Ultrason Imaging. 1990;12:84-98.

Deutsch R. System analysis techniques. Englewood Cliffs: Prentice-Hall, 1969.

Dickinson RJ, Hill CR. Measurement of soft tissue motion using correlation between A-scans. Ultrasound Med Biol. 1982;8:263-271.

Dotti D, Lombardi R. Estimation of the angle between ultrasound beam and velocity through correlation functions. IEEE Trans Ultrason Ferroel Freq Contr. 1996;43:864-869.

Dotti D, Lombardi R, Piazzi P. Vectorial measurement of blood velocity by means of ultrasound. Med Biol Eng Comput. 1992;30:219-225.

Embree PM, O'Brien WD. Volumetric blood flow via time-domain correlation: experimental verification. IEEE Trans Ultrason Ferroel Freq Contr. 1990;37:176-189.

Evans DH. Techniques for Color-Flow Imaging. In: Wells PNT, ed. Advances in Ultrasound Techniques and Instrumentation. New York: Churchill Livingstone, 1993: 87-107.

Ferrara K, DeAngelis G. Color flow mapping. Ultrasound Med Biol. 1997;23:321-345.

Foster SG, Embree PM, O'Brien WD. Flow velocity profile via time-domain correlation: error analysis and computer simulation. IEEE Trans Ultrason Ferroel Freq Contr. 1990;37:164-175.

Gao L, Parker KJ, Lerner RM, Levinson SF. Imaging of the elastic properties of tissue - A review. Ultrasound Med Biol. 1996;22:959-977.

Gold B, Oppenheim AV, Rader CM. Theory and implementation of the discrete Hilbert transform. In: Rabiner LR, Rader CM, ed. Digital Signal Processing. New York: IEEE Press, 1972: 94-109.

Hoeks APG, Arts TGJ, Brands PJ, Reneman RS. Comparison of the performance of the RF cross correlation and Doppler autocorrelation technique to estimate the mean velocity of simulated ultrasound signals. Ultrasound Med Biol. 1993;19:727-740.

Hoeks APG, Arts TGJ, Brands PJ, Reneman RS. Processing scheme for velocity estimation using ultrasound RF cross correlation techniques. Eur J Ultrasound. 1994;1:171-182.

Ledoux LAF, Willigers JM, Brands PJ, Hoeks APG. Experimental verification of the correlation behavior of analytic ultrasound radio frequency signals received from moving structures. Ultrasound Med Biol. 1998;24:1383-1396.

Li W. Image and signal processing in intravascular ultrasound. PhD Thesis Erasmus University Rotterdam, 1997.

Loupas T, Powers JT, Gill RW. An axial velocity estimator for ultrasound blood flow imaging, based on a full evaluation of the Doppler equation by means of a two-dimensional autocorrelation approach. IEEE Trans Ultrason Ferroel Freq Contr. 1995;42:672-688.

Ophir J, Céspedes I, Ponnekanti H, Yazdi Y, Li X. Elastography: a quantitative method for imaging the elasticity of biological tissues. Ultrason Imaging. 1991;13:111-134.

Press WH, Flannery BP, Teukolsky SA, Vetterling WT. Numerical Recipes: the art of scientific computing. Cambridge: Cambridge University Press, 1986.

Ramamurthy BS, Trahey GE. Potential and limitations of angle-independent flow detection algorithms using radio-frequency and detected echo signals. Ultrason Imaging. 1991;13:252-268.

Torp H, Kristoffersen K, Angelsen BAJ. Autocorrelation techniques in color flow imaging: signal model and statistical properties of the autocorrelation estimates. IEEE Trans Ultrason Ferroel Freq Contr. 1994;41:604-612.

Trahey GE, Hubbard SM, von Ramm OT. Angle independent ultrasonic blood flow detection by frame-to-frame correlation of B-mode images. Ultrasonics. 1988;26:271-276.

Trahey GE, Smith SW, von Ramm OT. Speckle pattern correlation with lateral aperture translation: experimental results and implications for spatial compounding. IEEE Trans Ultrason Ferroel Freq Contr. 1986;33:257-264.

Wilson LS, Robinson DE. Ultrasonic measurement of small displacements and deformations of tissue. Ultrason Imaging. 1982;4:71-82.

Chapter 5

Angle-independent motion measurement by correlation of ultrasound signals assessed with a single circular-shaped transducer

L.A.F. Ledoux, J.M. Willigers, P.J. Brands, A.P.G. Hoeks

Ultrasonic Imaging, accepted for publication (June 1999).

Angle-independent motion measurement by correlation of ultrasound signals assessed with a single circular-shaped transducer

5.1 Abstract

In medicine, pulsed ultrasound is a widespread noninvasive technique to measure motion in the direction of the ultrasound beam, i.e., axial motion. The magnitude of the actual motion can be determined only if the angle between the ultrasound beam and the direction of motion (transducer-to-motion angle) is known. For blood flow measurements, current pulsed ultrasound systems assume this angle to be equal to the angle between the ultrasound beam and the longitudinal direction of the blood vessel. The angle is estimated from a two-dimensional brightness-mode (B-mode) image that is obtained prior to the blood flow measurement. For tissue motion measurements, current pulsed ultrasound systems are mostly unable to determine the transducer-to-motion angle. Recently (chapter 4), a model has been derived for the correlation of (analytic) radiofrequency (RF) signals, assessed with a circular-shaped ultrasound transducer along the same line of observation. In the present chapter, this model is used to derive estimators, requiring only the calculation of a few correlation coefficients, for the motion components (axial, lateral and actual) and for some of the signal parameters (center frequency, bandwidth and signal-to-noise ratio) of the assessed RF-signals. The transducer-to-motion angle can be derived from the estimated motion components. For the evaluation of the estimators, RF-signals were acquired with a motion-controlled experimental arrangement. The results of the evaluation study show that the transducer-to-motion angle can be estimated with a mean standard deviation of less than 2^{o}.

5.2 Introduction

In medicine, pulsed ultrasound is employed to measure noninvasively motion of blood or tissue. In the current chapter, motion is defined as the displacement that occurs during the time interval between two consecutive activation pulses. Motion defined this way can be converted to velocity by multiplying it by the pulse repetition frequency. Most pulsed ultrasound systems apply motion estimation algorithms that are only able to estimate the motion component in the direction of the ultrasound beam (i.e., the axial motion). The magnitude of the actual motion is derived from the axial motion by assuming a known angle between the axis of the ultrasound beam and the motion direction (transducer-to-motion angle). The precision of the estimated magnitude of the actual motion depends heavily on the precision with which this angle is known (Phillips et al. 1989). For laminar blood flow velocity measurements, the transducer-to-motion angle is assumed to be equal to the transducer-to-vessel angle and is estimated from the corresponding 2-dimensional

brightness mode (B-mode) image showing a longitudinal cross-section of the vessel. The estimated angle is assumed not to vary during the complete cardiac cycle. In a preliminary study by Fei et al. (Fei et al. 1997), it is suggested that the transducer-to-motion angle changes during the cardiac cycle. If this is true, the application of a constant transducer-to-motion angle will introduce a time-dependent bias in the flow velocity measurements. For tissue motion measurements, it is currently almost impossible to predict the local transducer-to-motion angle within the tissue, because the motion direction of a relatively small tissue segment cannot be registered accurately from a B-mode image, varies with position in the image and changes in time. To circumvent the problems mentioned above, it would be very helpful if the transducer-to-motion angle or the actual motion could be estimated from the radiofrequency (RF) signals received in motion mode (M-mode) without any restrictions.

During the last decade, a number of strategies have been introduced for the automatic registration of the transducer-to-motion angle or, equivalently, of the actual motion, but so far none of those methods has been incorporated in commercially-available scanners. A short overview of a number of these motion-vector estimation methods is presented by Fish et al. (Fish et al. 1997). Some of the methods are based on speckle tracking (Bohs et al. 1995; Bohs et al. 1998; Ramamurthy and Trahey 1991; Trahey et al. 1987; Wilson and Gill 1993), whereas other methods are based on the application of a set of transducers and/or modification of the transmit/receive protocol (Anderson 1998; Beach et al. 1996; Jensen and Munk 1998; Katakura and Okujima 1995; Ogura et al. 1997; Overbeck et al. 1992; Yeung 1998). All methods have their limitations making them not attractive for application in commercial scanners. Some of the encountered limitations are that they are only able to estimate the actual motion at one or a few axial positions, are only able to estimate 2-D motion, are very time-consuming and/or have complex hardware requirements.

A better approach would be if the actual motion could be determined, with a high spatial resolution, directly from the RF-signals assessed with a single transducer along the same line of observation (M-mode). This goal can be reached by means of correlation of consecutive RF-segments. Correlation of RF-segments reveals information about the axial and lateral (perpendicular to the ultrasound beam) motion components, which can be combined to determine the magnitude of the actual motion. Correlation of consecutive RF-segments obtained from axially-moving structures results in an axial motion dependent shift of the lag with maximal correlation (Bonnefous and Pesqué 1986; de Jong et al. 1990), whereas correlation of RF-segments obtained from laterally-moving structures results in a decrease of

the maximal obtainable correlation with increasing temporal lag between the RF-segments (Dotti et al. 1992; Li et al. 1997). Recently, a model was derived for the correlation of RF-signals assessed in M-mode (chapter 4 or (Ledoux et al. 1999)). For a transducer with a circular ultrasound beam, it was shown that a fit of the correlation model with correlation coefficients calculated from measured signal segments (for a number of different combinations of the axial and temporal lags) resulted in angle-independent estimates for the magnitude of the actual motion. In the present chapter, the correlation model is used to derive estimators for the motion components (axial, lateral and actual) and for some signal parameters of the assessed RF-signals (center frequency, bandwidth and signal-to-noise ratio). The performance of the estimators is evaluated using RF-signals acquired with an experimental set-up able to generate controlled-motion components.

5.3 Theory

Most conventional pulsed ultrasound systems register real RF-signals. To separate the instantaneous amplitude and phase of the RF-signals, a feature that simplifies the derivation of the estimators (see below), the real RF-signals are made analytic (Picinbono 1997). An analytic RF-signal is an RF-signal to which a frequency-independent -90^{o} phase shifted copy of the real signal is added. This can be reached by means of a Hilbert-transformation (Gold et al. 1972). One such transformation generates analytic RF-signals by removing the negative frequencies and doubling the power spectral density distribution of the real RF-signals for positive frequencies. The single-sideband power spectral density distribution of an analytic RF-signal is approximately Gaussian-shaped with center frequency f_C [Hz] (Hoeks et al. 1993) and equivalent power bandwidth BW_{EQ} [Hz], which is the width of a rectangular power spectral density distribution with the same height and area as the original distribution.

For pulsed ultrasound motion measurements, a number of consecutive RF-signals are recorded along the same line of observation (M-mode) and stored as a matrix in which the rows contain the acquired RF-signals (Ledoux et al. 1997). Before further processing, the RF-signals must be made analytic. The sample points of an RF-signal are directly related to the axial distance traveled by the transmitted pressure waves. Hence, (the center of) a short segment of an RF-signal may be related to a certain depth of measurement. The correlation between two such RF-segments with a certain temporal and axial lag between them can be used to retrieve local motion and signal information (de Jong et al. 1990).

For RF-signals assessed in M-mode with a circular single-element transducer, the correlation coefficient R between two analytic RF-segments at temporal lag T and axial lag Z can be modeled as (for derivation see Appendix A (section 5.8.1) or chapter 4)

$$R(T,Z) = (P_S + P_{N_r}) \exp\left[T^2 C_B(z_r) S_{LAT}^2 - \frac{4\pi BW_{EO}^2}{c^2}\left(\frac{Zc}{2f_S} - TS_{AX} \right)^2 \right] \times \exp\left[j\frac{4\pi f_C}{c}\left(\frac{Zc}{2f_S} - TS_{AX} \right) \right] \quad (5\text{-}1)$$

where c [m/s] is the sound velocity in the medium under investigation, f_S [Hz] is the sample frequency of the RF-signals, z_r [m] is the axial place of estimation, P_S [-] is the normalized ($P_S + P_N = 1$) signal power of the received RF-signal and P_N [-] is the normalized noise power ($P_{N_{r=0}} = P_N$ and $P_{N_{r\neq 0}} = 0$). $C_B(z)$ [m^{-2}] is a negative value that is dependent on some characteristics of the ultrasound beam at depth z (e.g., local beam width and local shape of wavefront, see Appendix A (section 5.8.1)). S_{AX} [m] and S_{LAT} [m] are the magnitudes of the axial and lateral motion components of the actual motion S_{ACT} [m] of the scatterers during the interval between the registration of two consecutive RF-signals (Fig. 5-1).

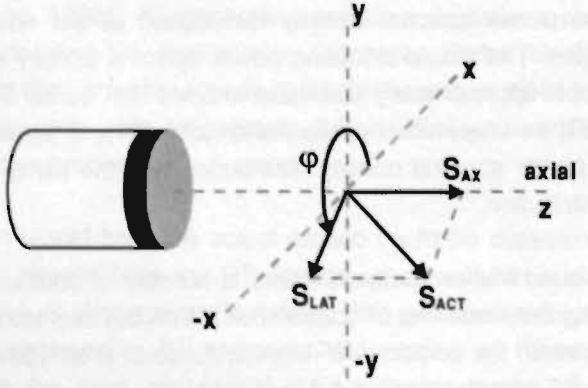

Fig. 5-1 Schematic representation of a circular transducer and the orientation of the Cartesian coordinate axes. The actual motion (S_{ACT}) is decomposed into axial (S_{AX}) and lateral (S_{LAT}) motion components.

The correlation model (Eq. (5-1)) can be applied to derive estimators, which are based on the calculation of a few correlation coefficients, for the signal and motion parameters in the model. The signal parameters of the RF-signals for which estimators can be derived are: (1) the center frequency, (2) the equivalent bandwidth and (3) the signal-to-noise ratio. The motion parameters for which estimators can be derived are: (1) the magnitude and sign of the axial motion, (2) the magnitude of the lateral motion and (3) the magnitude of the actual motion.

The correlation model (Eq. (5-1)) is a complex function, because it is derived for analytic RF-signals. Therefore, the amplitude and phase characteristics of the correlation model can be separated by considering the modulus and argument of the model, respectively. It should be noted that the correlation model for real RF-signals is equal to the real part of the correlation model and consists of a multiplication of an exponent term with a cosine term. For the latter model, it would be very difficult to derive analytic equations for the signal parameter and motion estimators without any additional assumptions (de Jong 1991).

The estimators derived from the complex correlation model can be divided into two classes. One class of estimators is based on the argument of the correlation model, i.e.,

$$\arg[R(T,Z)] = \frac{4\pi f_C}{c}\left(\frac{Zc}{2f_S} - TS_{AX}\right) \tag{5-2}$$

and can be applied to derive estimators for the center frequency and the axial motion. The other class of estimators employs the modulus of the correlation model, i.e.,

$$|R(T,Z)| = \left(P_S + P_{N_r}\right)\exp\left[T^2 C_B(z_t) S_{LAT}^2 - \frac{4\pi BW_{EO}^2}{c^2}\left(\frac{Z c}{2 f_S} - T S_{AX}\right)^2\right] \tag{5-3}$$

and can be applied to derive estimators for the signal-to-noise ratio, the equivalent bandwidth, the lateral motion, the axial motion and the beam characteristic $C_B(z)$. Estimators based on the argument of the correlation model are more accurate, i.e., they are less influenced by the signal-to-noise ratio and beam effects than those based on the modulus, but the argument has the disadvantage that it is periodic. Hence, argument-based estimators are susceptible to aliasing (Lai et al. 1997).

In the following, the estimators derived from the correlation model are presented in an optimal form in which the lags of the correlation coefficients required for the estimators are chosen such that the number of different correlation coefficients needed for all the estimators is as small as possible. In appendix B (section 5.8.2), each estimator is presented in a general form for which the lags of the correlation coefficients can be set arbitrarily. The estimators derived from the correlation model are marked with a ^.

5.3.1 Center frequency

From the argument of the correlation model the following estimator for the local center frequency of the RF-signals can be derived

$$\hat{f}_C = \frac{f_S}{2\pi} \arg[R(0,1)] \tag{5-4}$$

This argument-based estimator does not alias as long as the center frequency is below $0.5 f_S$ (conforming to the Nyquist-criterion). This is the same estimator as was already derived by Brands et al. (Brands et al. 1997).

5.3.2 Axial motion

The following estimator for the magnitude and sign of the axial motion during the time interval between the registration of two consecutive RF-signals can be derived from the argument of the correlation model

$$\hat{S}_{AX_{ARG}} = -\frac{c}{4\pi \hat{f}_C} \arg[R(1,0)] \tag{5-5}$$

This is the same axial motion estimator as was introduced by Loupas et al. (Loupas et al. 1995) and Brands et al. (Brands et al. 1997). The latter demonstrated that this estimator is unbiased with a high precision. The magnitude of the maximal unambiguously detectable axial motion with this argument-based estimator is equal to

$$\left|S_{AX_{ARG_{MAX}}}\right| = \frac{c}{4f_C} \tag{5-6}$$

For the following axial motion estimator, derived from the modulus of the correlation model, the maximal detectable axial motion is much higher.

$$\hat{S}_{AX_{MOD}} = \frac{c}{4f_S}\left(\frac{\ln\left[R(1,-1)^{-1}|R(1,1)|\right]}{\ln\left[R(1,1)^{-1}|R(1,-1)^{-1}|R(1,0)|^2\right]}\right) \tag{5-7}$$

This estimator requires only correlation coefficients at temporal lag $T = 1$. Eq. (5-3) shows that the modulus part of the correlation function at a certain temporal lag has a Gaussian shape (Appendix C (section 5.8.3), Fig. C1). The location of the maximum of that shape is dependent on the axial motion. As the axial motion gets too large, the correlation coefficients $|R(1,-1)|$, $|R(1,0)|$ and $|R(1,1)|$ become very small. Small correlation coefficients are less reliable and might be caused by spurious correlation of noise. For a minimal acceptable value $|R(1,0)|_{MIN}$ of the correlation coefficient $|R(1,0)|$, the maximal detectable modulus-based axial motion is limited by

$$\left|S_{AX_{MOD_{MAX}}}\right| = \frac{c}{2BW_{EQ}}\sqrt{\frac{1}{\pi}\left(C_B(z_t)S_{LAT}^2 - \ln\left[\frac{|R(1,0)|_{MIN}}{P_S}\right]\right)} \tag{5-8}$$

As can be seen, the maximal detectable axial motion is, apart from the correlation coefficient, also dependent on the bandwidth, the lateral motion, the signal-to-noise ratio and the local beam characteristics. For a center frequency of 5 MHz and the settings BW_{EQ} = 2 MHz, c = 1490 m/s, C_B = -1.4 mm^{-2} (plane wave; -6dB beam width = 1.5 mm), S_{LAT} = 100 µm, P_S = 0.9 ($SNR \approx 10$ dB) and $|R(1,0)|_{MIN}$ = 0.2, the modulus-based maximal detectable axial motion is more than three times larger than the argument-based one.

Using a search algorithm for the axial lag with maximum correlation at temporal lag $T = 1$ can increase the modulus-based maximal detectable axial motion, but this is at the expense of an increased computation time. In Appendix C (section 5.8.3), a possible search algorithm is presented which requires the calculation of a minimal number of correlation coefficients. With such an algorithm, the maximal detectable axial motion is limited by the axial length of the RF-segments considered for the correlation and is approximately equal to

$$\left|S_{AX_{MOD_{MAX\,SEARCH}}}\right| \approx \frac{cN_Z}{2f_S} \tag{5-9}$$

where N_Z is the length of the RF-segment in sample points. Comparison of Eqs. (5-6) and (5-9) shows that for a spatial sample ratio of four (i.e., $f_S = 4f_C$), the maximal detectable axial motion determined with the modulus-based estimator with search algorithm is a factor $0.5N_Z$ higher than the argument-based estimator. The limitation of the modulus-based estimator is caused by the fact that correlation is only possible as long as part of the correlated signals originate from the same scatterers.

Estimation of the axial motion based on the modulus of the correlation coefficients is not as stable as the one based on the argument of the correlation coefficients, but it is applicable for considerably larger axial motion components. The precision of axial motion estimates larger than $\left|S_{AX_{ARG_{MAX}}}\right|$ can be improved by using the modulus-based estimates to unwrap the argument-based ones. The estimator for the "unwrapped" argument-based axial motion is given by

$$\hat{S}_{AX_{UNWRAP}} = -\frac{c}{4\pi \hat{f}_C}\left(\arg\left[R(1,0)\right] - 2\pi n\right) \tag{5-10}$$

where n is an integer such that the difference between $\hat{S}_{AX_{UNWRAP}}$ and $\hat{S}_{AX_{MOD}}$ is as small as possible.

5.3.3 Equivalent bandwidth

The equivalent bandwidth of the RF-signals can be estimated with

$$\hat{BW}_{EQ} = f_S \sqrt{-\frac{1}{2\pi}\ln\left[\frac{\left|R(1,Z+1)\right|\left|R(1,Z-1)\right|}{\left|R(1,Z)\right|^2}\right]} \tag{5-11}$$

where the axial lag $Z = \text{round}\left[2c^{-1}f_S\hat{S}_{AX_{MOD}}\right]$.

5.3.4 Magnitude of lateral motion

The lateral motion S_{LAT} can not be separated from the depth-dependent beam characteristic $C_B(z)$. Therefore, it is not possible to derive an estimator for the lateral motion with exclusion of the beam characteristic. Only the following estimator for $C_B(z)\,S_{LAT}^2$ can be derived

$$\widehat{C_B(z_t)S_{LAT}^2} = \frac{4\pi B\tilde{W}_{EQ}^2}{c^2}\left(\hat{S}_{AX_{MOD}}^2 - \frac{Zc}{2f_S}\right) - \frac{1}{3}\ln\left[\frac{|R(1,Z)|}{|R(2,2Z)|}\right] \tag{5-12}$$

where the axial lag is again $Z = \text{round}\left[2c^{-1}f_S\hat{S}_{AX_{MOD}}\right]$.

The beam characteristic $C_B(z)$ can be determined with Eq. (5-A7), but then the beam width and the shape of the wavefront must be known at depth z. Normally, these parameters are not known and measuring them for the complete depth range would be very time consuming. An easier approach is to estimate $C_B(z)$ based on a set of RF-signals resulting from a scattering object that moves with known motion (S_{ACT}). It is then possible to estimate the lateral motion component using

$$\hat{S}_{LAT_{ACT}} = \sqrt{S_{ACT}^2 - \hat{S}_{AX_{UNWRAP}}^2} \tag{5-13}$$

After substitution of this lateral motion component in Eq. (5-12), the estimate for the beam characteristic $C_B(z)$ is given by

$$\hat{C}_B(z) = \frac{\widehat{C_B(z)S_{LAT}^2}}{\hat{S}_{LAT_{ACT}}^2} \tag{5-14}$$

This estimator for the beam characteristic $C_B(z)$ can be applied to create a depth-dependent calibration curve for the beam characteristic. Once such a calibration curve is available, the magnitude of the lateral motion can be estimated by combining the corresponding calibration value of the beam characteristic with Eq. (5-12), resulting in

$$\hat{S}_{LAT} = \sqrt{\frac{\widehat{C_B(z_t)S_{LAT}^2}}{\hat{C}_B(z_t)}} \tag{5-15}$$

The direction of the lateral motion component cannot be predicted, because lateral motion does not specify a direction since the vector is located in the plane perpendicular to the ultrasound beam (Fig. 5-1).

The maximal detectable lateral motion is mainly limited by the width of the ultrasound beam (included in the beam characteristic $C_B(z)$) and the signal-to-noise ratio. The estimator for $C_B(z)S_{LAT}^2$ requires a correlation coefficient at temporal lag $T = 2$. Therefore, a minimal correlation is required between the RF-segments at temporal lag $T = 2$, resulting in the following approximation for the maximal measurable lateral motion

$$S_{LAT_{MAX}} = \sqrt{\frac{1}{4C_B(z)} \ln\left[\frac{|R(2,2Z)|_{MIN}}{P_S}\right]} \tag{5-16}$$

where $|R(2,2Z)|_{MIN}$ is the minimal acceptable value of the correlation coefficient $|R(2,2Z)|$. Assuming $C_B = -1.4\ mm^{-2}$ (plane wave; -6 dB beam width $\approx$ 1.5 mm), $P_S = 0.9$ (SNR = 10 dB) and $|R(2,2Z)|_{MIN} = 0.2$, the maximal detectable lateral motion is approximately 500 µm in the interval between the acquisition of two consecutive RF-signals. This matches approximately the maximal axial motion.

5.3.5 Magnitude of actual motion

Once the magnitudes of the axial and lateral motion components have been estimated with Eqs. (5-10) and (5-15), respectively, the magnitude of the actual motion can be estimated with

$$\hat{S}_{ACT} = \sqrt{\hat{S}_{AX_{UNWRAP}}^2 + \hat{S}_{LAT}^2} \tag{5-17}$$

5.3.6 Transducer-to-motion angle

The local transducer-to-motion angle, which is the angle between the actual motion direction and the ultrasound beam, is equal to

$$\hat{\alpha} = \arctan\left(\frac{\hat{S}_{LAT}}{\hat{S}_{AX_{UNWRAP}}}\right) \tag{5-18}$$

where *arctan* is the four quadrant arctangent.

5.3.7 Signal-to-noise ratio

The following estimator is derived for the normalized signal power

$$\hat{P}_S = |R(1,Z)| \exp\left[\frac{4\pi B\hat{W}_{EQ}^2}{c^2}\left(\frac{Zc}{2f_S} - \hat{S}_{AX_{MCO}}\right)^2 - \overbrace{C_B(z_t)S_{LAT}^2}\right] \tag{5-19}$$

where the axial lag is again $Z = \text{round}\left[2c^{-1}f_S\hat{S}_{AX_{MCO}}\right]$.

Because of the normalization, the normalized noise power is equal to

$$\hat{P}_N = 1 - \hat{P}_S \tag{5-20}$$

Combination of the estimated signal (Eq. (5-19)) and noise (Eq. (5-20)) powers leads to the following estimator for the signal-to-noise ratio in decibels

$$\hat{SNR}_{dB} = 10\ {}^{10}\log\left(\frac{\hat{P}_S}{\hat{P}_N}\right) \tag{5-21}$$

It should be noted that this estimator for the signal-to-noise ratio is independent of the shape of the (axial) power spectral density distribution of the noise.

5.4 Experimental set-up

The estimators presented in the previous section are evaluated with RF-signals assessed with the experimental set-up shown in Fig. 5-2. With this arrangement it is possible to acquire RF-signals with known motion information, since the transducer is displaced by two computer-controlled stepper motors. The first stepper motor moves the transducer in a linear way with a minimal step size of 100 µm governing the actual motion S_{ACT} of the assessed RF-data. The second stepper motor rotates the transducer with a minimal angle step size of 0.72° governing the transducer-to-motion angle α. Depending on the position of the transducer, the axial S_{AX} and lateral S_{LAT} motion components are given by

$$S_{AX} = S_{ACT}\cos(\alpha) \tag{5-22}$$

$$S_{LAT} = S_{ACT}\sin(\alpha) \tag{5-23}$$

During a measurement, the transducer is displaced at a step interval of 110 ms. To minimize settling effects, a pulsed RF-signal is assessed 100 ms after the displacement of the transducer. Unless otherwise mentioned, the step size (S_{ACT}) is 100 µm between acquisitions.

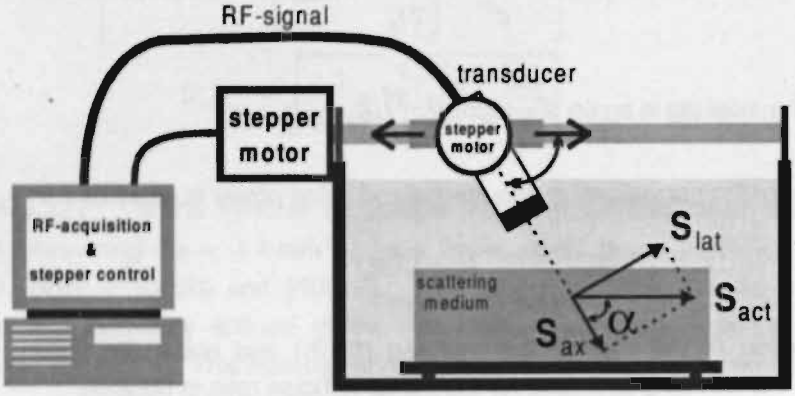

Fig. 5-2 Schematic representation of the experimental set-up.

The transmission/reception is governed by a custom-made board. A custom-made PC plug-in board governs the digitization of the RF-signals (dynamic range 12 bits; sample frequency f_S = 20 MHz). The RF-signals are stored as a matrix (rows contain the consecutive signals) on hard disk. Before processing, the RF-signals are digitally band-pass filtered (2^{nd} order Butterworth: $f_{LOW} = 0.05\, f_S$ and $f_{HIGH} = 0.45\, f_S$) and are made analytic by removing the negative frequencies in the power spectral density distribution of the RF-signals and doubling the positive frequencies (Wilson and Robinson 1982).

The transducer is a circular single-element MLA 50 BS of KB-Aerotech (Lewistown, Pennsylvania, USA) with a diameter of 6 mm, a center frequency of approximately 5 MHz and its focus at approximately 15 mm. The transducer is activated with two periods of a 5 MHz square wave with a peak-to-peak voltage of 30 V.

The target of the measurements was a rectangular scattering object (6 cm × 11 cm × 13 cm) made of a 1% mass-concentration Agarose (Life Technologies, Paisley, Scotland) solution to which a 1% mass-concentration Carborundum particles (≈ 5 µm) was added. The sound velocity in the target is approximately 1490 m/s.

The estimators make use of correlation coefficients that are calculated from segments of the RF-signals. Determining the mean correlation of a set of consecutive RF-segments located within a data window increases the precision of the calculated correlation coefficients (Jensen 1994). The position of the data window within the RF-matrix relates the data to a certain axial position and moment during the measurement. The data window contains N_z sample points in the axial direction and N_T RF-segments in the temporal direction. These dimensions limit the possible axial (depth) and temporal resolutions of the estimators. The normalized correlation coefficient for temporal lag T and spatial lag Z between the sample points within a selected data window can be calculated with

$$R(T,Z)=\frac{\sum_{t=1}^{N_T-|T|}\sum_{z=1}^{N_Z-|Z|} W_1^* W_2}{\sqrt{\left(\sum_{t=1}^{N_T-|T|}\sum_{z=1}^{N_Z-|Z|} W_1^* W_1\right)\left(\sum_{t=1}^{N_T-|T|}\sum_{z=1}^{N_Z-|Z|} W_2^* W_2\right)}}$$

$$W_i = w(t-T_i, z-Z_i) - \frac{\sum_{\tau=1}^{N_T-|T|}\sum_{\zeta=1}^{N_Z-|Z|} w(\tau-T_i, \zeta-Z_i)}{(N_T-|T|)(N_Z-|Z|)} \qquad i=1 \text{ or } 2$$

$$|T| \le N_T - 1 \quad \text{and} \quad |Z| \le N_Z - 1 \tag{5-24}$$

$$\text{if} \quad T \ge 0 \quad \text{then} \quad T_1 = 0 \quad \text{and} \quad T_2 = -T \quad \text{else} \quad T_1 = T \quad \text{and} \quad T_2 = 0$$

$$\text{if} \quad Z \ge 0 \quad \text{then} \quad Z_1 = 0 \quad \text{and} \quad Z_2 = -Z \quad \text{else} \quad Z_1 = Z \quad \text{and} \quad Z_2 = 0$$

where $w(t,z)$ is the z-th sample of the analytic RF-signal in the t-th row of the data window. Unless otherwise mentioned, the data window of which the center is located at $z = 50$ mm is considered for the calculation of the desired correlation coefficients. The data window contained 32 sample points in the axial direction (approximately 1.2 mm) and 100 RF-segments in the temporal direction (approximately 10 ms at a pulse repetition frequency of 10 kHz).

Table 5-1 Expected, estimated and correlation model fitted mean values ± standard deviations (n=16) of the signal parameters: center frequency, equivalent bandwidth and signal-to-noise ratio.

	$\hat{f}_C$ [MHz]	$\hat{BW}_{EQ}$ [MHz]	$\hat{SNR}$ [dB]
Expected	4.79 ± 0.03 (0.6%)	1.65 ± 0.07 (4.2%)	?
Estimators	4.74 ± 0.08 (1.7%)	1.67 ± 0.12 (7.2%)	27.8 ± 1.6 (5.8%)
Model Fit	4.73 ± 0.12 (2.5%)	1.67 ± 0.13 (7.8%)	26.4 ± 1.6 (6.1%)

5.5 Results

5.5.1 Signal parameters estimators

The signal parameters of the RF-signals that can be estimated are the center frequency (Eq. (5-4)), the equivalent bandwidth (Eq. (5-11)) and the signal-to-noise ratio (Eq. (5-21)). Table 5-1 shows the results of the estimators for RF-signals assessed with a transducer-to-motion angle of 120° and a step size of 100 µm. The data window ($N_T = 100$, $N_Z = 32$) for the estimators was located at $z = 50$ mm. The corresponding expected values for the estimated signal parameters can not be assessed directly from the settings of the experimental setup. A rough approximation for the expected center frequency and equivalent bandwidth can be obtained by means of a fit of an ideal Gaussian power spectral density distribution through the observed one. The expected values based on the fit used the mean power spectral density distribution of 100 RF-segments ranging from approximately $z = 47.5$ mm to $z = 52.5$ mm (i.e., 128 sample points). The expected signal-to-noise ratio cannot be determined, because only the signal plus noise power can be estimated from the mean power spectral density distribution. The signal or noise power alone can not be determined, so it is not possible to give an approximation of the expected signal-to-noise ratio.

Because the noise contribution to the measured RF-signals was very small, the performance of the signal-to-noise ratio estimator is evaluated by adding noise with known power to the measured RF-signals. First, white Gaussian noise was generated with the same power as the measured RF-signals (variance RF-signal = variance noise) and added to the measured signals. This should result in an

estimated signal-to-noise ratio of 0 dB, because the influence of the noise in the measured RF-signals was negligible. Next, the noise was iteratively doubled or halved before addition to the measured signals. Thereafter, the signal-to-noise ratios were estimated. The estimated signal-to-noise ratios are plotted in the graph of Fig. 5-3 (solid line). The diagonal dashed line shows the expected trend if the measured RF-signals were indeed noise free. The large standard deviation at the expected signal-to-noise ratio of –26 dB is caused by one outlier.

Table 5-1 shows also the results for the signal parameters obtained by means of a least-squares fit (Matlab function "fmins") of the correlation model with the correlation coefficients calculated from the corresponding data window. For the center frequency, the argument part of the correlation model (Eq. (5-2)) is fitted with the correlation coefficients with temporal lags between –1 and 1 and axial lags between –8 and 8. For the equivalent bandwidth and the signal-to-noise ratio, the modulus part of the correlation model (Eq. (5-3)) is fitted with the correlation coefficients with a positive temporal lag greater than zero (to exclude the influence of noise) and a modulus larger than 0.9.

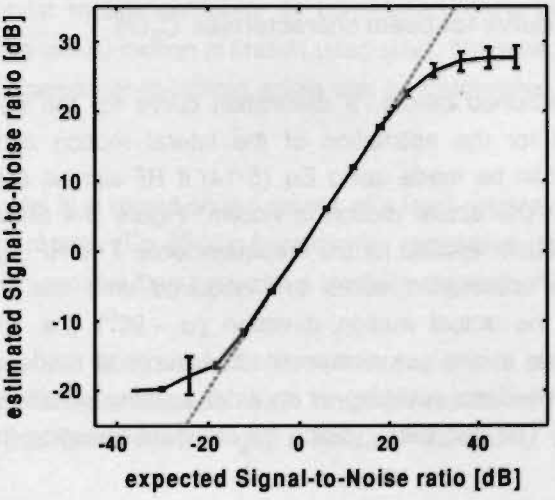

Fig. 5-3 Expected signal-to-noise ratio based on the addition of white Gaussian noise with known power versus the estimated signal-to-noise ratio. The solid line shows the estimated signal-to-noise ratios whereas the dashed line shows the expected trend if the measured RF-signals were noise free. The error bars indicate the standard deviation (n=16).

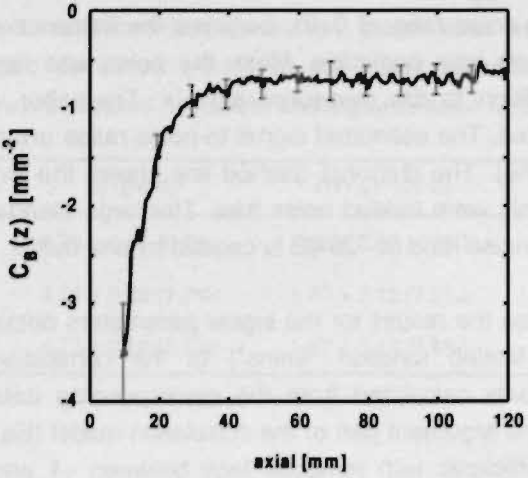

Fig. 5-4 Calibration curve for the beam characteristic $C_B(z)$ of the transducer applied for the measurements. The error bars indicate the standard deviation (n=16).

5.5.2 Calibration curve for beam characteristic $C_B(z)$

As has been mentioned before, a calibration curve for the beam characteristic $C_B(z)$ is needed for the estimation of the lateral motion component. Such a calibration curve can be made using Eq. (5-14) if RF-signals are received from a structure of which the actual motion is known. Figure 5-4 shows the calibration curve of the transducer applied for the measurements. The RF-signals used for the generation of the calibration curve are acquired with the transducer placed perpendicular to the actual motion direction ($\alpha = 90^{\circ}$) (i.e., the lateral motion component is equal to the actual motion). The curve is made using axially half-overlapping data windows resulting in an axial spacing of 0.6 mm between each estimate of $C_B(z)$. The errorbars indicate the standard deviation (n=16).

5.5.3 Motion estimators

The motion estimators are evaluated with RF-signals assessed at a transducer-to-motion angle of 75° and a step size of 100 µm. Table 5-2 shows the expected, estimated and correlation model fitted motion components at an axial distance of z = 50 mm where $C_B(50\,mm)$ = -0.718 mm^{-2} is applied.

Table 5-2 Expected, estimated and correlation model fitted mean values ± standard deviations (n=16) of the different motion components at $z = 50$ mm ($C_B(50\,mm) = -0.718$ mm^{-2}) for a measurement performed at a transducer-to-motion angle of 75° and a step size of 100 µm.

	$\hat{S}_{AX_{UNWRAP}}$ [µm]	$\hat{S}_{LAT}$ [µm]	$\hat{S}_{ACT}$ [µm]	$\hat{\alpha}$ [°]
Expected	25.8	96.6	100.0	75.0
Estimators	25.8 ± 0.5 (1.9%)	94.7 ± 7.9 (8.3%)	98.1 ± 7.6 (7.8%)	74.7 ± 1.1 (1.5%)
Model Fit	26.0 ± 1.9 (7.3%)	93.3 ± 8.3 (8.9%)	96.8 ± 8.0 (8.3%)	74.3 ± 1.7 (2.3%)

The exact transducer-to-motion angle is difficult to determine in the experimental set-up. Therefore, the expected values have been determined in another way. Brands et al. (Brands et al. 1997) showed that the argument-based axial motion estimator is unbiased with a high precision. Therefore, the mean value of the argument-based axial motion estimator is considered to be the expected axial motion. Because the actual motion is known (step size), the expected lateral motion and the expected transducer-to-motion angle can be determined using Eqs. (5-22) and (5-23).

The correlation model fit is based on the results of a least-squares fit of the modulus of the correlation model (Eq. (5-3)) considering correlation coefficients with a positive temporal lag greater than zero and a modulus larger than 0.9.

It should be noted that the transducer-to-motion angles are presented as mean plus/minus the standard deviation although the angle results do not have a normal distribution. This has been done to get a global indication of the quality of the estimated angles.

To get a global overview of the performance of the motion estimators, measurements have been performed at 28 different transducer-to-motion angles ranging from approximately 52° to 130° in steps of 2.88°. Angles outside this range were not possible with the current set-up, because of limitations in the experimental set-up. For each transducer position, the scattering object was placed in such a way that the axial distance $z = 50$ mm was inside the object. Figure 5-5A shows the

sector image that can be obtained from the RF-signals acquired at each of the 28 transducer positions, if only the transducer is rotated and the scattering object is not displaced. The B-mode image shows the scattering object (width: 11 cm; height: 6 cm) resting on a shelf. At each angle 100 RF-signals are assessed. Between the assessment of two consecutive RF-signals, the stepper motor makes a step of 100 µm. The actual motion direction was in the same plane as was described by the rotation of the transducer. As a consequence, the axial and lateral motion components will be different for each transducer-to-motion angle. A schematic representation of the decomposition of the actual motion for three transducer positions is shown in Fig. 5-5B.

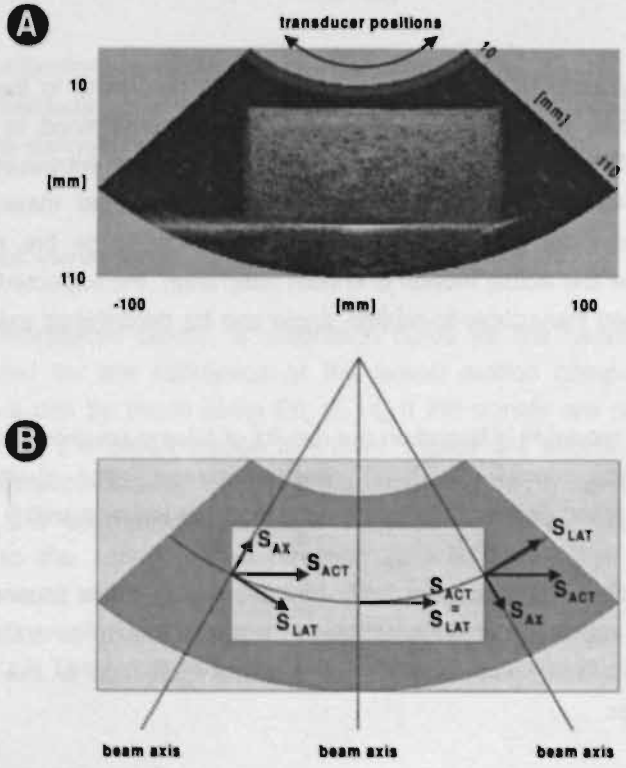

Fig. 5-5 (A) B-mode sector image composed of the combination of the first RF-signals assessed at each of the 28 transducer positions if the scattering object was not displaced during the rotation of the transducer. (B) Schematic representation of the decomposition of the actual motion in axial and lateral motion components for three transducer positions.

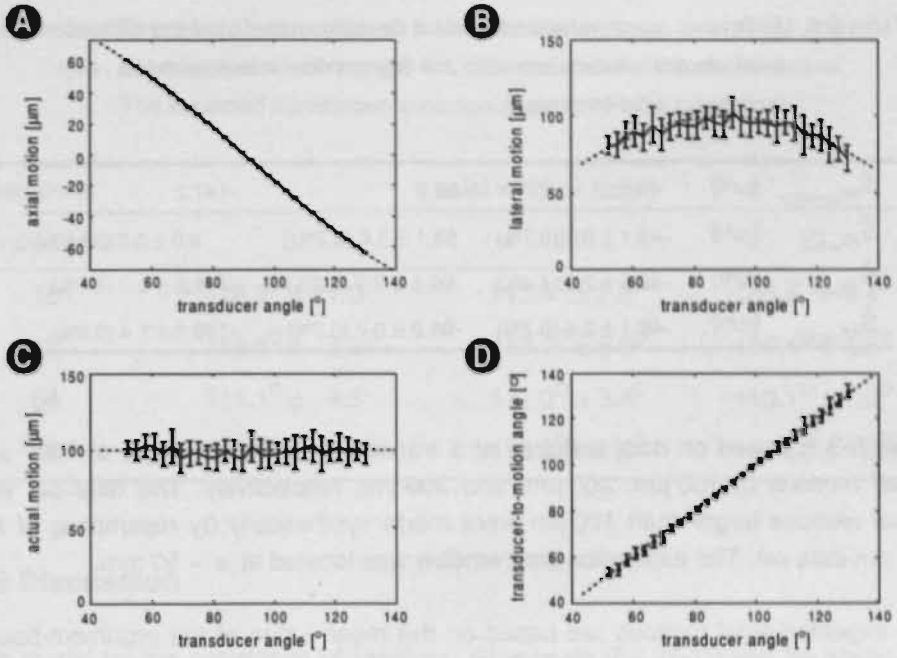

Fig. 5-6 Overview of all motion estimations for a large number of transducer-to-motion angles. The graphs show the estimated (solid line) and expected (dashed line) axial motion (A), lateral motion (B), actual motion (C) and transducer-to-motion angle (D). The error bars indicate the standard deviation (n=16).

For each of the transducer positions, the data window was located at an axial distance of z = 50 mm ($C_8(50\,mm)$ = -0.718 mm^{-2}). Figures 5-6A, 5-6B and 5-6C show the estimated (solid line) and expected (dashed line) axial, lateral and actual motions, respectively. Figure 5-6D shows the estimated (solid line) and expected (dashed line) transducer-to-motion angle.

5.5.4 Unwrapped axial motion

The unwrapped axial motion estimator (Eq. (5-10)) is able to estimate axial motions that are larger than is possible with the argument-based axial motion estimator (Eq. (5-5)). This is demonstrated in Table 5-3. The motion above which the argument-based axial motion estimator aliases is for the experimental set-up, in accordance with Eq. (5-6), approximately 75 µm per time interval between the registration of consecutive RF-signals.

Table 5-3 Estimated mean values ± standard deviations (n=16) of the different axial motion estimators at $z = 50$ mm for measurements with increasing axial motions.

$\hat{S}_{AX_{EXPECTED}}$	[μm]	-49.1	-98.2	-147.2
$\hat{S}_{AX_{ARG}}$	[μm]	-49.1 ± 0.4 (0.7%)	58.1 ± 3.6 (6.2%)	9.0 ± 3.2 (35.3%)
$\hat{S}_{AX_{MOD}}$	[μm]	-49.6 ± 2.2 (4.4%)	-99.5 ± 2.3 (2.3%)	-148.2 ± 3.2 (2.1%)
$\hat{S}_{AX_{UNWRAP}}$	[μm]	-49.1 ± 0.4 (0.7%)	-98.2 ± 0.7 (0.7%)	-146.9 ± 1.4 (0.9%)

Table 5-3 is based on data acquired at a transducer-to-motion angle of 120^{O} and actual motions of 100 μm, 200 μm, and 300 μm, respectively. The data set with actual motions larger than 100 μm were made synthetically by resampling of the 100 μm data set. The estimation data window was located at $z = 50$ mm.

The expected axial motions are based on the mean value of the argument-based axial motion estimate for the data set with actual motion of 100 μm. For the expected values of the data sets with larger actual motions, this mean value is multiplied with the resampling factor of the corresponding data sets.

5.5.5 Influence of size of data window

The size of the data window (i.e., the number of temporal and spatial sample points within the data window) has a strong impact on the precision of the correlation coefficients. The more sample points are within the data window, the more reliable the values of the correlation coefficients will be (Jensen 1994; Ledoux et al. 1998), but this is at the expense of a decreased resolution. The influence of the size of the data window on the performance of the estimators is demonstrated in Table 5-4. The table shows the estimated transducer-to-motion angle for different sizes of the data window. The expected transducer-to-motion angle is 109.8^{O} and is derived from the argument-based axial motion estimate for the largest data window ($N_T = 100$, $N_Z = 32$). The beam characteristic C_B is depth-dependent and, therefore, calibration curves have been made for each of the applied axial window sizes. The values for the beam characteristic at axial distance $z = 50$ mm for the axial window sizes of 8, 16 and 32 sample points are -0.784 mm^{-2}, -0.788 mm^{-2}, and -0.718 mm^{-2}, respectively.

Table 5-4 Estimated mean values ± standard deviations (n=16) of the transducer-to-motion angle for different sizes of the data window. The expected transducer-to-motion angle is 109.8°.

temporal window size	axial window size 8	16	32
16	$116.2^{\circ} \pm 11.0^{\circ}$	$112.4^{\circ} \pm 7.9^{\circ}$	$109.5^{\circ} \pm 4.4^{\circ}$
32	$113.8^{\circ} \pm 8.0^{\circ}$	$112.7^{\circ} \pm 6.9^{\circ}$	$110.4^{\circ} \pm 4.5^{\circ}$
64	$111.1^{\circ} \pm 4.5^{\circ}$	$111.0^{\circ} \pm 3.4^{\circ}$	$110.1^{\circ} \pm 1.9^{\circ}$
100	$110.1^{\circ} \pm 3.9^{\circ}$	$110.2^{\circ} \pm 2.9^{\circ}$	$109.6^{\circ} \pm 1.5^{\circ}$

5.6 Discussion

The model for the correlation of (analytic) RF-signals (Eq. (5-1)) can be applied to determine the magnitude of the actual motion or the transducer-to-motion angle. This information can be extracted from the measured RF-signals by means of a fit between the correlation model and the calculated correlation coefficients. This is an iterative and time consuming approach which can be speeded up considerably when the estimators presented in the current chapter are applied. These estimators require the calculation of only a few correlation coefficients. Tables 5-1 and 5-2 show that the results of the estimators have almost the same or even a little better accuracy and precision than the fitted results and that they are obtained with a considerable lower computational load.

The results in Table 5-1 show that the center frequency and equivalent bandwidth can be estimated reliably with the proposed estimators. The performance of the signal-to-noise ratio estimator could not be verified directly, because the expected signal-to-noise ratio could not be determined. The results in Fig. 5-3 show that the signal-to-noise ratio estimator works properly in the range from –20 dB to 20 dB. The deviation between the expected curve and the estimated one at higher signal-to-noise ratios is caused by the residual noise in the measured RF-signals. For these high signal-to-noise ratios, the noise in the measured RF-signals is larger than the added noise and, thus, the estimated signal-to-noise ratio is no longer dominated by the added noise. Probably, the estimates for the higher signal-to-noise ratios will be underbiased, because for a signal-to-noise ratio of, e.g., 36 dB,

the normalized signal power is equal to 0.99975. It is questionable if the normalized signal power can be estimated with such a precision. Signal-to-noise ratios worse than –20 dB cannot be estimated, because the correlation of noisy signals is not exactly zero due to incidental correlation between noisy signals.

The signal parameter estimators might be used to get some indication of the local attenuation. Furthermore, the signal-to-noise ratio estimator might be used as a threshold to decide whether the estimated parameters are indeed based on signal characteristics or on noise.

Brands et al. (Brands et al. 1997) also introduced a correlation-based estimator for the signal-to-noise ratio, but that estimator is not corrected for the lateral motion. Dependent on the lateral motion, the results of that signal-to-noise ratio estimator will deviate from the results of the current one, which is corrected for the temporal decrease of the correlation caused by lateral motion.

Figure 5-4 shows that the calibration curve for the beam characteristic $C_B(z)$ is almost flat in the range from $z = 40$ mm to $z = 120$ mm. Eq. (5-A7) shows that the beam characteristic $C_B(z)$ depends mainly on the local beam width of the ultrasound beam and the local curvature of the wave front. In the far field, the beam width normally increases with increasing depth, whereas the curvature of the wave front decreases with increasing depth, making the wavefront almost equal to that of a plane wave. Obviously, both effects compensate each other almost in the range from $z = 40$ mm to $z = 120$ mm, so the beam characteristic $C_B(z)$ is rather constant in that range.

Figure 5-4 shows also that the standard deviation on the calibration curve is absolutely larger (relatively, it is almost the same) in the region before the focus (approximately 15 mm). This region is the near field of the transducer. The correlation model assumed a Gaussian beam profile. In the near field, the beam profile is not Gaussian, but consists of local maxima and minina.

For the experimental set-up, the argument-based axial motion estimator aliases for axial motions larger than approximately 75 µm during the interval between the registration of consecutive RF-signals, as can be seen in Table 5-3. The table shows also that the modulus-based axial motion estimator is not susceptible for aliasing. These modulus-based motion estimates are used to unwrap the aliased argument-based motion estimates, resulting in a better precision (smaller standard deviation) of the axial motion estimates as can be seen in Table 5-3.

Table 5-2 and the Fig. 5-6A and 5-6B show that the precision and accuracy of the lateral motion estimates are not as good as those of the (unwrapped) axial motion. This is caused by the fact that the axial resolution, which depends on the transmitted pulse length, is better than the latter resolution, which depends on the beam width. Therefore, lateral motions cause a slower change of the shape of the RF-signals than do axial motions of the same size (Bohs et al. 1998). Hence, incidental disturbances in the scattering object are more pronounced in the lateral motion estimates than in the axial motion estimates.

From the axial and lateral motion estimates, the magnitude of the actual motion is estimated with a standard deviation smaller than 10% (Table 5-2 and Fig. 5-6C) for the currently-applied data window. The standard deviation mainly originates from the lateral motion component, because the standard deviation of the lateral motion is much more pronounced than that of the axial motion. A close look at Fig. 5-6C shows that the mean value of more than half of the actual motion estimates is located below the expected value. This might suggest that the actual motion estimator (and thus the lateral motion estimator) is slightly underbiased. This underbias might be caused by incidental correlation of the noise in the consecutive RF-signals, so that the temporal decorrelation is reduced, resulting in a somewhat smaller estimate for the lateral motion.

Figure 5-6D shows that the transducer-to-motion angle can be estimated quite accurately. The mean standard deviation of the angle estimates shown in Fig. 5-6D is less than 2^{o}. In practical situations, where estimations are performed at a number of adjacent axial positions where almost the same results are expected, the standard deviation can be reduced by applying a median filter. Figure 5-6D shows also that the standard deviation of the estimates of the angle is the smallest at 90^{o} and increases for increasing and decreasing angles. This is a result of the fact that the transducer-to-motion angle is not linearly related to the axial and lateral motion components, as is shown in Eq. (5-18). For small values of the ratio S_{LAT}/S_{AX}, the precision of the lateral motion component contributes heavily to the precision of the estimate of the angle. It should be noted that the results shown in Fig. 5-6 are based on data obtained at transducer-to-motion angles around 90^{o}. Conventional Doppler techniques are not able to estimate motion in this region.

The relation between the transducer-to-motion angle and the actual motion is not linear. Thus, a small fluctuation in the transducer-to-motion angle may correspond with a relatively larger fluctuation in the actual motion estimates, stressing the necessity of a good estimator for the transducer-to-motion angle. The standard

deviation of less than 2° is in the range of the precision of estimates for the transducer-to-motion angle derived from B-mode images as are applied for blood flow measurements; however, for the generation and processing of B-mode images, complex and expensive hardware is required. Furthermore, the estimator is able to estimate continuously the transducer-to-motion angle in time as well as in axial position, whereas in the case of a B-mode image, the angle can only be estimated at the beginning of the measurement and at a single position, not taking into account, for example, any relative displacement of the transducer, vessel or tissue during the measurement. Since a B-mode image of the longitudinal cross-section of the vessel is no longer required to determine the transducer-to-motion angle, it is possible to measure motion in the direction perpendicular to the vessel. This might facilitate the measurement of blood volume flow. The estimators also make the measurement of tissue motion possible, as currently it is very difficult to obtain the transducer-to-motion angle for tissue motion.

Table 5-4 shows that the precision and accuracy of the estimates for the transducer-to-motion angle increase with increasing temporal and/or axial data window sizes, but this is at the expense of a decreased resolution. Furthermore, in an in-vivo situation, the motion of the blood or tissue within a larger data window is probably inhomogeneous. This motion dispersion might affect the performance of the motion estimators.

For relatively small axial motions ($|S_{AX}| < 0.5 S_{AX_{ARG_{MAX}}}$), all parameters can be estimated using only 5 correlation coefficients, namely $R(0,1)$, $R(1,0)$, $R(1,-1)$, $R(1,1)$ and $R(2,0)$. For larger axial motions, a few more correlation coefficients are required, because the axial lag with maximal correlation at temporal lag $T = 1$ has to be found.

The current estimation method provides only the magnitude of the actual motion, not the complete orientation of the three-dimensional motion vector. For in vivo clinical applications, this might still be a shortcoming if the true three-dimensional motion vector is required. If only a local evaluation of the motion behavior of tissue or blood is required then the magnitude of the actual motion is sufficient. Furthermore, for blood flow velocity measurements (e.g., Doppler measurements) it is assumed that blood flow is in the direction of the blood vessel, which reduces the three-dimensional velocity vector to a two dimensional one. In that case, the current method can be applied to automatically determine the transducer-to-motion angle, which up to now has to be determined manually. For the measurement of, for

example, vessel wall motion or tissue elasticity, it would be very beneficial if the transducer could be placed such that only axial motion would be observed. The current method can be utilized to reach that goal.

5.7 Conclusions

It has been shown that from the model for the correlation of analytic RF-signals assessed along a single line of observation with a transducer with a circular beam shape estimators can be derived for the parameters in the model. The estimators require only a few correlation coefficients and a calibration curve for the parameter that describes the beam characteristics (including beam width and curvature of the wave front). The calibration curve is constructed once using RF-signals obtained from a scattering structure that moves with a known motion. Estimators are derived for the center frequency, bandwidth and signal-to-noise ratio of the RF-signals, for the axial motion, and for the magnitudes of the lateral and actual motion components during the interval between the acquisition of consecutive RF-signals. The transducer-to-motion angle can be derived from the estimated motion components. The standard deviation of the estimates for the transducer-to-motion angle is less than 2^{o} in the experimental set-up, which is good enough to make tissue motion measurements possible or to measure blood flow velocity with a single transducer, even in curved vessels and bifurcations.

5.8 Appendices

5.8.1 Appendix A: Summary of derivation of correlation model

An RF-signal can be modeled as

$$RF_0(t) = \int_{-\infty}^{\infty}\int_{-\infty}^{\infty}\int_{-\infty}^{\infty} f_t(x,y,z)\, g(x,y,z)\, dx\, dy\, dz \qquad (5\text{-}A1)$$

where t is the time after the activation pulse, $f_t(\,)$ is the sensitivity function (pressure wave volume insonifying the scatterers contributing to the RF-sample at t seconds after activation) and $g(\,)$ is the space distribution of the scatterers. The

z-coordinate corresponds to the axial direction, whereas the x- and y-coordinates are two perpendicular directions in the plane perpendicular to the axial direction (Fig. 5-1). In the case of analytic RF-signals the sensitivity function is complex.

Due to motion of the scatterers, the T-th RF-signal RF_T after the initial one RF_0, assessed along the same line of observation (M-mode), can be modeled as:

$$RF_T(t) = \int\int\int f_t(x,y,z)\, g(x - TS_{LAT}\cos(\varphi), y - TS_{LAT}\sin(\varphi), z - TS_{AX})\, dx\, dy\, dz \qquad (5\text{-A2})$$

where S_{AX} [m] and S_{LAT} [m] are the magnitudes of the axial and lateral motion components of the scatterers during the time interval between the acquisition of two consecutive RF-signals, respectively. The angle φ determines the direction of the lateral motion component and is defined as the counterclockwise angle between the positive x-axis and the direction of the lateral motion component (Fig. 5-1).

The correlation at temporal lag T and axial lag Z of two analytic RF-signals is defined as

$$R(T,Z) = \left\langle RF_0^*(t)\, RF_T\left(t + \frac{Z}{f_S}\right)\right\rangle \qquad (5\text{-A3})$$

where f_S [Hz] is the sample frequency, * denotes the complex conjugate and $\langle\ \rangle$ denotes mathematical expectation.

Applying Eqs. (5-A1), (5-A2) and (5-A3), the normalized correlation ($|R(0,0)| = 1$) of analytic RF-signals is given by:

$$R(T,Z) = \int\int\int f_t^*(x,y,z)\, f_{t+\frac{Z}{f_S}}(x + TS_{LAT}\cos(\varphi), y + TS_{LAT}\sin(\varphi), z + TS_{AX})\, dx\, dy\, dz \qquad (5\text{-A4})$$

Assuming that (1) the received analytic RF-signals have a Gaussian-shaped power spectral density distribution with center frequency f_C [Hz] and equivalent power bandwidth BW_{EQ} [Hz], (2) the ultrasound beam has a circular shape with a Gaussian intensity distribution in the lateral plane and (3) the shape of the wavefront is approximately parabolic, then the sensitivity function can be modeled as

$$f_t(x,y,z) = \exp\left[\frac{dB\ln[10]}{5w_{dB}^2(z_t)}(x^2+y^2) - \frac{8\pi\, BW_{EO}^2}{c^2}(z_t - z)^2\right] \times \exp\left[j\left(\frac{4\pi\, f_C}{c}\left(z_t - z - \frac{0.5\Delta L(X,Y,z_t)}{X^2+Y^2}(x^2+y^2)\right) + \psi\right)\right] \tag{5-A5}$$

where $w_{dB}(z)$ [m] is the lateral round-trip beam width at axial distance z at a specified power level (in dB) with respect to the peak value, z_t (= $0.5ct$) [m] is the axial distance corresponding to t seconds after activation, c [m/s] is the sound velocity in the medium under investigation, ψ [rad] is a random initial phase and $\Delta L(x,y,z)$ [m] is the additional axial round-trip distance traveled by a curved wave front compared to the corresponding plane wave front at position (x,y,z).

Substitution of Eq. (5-A5) in Eq. (5-A4) and including noise (noise within an RF-signal has the same power spectral density distribution as the RF-signal and is not correlated in time) results in the following equation for the normalized correlation of analytic RF-signals

$$R(T,Z) = (P_S + P_{N_T})\exp\left[T^2 C_B(z_t) S_{LAT}^2 - \frac{4\pi BW_{EO}^2}{c^2}\left(\frac{Zc}{2f_S} - TS_{AX}\right)^2\right] \times \exp\left[j\frac{4\pi f_C}{c}\left(\frac{Zc}{2f_S} - TS_{AX}\right)\right] \tag{5-A6}$$

$$C_B(z_t) = \frac{dB\ln[10]}{10w_{dB}^2(z_t)} + \frac{40\pi^2 f_C^2 w_{dB}^2(z_t)\Delta L^2(X,Y,z_t)}{c^2 dB\ln[10](X^2+Y^2)^2} \tag{5-A7}$$

where P_S is the normalized ($P_S + P_N = 1$) signal power of the received RF-signal, $P_{N_{T=0}} = P_N$ and $P_{N_{T\neq 0}} = 0$ is the normalized noise power and $C_B(z_t)$ is a negative value that is dependent on some characteristics of the ultrasound beam at depth z_t.

A more detailed description of the derivation of this model for the correlation of analytic RF-signals is presented in chapter 4 or (Ledoux et al. 1999).

5.8.2 Appendix B: Estimators in general form

In the following, all signal parameter and motion estimators are presented in a general form for which the lags of the correlation coefficients can be freely set. The lags of the estimators based on the argument of the correlation coefficients should be chosen such that the resulting estimators do not give aliased estimates. The lags of the estimators based on the modulus of the correlation coefficients should be chosen such that the corresponding modulus of the correlation coefficients are relatively large. The "general" estimators are:

- Center frequency:

$$\hat{f}_C = \frac{f_S}{2\pi} \frac{\arg[R(0,Z_1)] - \arg[R(0,Z_2)]}{Z_1 - Z_2} \tag{5-B1}$$

where $Z_1 \neq Z_2$. This estimator is based on the argument of the correlation model and is therefore susceptible to aliasing.

- Axial motion (argument-based):

$$\hat{S}_{AX_{ARG}} = \frac{c}{4\pi \hat{f}_C} \frac{\arg[R(T_1,Z_1)] - \arg[R(T_2,Z_2)]}{T_2 - T_1} + \frac{c}{2f_S} \frac{Z_2 - Z_1}{T_2 - T_1} \tag{5-B2}$$

where $T_1 \neq T_2$. This argument based estimator is susceptible to aliasing.

- Axial motion (modulus-based):

$$\hat{S}_{AX_{MOD}} = \frac{c}{4f_S T} \frac{\ln\left[|R(T,Z_1)|^{Z_2^2 - Z_3^2} |R(T,Z_2)|^{Z_3^2 - Z_1^2} |R(T,Z_3)|^{Z_1^2 - Z_2^2}\right]}{\ln\left[R(T,Z_1)^{Z_2 - Z_3} |R(T,Z_2)|^{Z_3 - Z_1} |R(T,Z_3)|^{Z_1 - Z_2}\right]} \tag{5-B3}$$

where $Z_1 \neq Z_2 \neq Z_3 \neq Z_1$ and $T \neq 0$.

- Equivalent bandwidth:

$$\hat{BW}_{EQ} = f_S \sqrt{\frac{(Z_2 - Z_1)\ln\left[\frac{|R(T,Z_3)|}{|R(T,Z_1)|}\right] - (Z_3 - Z_1)\ln\left[\frac{|R(T,Z_2)|}{|R(T,Z_1)|}\right]}{\pi\left((Z_2 - Z_1)(Z_1^2 - Z_3^2) - (Z_3 - Z_1)(Z_1^2 - Z_2^2)\right)}} \qquad (5\text{-B4})$$

where $Z_1 \neq Z_2 \neq Z_3 \neq Z_1$. Temporal lag T is only allowed to be zero if the noise has the same power spectral density distribution as the signal or if only a rough approximation of the bandwidth is desired. If temporal lag $T = 0$ is applied then the axial lags could best be $Z_1 = 0$, $Z_2 = -1$ and $Z_3 = 1$.

- Lateral motion plus beam characteristic $C_B(z)$:

$$\widehat{C_B(z)S_{LAT}^2} = \frac{\ln\left[\frac{|R(T_1,Z_1)|}{|R(T_2,Z_2)|}\right]}{\left(T_1^2 - T_2^2\right)} + \frac{4\pi \hat{BW}_{EQ}^2}{c^2}\left(\hat{S}_{AX_{MOD}}^2 + \frac{T_1Z_1 - T_2Z_2}{T_2^2 - T_1^2}\frac{c\hat{S}_{AX_{MOD}}}{f_S} + \frac{Z_2^2 - Z_1^2}{T_2^2 - T_1^2}\frac{c^2}{4f_S^2}\right) \qquad (5\text{-B5})$$

where $0 \neq |T_1| \neq |T_2| \neq 0$.

5.8.3 Appendix C: Search for maximal correlation at temporal lag 1

The axial lag with maximal correlation at temporal lag 1 is located at $Z = \text{round}\left[2c^{-1}f_S S_{AX}\right]$. If no indication of the axial motion or any a priori information (e.g., estimates of neighboring data segments) is available, the axial lag with maximal correlation has to be searched. The following procedure can be applied to find that lag with the calculation of a minimal number of correlation coefficients. The first step of the procedure is to find a spatial lag at temporal lag $T = 1$ for which the value of the modulus of the correlation coefficient is larger than a given threshold THR. This threshold is chosen in such a way that spurious correlations are smaller than this threshold value. Furthermore, the maximal correlation at temporal lag $T = 1$, which is dependent on the signal-to-noise ratio and the lateral motion,

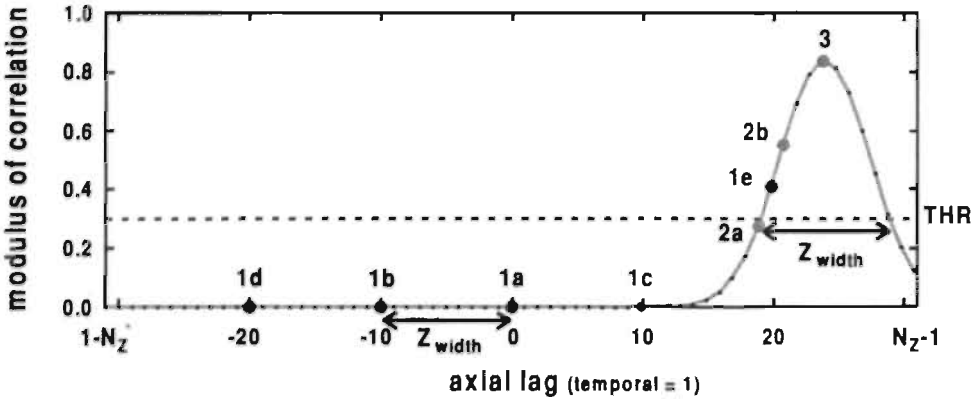

Fig. 5-C1 Schematic representation of the procedure for the determination of the axial lag with maximal correlation at temporal lag $T = 1$. Correlation coefficients (1a) to (1e) are calculated to get a fast search for a correlation coefficient larger than threshold THR. The correlation coefficient (1e), which is the first found correlation coefficient larger than THR, plus the coefficients (2a) and (2b) are substituted in Eq. (5-B3) to get an estimate for the axial motion. This estimate can be applied to determine the lag of the maximal correlation (3).

should be considerably larger than the threshold value. The search for a correlation coefficient with a value larger than the threshold value THR starts with the calculation of $|R(1,0)|$. If this value is smaller than the threshold value, then iteratively the correlation coefficients $|R(1,-n\,Z_{width})|$ and $|R(1,n\,Z_{width})|$ are determined for increasing (integer) values of n until a correlation coefficient is found that is larger than the threshold value (numbers 1a to 1e in Fig. 5-C1), where Z_{width} is the axial width at temporal lag $T = 1$ of the modulus of the correlation function at the threshold level (Fig. 5-C1). This width can be calculated as follows

$$Z_{width} = \frac{2f_S}{B\hat{W}_{EQ}} \sqrt{-\frac{1}{\pi}\left(\ln[THR] - \ln\left[\hat{P}_S \exp\left[\widehat{C_B(z,)S^2_{LAT}}\right]\right]\right)} \qquad (5\text{-}C1)$$

where $\hat{P}_S \exp\left[\widehat{C_B(z_t)S^2_{LAT}}\right]$ is the maximum correlation value at temporal lag $T = 1$. $\hat{C}_B(z_t)$ is known from the calibration curve and $\hat{BW}_{EQ}$ can be approximated by substituting $T = 0$ in Eq. (5-B4), but $\hat{P}_S$ and $\hat{S}_{LAT}$ cannot be determined before the location of the maximal correlation is known. Therefore, only an estimate for the maximum correlation value at temporal lag $T = 1$ can be given based on the worst-case signal power and the maximal expected lateral motion.

Once an axial lag has been found for which the correlation coefficient is larger than *THR* (1e in Fig. 5-C1) the iterative loop has to stop. This axial lag can be applied to estimate the axial motion with Eq. (5-B3). At temporal lag $T = 1$, the axial lag with maximal correlation is located at $Z = \text{round}\left[2c^{-1} f_S \hat{S}_{AX_{MOD}}\right]$.

5.9 References

Anderson ME. Multi-dimensional velocity estimation with ultrasound using spatial quadrature. IEEE Trans Ultrason Ferroel Freq Contr. 1998;45:852-861.

Beach KW, Dunmire B, Overbeck JR, Waters D, Billeter M, Labs K-H, Strandness Jr. DE. Vector Doppler systems for arterial studies. Part I: Theory. Vasc Invest. 1996;2:155-165.

Bohs LN, Friemel BH, Trahey GE. Experimental velocity profiles and volumetric flow via two-dimensional speckle tracking. Ultrasound Med Biol. 1995;21:885-898.

Bohs LN, Geiman BJ, Anderson ME, Breit SM, Trahey GE. Ensemble tracking for 2D vector velocity measurement: experimental and initial clinical results. IEEE Trans Ultrason Ferroel Freq Contr. 1998;45:912-924.

Bonnefous O, Pesqué P. Time domain formulation of pulse-Doppler ultrasound and blood velocity estimation by cross correlation. Ultrason Imaging. 1986;8:73-85.

Brands PJ, Hoeks APG, Ledoux LAF, Reneman RS. A radio frequency domain complex cross-correlation model to estimate blood flow velocity and tissue motion by means of ultrasound. Ultrasound Med Biol. 1997;23:911-920.

de Jong PGM. Measurement of myocardial tissue deformation by correlation interpolation of pulsed ultrasonic echo signals. Thesis: University of Limburg, 1991.

de Jong PGM, Arts T, Hoeks APG, Reneman RS. Determination of tissue motion velocity by correlation interpolation of pulsed ultrasonic echo signals. Ultrason Imaging. 1990;12:84-98.

Dotti D, Lombardi R, Piazzi P. Vectorial measurement of blood velocity by means of ultrasound. Med Biol Eng Comput. 1992;30:219-225.

Fei D-Y, Danhui DL, Fu C-T, Makhoul RG, Fisher MR. Feasibility of angle independent Doppler color imaging for in vivo application: preliminary study on carotid arteries. Ultrasound Med Biol. 1997;23:59-67.

Fish PJ, Hoskins PR, Moran C, McDicken WN. Developments in cardiovascular ultrasound: Part 1: signal processing and instrumentation. Med Biol Eng Comput. 1997;35:561-569.

Gold B, Oppenheim AV, Rader CM. Theory and implementation of the discrete Hilbert transform. In: Rabiner LR, Rader CM, ed. Digital Signal Processing. New York: IEEE Press, 1972: 94-109.

Hoeks APG, Arts TGJ, Brands PJ, Reneman RS. Comparison of the performance of the RF cross correlation and Doppler autocorrelation technique to estimate the mean velocity of simulated ultrasound signals. Ultrasound Med Biol. 1993;19:727-740.

Jensen JA. Artifacts in blood velocity estimation using ultrasound and cross-correlation. Med Biol Eng Comput. 1994;32:S165-S170.

Jensen JA, Munk P. A new method for estimation of velocity vectors. IEEE Trans Ultrason Ferroel Freq Contr. 1998;45:837-851.

Katakura K, Okujima M. Ultrasonic vector velocity measurement by projection computed velocimetry. IEEE Trans Ultrason Ferroel Freq Contr. 1995;42:889-898.

Lai X, Torp H, Kristoffersen K. An extended autocorrelation method for estimation of blood velocity. IEEE Trans Ultrason Ferroel Freq Contr. 1997;44:1332-1342.

Ledoux LAF, Brands PJ, Hoeks APG. Reduction of the clutter component in Doppler ultrasound signals based on singular value decomposition: a simulation study. Ultrason Imaging. 1997;19:1-18.

Ledoux LAF, Willigers JM, Brands PJ, Hoeks APG. Experimental verification of the correlation behavior of analytic ultrasound radio frequency signals received from moving structures. Ultrasound Med Biol. 1998;24:1383-1396.

Ledoux LAF, Willigers JM, Brands PJ, Hoeks APG. Modeling of the correlation of analytic ultrasound radiofrequency signals for angle-independent motion detection. Ultrason Imaging. 1999;(in press 1999):

Li W, Lancée CT, Céspedes EI, van der Steen AFW, Bom N. Decorrelation of intravascular echo signals: potentials for blood velocity estimation. J Acoust Soc Am. 1997;102:3785-3794.

Loupas T, Powers JT, Gill RW. An axial velocity estimator for ultrasound blood flow imaging, based on a full evaluation of the Doppler equation by means of a two-dimensional autocorrelation approach. IEEE Trans Ultrason Ferroel Freq Contr. 1995;42:672-688.

Ogura Y, Katakura K, Okujima M. A method of ultrasonic 3-D computed velocimetry. IEEE Trans Biomed Eng. 1997;44:823-830.

Overbeck JR, Beach KW, Strandness DE. Vector Doppler: accurate measurement of blood velocity in two dimensions. Ultrasound Med Biol. 1992;18:19-31.

Phillips DJ, Beach KW, Primozich J, Strandness Jr DE. Should results of ultrasound Doppler studies be reported in units of frequency or velocity? Ultrasound Med Biol. 1989;15:205-212.

Picinbono B. On instantaneous amplitude and phase of signals. IEEE Trans Sign Proc. 1997;45:552-560.

Ramamurthy BS, Trahey GE. Potential and limitations of angle-independent flow detection algorithms using radio-frequency and detected echo signals. Ultrason Imaging. 1991;13:252-268.

Trahey GE, Allison JW, von Ramm OT. Angle independent ultrasonic detection of blood flow. IEEE Trans Biomed Eng. 1987;34:965-967.

Wilson LS, Gill RW. Measurement of two-dimensional blood velocity vectors by the ultrasonic speckle projection technique. Ultrason Imaging. 1993;15:286-303.

Wilson LS, Robinson DE. Ultrasonic measurement of small displacements and deformations of tissue. Ultrason Imaging. 1982;4:71-82.

Yeung K-WW. Angle-insensitive flow measurement using Doppler bandwidth. IEEE Trans Ultrason Ferroel Freq Contr. 1998;45:574-580.

Chapter 6

Reduction of the clutter component in Doppler ultrasound signals based on Singular Value Decomposition: *a simulation study*

L.A.F. Ledoux, P.J. Brands, A.P.G. Hoeks

Ultrasonic Imaging, 19: 1-18; (1997).

Reduction of the clutter component in Doppler ultrasound signals based on Singular Value Decomposition: a simulation study

6.1 Abstract

In pulsed Doppler ultrasound systems, the ultrasound radiofrequency (RF) signals received can be employed to estimate noninvasively the time-dependent blood flow velocity distribution within an artery. The RF-signals are composed of signals originating from clutter (e.g., vessel walls) and scatterers (e.g., red blood cells). The clutter, which is induced by stationary or slowly-moving structure interfaces, must be suppressed to get reliable estimates of the mean blood flow velocities. In conventional pulsed Doppler systems, this is achieved with a static temporal high-pass filter. The static cut-off frequency and the roll-off of these filters cause that the clutter is not always optimally suppressed. This chapter introduces a clutter removal filter that is based on Singular Value Decomposition (SVD). Unlike conventional high-pass filters, which take into account only the information of the temporal direction, the SVD filter makes use of the information of the temporal and spatial directions. The advantage of this approach is that it does not matter where the clutter is located in the RF-signal. The performance of the SVD filter is examined with computer-generated Doppler RF-signals. The results are compared with those of a standard linear regression (SLR) filter. The performance of the SVD filter is good, especially if a large temporal window (i.e., approximately 100 RF-signals) is applied, which improves the performance for low blood flow velocities. A major disadvantage of the SVD filter is its computational complexity, which increases considerably for larger temporal windows.

6.2 Introduction

Pulsed Doppler ultrasound systems can be adapted to estimate noninvasively the time-dependent blood flow velocity distribution within a blood vessel. The time interval between consecutively-received radiofrequency (RF) signals corresponds to the pulse repetition frequency (PRF). The PRF determines the maximum Doppler frequency, namely $PRF/2$, which can be detected unambiguously in accordance with the Nyquist sampling theorem. The relation between the blood flow velocity v [m/s] and the Doppler frequency f_{dop} [Hz] is given by:

$$v = \frac{c}{2\cos(\alpha)} \frac{f_{dop}}{f_c} \tag{6-1}$$

where f_c [Hz] is the frequency of the emitted sound waves, c [m/s] the speed of sound in tissue, and α [°] is the angle between the sound beam and the direction of the velocity.

A hypothesis is that vessel wall anomalies may find their origin in a disturbed wall shear stress (Hoeks and Reneman 1995). Wall shear stress τ [Pa] is the tangential force field that acts on the vessel wall. It can be determined as follows:

$$\tau = \eta \left. \frac{\delta v}{\delta \rho} \right|_{\rho = R} \tag{6-2}$$

where η [Pa·s] is the viscosity of the blood, $\delta v/\delta \rho$ [1/s] is the wall shear rate, v [m/s] is the blood flow velocity in the axial direction of the blood vessel, ρ [m] is the radial position, and R [m] is the radius of the blood vessel. Eq. (6-2) shows that the wall shear stress can be determined if the viscosity of the blood and the wall shear rate are known. The wall shear rate can be derived from the blood flow velocity near the wall.

The RF-signals received include information of the region in front of the anterior vessel wall up to the region behind the posterior vessel wall; they are a mixture of scatter and clutter. Scatter is induced by moving red blood cells, whereas clutter is induced by stationary or slowly-moving structure interfaces (e.g., vessel walls, reverberations). The RF-signals are corrupted to some extent by some additive wideband noise.

The consecutively-received RF-signals can be considered as an RF-matrix. The N_T rows of this matrix contain the individual RF-signals (Fig. 6-1A), whereas the N_Z columns contain the so-called LF (low frequency) signals (Fig. 6-1B). Each LF-signal corresponds to one depth and contains the Doppler information that is necessary for the estimation of the local blood flow velocity. This Doppler information can be visualized by the power spectral density distribution of such an LF-signal (Fig. 6-1C). The clutter component has a relatively high amplitude, a narrow temporal bandwidth, and a low temporal mean frequency (maximum vessel wall velocity is approximately 10 mm/s), whereas the scatter component has a relatively low amplitude, a broader temporal bandwidth, and a temporal mean frequency that can vary between $-PRF/2$ and $PRF/2$. The noise has a uniform distribution over the frequency range $[-PRF/2, PRF/2]$ and a low amplitude.

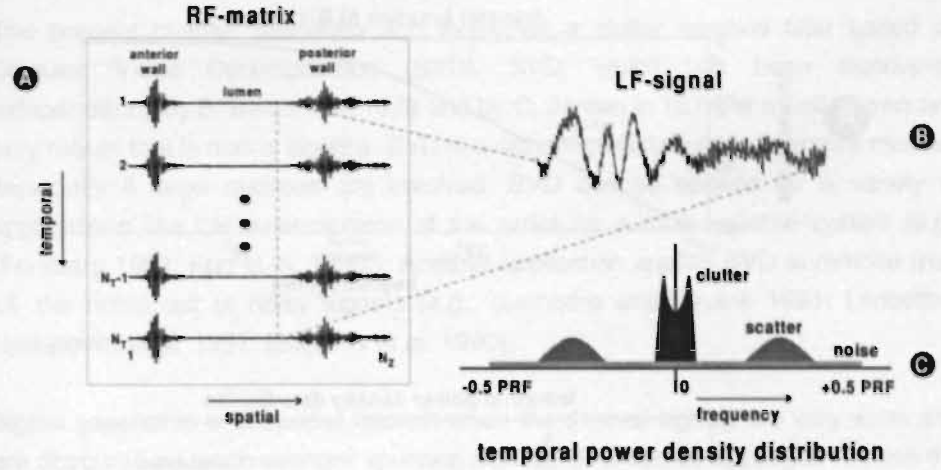

Fig. 6-1 (A) A schematic representation of an RF-matrix. (B) An LF signal. (C) A schematic representation of the (temporal) power density distribution of an LF-signal.

In order to obtain reliable estimates of the mean blood flow velocities by means of a single mean frequency estimator, the clutter must be removed or at least be strongly suppressed. In conventional pulsed Doppler systems, this is achieved with a static temporal high-pass filter. Fig. 6-2A shows a transfer function that is typical for high-pass filters. The transfer function shown corresponds to a standard linear regression (SLR) filter (Hoeks et al. 1991) that makes use of a (temporal) window of 17 sample points. The SLR filter has the advantage, unlike most common high-pass filters, of having no settling time. On the other hand, its cut-off frequency is set by the number of (temporal) points considered.

Figure 6-2B shows an artificial temporal power density distribution that could be found in the region close to a vessel wall, where clutter is very strongly present and the scatter frequencies are rather low. The figure shows also the temporal power density distribution of the same LF signal after it is filtered with the SLR filter.

Figure 6-2B shows some of the disadvantages that are typical for static high-pass filters. First, it must be noted that extreme high clutter peaks are not optimally suppressed when the roll-off of the filter is not steep enough. Furthermore, the transfer function does corrupt scatter signals corresponding to low blood flow velocities. Both effects cause the estimated blood flow velocities to be incorrect. Those problems can be reduced by applying a higher order high pass filter (i.e., one with a steeper roll-off).

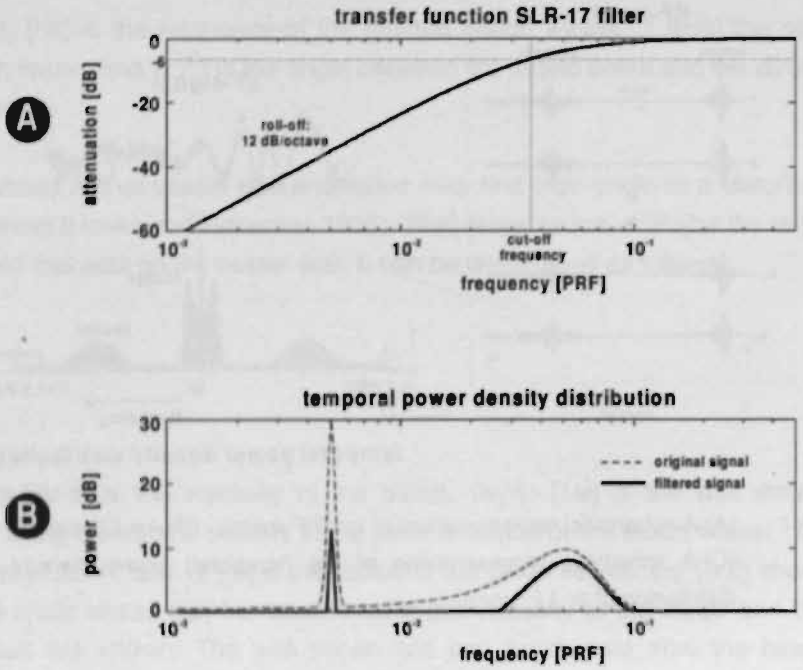

Fig. 6-2 (A) The transfer function of a standard linear regression filter making use of a (temporal) window of 17 sample points (SLR-17). (B) The effects of the SLR-17 filter on an artificial temporal power density distribution of an LF-signal. The dashed line corresponds to the original spectrum, whereas the solid line corresponds to the SLR-17 filtered signal.

Another disadvantage is that the cut-off frequency of the filter has direct influence on the minimal measurable velocity of the scatterers. The cut-off frequency is chosen in such a way that the highest expected temporal frequency induced by clutter is suppressed a certain number of decibels. Because of the roll-off, the cut-off frequency has to be some octaves higher than the highest expected temporal clutter frequency. The highest expected temporal clutter frequency is time-dependent and not always easy to estimate. A clutter removal filter with an adaptive cut-off frequency ((Brands et al. 1995b), (Brands et al. 1995a)) makes it possible to measure lower velocities of the scatterers than is possible with conventional static high-pass filters, but it has to make use of system-dependent thresholds. These thresholds are necessary to prevent the filter from adapting its cut-off frequency to the main scatter frequency in regions where the scatter component is dominant.

The present chapter describes and examines a clutter removal filter based on Singular Value Decomposition (SVD). SVD, which has been discovered independently by E. Beltrami in 1873 and by C. Jordan in 1874, is a well-known and very robust tool in matrix algebra. SVD is a rather computationally intensive method, especially if large matrices are involved. SVD can be applied for a variety of applications like the determination of the order for a multi-variable system (e.g., (Forsberg 1991; Fort et al. 1995)). Another application applies SVD to remove (part of) the noise out of noisy signals (e.g., (Lamothe and Stroink 1991; Ledbetter-Nellepovitz et al. 1991; Muijtjens et al. 1990)).

Signal separation is of special interest when the desired signals are very weak and are obscured by much stronger spurious signals. SVD can be applied to remove the spurious signals in those situations. For example, this is demonstrated by Callaerts et al. (Callaerts et al. 1990), who applied SVD to extract the fetal electrocardiogram from cutaneous electrode signals.

In the following, it is described how SVD can be applied to distill the weak scatter signal from the RF-signal (i.e., how SVD, and under what restrictions, can be employed to suppress the clutter component). The performance of the SVD filter is examined with simulated Doppler RF-signals. To get an impression of the performance of the SVD filter, the results of the performance tests are compared with those of the standard linear regression filter.

6.3 Theory

6.3.1 Introduction to singular value decomposition

This section gives a short summary of some of the aspects of the singular value decomposition (SVD). More detailed information about the SVD can be found in (Callaerts 1991; Forsythe et al. 1977; Golub and Van Loan 1983; Press et al. 1986; Stewart 1973).

The SVD of any real matrix $M \in \Re^{N_T \times N_Z}$ can be written as the following unique real factorization:

$$M = USV^T \tag{6-3}$$

where the superscript ^{T} signifies the transpose of a matrix; $U \in \Re^{N_T \times N_T}$ is an orthonormal matrix, called the left singular matrix, which columns u_i $(1 \le i \le N_T)$ contain the eigenvectors of the outer product MM^T; $V \in \Re^{N_Z \times N_Z}$ is an orthonormal matrix, called the right singular matrix, which columns v_i $(1 \le i \le N_Z)$ contain the eigenvectors of the inner product M^TM; and $S \in \Re^{N_T \times N_Z}$ is a diagonal matrix with real, non-negative diagonal elements. The diagonal elements σ_i (with $1 \le i \le l = \min(N_T, N_Z)$) of S are called the singular values of matrix M. The singular values σ_i are ordered from large to small (i.e., monotonically decreasing). The nonzero singular values of matrix M are equal to the square root of the nonzero eigenvalues of the outer product MM^T and of the inner product M^TM.

6.3.2 Principles of SVD-based signal separation

The SVD factorisation of matrix M shown in Eq. (6-3) can also be written as (the so-called dyadic decomposition):

$$M = \sum_{i=1}^{l} u_i \sigma_i v_i^T = \sum_{i=1}^{l} \sigma_i u_i v_i^T. \tag{6-4}$$

If the rows of matrix M contain signals with almost the same characteristics, then Eq. (6-4) can be interpreted as follows. Each signal in the rows of matrix M is split up into l subsignals. The multiplication of the orthonormal vectors u_i and v_i^T determines the shape of the subsignals, whereas the multiplication of $u_i v_i^T$ with the singular value σ_i determines the amplitude of the subsignals. Because the length of the orthonormal vectors u_i and v_i is unity, the singular values σ_i may be considered as a measure for the contribution of each of the subsignals to the original signals in the rows of matrix M. The singular values are ordered monotonically decreasing; therefore, the subsignals will be ordered from large to small.

The RF-matrix (Fig. 6-1A) is a matrix in which the rows contain signals with almost the same characteristics, namely the consecutive RF-signals. It is a commonly-accepted notion that the difference between consecutive RF-signals is relatively small, because of the relatively high *PRF* (typically between 5 and 10 kHz). Periods of up to 10 milliseconds (even during systole) may still be considered as stationary. Therefore, the RF-matrix considered for processing may

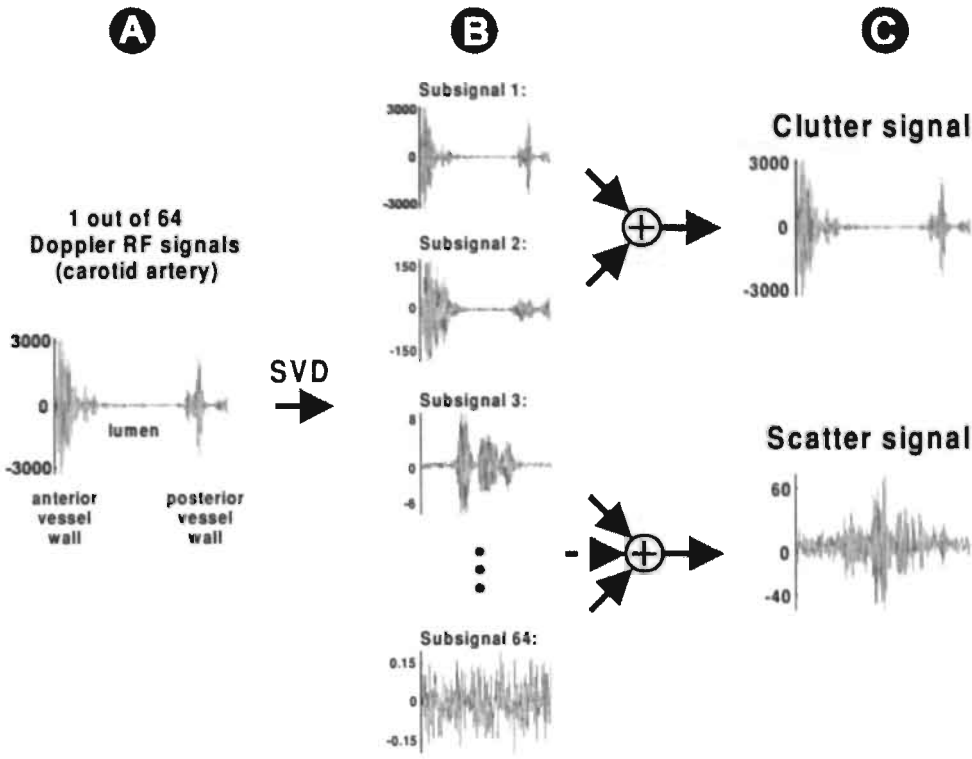

Fig. 6-3 (A) One of the RF-signals out of an RF-matrix that contains 64 RF-signals. (B) The subsignals of the RF-signal resulting from the SVD of the RF-matrix. (C) Top: Summation of the strongest subsignals results in the clutter signal. Bottom: Summation of the remaining subsignals results in the scatter signal.

contain consecutive RF-signals corresponding to a period of time with a maximum duration of 10 ms, i.e.,

$$\frac{N_T}{PRF} < 10\,\text{ms} \tag{6-5}$$

where N_T is the number of temporal sample points (i.e., the number of RF-signals in the RF-matrix).

Figure 6-3 shows the concept of SVD-based RF-signal separation. Figure 6-3A shows one of the RF-signals out of an RF-matrix that contains 64 measured RF-signals (note that the number of sample points of an RF-signal must be equal to or larger than the number of RF-signals in the matrix). If SVD is applied to the RF-matrix, then the RF-signal of Fig. 6-3A is split up into 64 subsignals. Some of these subsignals are shown in Fig. 6-3B. The idea of SVD clutter removal is that the strongest subsignals correspond to the clutter and the remaining subsignals to signals originating from the scatterers. The maxima of the two strongest subsignals (Fig. 6-3B) are located on the places where the vessel wall was situated. These two signals are summed to form the clutter signal. The remaining subsignals are summed to form the scatter signal. These clutter and scatter signals are shown in Fig. 6-3C.

Formally written in terms of SVD, the RF-matrix M_{RF} with $N_T \leq N_Z$ is expressed as:

$$M_{RF} = U_{RF} S_{RF} V_{RF}^T \tag{6-6}$$

where $M_{RF} \in \Re^{N_T \times N_Z}$, $U_{RF} \in \Re^{N_T \times N_T}$, $S_{RF} \in \Re^{N_T \times N_Z}$, and $V_{RF} \in \Re^{N_Z \times N_Z}$. Eq. (6-6) can also be written as:

$$M_{RF} = \begin{bmatrix} U_C & U_S \end{bmatrix} \begin{bmatrix} S_C & O_{S2} O_{S3} \\ O_{S1} & S_S O_{S4} \end{bmatrix} \begin{bmatrix} V_C^T \\ V_S^T \\ O_{V1}^T \end{bmatrix} \tag{6-7}$$

where $U_C \in \Re^{N_T \times p}$ and $U_S \in \Re^{N_T \times (N_T - p)}$; $S_C \in \Re^{p \times p}$ and $S_S \in \Re^{(N_T - p) \times (N_T - p)}$; $V_C \in \Re^{N_Z \times p}$ and $V_S \in \Re^{N_Z \times (N_T - p)}$; and $O_{S1} \in \Re^{(N_T - p) \times p}$, $O_{S2} \in \Re^{p \times (N_T - p)}$, $O_{S3} \in \Re^{p \times (N_Z - N_T)}$, $O_{S4} \in \Re^{(N_T - p) \times (N_Z - N_T)}$, and $O_{V1} \in \Re^{N_Z \times (N_Z - N_T)}$ are matrices with all elements equal to zero (zero-matrices). If the matrices with subscript c correspond to the clutter and those with subscript s to the scatter, then the scatter matrix M_S, whose row signals contain only the scatter component of the RF signals, can be determined as:

$$M_S = U_S S_S V_S^T \tag{6-8}$$

where $M_S \in \Re^{N_T \times N_Z}$.

Eq. (6-8) is only an approximation of the scatter matrix if the clutter and scatter signals fulfill some restrictions. These restrictions are:

- *Consecutive clutter signals must have a relatively high correlation.*
  The correlation between the signals in a matrix determines the number of nonzero singular values. If the signals have a high correlation, then the number of nonzero singular values will be small (note that very small singular values are considered to be zero, because they are for the greater part caused by noise.). If the clutter signals have a high correlation, then only p of the N_T singular values of the clutter matrix $M_C \in \Re^{N_T \times N_Z}$ (with $N_T < N_Z$) are nonzero, which means that the clutter signals can be described with only p subsignals. In practice, consecutive clutter signals have indeed a high correlation (small bandwidth), even when an RF-matrix is used with the maximum number of RF-signals (Eq. (6-5)), because the motion of the clutter is very low (maximum velocity vessel wall is approximately 10 mm/s). This restriction is always fulfilled for time segments smaller than 10 ms.

- *Clutter must be the dominant component in the RF-signal.*
  In accordance with Eq. (6-7), the largest singular values should correspond to the clutter (i.e., the smallest clutter singular value should be larger than the largest scatter singular value). This requirement is satisfactorily fulfilled if the clutter signal is at least somewhere dominantly present in the RF-signal. In practice, the clutter always dominates in the RF-signals (Fig. 6-1), because the vessel walls are always strongly present in an RF-signal. The SVD filter is a 2-D filter (i.e., it is applied on a matrix not only on a vector); therefore, it does not matter where the clutter is located in the RF-signal. Thus, this restriction is fulfilled in practice.

- *Clutter and scatter signals must be uncorrelated.*
  The first p singular values should correspond to the clutter. This requires that the first p column vectors of the left and right singular matrices also must correspond to the clutter. From the definition of the SVD, it is known that both singular matrices are orthonormal. Therefore, the following equations are valid for the left singular vectors:

$$U_C^T U_S = O_U \tag{6-9}$$

$$\Rightarrow V_C S_C^T U_C^T U_S S_S V_S^T = O_{MTM} \tag{6-10}$$

$$\Rightarrow M_C^T M_S = O_{MTM} \tag{6-11}$$

where $O_U \in \Re^{p\times(N_T-p)}$ and $O_{MTM} \in \Re^{N_Z\times N_Z}$ are zero-matrices; $M_C \in \Re^{N_T\times N_Z}$ is the clutter matrix; and $M_S \in \Re^{N_T\times N_Z}$ is the scatter matrix. The following equations are valid for the right singular vectors:

$$V_C^T V_S = O_V \tag{6-12}$$

$$\Rightarrow U_C S_C V_C^T V_S S_S^T U_S^T = O_{MMT} \tag{6-13}$$

$$\Rightarrow M_C M_S^T = O_{MMT} \tag{6-14}$$

where $O_V \in \Re^{p\times(N_T-p)}$ and $O_{MMT} \in \Re^{N_T\times N_T}$ are zero-matrices; $M_C \in \Re^{N_T\times N_Z}$ is the clutter matrix; and $M_S \in \Re^{N_T\times N_Z}$ is the scatter matrix.

Eqs. (6-11) and (6-14) show that the clutter and scatter signals must be uncorrelated. As long as the velocity of the scatterers is high, the scatter and clutter signals are almost uncorrelated, but for low velocities of the scatterers, the correlation between clutter and scatter signals will increase. This correlation will reduce as the number of RF-signals in the RF-matrix is increased.

6.3.3 Methods to extract scatter matrix from RF-matrix

The easiest way to extract the scatter matrix M_S from the RF-matrix is to replace in Eq. (6-7) one or more of the matrices U_C, S_C, and V_C, which correspond to the p significantly larger singular values, with a zero matrix. This leads to:

$$M_S = \begin{bmatrix} O_{Uc} & U_S \end{bmatrix} \begin{bmatrix} O_{Sc} & O_{S2}O_{S3} \\ O_{S1} & S_S O_{S4} \end{bmatrix} \begin{bmatrix} O_{Vc}^T \\ V_S^T \\ O_{V1}^T \end{bmatrix} \tag{6-15}$$

where $O_{Uc} \in \Re^{N_T\times p}$, $O_{Sc} \in \Re^{p\times p}$, and $O_{Vc} \in \Re^{N_Z\times p}$.

The SVD algorithm is a computationally-intensive algorithm. A reduction in computation time can be reached if the following method is applied to determine the scatter matrix. It is assumed that the number of spatial sample point N_Z of the RF-matrix is larger than the number of temporal sample points N_T. The clutter

velocity is always very low; Therefore, the number of clutter singular values is rather low ($p << N_T$). Because the left singular matrix is orthonormal, which involves that $UU^T = U^T U = I$, where I is the unity matrix, it follows that:

$$M_{RF} = IM_{RF} = UU^T M_{RF} \tag{6-16}$$

The clutter matrix can now be determined by making use of only the left singular vectors that correspond to the p largest singular values (i.e., U_C). This results in:

$$M_C = \begin{bmatrix} U_C & O_{Us} \end{bmatrix} \begin{bmatrix} U_C^T \\ O_{Us}^T \end{bmatrix} M_{RF} \left(= U_C S_C V_C^T \right) \tag{6-17}$$

The scatter matrix can now easily be determined by subtraction of the clutter matrix from the RF-matrix, i.e.,

$$M_S = M_{RF} - M_C \tag{6-18}$$

$$\Rightarrow M_S = \left(I - U_C U_C^T \right) M_{RF} \tag{6-19}$$

where $I \in \Re^{N_T \times N_T}$ is a unity matrix.

The computation time is reduced, because only the singular values and the p largest left singular vectors have to be determined. The right singular matrix V, which is larger than the left singular matrix U, is not needed in this approach. Also, only a very small part of the U matrix has to be determined. The singular values, which are necessary to determine the number of significantly larger singular values, are equal to the square root of the nonzero eigenvalues of the outer product $M_{RF} M_{RF}^T$ and the p left singular vectors are equal to the eigenvectors corresponding to the largest eigenvalues. The reduction of the RF-matrix $M_{RF} \in \Re^{N_T \times N_Z}$ to the size of the outer product $M_{RF} M_{RF}^T \in \Re^{N_T \times N_T}$ reduces the computation time also considerably, especially if $N_T << N_Z$. The multiplication $M_{RF} M_{RF}^T$ causes the smaller singular values to be computed less precisely, but this is no problem since only the large singular values are required to determine the corresponding eigenvectors.

6.4 Methods applied for verification

6.4.1 Simulation of Doppler RF-signals

The performance of the SVD filter is examined by means of simulated Doppler RF-signals. The simulations are based on a slightly modified version of the simulation method described by Hoeks et al. (Hoeks et al. 1993). The modification makes it possible to include more than one Doppler component in the simulated RF-signals.

The simulation method creates RF-matrices M_{RF} that contain N_T RF-signals with a length of N_Z sample points ($M_{RF} \in \Re^{N_T \times N_Z}$). The characteristics of the RF-signals are determined by the quality factor Q (i.e., the ratio of the center frequency f_C and the equivalent power bandwidth of the RF-signal). The RF-noise quality factor is assumed to be equal to Q, which is the case for most of the ultrasound systems. The Nyquist sampling theorem orders that the sample frequency f_S should at least be $4f_C$ ($f_S = 4f_C$ is applied for the simulations), because the highest frequency component present in an RF-signal (with $Q \geq 2$) is approximately equal to $2f_C$.

The base of the simulation method is that some long RF-signals are generated as follows. In the frequency domain, two (long) series (e.g., length of 16K) of randomly-generated values, with zero mean and Gaussian amplitude distribution, are combined to yield the complex spectrum of white noise. The two series are multiplied by the square root of a Gaussian function centered at the desired center frequency f_C. The width of the spectral distribution is specified by the quality factor Q. The inverse Fast Fourier Transform of the complex signal converts the signal to the time domain. The mean power of the RF-signal is normalized, so that a 0 dB level is defined.

An RF-signal is a summation of clutter, scatter and some additive wideband noise. The noise component of the N_T consecutive RF-signals is created by randomly selecting a block of N_Z samples out of a long RF-signal. The clutter and scatter component introduce a velocity shift which is simulated by sliding an observation window stepwise over a long RF-signal. Velocity dispersion is achieved by considering the sum of N signals (N must be odd and $N > 1$), where each signal is subjected to a different randomly fluctuating velocity. The begin position $bp_n(k)$ for the n^{th} component ($1 \leq n \leq N$) of the k^{th} ($1 \leq k \leq N_T$) clutter or scatter signal can be expressed as:

$$bp_n(k) = bp_n(k-1) + \frac{f_s}{f_c}\left\{ v_{AX} + vw\left(\frac{2n-N-1}{2(N-1)} + \frac{e}{N} \right) \right\} \qquad (6\text{-}20)$$

where v_{AX} is the mean of the imposed velocity in the direction of the sound beam (expressed in units of $\lambda\ PRF$, where λ is the wavelength of ultrasound in tissue), vw $[\lambda\ PRF]$ is the width of the imposed rectangular velocity distribution, and $|e| \leq 0.5$ is a random value from a uniform probability distribution. The first begin position $bp_n(0)$ is random. The value of the begin position $bp_n(k)$ is a float, which involves the necessity for an interpolation algorithm to interpolate between sample points. The linear interpolation method, which was employed in the original method, is not accurate enough; Therefore, the cubic spline method is applied. An additional four times oversampling of the RF-signals is employed (note that f_s changes in Eq. (6-20)) to enhance the accuracy of the cubic spline interpolation method. After cubic spline interpolation, the oversampling is undone by means of decimation.

For the generation of the scatter component, 21 separate ($N = 21$) RF-signals are used, whereas for the generation of the clutter component only 1 ($N = 1$) RF-signal is used, because clutter introduces almost no velocity dispersion (i.e., $vw = 0$ in Eq. (6-20)).

The clutter and scatter RF-signals are multiplied with their signal-to-noise ratios SNR [dB] (note that if $N > 1$, then the RF-signal must first be rescaled). Finally, the simulated clutter, scatter, and noise signals are summed to form the Doppler RF-signal. Each simulated RF-matrix can be characterized by means of a set of parameters that form the so-called signal space S_P. This signal space contains the following 8 parameters:

$$S_P = \{N_Z, N_T, Q, SNR_S, v_S, vw_S, SNR_C, v_C\} \qquad (6\text{-}21)$$

where the subscript s corresponds to scatter parameters and the subscript c corresponds to clutter parameters.

6.4.2 Performance evaluation of clutter filters

The performance of a clutter filter can be evaluated as follows. Generate an RF-matrix that contains a scatter and clutter component and filter this matrix with the clutter filter. Next, application of a velocity estimation algorithm on the filtered RF-matrix should result in an estimated velocity close to the value applied for the simulation of the scatter component. The deviation between the estimated velocity of the scatterers and the velocity applied for the simulation is caused by the clutter filter and the velocity estimator.

The deviation DEV has a systematic part (the bias BS) and a random part (the standard deviation SD) (Brands and Hoeks 1992) and is given by:

$$DEV = \sqrt{SD^2 + BS^2} \tag{6-22}$$

If the deviation of the velocity estimates of only the scatter matrix (DEV_{EST}) is determined (i.e., no filter necessary), then it is possible to get the following estimation for the deviation caused by the clutter filter DEV_{FILT}:

$$DEV_{FILT} = DEV_{FILT\&EST} - DEV_{EST} \tag{6-23}$$

where $DEV_{FILT\&EST}$ is the deviation in the velocity estimates after clutter filtering of the RF-matrix. In the rest of this chapter, the term deviation in accordance with Eq. (6-23) will be applied as a measure for the performance of the clutter filter.

In this study, the cross-correlation model (CCM) estimator ((de Jong et al. 1990; Hoeks et al. 1993)) is applied to estimate the axial velocity. The estimated axial velocity $\hat{v}_{AX}$ [$\lambda\ PRF$] in the direction of the sound beam is given by:

$$\hat{v}_{AX} = \frac{f_c}{f_s} \cdot \frac{\arctan2\left[\dfrac{0.5(R(1,1) - R(1,-1))}{R(1,0)\sin[\arccos[R(0,1)/R(0,0)]]}\right]}{\arccos\left[\dfrac{R(0,1)}{R(0,0)}\right]} \tag{6-24}$$

where ^ denotes an estimation and arctan2 denotes a double argument arctangent operation retaining the sign information of the arguments. $R(T, Z)$ is the correlation term from a given rectangular estimation window in an RF-matrix, where Z is the discrete shift in the spatial direction and T is the discrete shift in the temporal direction.

6.4.3 Standard linear regression filter

To get an impression of the overall performance of the SVD filter, the results of this filter are compared with those of another high pass filter, namely, the standard linear regression filter (SLR) (Hoeks et al. 1991). The SLR filter has, like the SVD filter, no settling time and it does not introduce phase distortion, so its results are easy to compare with those of the SVD filter. The SLR filter can be described as follows:

$$OUT(i) = IN(i) - \frac{1}{N_T}\sum_{i=-h}^{h} IN(i) - i\frac{\sum_{i=-h}^{h} i\,IN(i)}{\sum_{i=-h}^{h} i^2} \qquad (6\text{-}25)$$

where $h = 0.5(N_T - 1)$ (note that N_T must be odd), $IN(\ )$ is the value of the inputted sample point, and $OUT(\ )$ is the value of the outputted sample point (i.e. filtered, sample point).

6.5 Results

6.5.1 Verification of SVD clutter removal restrictions

One way to examine if Doppler signals indeed fulfill the restrictions of the SVD-based clutter removal filter is to examine which of the singular values of the RF-matrix correspond to clutter and which to scatter. This is done by comparing the singular values of a simulated reference RF-matrix with those of a simulation in which one of the parameters of the reference setting is changed. This comparison shows which of the singular values change when a certain signal parameter is varied.

Table 6-1 Settings of the simulations belonging to Fig. 6-4, which shows that the clutter and scatter singular values can be separated. Simulation number 1 contains the parameters of the reference setting. For each of the other five simulations, one of the reference parameters (BOLD) is changed. In the simulations with the numbers 2 and 3, one of the clutter parameters is changed, whereas in the simulations with the numbers 4, 5 and 6, one of the scatter parameters is changed.

Simulation number	N_Z [-]	N_T [-]	Q [-]	SNR_C [dB]	v_C [λPRF]	SNR_S [dB]	v_S [λPRF]	vw_S [λPRF]
1	512	32	2	30	0.005	10	0.20	0.05
2	512	32	2	**40**	0.005	10	0.20	0.05
3	512	32	2	30	**0.010**	10	0.20	0.05
4	512	32	2	30	0.005	**20**	0.20	0.05
5	512	32	2	30	0.005	10	**0.40**	0.05
6	512	32	2	30	0.005	10	0.20	**0.10**

To get a realistic reference setting, the following parameters are applied. The reference matrix contains 32 RF-signals with 512 (spatial) sample points and an RF-signal quality factor Q of 2. The clutter velocity v_C is set at 0.005 λPRF, which corresponds to a velocity of 10 mm/s in the direction of the sound beam (if f_C = 5 MHz, PRF = 6 kHz, c = 1550 m/s). The velocity of the scatterers is chosen rather high, namely v_S = 0.2 λPRF, so that the correlation between the clutter and scatter signals is rather low. The width of the velocity of the scatterers vw_S is set at 0.05 λPRF. The signal-to-noise ratio of the scatter signal SNR_S is set at 10 dB, whereas the clutter signal-to-noise ratio SNR_C is set at the relative low value of 30 dB. This setting is listed as simulation number 1 in Table 6-1.

The singular values resulting from the SVD of the simulated reference RF-matrix are shown as solid lines in both top graphs of Fig. 6-4. The singular values are normalized, i.e., each singular value is divided by the largest singular value of this reference simulation. Five more simulations are performed in which the value of one of the signal parameters SNR_C, v_C, SNR_S, v_S, or vw_S is changed (simulation numbers 2-6 in Table 6-1) to examine the influence of the individual signal

parameters on the singular values. The two left graphs of Fig. 6-4 show the influence on the singular values caused by the change of one of the clutter parameters, i.e., SNR_C and v_C (simulation numbers 2 and 3 in Table 6-1), whereas the two right graphs show the influence on the singular values caused by the change of one of the scatter parameters, i.e., SNR_S, v_S, and vw_S (simulation numbers 4, 5 and 6 in Table 6-1).

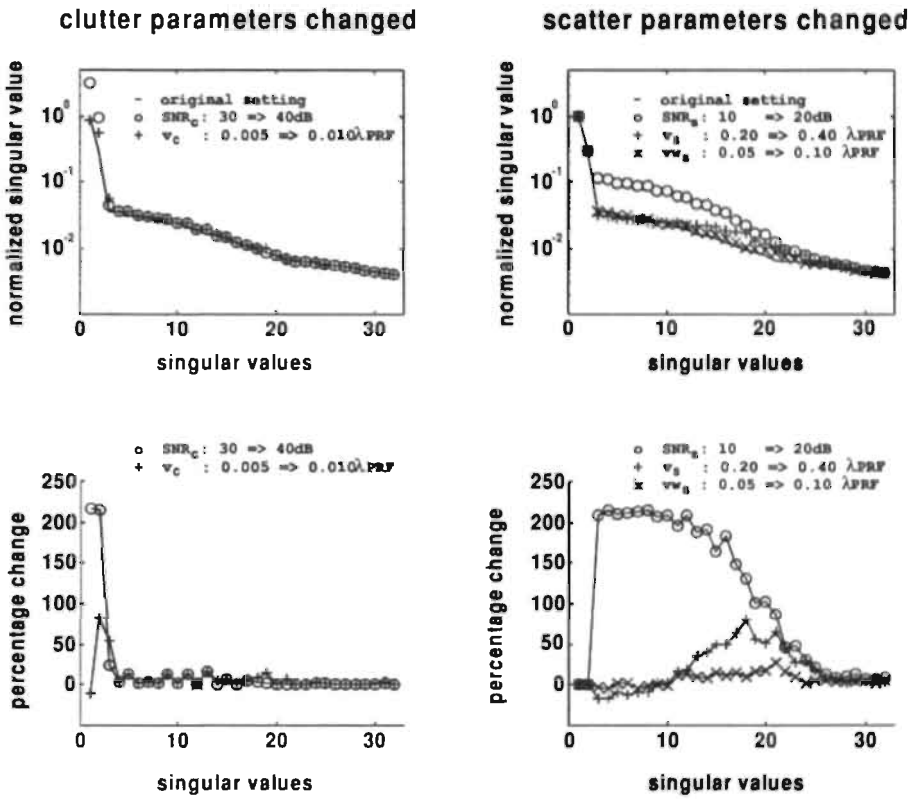

Fig. 6-4 The influence of a changed signal parameter on the singular values. The left graphs correspond to simulations in which one of the clutter parameters is changed, whereas the right graphs correspond to simulations in which one of the scatter parameters is changed. The singular values in the top graphs are normalized, i.e., divided by the maximum singular value that occurs in the SVD of the reference matrix (simulation number 1). The bottom graphs show the percentage change of each of the singular values caused by the change of a specific signal parameter.

To get a better view regarding which of the singular values are changed, the percentage change of each singular value caused by the change of a signal parameter is determined. The percentage change *pc* of the *i*-th singular value caused by a change of signal parameter *par* is defined as:

$$pc_{i,par} = \left[\frac{\sigma_{i,par} - \sigma_{i,ref}}{\sigma_{i,ref}} \right] \times 100\% \qquad (6\text{-}26)$$

where $\sigma_{i,ref}$ is the *i*-th singular value of the reference matrix and $\sigma_{i,par}$ is the *i*-th singular value of the simulation in which parameter *par* is changed. The bottom graphs of Fig. 6-4 show the percentage change corresponding to the top graphs.

The bottom left graph of Fig. 6-4 shows that the change of a clutter parameter results in a remarkable change of mainly the first few singular values, whereas the bottom right graph of Fig. 6-4 shows that the first few singular values almost do not change when a scatter parameter is changed, while the remaining singular values do change. This confirms that the clutter and scatter singular values indeed can be separated and that the first few singular values correspond to the clutter.

The results of Fig. 6-4 show that for the applied simulation settings, the behavior of the singular values are in agreement with the restrictions of the SVD filter. There are only a few clutter singular values, which means that the simulated clutter signals indeed had a high correlation. For the simulated signals, only the first few singular values changed when a clutter parameter was changed, which means that clutter signals were dominantly present in the RF-signal even for this relatively low clutter signal-to-noise ratio. For the applied simulations, the clutter and scatter signals were also uncorrelated, because the clutter and scatter singular values are split up in two nicely separated blocks. This is to be expected because the velocity of the scatterers is rather high compared to the clutter velocity.

6.5.2 Influence of SVD window size on accuracy

A close look at the bottom graphs of Fig. 6-4 shows that the distinction between the clutter and scatter singular values is not that clear, because the third singular value changes considerably in the case of a changed clutter parameter as well as in the case of a changed scatter parameter. This might be caused by the fact that the SVD window size (i.e., the number of spatial sample points N_z and the number of RF-signals N_T in the RF-matrix) is not properly chosen, so that the clutter and scatter singular values cannot be split in an optimal way.

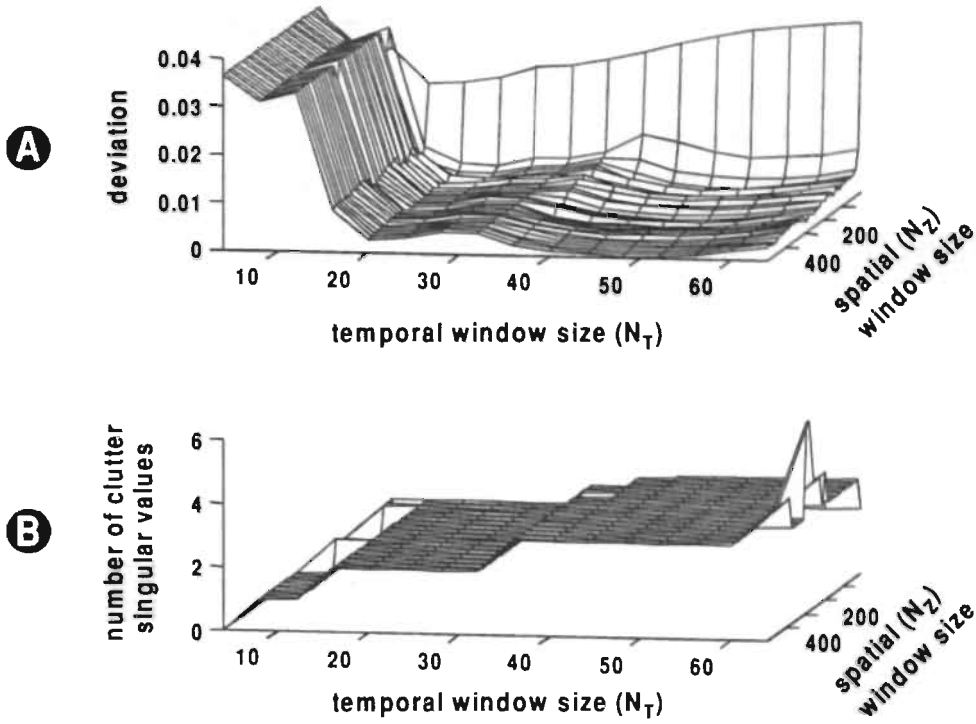

Fig. 6-5 The influence of the SVD window size on the accuracy of the SVD clutter removal filter. (A) shows the minimal achievable deviation in the velocity estimation as a function of the SVD window size and (B) shows the number of removed clutter singular values as a function of the SVD window size.

The influence of the SVD window size on the accuracy of the SVD filter is examined by filtering a simulated RF-matrix with different SVD window sizes. The temporal SVD window size is varied between 4 and 64 with a step size of 4 and the spatial window size is varied between 16 and 512 with a step size of 16. The signal space of the simulated RF-matrix is $S_p = \{N_Z = 2048;\ N_T = 64;\ Q = 2;\ SNR_S = 10;\ v_S = 0.05;\ vw_S = 0.05;\ SNR_C = 40;\ v_C = 0.005\}$. The SVD window is moved nonoverlappingly over the RF-matrix in such a way that a matrix with at least 32 RF-signals with 800 sample points is filtered. This makes it possible to get 100 independent velocity estimates with the CCM estimator with a velocity window of 32 temporal and 8 spatial sample points. These 100 estimates are evaluated to determine the deviation of the clutter filter conforming to Eq. (6-23). For each SVD window size, it is determined which number of removed singular values (Fig. 6-5B)

resulted in the smallest deviation (Fig. 6-5A). Figure 6-5A shows that the deviation is rather large for small (approximately smaller than 20 sample points) temporal and spatial SVD window sizes, because the velocity of the scatterers is relatively low. A further enlargement of the spatial SVD window size has no influence on the deviation, whereas enlargement of the temporal window size has a considerable influence. The deviation increases slightly for some SVD window sizes (e.g., in the regions with approximately 30 and 60 temporal sample points). Also if other signal spaces are applied, these small deteriorations of the deviation are always present, but not always on the same places. These SVD window size dependent deteriorations are caused by the fact that the clutter and scatter component share one singular value for some SVD window sizes, like singular value 3 in the bottom graphs of Fig. 6-4. Comparison of Fig. 6-5A with Fig. 6-5B shows that the aforementioned deterioration of the deviation increases if the number of clutter singular values to be removed is about to change and decreases as soon as the number of clutter singular values to be removed is changed.

6.5.3 Influence of scatterer velocity on deviation

The most important restriction of the SVD clutter removal filter is, as has already been mentioned, that the clutter and scatter signals must be uncorrelated. The correlation is mainly determined by the difference between the velocities of both. If both velocities are low, then the correlation will be high, whereas the correlation will be low as the velocity of the scatterers is high. To examine how well this restriction is fulfilled, it is examined how the deviation of the filter (conforming to Eq. (6-23)) behaves as a function of the velocity of the scatterers. Therefore, simulations are performed where the velocity of the scatterers v_S is varied between 0.005 λPRF and 0.45 λPRF with a velocity width vw_S of 0.05 λPRF. The clutter velocity v_C is maintained at 0.005 λPRF. The behavior of the filter is examined for clutter signal-to-noise ratios SNR_C of 20 dB and 40 dB, whereas the signal-to-noise ratio of the scatter signals SNR_S is set at 10 dB. To include the influence of the number of RF-signals N_T in the RF-matrix, matrices are simulated with 17, 33, and 101 RF-signals (note that if PRF = 10 kHz, then in accordance with Eq. (6-5), the maximum number of RF-signals is 100). The RF-signals have a quality factor Q of 2 and contain 800 sample points (N_z), so that 100 independent velocity estimates are obtained with a spatial velocity estimation window of 8 sample points. The temporal velocity estimation window size is equal to the number of RF-signals in the RF-matrix. The SVD window size is equal to the size of the RF-matrix (i.e., the complete RF-matrix is SVD filtered in a single pass).

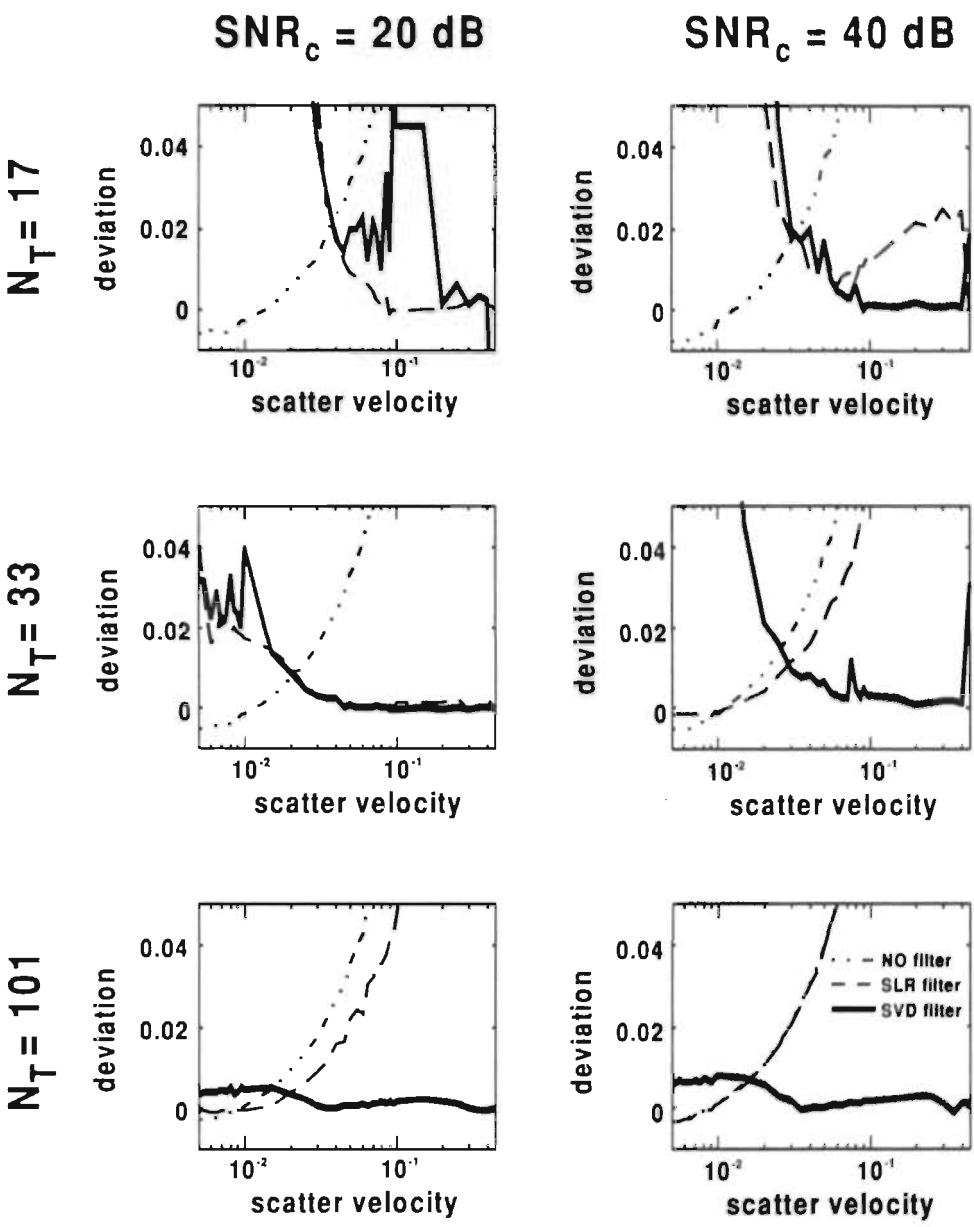

Fig. 6-6 The deviation in the estimated velocities of the scatterers caused by NO filter (dashed-dotted line), SVD filter (solid line) and SLR filter (dashed line). The signal space of the simulated RF-matrices can be summarized as: $S_P = \{N_Z = 800;\ N_T = 17,\ 33,\ \text{or}\ 101;\ Q = 2;\ SNR_S = 10;\ v_S = \text{variable};\ vw_S = 0.05;\ SNR_C = 20\ \text{or}\ 40;\ v_C = 0.005\}$ (see Glossary for symbols).

Table 6-2 Number of clutter singular values in the simulated RF-matrices corresponding to Fig. 6-6.

N_T	SNR_C	
	20 dB	40 dB
17	2	2
33	2	3
101	3	4

The number of clutter singular values is determined as follows. Because only the velocity of the scatterers is varied, the clutter signals will be the same and thus the number of clutter singular values must be constant and independent of the velocity of the scatterers. For some relative high velocities of the scatterers ($v_s > 0.3\ \lambda PRF$), it has been determined what number of removed singular values resulted in the smallest deviation of the estimated velocity of the scatterers. The observed number of clutter singular values are applied for all velocities of the scatterers and are listed for each simulation setting in Table 6-2.

To get some indication of the performance of the SVD filter, the results of the SVD filter are compared with those of the SLR filter. The results are shown in Fig. 6-6 for each of the 6 simulated RF-matrices. The graphs show the deviation of the velocity estimates as a function of the velocity of the scatterers. The thick solid line corresponds to the SVD filter, whereas the thick dashed line corresponds to the SLR filter. The thin dashed line corresponds to the situation that the RF-matrix is not filtered.

The top two graphs show that the performance of the SVD filter with a temporal SVD window of 17 RF-signals is as good as the performance of the SLR filter (In one situation is the SLR filter better, in the other situation the SVD filter.). The RF-signals must be split up in more than 17 subsignals to get a better separation of the RF-signals. The middle two graphs show that the SVD filter works well with a temporal SVD window of 33 RF-signals, but the performance is much better, especially for low velocities of the scatterers, when a temporal SVD window of 101 RF-signals is applied (note that the SLR filter does not work any more for such large temporal windows, because its cut-off frequency, which is reciprocally related to the temporal window size, becomes too low). The deviation for low velocities of the scatterers is still low, because the low frequencies are not completely suppressed as is the case with common high-pass filters.

6.6 Discussion

The deviation caused by the SVD filter can be explained by the SVD window size, and the fact that the first dominant singular values do not always describe the clutter signal completely, because clutter and scatter signals are not completely uncorrelated. The bottom left graph of Fig. 6-4 shows that variation of a clutter parameter not only influences the first largest singular values, but that it also very slightly influences some of the other singular values, e.g., the singular values 9, 11 and 13. The percentage change of these singular values is relatively small compared to that of the first singular values, and therefore, the contribution of the corresponding subsignals to the overall clutter signal is very small. The change of these singular values introduces only a very minor inaccuracy in the performance of the SVD clutter filter. Part of this inaccuracy can be reduced by applying a larger temporal SVD window, which causes the correlation between clutter and scatter signals to decrease even for low velocities of the scatterers (better discrimination).

As is shown in Fig. 6-5 (and Fig. 6-6), the influence of the SVD window size on the performance of the filter decreases when the size of the window is enlarged in both the temporal and the spatial direction. The larger number of signals causes a decreasing correlation between all signals in the matrix. Another consequence of larger SVD window sizes is that more singular values can be determined, and thus, each RF-signal can be split up in more subsignals. The clutter and scatter can be separated with more detail, and thus, more accurately.

Figure 6-6 shows that clutter filtering only makes sense as long as the deviation of the velocity estimates is smaller when the RF-matrix is filtered (thick lines and dashed lines) then when no filter is applied (dashed-dotted lines). In the bottom graphs of Fig. 6-6, it can be seen that the error introduced by the SVD filter (with a large window size) is relatively small even for low velocities of the scatterers. This shows that the SVD filter (with a large window size) can be applied to estimate velocities of the scatterers without a threshold for the lowest measurable velocity of the scatterers.

To make the SVD clutter filter applicable in practice, a robust algorithm is needed that automatically decides how many singular values correspond to the clutter. The automatic separation of the singular values is in general the main problem of the

SVD-based signal separation method (e.g., (Forsberg 1991; Fort et al. 1995; Golub and Van Loan 1983; Lamothe and Stroink 1991; Muijtjens et al. 1990; Ownby and Stanley 1990)). All these authors give a solution for this problem, applicable for the specific signals considered (number and characteristics of the signals). It still has to be examined if one of these methods is suited for automatic separation of clutter and scatter signals or that another method is needed. In appendix A (section 6.8), a possible algorithm for the automatic separation of clutter and scatter singular values is presented.

The SVD clutter filter has been evaluated by means of simulated Doppler RF-signals. These signals were simulated as realistically as possible, but are not completely the same as measured RF-signals. The shapes of the spatial and temporal spectral power density distribution and of the temporal signal of simulated RF-signals are equal to those of measured RF-signals, but the spatial distribution of simulated signals is not the same because the spatial clutter and scatter distribution is uniform. In measured RF-signals, the clutter is mainly located at positions corresponding to the vessel walls and the scatter at positions corresponding to the lumen. Also, the velocities of the clutter and scatterers are uniform in the simulated RF-signals. In measured RF-signals, the spatial velocities of the clutter and the scatterers are not uniform, because the anterior and posterior vessel walls move in opposite direction and at different velocities, and the blood flow velocity is low near the vessel walls and high at the center of the lumen. These differences between simulated and measured RF-signals might cause the SVD clutter filter to behave slightly differently for measured RF-signals, because more (spatial) information is enclosed in measured RF-signals.

The velocity of the clutter and the scatterers is not stationary in practice, but, as has been shown by Eq. (6-5), the RF-signals corresponding to a period of 10 ms may in practice be considered to be almost stationary. Figure 6-6 showed that a large temporal SVD window size (i.e., 101 RF-signals) resulted in the best performance. Combining this large temporal window size with Eq. (6-5) shows that the problem can be solved if a pulse repetition frequency of 10 kHz or more is applied.

A closer look at the graphs of Fig. 6-4 shows that the smallest singular values almost do not change when a simulation parameter is varied. This might be an indication that these singular values correspond to noise. It would be possible to

remove this noise if these singular values were clearly smaller than those of the scatter. This is not the case, so these singular values do not form such a distinct group as the clutter singular values. Therefore, in practice it will be difficult to remove the noise automatically with SVD signal separation.

6.7 Conclusions

It has been shown that SVD can be applied to remove the clutter in an RF-matrix. This is possible because the clutter and scatter signals fulfill certain restrictions. Two of the three restrictions, namely, that the clutter must be dominant in the RF-signal and that consecutive clutter signals must have a high correlation, are in practice always satisfied. The third restriction, that the clutter and scatter signals are uncorrelated, is well satisfied for high velocities of the scatterers. For low scatter velocities and only a few RF-signals, this restriction is less satisfied, giving the SVD filter the same performance as other clutter filters. Because the complexity of most other clutter filters is much lower, the SVD filter will certainly not be the filter of choice if only a few RF-signals are available, as in color Doppler. For a large set of simulated RF-signals (i.e., approximately 100 RF-signals), which in practice is only possible if a relative high pulse repetition frequency is employed (i.e., approximately 10 kHz), the performance of the SVD filter is very constant for a large range of velocities of the scatterers.

The performance of the SVD filter is almost independent of the signal-to-noise ratio of the clutter. The only restriction is that the clutter must dominate the scatter somewhere in the RF-signal.

A great advantage of the SVD filter compared to static high-pass filters is that it is a 2-dimensional filter. Therefore, it is not important where the clutter is located in the RF-signal as long as it is present in the RF-signal. No extra tests and/or system dependent thresholds are required for the detection of the clutter.

The main disadvantage of the SVD filter is that the algorithm is rather time consuming, but this should not be such a great problem as computers get faster almost every month.

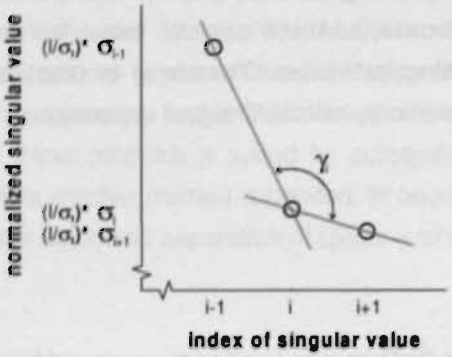

Fig. 6-A1 Schematic representation of the angle between consecutive singular values.

6.8 Appendix A: Separation of clutter and scatter singular values

The following algorithm (SV-angle) is a possible method for the automatic separation of the clutter singular values from the scatter singular values. The SV-angle algorithm bases the number of clutter singular values p on the angles γ_i [^{O}] between consecutive singular values as is shown in Fig. 6-A1. The distance between consecutive singular values is equidistant and equal to one, because the horizontal axis represents the indices of the singular values. Because clutter singular values are much larger than scatter singular values, the variation in the angles γ_i will be larger for clutter singular values than for scatter singular values. The SV-angle algorithm makes use of this difference. The algorithm consists of the following steps:

1. *Normalize singular values:*
   Normally, all singular values σ_i are much larger than one in which case all angles γ_i are close to 180^O. The variation in these angles is very small such that it is very difficult to find a general applicable threshold for the automatic separation of the clutter and scatter angles. Normalization of the singular values such that the maximal values on the horizontal and vertical axes are equal causes a larger variation in the angles γ_i. The singular values are normalized such that the value of the first (i.e., the largest) singular value σ_1 is equal to the number of singular values I.

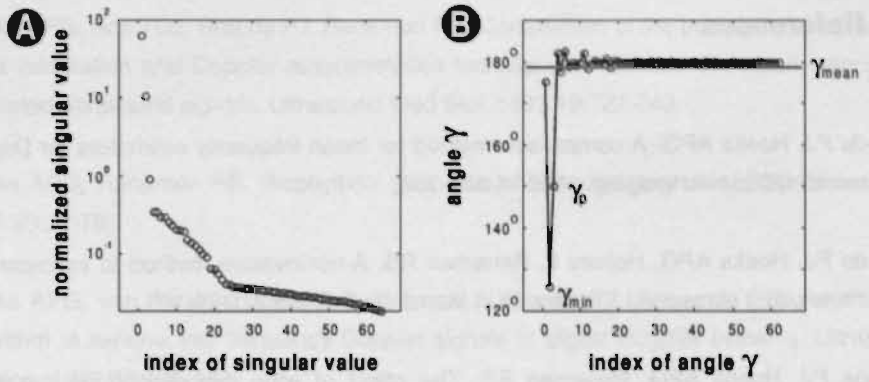

Fig. 6-A2 (A) Example of a set of normalized singular values. (B) The corresponding angles γ_i between the consecutive normalized singular values.

2. *Determine the angles γ_i:*

The angles γ_i between consecutive singular values are determined as follows:

$$\text{if } |\sigma_{i-1} - \sigma_i| > |\sigma_{i+1} - \sigma_i|$$

$$\gamma_{i-1} = \arccos\left[\frac{(\sigma_{i-1} - \sigma_i)(\sigma_{i+1} - \sigma_i) - 1}{\sqrt{(\sigma_{i-1} - \sigma_i)^2 + 1}\sqrt{(\sigma_{i+1} - \sigma_i)^2 + 1}}\right] \tag{6-A1}$$

else

$$\gamma_{i-1} = 360^o - \arccos\left[\frac{(\sigma_{i-1} - \sigma_i)(\sigma_{i+1} - \sigma_i) - 1}{\sqrt{(\sigma_{i-1} - \sigma_i)^2 + 1}\sqrt{(\sigma_{i+1} - \sigma_i)^2 + 1}}\right]$$

where $i = 2, 3, \cdots, (I - 1)$. The angle γ_i is based on three singular values, therefore only $I - 2$ angles can be calculated. Fig. 6-A2 gives an example of a set of (normalized) singular values and the corresponding angles γ_i.

3. *Determine number of clutter singular values:*

The mean γ_{mean} (horizontal line in Fig. 6-A2B) of the angles γ_i is applied to separate the clutter singular values from the scatter singular values. As long as the angles γ_i corresponding to the first largest singular values are smaller than γ_{mean}, the angles are still based on clutter singular values. The index of the last angle γ_i smaller than γ_{mean} determines the number of clutter singular values (γ_p in Fig. 6-A6B). The search for this angle should start from the angle index at which the smallest angle γ_i occurs (γ_{min} in Fig. 6-A6B).

6.9 References

Brands PJ, Hoeks APG. A comparison method for mean frequency estimators for Doppler ultrasound. Ultrasonic Imaging. 1992;14:367-386.

Brands PJ, Hoeks APG, Hofstra L, Reneman RS. A noninvasive method to estimate wall shear rate using ultrasound. Ultrasound in Med & Biol. 1995a;21:171-185.

Brands PJ, Hoeks APG, Reneman RS. The effect of echo suppression on the mean velocity estimation range of the RF cross-correlation model estimator. Ultrasound in Med & Biol. 1995b;21:945-959.

Callaerts D. Singular value decomposition in digital signal processing. Journal A. 1991;32:11-16.

Callaerts D, De Moor B, Vandewalle J, Sansen W, Vantrappen G, Janssens J. Comparison of SVD methods to extract the foetal electrocardiogram from cutaneous electrode signals. Medical & Biological Engineering & Computing. 1990;28:217-224.

de Jong PGM, Arts T, Hoeks APG, Reneman RS. Determination of tissue motion velocity by correlation interpolation of pulsed ultrasonic echo signals. Ultrason Imaging. 1990;12:84-98.

Forsberg F. On the usefulness of singular value decomposition - ARMA models in Doppler ultrasound. IEEE Trans Ultrason Ferr Freq Control. 1991;38:418-428.

Forsythe GE, Malcolm MA, Moler CB. Computer Methods for Mathematical Computations. Englewood Cliffs: Prentice-Hall, 1977.

Fort A, Manfredi C, Rocchi S. Adaptive SVD-based AR model order determination for time-frequency analysis of Doppler ultrasound signals. Ultrasound in Med & Biol. 1995;21:793-805.

Golub GH, Van Loan CF. Matrix Computations. Baltimore: Johns Hopkins University Press, 1983.

Hoeks APG, Arts TGJ, Brands PJ, Reneman RS. Comparison of the performance of the RF cross correlation and Doppler autocorrelation technique to estimate the mean velocity of simulated ultrasound signals. Ultrasound Med Biol. 1993;19:727-740.

Hoeks APG, Reneman RS. Biophysical principles of vascular diagnosis. JClinUltrasound. 1995;23:71-79.

Hoeks APG, van de Vorst JJW, Dabekaussen A, Brands PJ, Reneman RS. An efficient algorithm to remove low frequency Doppler signals in digital Doppler systems. Ultrasonic Imaging. 1991;13:135-144.

Lamothe R, Stroink G. Orthogonal expansions: their applicability to signal extraction in electrophysiological mapping data. Medical & Biological Engineering & Computing. 1991;29:522-528.

Ledbetter-Nellepovitz CC, Rao BD, Fronek A. Determination of in vitro simulated blood cell velocity by laser-Doppler with state space methods. Microvascular research. 1991;41:164-172.

Muijtjens AMM, Roos JMA, Prinzen TT, Hasman A, Reneman RS, Arts T. Noise reduction in estimating cardiac deformation from marker tracks. Am J Physiol. 1990;258:H599-H605.

Ownby DW, Stanley JG. Nonlinear optical effects in oxygen-binding reactions of hemoglobin A0. Biophysical Chemistry. 1990;37:395-406.

Press WH, Flannery BP, Teukolsky SA, Vetterling WT. Singular value decomposition. In: Press WH, Flannery BP, Teukolsky SA, ed. Numerical Recipes: the art of scientific computing. Cambridge: Cambridge University Press, 1986: 52-64.

Stewart GW. Introduction to Matrix Computations. Orlando: Academic Press, 1973.

Chapter 7

In-vivo validation:

preliminary results

In-vivo validation: preliminary results

7.1 Abstract

In the current chapter, some possible in-vivo applications of the techniques presented in the previous chapters are shown. Only preliminary results of these applications will be given since a thorough in-vivo validation has still to be performed.

The SVD-clutter filter presented in Chapter 6 is evaluated with in-vivo data obtained from the a. Carotis Communis. In section 7.2, it is demonstrated how the SVD-clutter filter can be used for in-vivo measurement of blood flow velocities within a blood vessel. To get an indication of the performance of the SVD-clutter filter, axial velocity estimates obtained after SVD-clutter filtering of the RF-signals will be compared with estimates obtained after clutter filtering with Butterworth high-pass filters. The axial velocity estimator is used, because this estimator is very stable (Chapter 5).

In the future, the measurement of tissue motion will be one of the main applications of the absolute motion estimation technique presented in Chapter 5, because the possibilities of other noninvasive tissue motion measurement techniques are very limited. For the in-vivo validation of the current motion estimation technique, it is required that the absolute motion of the organ or structure under investigation is known. Therefore, the motion pattern obtained with another technique should be compared with the pattern obtained with the current absolute motion estimation technique. This extensive study has still to be done. In section 7.3, the absolute velocity (or motion) estimator will be evaluated with data from the a. Carotis Communis. Blood flow measurements are not the ideal situation for the evaluation of the absolute velocity estimator, because noninvasive blood flow ultrasound signals have a much lower signal-to-noise ratio than tissue motion signals. Therefore, they require the employment of a clutter filter, which affects the amplitude behavior of the RF-signals, as will be discussed in section 7.3. On the other hand, blood flow in the a. Carotis Communis can be assumed to have a single direction, because this artery is nearly straight over a reasonable range. Hence, the magnitude and direction of the blood flow in the a. Carotis Communis can easily be assessed with conventional echographic scanners. The absolute velocity provided by those scanners is based on the compensation of the measured axial velocity for the transducer-to-motion angle that is estimated from the corresponding brightness

mode (B-mode) image, showing the longitudinal cross-section of the vessel under investigation. To get an indication of the in-vivo performance of the absolute velocity estimator, the results of the angle-independent absolute velocity estimator presented in Chapter 5 are compared with those of the axial motion estimator presented in Chapter 5 corrected for the transducer-to-motion angle obtained from the 2-D B-mode image.

All RF-data considered in this Chapter are acquired in Doppler-mode with an Ultramark 9 (Advanced Technology Laboratories, Bellevue, WA, USA) using a broadband curved array transducer (C9-5 ICT, estimated center frequency (f_c) 5.3 MHz). The focus is set at either 20 mm or 36 mm, the sample volume is 1 mm and the pulse repetition frequency (PRF) is 10 kHz. The excitation pulse width is approximately equal to the length of the sample volume. A custom made digital PC IO-card acquires the RF-signals (sample frequency f_s is 20 MHz). During each measurement, one second of M-mode data is acquired (i.e., 10.000 RF-signals). The RF-segments that are recorded range from the front of the anterior vessel wall to the back of the posterior wall (approx. 200 sample points). If the SVD-clutter filter is used, packages of 100 RF-signals (i.e., 10 ms) are filtered. If high-pass clutter filters are used, the entire data set is filtered in one pass to reduce settling time effects to a minimum. After clutter filtering, the RF-signals are zero-phase band-pass filtered (2^{nd}-order Butterworth: $f_{low} = 0.05\, f_s$, $f_{high} = 0.45\, f_s$). Zero-phase distortion is obtained by first filtering the signals in the forward direction, after which the (filtered) signals are filtered in the backward direction. The order with which the signals are filtered is twice the order of the band-pass filter except for the borders, where the order is not doubled because of the settling time of the filter in both directions. After filtering, a Hilbert-transformation is used to make the RF-signals analytic. The (unwrapped) axial motion estimator of Eq. (5-10) is applied for the estimation of the axial motion. The absolute motion is estimated with the method presented in sections 5.2.4 and 5.2.5 where the motion estimates are converted to velocity estimates by multiplying the motion estimates with the pulse repetition frequency. The axial size (N_z) of the data window for the velocity estimators is 16 sample points (i.e., approximately 600 μm) and the temporal size (N_T) is 100 sample points (i.e., 10 ms). Consecutive data windows are half-overlapping in the axial direction (spatial inter data window distance is 300 μm) as well as in the temporal direction (temporal inter data window distance is 5 ms).

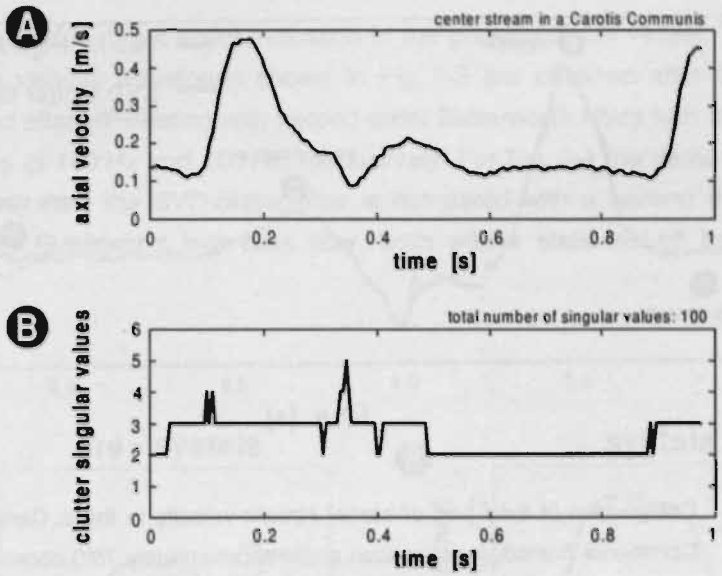

Fig. 7-1 (A) Axial part of center stream velocity in the a. Carotis Communis (transducer-to-motion angle approximately 66°) obtained after SVD-clutter filtering of the RF-signals using the SV-angle algorithm. (B) Number of clutter singular values determined with the SV-angle algorithm for each of the applied data windows.

7.2 SVD-clutter filter

7.2.1 In-vivo results SVD-clutter filter

The main part of the SVD-clutter filter is the separation of the clutter singular values from the scatter (and noise) singular values. The SVD-clutter filter evaluated in this section applies the SV-angle algorithm (section 6.8) to isolate the clutter singular values. Figure 7-1A shows the axial part of the center stream velocity in the a. Carotis Communis obtained after SVD-clutter filtering of the RF-signals. The axial positions of the applied data windows are corrected for the overall motion of the vessel (i.e., vessel wall tracking). The RF-signals were obtained at a transducer-to-vessel (i.e., transducer-to-motion) angle of 66°. Figure 7-1B shows the number of clutter singular values determined with the SV-angle algorithm for each of the temporal data windows corresponding to Fig. 7-1A.

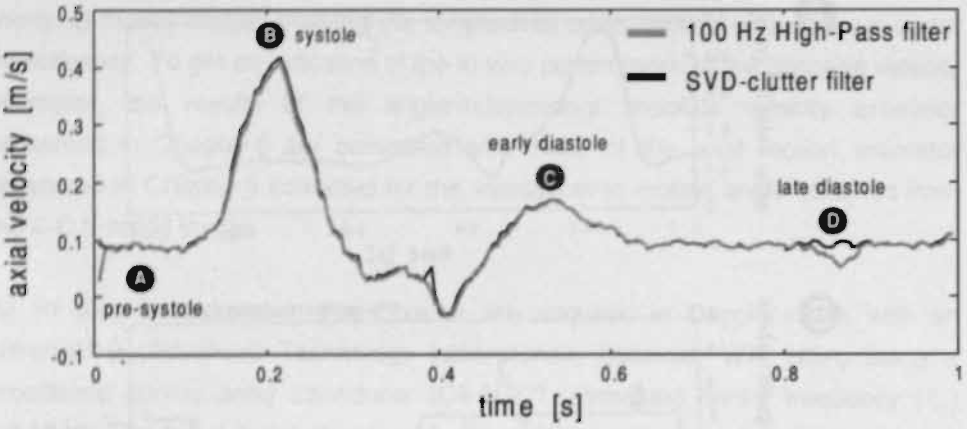

Fig. 7-2 Comparison of axial part of center stream velocity in the a. Carotis Communis (transducer-to-motion angle approximately 70^{O}) obtained after SVD-clutter filtering (black line) and after high-pass filtering (2^{nd}-order Butterworth) with a static cut-off frequency of 100 Hz (gray line) of the RF-signals.

To evaluate the performance of the SVD-clutter filter, axial velocity estimates obtained after SVD-clutter filtering of the RF-signals are compared with estimates obtained after filtering of the RF-signals with Butterworth high-pass (HP) filters with various cut-off frequencies and of different orders. Figure 7-2 shows the comparison of the axial part of the center stream velocity in the a. Carotis Communis (transducer-to-motion angle approximately 70^{O}) obtained after SVD-clutter filtering and after HP-filtering with a second order Butterworth filter with a static cut-off frequency of 100 Hz.

Near the center of the vessel, the influence of the clutter is (normally) the smallest. Therefore, the clutter filters can better be evaluated with spatial velocity waveforms, because near the vessel wall the influence of the clutter is maximal. Figures 7-3 and 7-4 show some spatial blood flow velocities waveforms corresponding to the center stream velocity waveform of the a. Carotis Communis shown in Fig. 7-2. In each of these figures, (A) corresponds to the pre-systole ((A) in Fig. 7-2), (B) to the systole ((B) in Fig. 7-2), (C) to the early diastole ((C) in Fig. 7-2), and (D) to the late diastole ((D) in Fig. 7-2). Furthermore, in each graph the first RF-signal of the corresponding

data set is plotted to get some indication of the position of the vessel. The spatial blood flow velocity waveforms shown in Fig. 7-3 are obtained after SVD-clutter filtering and after HP-filtering with second order Butterworth filters with static cut-off frequencies of 100 Hz and 200 Hz, respectively. For Fig. 7-4 the same RF-data is applied, only now the SVD-clutter filter is compared with a second order and a fourth order Butterworht high-pass filter, both with a static cut-off frequency of 200 Hz.

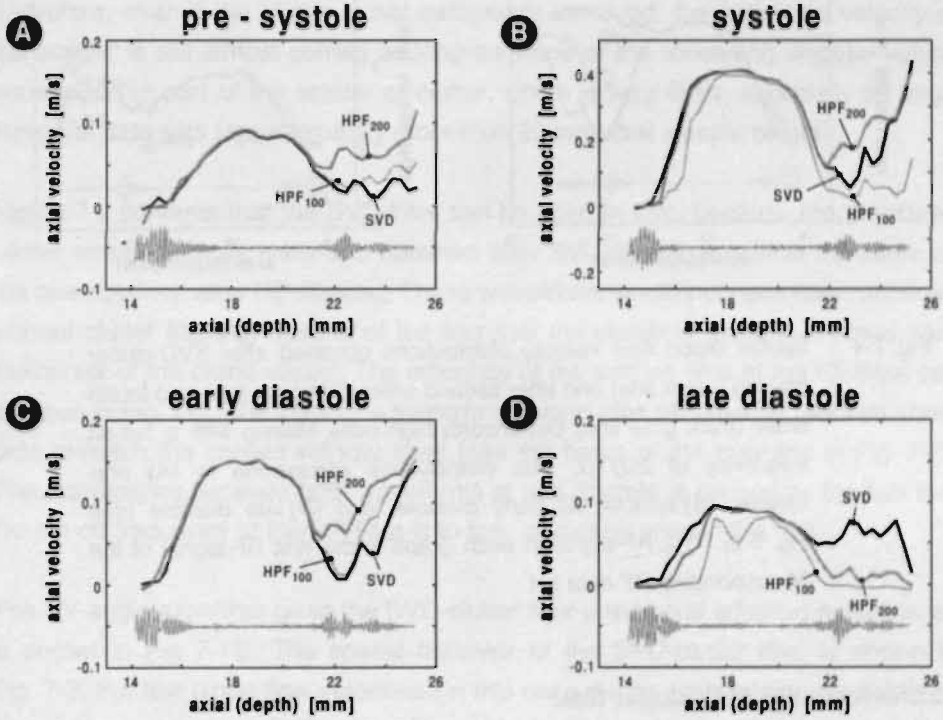

Fig. 7-3 Spatial blood flow velocity distributions obtained after SVD-clutter filtering (black line) and high-pass filtering (2nd-order Butterworth) with a cut-off frequencies of 100 Hz (thin gray line) and 200 Hz (solid gray line), respectively. The distributions correspond to (A) pre-systole, (B) systole, (C) early diastole, and (D) late diastole (see Fig. 7-2). The RF-signal in each graph is the first RF-signal of the corresponding RF-data set.

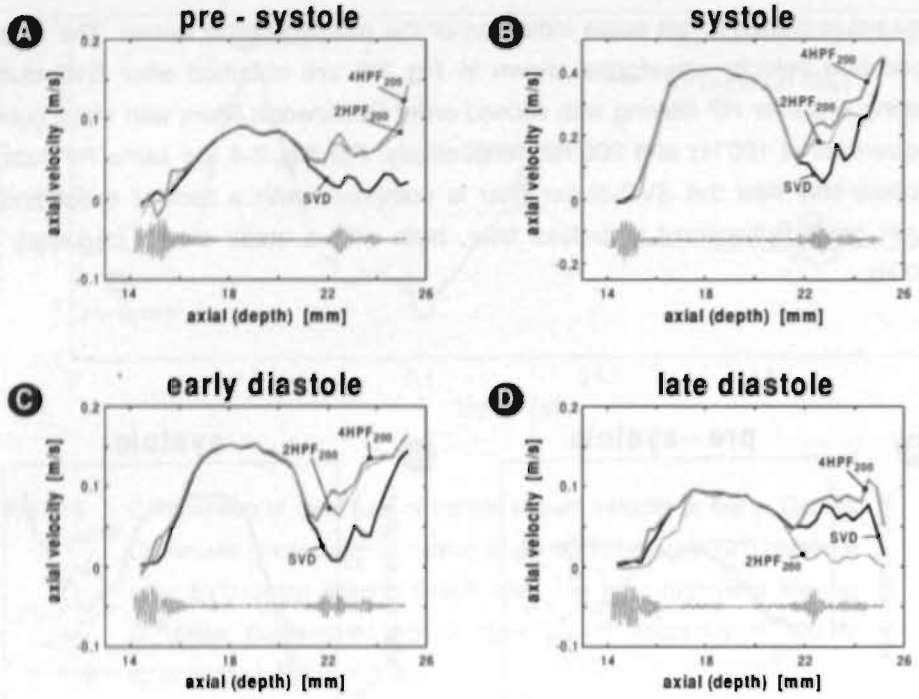

Fig. 7-4 Spatial blood flow velocity distributions obtained after SVD-clutter filtering (black line) and after second order (thin gray line) and fourth order (thick gray line) Butterworth high-pass filtering with a cut-off frequency of 200 Hz. The distributions correspond to (A) pre-systole, (B) systole, (C) early diastole, and (D) late diastole (see Fig. 7-2). The RF-signal in each graph is the first RF-signal of the corresponding RF-data set.

7.2.2 Discussion SVD-clutter filter

The results shown in Figures 7-1 to 7-4 show that the SVD-clutter filter indeed can be applied for in-vivo blood flow velocity measurements. Application of the SV-angle algorithm to separate the clutter singular values from the scatter singular values gives the SVD-clutter filter a kind of adaptive filter behavior. Generally, the number of clutter singular values depends on the velocity of the clutter. The higher the clutter velocity, the more clutter singular values have to be removed. Figure 7-1B shows that the SV-angle algorithm detects indeed more clutter singular values

(approx. 3) during systole, in which phase the clutter and scatter velocities are the largest, than during diastole (approx. 2). The only exception occurs at the velocity dip (dicrotic notch) directly after the systolic peak velocity (see Fig. 7-1A at approx. 0.35 ms). At that moment, the scatter velocity is so low that the clutter and scatter velocities are almost the same. In that case, the singular values can not be separated into clutter and scatter ones, because there is no distinction between both types. The number of clutter singular values determined by the SV-angle algorithm will in that region be arbitrary. Although the clutter is not filtered optimal in that region, the axial velocity estimates will not have a very large error, because both the clutter and the scatter have almost the same velocity in that region. Therefore, even if the clutter is not completely removed, the estimated velocity of the scatter is still almost correct as long as some of the remaining singular values correspond to part of the scatter or clutter, which is very likely, especially for large temporal data sets (approximately more than 20 temporal sample points).

Figure 7-2 confirms that the SVD-filter can be used in-vivo, because the measured center stream velocity waveform obtained after SVD-filtering is almost the same as the one obtained after HP-filtering. These waveforms would not have been obtained without clutter filtering, despite of the fact that the clutter is (mostly) minimal near the center of the blood vessel. The influence of the settling time of the HP-filter can be seen in Fig. 7-2. The velocity waveform obtained after HP-filtering requires some time to reach the correct velocity level (see the begin of the gray line in Fig. 7-2). The discrepancy between both waveforms at late diastole is caused by the fact that the cut-off frequency of the HP-filter is to low, as can be seen in Fig. 7-3.

The SV-angle algorithm gives the SVD-clutter filter a temporal adaptive behavior, as is shown in Fig. 7-1B. The spatial behavior of the SVD-clutter filter is shown in Fig. 7-3. For low blood flow velocities (in this case during pre-systole and diastole), the performance of the SVD-clutter filter with the SV-angle algorithm is comparable with static HP-filters with low (100 Hz) cut-off frequencies (Figs. 7-3A and 7-3C), while for high blood flow velocities (mainly during systole) it is comparable with static HP-filters with high (200 Hz) cut-off frequencies (Figs. 7-3B). An exception on this observation is shown in Fig. 7-3D where the performance after SVD-clutter filtering is comparable with that obtained after HP-filtering with a high cut-off frequency, despite the relatively low blood flow velocity. At that specific location, the order of the HP-filter is too low, such that the roll-off of the filter is not steep enough to suppress the clutter entirely. Figure 7-4D shows that the velocity waveform is

indeed smoother if a fourth order HP-filter is applied. The application of a higher order filter has no influence on the spatial velocity waveforms of the other positions (Figs. 7-3A, 7-3B and 7-3C), because at those locations the roll-off of the second order HP-filter is obvious steep enough to suppress the clutter. Furthermore, a higher order filter has a longer settling time. Therefore, application of a higher order HP-filter is not always more beneficial than a lower order filter for in-vivo measurements.

Figures 7-3 and 7-4 show that the results obtained after SVD-clutter filtering, especially in the region before the posterior wall, are comparable with those of an "ideal" clutter HP-filter, i.e., a filter of which the order and the cut-off frequency is ideally matched to the specific RF-data set, bot spatially as well as temporarily. To obtain good results with a HP-clutter filter, the cut-off frequency should be dependent on the local scatter and clutter velocities. This requires a priori information about the local blood flow velocity as is available in the SVD-filter based on the values of the singular values. To obtain this a priori information using a HP-filter, it is, for example, required to estimate before clutter filtering the local velocity of the clutter to determine the cut-off frequency of the HP-filter in an adaptive way. This increases the computational load of the HP-filter considerably (note that off-line processing is assumed). Each change of the cut-off frequency requires a new settling time of the filter, which makes the adaptive change of the cut-off frequency in practice almost impossible. Brands et al. (Brands et al. 1995) introduced an adaptive HP-clutter filter that not changed the cut-off frequency, but that corrected the RF-signals prior to clutter filtering for the clutter motion. This is done by shifting the temporal frequency distribution toward zero frequency, where the shift is given by the locally estimated mean axial motion of the clutter. For the RF-data sets that are evaluated, this approach gives only adaptive results if a very low (50 Hz) cut-off frequency is applied, because the temporal frequency of clutter due to vessel wall motion is generally less than 25 Hz. For higher cut-off frequencies, the performance of this adaptive HP-clutter filter is almost identical to a static HP-filter, because the low temporal clutter frequency (less than 25 Hz) is well within the range of the HP-filter. Hence, it is very difficult to make a HP-filter as adaptive as the SVD-clutter filter. This makes the SVD-clutter filter an attractive alternative if an adaptive clutter filter is required, because the SVD-filter is comparable with an "ideal" HP-filter, but it has no settling time. Hence, it can very quickly adapt to changes.

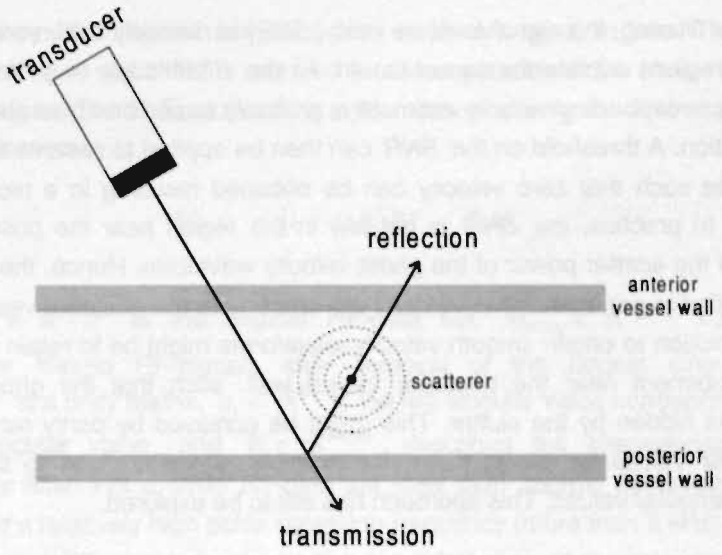

Fig. 7-5 Insonification of scatterers within the lumen due to partial reflection of the sound waves at the posterior vessel wall.

The spatial velocity waveforms of Figs. 7-3 and 7-4 show that a problem occurs at the posterior vessel wall, where the velocity waveform is not zero, as would be expected. In this region, velocities are detected that have the same sign as the blood flow in the lumen. Hence, these velocities can not be caused by noise, which would result in random (plus or minus) velocity estimates in that region. A possible explanation for these consistent velocities is that they are the consequence of a ghost velocity waveform. Due to the difference in acoustic impedance near the posterior wall, part of the emitted acoustic waves will be transmitted into the posterior wall, while the remaining part will be reflected in another direction (Chapter 2). The reflected waves pass again through the lumen of the blood vessel, as is shown in Fig. 7-5. Because blood behaves as scatterers, the reflected sound waves will omnidirectionally be reflected, so that part of these waves will reach the transducer at the same moment as the reflections from the posterior vessel wall and the region behind. As long as the power of those scatterers is larger than that of the noise and the velocity is larger than that of the clutter, a ghost velocity waveform will occur starting at the posterior vessel wall. Due to the mirrored ghost velocity waveform and the limited axial resolution, it is very difficult to obtain a nice velocity waveform near the posterior vessel wall.

After clutter filtering, the signal-to-noise ratio (*SNR*) is normally assumed to be very low in the regions outside the vessel lumen. As the *SNR* is low (e.g., smaller than 0 dB), the corresponding velocity estimate is probably based on noise and will carry no information. A threshold on the *SNR* can then be applied to remove these kinds of estimates such that zero velocity can be obtained resulting in a nicer velocity waveform. In practice, the *SNR* is not low in the region near the posterior wall, because of the scatter power of the ghost velocity waveform. Hence, the *SNR* can not be applied to get a smoother velocity waveform near the posterior vessel wall. A possible solution to obtain smooth velocity waveforms might be to retain part of the clutter component near the posterior vessel wall, such that the ghost velocity waveform is hidden by the clutter. This might be achieved by partly removing the first singular values by giving them, for example, a value close to that of the remaining singular values. This approach has still to be explored.

The main disadvantage of the SVD-clutter filter is that is consumes more computation time than a static HP-filter, but it has the advantage that its adaptive behavior is directly enclosed in the already calculated singular values. For an RF-data set with 100 temporal and 512 spatial sample points, the computation time required in Matlab by the SVD-filter is less than a factor two more than required by a static Butterworth high-pass filter. For smaller data sets, the difference is even smaller. Efficient implementation of the SVD-filter might reduce the difference even further

Unlike HP-filters, the SVD-filter filters packages of RF-signals. The consequence of this approach is that there may occur discrepancies in the RF-data set at the borders between filtered packages of RF-signals. In practice, no significantly different velocity waveforms are obtained if RF-data sets are applied for the velocity estimators that include such a border (either in the temporal direction or in the spatial direction).

The SVD-clutter filter has been evaluated in-vivo with RF-data sets with a relatively large amount of 100 RF-signals, because, as has been shown in Chapter 6, the performance of the SVD-clutter filter is best for large temporal data sets. For small temporal data sets (approximately less than 20 temporal sample points), the performance of the SVD-clutter filter is almost the same as a zero-filter, which removes the mean of the LF-signals (these are composed of points of consecutive RF-signals at a single depth; see Fig. 6-1). This can be demonstrated as follows. The number of clutter singular values in an RF-data set with less than

approximately 20 temporal sample points is always equal to one. This has the advantage that no algorithm is required for the separation of the clutter and scatter singular values. The SVD-clutter filter with removal of only the first singular value can be written as

$$M_{SVD1} = (I - u_1 u_1^T) M = F\,M \tag{7-1}$$

where $M \in \Re^{N_T \times N_Z}$ is the original RF-data set, $M_{SVD1} \in \Re^{N_T \times N_Z}$ contains the SVD-clutter filtered RF-signals after removal of the largest singular value, $I \in \Re^{N_T \times N_T}$ is a unity matrix, $u_1 \in \Re^{N_T}$ is the left singular value corresponding to the largest singular value, and $F \in \Re^{N_T \times N_T}$ describes the characteristics of the SVD-clutter filter. For a small RF-data set (less than approx. 20 temporal sample points) and a relatively high pulse repetition frequency (more than 2 kHz), the clutter in consecutive RF-signals is almost the same because of the slow motion of the clutter structures. In that case, all N_T elements of the orthonormal left singular vector u_1 are equal to $\sqrt{1/N_T}$, resulting in the following description for the matrix F of Eq. (7-1)

$$\begin{aligned} &\text{if} \quad r == c \\ &\quad F(r,c) = 1 - \frac{1}{N_T} \\ &\text{else} \\ &\quad F(r,c) = -\frac{1}{N_T} \end{aligned} \tag{7-2}$$

where r is the row index ranging from 1 to N_T, and c is the column index ranging from 1 to N_T. Substitution of Eq. (7-2) in Eq. (7-1) results in the following description for the SVD-clutter filter for small temporal data sets

$$M_{SVD1}(r,c) = M(r,c) - \frac{\sum_{t=1}^{N_T} M(t,c)}{N_T} \tag{7-3}$$

where r is the row index ranging from 1 to N_T, and c is the column index ranging from 1 to N_Z. A zero filter removes the mean of the data in the columns of the RF-data set (i.e., from the low frequency signals). Hence, the zero filter is given by

$$M_{ZERO}(r,c) = M(r,c) - \frac{\sum_{t=1}^{N_T} M(t,c)}{N_T} \tag{7-4}$$

where $M_{ZERO} \in \Re^{N_T \times N_Z}$ contains the zero filtered RF-signals, r is the row index ranging from 1 to N_T, and c is the column index ranging from 1 to N_Z. Comparison of Eqs. (7-3) and (7-4) shows that the SVD-clutter filter for small temporal RF-data sets indeed approximates the zero filter under the assumption that all elements of the first left singular vector are equal to $\sqrt{1/N_T}$, which in practice is almost always the case. Because the SVD-clutter filter is almost a zero filter for small RF-data sets, it is advised to use a zero-filter for those data sets, because the computation time of the zero filter is less than that of the SVD-filter.

7.2.3 Conclusions SVD-clutter filter

The results of this in-vivo evaluation of the SVD-clutter filter (with SV-angle algorithm) show that the filter indeed can be applied for in-vivo blood flow velocity measurements. Despite of the larger computational load of the SVD-clutter filter (compared to a static high-pass filter), it has the advantage that the filter has a temporal adaptive character without the need of many additional calculations, as is the case for adaptive HP-filters. The SV-angle algorithm determines for each data set from the already calculated singular values the number of clutter singular values giving the SVD-clutter filter its temporal adaptive behavior. In contrast to other clutter filters, the SVD filter also includes spatial information in the clutter filter process, because it is a 2-D filter. Furthermore, the SVD-filter has no settling time and no roll-off. The only requirement is that clutter must be dominantly present somewhere within the RF-data set. For small temporal RF-data sets (less than 20 RF-signals), the performance of the SVD-filter is almost equal to that of a zero filter.

7.3 Absolute velocity measurement

7.3.1 Introduction absolute velocity measurement

Current ultrasonic echographic scanners are only able to measure the velocity component in the direction of the ultrasound beam (i.e., the axial velocity). Hence, absolute velocity measurements are only possible if the transducer-to-motion angle α [°] is known. The absolute velocity v [m/s] can then be derived from the axial velocity v_{AX} [m/s] after correction for the transducer-to-motion angle as is given by

$$v = \frac{v_{AX}}{\cos(\alpha)} \tag{7-5}$$

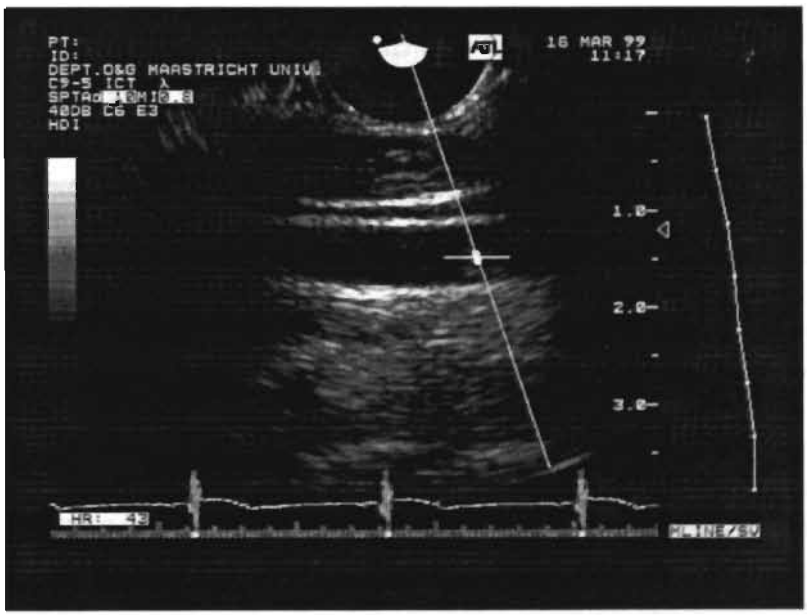

Fig. 7-6 B-mode image of a longitudinal cross-section of the a. Carotis Communis showing how the M-line (i.e., the line of observation) is positioned and the angle of observation is obtained.

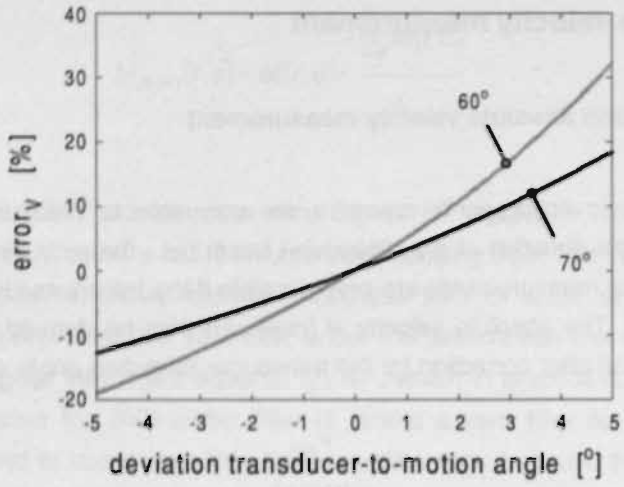

Fig. 7-7 Error in absolute velocity (based on axial velocity corrected for the transducer-to-motion angle) due to a deviation in the angle estimated from the B-mode image. The error is shown for two frequently applied transducer-to-motion angles, namely 60° and 70°.

One of the few in-vivo situations for which the transducer-to-motion angle with acceptable accuracy can be estimated with conventional scanners are blood flow velocity measurements in straight blood vessels like for example the a. Carotis Communis or the a. Brachialus. The blood flow in straight vessels is rather undisturbed. Therefore, the blood flow will be in the direction of the blood vessel. For the estimation of the axial velocity, ultrasound signals along a single line of observation (M-mode) are considered. The angle between the line of observation and the direction of the blood vessel is assumed to be a good approximation of the transducer-to-motion angle (Fig. 7-6).

The accuracy of the estimated transducer-to-motion angle determines the correctness of the absolute velocity estimates. A slight discrepancy in this angle results in a noticeable error in the estimated absolute velocity. This nonlinear error ($error_v$ [%]) is given by

$$error_v = \left[\frac{\cos(\alpha)}{\cos(\alpha + \delta\alpha)} - 1 \right] \times 100\% \qquad (7\text{-}6)$$

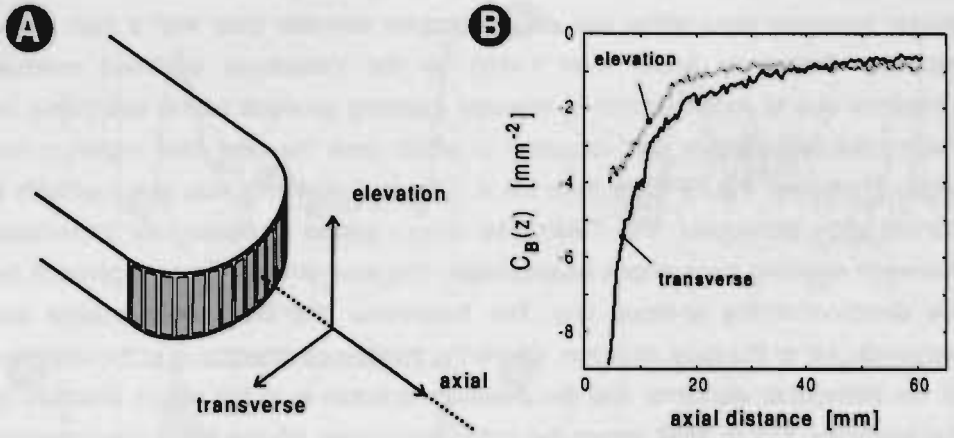

Fig. 7-8 (A) Schematic representation of a curved array transducer. The direction of the M-mode line is considered to be the axial direction. (B) Calibration curves for the beam characteristic C_B in transverse and elevation directions for the applied curved array transducer (focus at 36 mm).

where α [^{O}] is the actual transducer-to-motion angle and $\delta\alpha$ [^{O}] the deviation of the assumed transducer-to-motion angle. Figure 7-7 gives an indication of the degree of the error in the estimated absolute velocity (based on the axial velocity corrected for the transducer-to-motion angle) for two often applied transducer-to-motion angles, namely 60^{O} and 70^{O}.

The estimators presented in Chapter 5 can be applied to determine the transducer-to-motion angle (or the absolute velocity) directly from the measured M-mode RF-signals. In the current section, these estimators are applied to measure the blood flow velocity in the a. Carotis Communis. The results are compared with the results obtained with the technique of conventional scanners. The conventional technique requires a B-mode image to estimate the transducer-to-motion angle. Hence, a sector scanner or an array transducer is required. The absolute velocity estimation technique presented in Chapter 5 requires the application of a circular-shaped transducer. Hence, a mechanical sector scanner would be the transducer of first choice, because it contains a single circular element transducer

and it is able to generate B-mode images. Unfortunately, all available mechanical sector scanners were either not able to acquire M-mode data with a high pulse repetition frequency (more than 1 kHz), or the transducer exhibited residual vibrations due to motor control in M-mode (causing spurious lateral velocities), or the transducer element was too large in which case the near field region is too large. Therefore, the RF-data from the a. Carotis Communis was acquired with a curved array transducer (Fig. 7-8A). The array consists of rectangular transducer elements resulting in an elliptic beam shape. The axial direction is considered to be the direction of the M-mode line. The transverse and elevation directions are perpendicular to the axial direction, where the transverse direction is in the direction of the transducer elements and the elevation direction is in the height direction of the elements. Figure 7-8B shows the calibration curves for the beam characteristic C_B (see Chapters 4 and 5) in the transverse and elevation directions of the curved array transducer as the focus is set at 36 mm. For the (laminar) blood flow velocity measurements in the a. Carotis Communis, it is very likely that the flow is in the transverse direction as a longitudinal cross-section of the vessel is considered. Hence, the transverse calibration curve is used for the absolute velocity estimates. For the case that the blood flow is not completely in the transverse direction, the applied calibration curve will have a deviation. Only the lateral velocity component is influenced by the value of the beam characteristic. The error in the lateral velocity estimate ($error_{v_{LAT}}$ [%]) due to a deviation in the beam characteristic (δC_B [m^{-2}]) is given by

$$error_{v_{LAT}} = \left[\sqrt{\frac{C_B}{C_B + \delta C_B}} - 1 \right] \times 100\% \qquad (7\text{-}7)$$

where C_B [m^{-2}] is the actual value of the beam characteristic and $C_B + \delta C_B$ [m^{-2}] is the assumed beam characteristic. This equation shows that even if the flow is not completely in the transverse direction, which results in a small deviation of the calibration value for C_B, the error in the lateral velocity component will be relatively small. Since the absolute velocity is based on both the lateral and the axial velocity components and the error in the axial velocity is very small, the error in the absolute velocity estimates will even be smaller than that of the lateral velocity (see Eq. (4-29)).

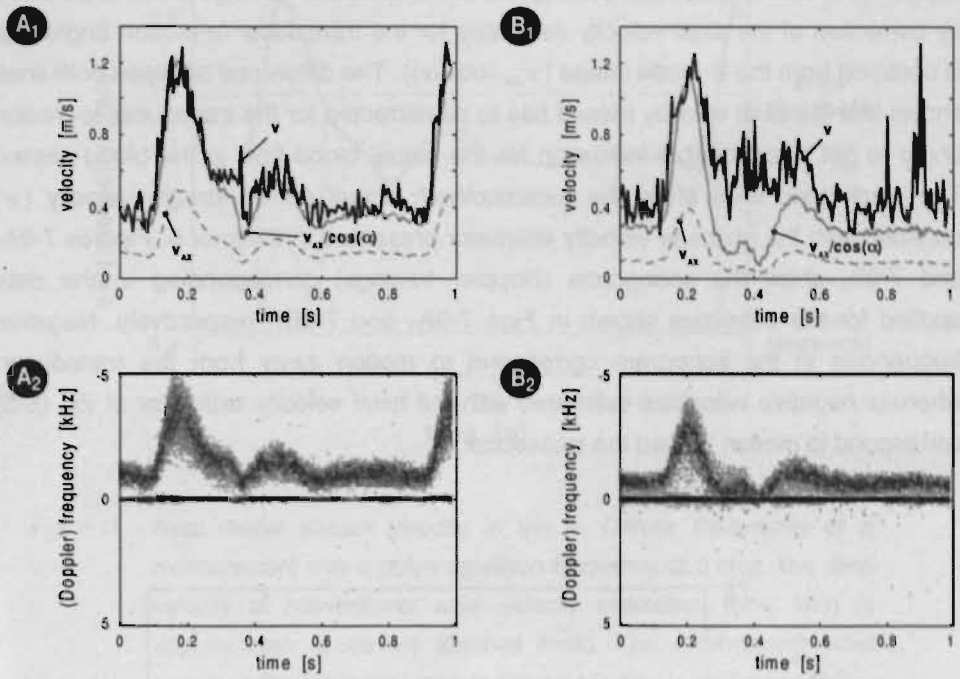

Fig. 7-9 Center stream velocity waveforms of the a. Carotis Communis of two different persons. (A_1) and (B_1) show the estimated axial velocity (dashed gray line), the estimated absolute velocity based on the axial velocity corrected for the transducer-to-motion angle as is obtained from the B-mode image (66^O and 70^O for subjects A and B, respectively) (solid gray line), and the absolute velocity estimated with the estimator presented in Chapter 5 (solid black line). (A_2) and (B_2) are the sonograms corresponding to (A_1) and (B_1), respectively.

7.3.2 In-vivo results absolute velocity measurement

Figure 7-9 shows the results from velocity measurements at the a. Carotis Communis of two different persons. Figures 7-9A_1 and 7-9B_1 show the center stream velocity waveforms of both persons obtained after SVD-clutter filtering of the RF-signals. The data applied for these figures were assessed at transducer-to-motion angles of 66^O and 70^O (based on B-mode images), respectively. The dashed gray lines correspond to the axial velocity (v_{AX}) obtained with the estimator of

Eq. (5-5). The solid gray lines correspond to the absolute velocity, which is obtained by correction of the axial velocity estimates for the transducer-to-motion angle that is obtained from the B-mode image ($v_{ax}/\cos(\alpha)$). The difference between both lines shows that the axial velocity indeed has to be corrected for the transducer-to-motion angle to get a reasonable indication for the actual blood flow in the blood vessel. The black solid lines show the (unsmoothed) actual center stream velocity (v) obtained with the absolute velocity estimator presented in Chapter 5. Figures 7-9A_2 and 7-9B_2 show the sonograms (Doppler tracings) corresponding to the data applied for the estimates shown in Figs. 7-9A_1 and 7-9B_1, respectively. Negative frequencies in the sonogram correspond to motion away from the transducer, whereas negative velocities estimated with the axial velocity estimator of Eq. (5-5) correspond to motion toward the transducer.

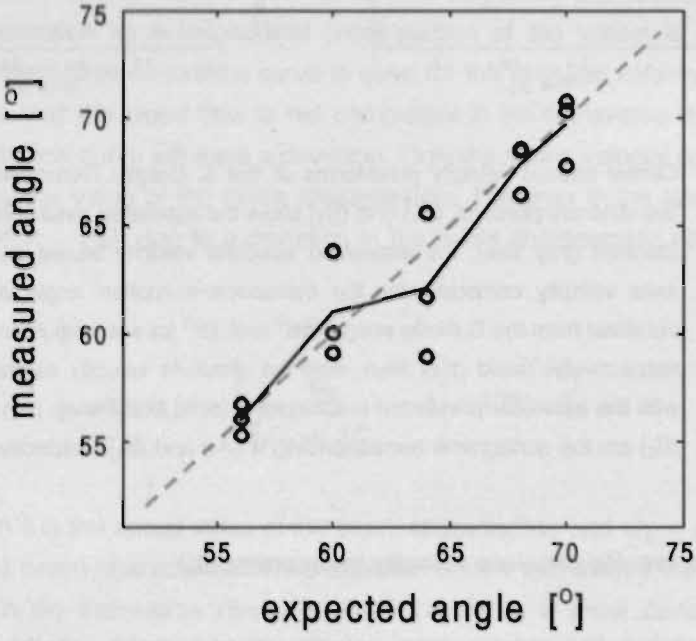

Fig. 7-10 Expected versus measured transducer-to-motion angles (at peak systole) for measurements at the a. Carotis Communis. The solid black line gives the average values for each expected angle and the dashed gray line shows the ideal situation.

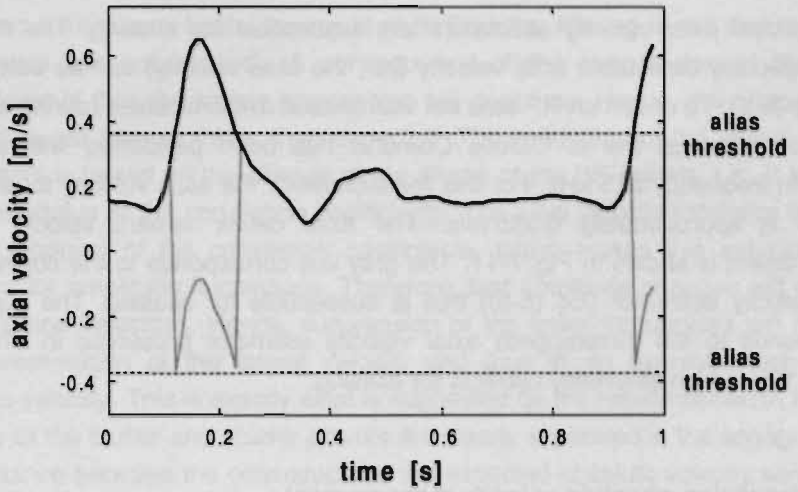

Fig. 7-11 Axial center stream velocity in the a. Carotis Communis of a measurement with a pulse repetition frequency of 5 kHz. The alias velocity of conventional axial velocity estimators (gray line) is approximately 0.385 m/s (dashed lines). The (unwrapped) axial velocity estimator presented in Chapter 5 (black line) corrects for possible aliasing.

Instead of estimating the absolute velocity, the velocity estimation technique presented in Chapter 5 can also be applied to estimate to transducer-to-motion angle. To get some kind of performance evaluation of the estimation technique, RF-data is assessed from the a. Carotis Communis (subject B of Fig. 7-9) at transducer-to-motion angles of 56^{o}, 60^{o}, 64^{o}, 68^{o}, and 70^{o}, respectively. At each transducer-to-motion angle three measurements were performed. Smaller angles were not possible, because at smaller angles only very little of the reflected energy will reach the transducer (angle of incident = angle of reflection), in which case it is very difficult to locate the vessel walls. Visual estimation of the transducer-to-motion angle is in that situation almost impossible. Larger angles were also not possible, because clutter filters are for angles near 90^{o} unable to separate the scatter from the clutter. For each measurement, the transducer-to-motion angle is estimated at peak systole with the estimator presented in Chapter 5. The results are shown in Fig. 7-10 (circles). The solid black line shows the mean of the estimated angles for each of the transducer-to-motion angles at which measurements were performed. The dashed gray line corresponds to the ideal situation.

Conventional axial velocity estimators are susceptible for aliasing. The maximal unambiguously detectable axial velocity (i.e., the alias velocity) can be determined with Eq. (5-6). To obtain an RF-data set with aliased axial velocities (during systole), a measurement at the a. Carotis Comunis has been performed with a pulse repetition frequency of 5 kHz. For this measurement, the alias velocity for the axial velocity is approximately 0.385 m/s. The axial center stream velocity of the measurement is shown in Fig. 7-11. The gray line corresponds to the conventional axial velocity estimator (Eq. (5-5)) that is susceptible for aliasing. The black line corresponds to the (unwrapped) axial velocity estimator presented in Chapter 5 (Eq. (5-10)), which inherently corrects for aliasing.

7.3.3 Discussion absolute velocity measurement

The results of Fig. 7-9A_1 suggest that the absolute velocity estimator presented in Chapter 5 indeed can be applied to estimate the absolute velocity, because there is a close resemblance between the estimated (black solid line) and the expected (gray solid line) velocity waveform. The variation on the estimated absolute velocity waveform is much larger than that of the estimated axial velocity (dashed gray line) waveform as was also found by the experiments described in Chapter 5. The variation on the waveform can significantly be reduced by, for example, low pass or median filtering of the absolute velocity waveform.

Unfortunately, the resemblance between the estimated and the expected absolute velocity waveforms is not always as good as is shown in Fig. 7-9A_1. Figure 7-9B_1 shows the same results as are shown in Fig. 7-9A_1 for a different person. Here, the resemblance between the estimated (black solid line) and the expected (gray solid line) is only acceptable during systole. During the other phases, the estimated absolute velocity is larger than the expected velocity. The explanation for the different performance results for both persons is given by the sonograms of Figs. 7-9A_2 and 7-9B_2 corresponding to the Figs. 7-9A_1 and 7-9B_1, respectively. In both sonograms, the clutter power is clearly located near the baseline (i.e., near zero frequency), whereas the scatter power is located at higher frequencies. The clear difference between both sonograms is that the clutter and scatter power is nicely separated in the sonogram of Fig. 7-9A_2, while in the sonogram of Fig. 7-9B_2 there is some interaction between the clutter and scatter powers. Clutter filtering of the data corresponding to the first sonogram will not influence the scatter power, while the lower frequencies of the scatter power of the data corresponding to the second sonogram will be affected (note that although the SVD-clutter filter is not

based on a frequency basis, the result of SVD-clutter filtering is still that the lower frequencies are suppressed). A consequence of the suppression of the lower frequencies is that the higher frequencies will dominate. Hence, the shape of the RF-signals will change faster than expected. The estimation of the lateral velocity component is based on the change of the shape of the RF-signals, i.e., it is based on the modulus of the correlation coefficients. The axial velocity estimator is based on the modulus of the correlation coefficients, which makes this estimator less sensitive for amplitude fluctuations. Therefore, fast amplitude changes will result in higher lateral velocities. Hence, suppression of the lower frequencies will result in an overestimation of the lateral velocity and thus in an overestimation of the absolute velocity. This is exactly what is suggested by the results shown in Fig. 7-9. As long as the clutter and scatter powers are clearly separated in the sonogram, the resemblance between the estimated and the expected absolute velocity waveforms is acceptable. For most persons (with laminar flow) the scatter and clutter are separated in the sonogram during systole.

The results of Fig. 7-10 show that the estimation method presented in Chapter 5 indeed can be applied to determine the transducer-to-motion angle and thus to measure the absolute velocity in an angle-independent way. In most situations, the estimated angles are close to the expected ones. The mean and standard deviation of the difference between the estimated and expected angles is -0.279° and 2.027°, respectively (correlation is 0.928). The discrepancy between both angles can not solely be dedicated to the estimation method. There are also other sources, that could not be excluded in the experiments, that may contribute to the error. The flow is assumed to be in the transverse direction of the transducer (transverse C_β calibration curve is used). A discrepancy in this assumption might have some influence on the results. Furthermore, the expected transducer-to-motion angle is determined from the B-mode image, which introduces an error. The estimated angle has been determined during peak systole, because then it is very likely that the scatter and clutter powers are nicely separateble from each other, such that clutter filtering will give optimal results. But during systole, the motion of the vessel is maximal, which may induce a deviation of the assumed angle.

Figure 7-11 shows that the (unwrapped) axial velocity estimator of Eq. (5-10) is indeed able to measure axial velocities that are larger than the alias velocity. This unwrapped axial velocity estimator does not require the beam characteristic C_β, but only the calculation of a few correlation coefficients. This estimator could be applied for alias free color flow mapping, such that turbulent blood flow would no longer be confused with aliasing.

7.3.4 Conclusions absolute velocity measurement

The results of this in-vivo evaluation of the absolute velocity estimation technique suggest that the estimation technique can be applied as the RF-signals that carry the information are not influenced by for example filtering. Blood flow velocity measurements during systole are therefore possible, because the scatter signals, which carry the blood flow velocity information, can almost completely be separated from the clutter in the frequency domain. During diastole, this is not the case for a lot of persons. In those situations, clutter filtering will influence the scatter signals resulting directly in an error (mostly an overestimation) in the estimated absolute velocity.

Tissue motion measurements do not require the application of a clutter filter and have even a much better signal-to-noise ratio than blood flow velocity measurements. The results of the current evaluation suggest that the absolute velocity estimation technique should be able to measure in-vivo absolute tissue motion. This has to be evaluated in future if a proper in-vivo evaluation procedure becomes available.

7.4 References

Brands PJ, Hoeks APG, Hofstra L, Reneman RS. A noninvasive method to estimate wall shear rate using ultrasound. Ultrasound in Med & Biol. 1995;21:171-185.

Chapter 8

General discussion, conclusions and recommendations

General discussion, conclusions and recommendations

The goal of the study was the development of an ultrasound based technique for the measurement of the absolute velocity (or motion) to enable the assessment of tissue motion (e.g., 2-D tissue elasticity), which is almost impossible with conventional echographic scanners. In Chapter 3, it is demonstrated that the correlation of analytic ultrasound radiofrequency (RF) signals obtained along a single line of observation (M-mode), amongst others, is influenced by the axial and lateral velocity components and thus by the absolute velocity. In Chapter 4, a model for this correlation behavior has been derived, linking the lateral velocity to the local width of the ultrasound beam and the local shape of the wave front. The latter two parameters were combined in a beam characteristic, for which, in the case of a circular-shaped transducer, a calibration curve can be made requiring only one reference measurement. Once the calibration curve for the beam characteristic is available, the local absolute velocity can be measured directly without knowledge about the transducer-to-motion angle.

The typical shape of the modulus of the correlation function of analytic RF-signals can be seen in Fig. 8-1A for the situation that the insonofied structures are not moving. From the observations presented in Chapter 3 and the correlation model derived in Chapter 4, it is known that the Gaussian shape (in axial direction) of the correlation function is a consequence of the power spectral density distribution of the RF-signals. The bandwidth of the RF-signals determines the (axial) width of the Gaussian shaped correlation function. The smaller the bandwidth of the RF-signals, the wider the correlation function will be. Noise in consecutive RF-signals is not correlated, which explains the higher modulus of the correlation coefficients at temporal lag zero in Fig. 8.1. The larger the signal-to-noise ratio, the smaller this increase in correlation will be. Axial motion of the structures under investigation results in a rotation of the correlation function (Figs. 8-1B and 8-1D), whereas lateral velocity results in a decrease of the correlation in the temporal direction (Fig. 8-1C and 8-1D). Hence, it must be concluded that the shape of the modulus of the correlation of analytic RF-signals depends on the signal-to-noise ratio, the bandwidth of the received RF-signals, the axial and lateral velocity and the beam characteristic. Furthermore, the shape of the modulus of the correlation function is influenced by the sound velocity in the medium under investigation and the sample frequency of the RF-signals. The center frequency has no influence on the modulus of the correlation function, but it has influence on the argument of the correlation function.

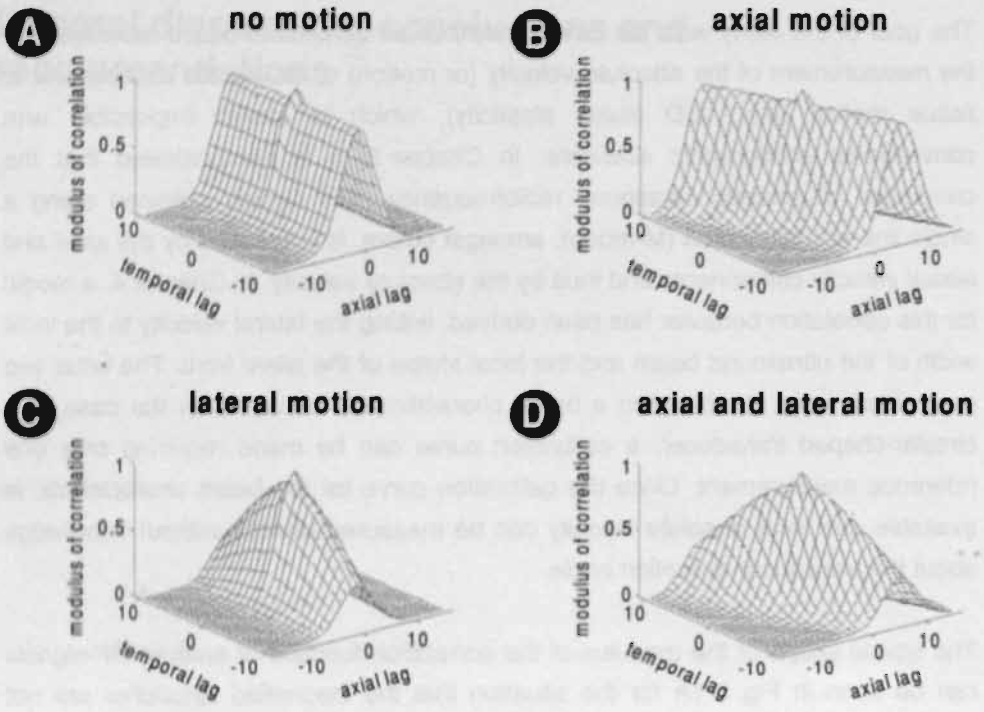

Fig. 8-1 Typical shape of the modulus of the correlation function of analytic RF-signals assessed along a single line of observation for four different kinds of motions of the insonified structures, namely for no motion (A), pure axial motion (B), pure lateral motion (C), and a combination of axial and lateral motion (D).

To decrease the computation time, estimators for, amongst others, the absolute velocity are derived from the correlation model (Chapter 5). These estimators do not require a fit or search algorithm (Bonnefous and Pesqué 1986), but only the calculation of a few correlation coefficients for each local estimate.

For the derivation of the correlation model, it was assumed that the lateral beam profile had a Gaussian shape. This is an acceptable assumption in the far field of the ultrasound beam, but in the near field the ultrasound beam has local maxima and minima. Hence, the lateral velocity estimator derived from the correlation model will not be ideal for lateral velocity measurements in the near field of the ultrasound

beam. Placing an ultrasound delay line in front of the transducer might be a solution to circumvent this problem. In that case, the near field will be situated inside the delay line, while all measurement locations will be located in the far field of the ultrasound beam. One of the main problems of delay lines was that they absorbed a great part of the emitted acoustic energy making them very unattractive for in-vivo measurements. Nowadays, delay lines are available that cause a minimal loss of energy (Panametrics Inc., Waltham, MA, USA). It has to be evaluated if, in practice, they indeed can be applied to bridge the near field.

The proposed absolute velocity measurement technique should fulfill a number of aims as is mentioned in Chapter 1. The degree of fulfillment of those aims is as follows:

1. *The method should be applicable for the measurement of blood flow velocities as well as for the measurement of tissue motion.*

   The in-vivo results presented in Chapter 7 show that the proposed absolute velocity estimation method is not an ideal technique for blood flow velocity measurements, since the scatter signals, which correspond to the blood flow, are influenced by dominant clutter signals. For blood flow velocity measurements, the clutter and scatter signals have to be separated. If the scatter and clutter signals can perfectly be separated, the proposed velocity estimation technique is able to estimate the absolute velocity in an angle-independent way. The results presented in Chapter 7 show that for measurements performed in the a. Carotis Communis "ideal" separation of the scatter and clutter signals is possible during systole in the center of the blood vessel. During that phase of the cardiac cycle, there is a great difference between the velocity of the scatter and clutter signals. During diastole, the difference between both velocities is mostly insufficient to allow "ideal" separation. In those situations, the velocity estimation technique will not provide a correct estimate of the absolute velocity.

   For disjunct clutter and scatter signals (e.g., during systole), the proposed method provides an estimate for the absolute velocity or the transducer-to-motion angle if a circular-shaped transducer is employed. For those measurements, it will no longer be necessary to determine the transducer-to-motion angle from the B-mode image. For blood flow velocity measurements

near bifurcations, junctions and in curves of blood vessels, the proposed method will not function properly, because in those situations it is very likely that there are regions in which the blood flow velocity is very low such that current clutter filters will not be able to retrieve the scatter signals.

Tissue motion measurements have the advantage that clutter filtering is not required. Furthermore, the signal-to-noise ratio of RF-signals originating from tissue is much better than that of RF-signals originating from scattering blood. In-vivo results of tissue motion measurements with the proposed motion estimation technique are not yet evaluated, but the results of the phantom measurements presented in Chapter 5 indicate that in future tissue motion measurements should be possible with the proposed motion estimation technique.

2. *The axial resolution of the method should be high.*
Conventional pulsed ultrasound velocity estimation techniques assume a long emission pulse which degrades axial (spatial) resolution. However in the proposed approach the axial resolution of the echo system and hence the axial size of the estimation window for the velocity estimates can be selected as small as possible to achieve a high axial resolution for velocity estimation and to avoid large velocity gradients within the window (Peronneau et al. 1974).

3. *The temporal resolution of the method should be high.*
For blood flow velocity measurements, a temporal resolution of maximally 10 ms would be acceptable, which for tissue motion measurements might even be more than 10 ms. The results of the phantom measurements presented in Chapter 5 and those of the in-vivo measurements presented in Chapter 7 show that a temporal estimation window of 10 ms is sufficient to obtain acceptable velocity estimates.

4. *The velocity resolution of the method should be high.*
The velocity resolution of the proposed velocity estimation technique is not limited to discrete values, because the technique is based on a model. The velocity resolution improves with an increasing size of the data window in temporal or axial (depth) direction.

5. *The computational load of the method should be as small as possible.*
   Under normal clinical conditions, the proposed method requires the calculation of five correlation coefficients for each local absolute velocity estimate. The same correlation coefficients can be used for the estimation of the center frequency, bandwidth and signal-to-noise ratio of the received RF-signals. The estimators presented by Loupas et al. (Loupas et al. 1995) and Brands et al. (Brands et al. 1997) require only the calculation of two correlation coefficients for each velocity estimate, but they are only able to provide the axial velocity in a way that is susceptible for aliasing. The current method requires for the estimation of the axial velocity the calculation of three correlation coefficients, but this axial velocity estimate is not susceptible for aliasing.

A clutter filter is required for the noninvasive measurement of blood flow velocities. The results of the in-vivo measurements, presented in Chapter 7, show that to obtain the best results during each phase of the cardiac cycle, a clutter filter is required with an adaptive behavior. Conventional high-pass filters are not able to have a fast adaptive behavior, because they require some settling time for each new cut-off frequency. In Chapter 6, a new clutter filtering technique is introduced based on singular value decomposition (SVD). Unlike high pass filters, which are based on the frequency characteristics of the RF-signals, the SVD clutter filter removes the strongest common signals from the RF-signals in the RF-data set, presumably originating from structures. The advantages of the SVD clutter filter are that it has no settling time, no static cut-off frequency and no roll-off. The results of the in-vivo measurements presented in Chapter 7 show that the performance of the SVD clutter filter is in most situations comparable with the performance of a (high order) high pass filter with an optimal cut-off frequency during each phase of the cardiac cycle, confirming that the SVD filter indeed has an adaptive behavior. Without imposing additional restrictions, the SVD clutter filter removes always a number of the singular values, and thus a part of the RF-signals, even if no clutter is present. Hence, the only requirement of the SVD clutter filter is that dominant clutter must be present somewhere in the RF-data set to be clutter filtered. The performance of the SVD clutter filter is best as the RF-data set is relatively large (i.e., approximately 100 RF-signals) in which case a good discrimination between the scatter and clutter signals is possible. On the other hand, it has been shown in Chapter 7 that for a relatively small RF-data set (i.e., approx. less than 20 RF-signals) the performance of the SVD clutter filter is almost identical with the performance of a mean filter. Off-line processing of the measured RF-signals in Matlab, shows that the computation time of the SVD clutter filter is less than twice that of a static high pass filter.

The main topic for the introduction of the SVD clutter filter was to try to develop a clutter filtering technique with which it would be able to measure low velocities more precisely, especially in the region near the vessel wall. In that case, the accuracy of wall shear rate measurements (see Chapter 6) would be enhanced. The results of Chapter 7 show that even after application of the SVD clutter filter, it is still difficult to assess the velocity distribution near the posterior vessel wall. Most likely, the source of the problem is a ghost velocity distribution that occurs near the posterior wall as a consequence of partial reflection (in another direction) of the sound waves by the posterior vessel wall. In that case, the received scatter signals will be an undistinguishable mixture of direct scattering and secondary scattering after reflection. As a consequence, the assessed shear rate at the posterior wall will be unreliable.

So far, the SVD filter has only be used to suppress clutter signals by removing the largest singular values that correspond to the clutter signals. It should also be possible to use the SVD filtering technique to suppress part of the noise in the RF-signals by removing the smaller singular values that correspond to the noise. This might lead to a better signal-to-noise ratio and thus to more stable velocity estimates. This approach should be explored more extensively.

Although the SVD clutter filter is not a frequency based filtering technique, the result of SVD clutter filtering is that low Doppler frequencies are suppressed. The results of the in-vivo blood flow velocity measurements of Chapter 7 show that all clutter filters, even the SVD filter, modify the scatter signals in those situations that the clutter and scatter signals have overlapping Doppler frequency spectra. The velocity estimators are no longer able to predict the absolute velocity in a correct way. Hence, there is still a demand for a clutter filter that is able to separate adequately the scatter and clutter signals under all possible conditions (wall motion is perpendicular to blood flow).

Absolute velocity estimators based on the Doppler equation (Eq. (2-16)) are unable to measure velocities that are pure lateral, because they correct the axial velocity (which is then zero) for the transducer-to-motion angle. The proposed absolute velocity estimation technique is insensitive for the transducer-to-motion angle (as long as no clutter filtering is required) and it is able to measure pure lateral motions.

The Doppler equation (Eq. (2-16)) shows that conventional axial velocity measurement techniques do not only require the Doppler frequency, the sound velocity in the medium under investigation and the transducer-to-motion angle, but they also require the local center frequency of the RF-signals. For wide band RF-signals, the local center frequency depends on the degree of (frequency) attenuation of the emitted sound energy. Higher frequencies are more susceptible for attenuation than lower frequencies (Chapter 2). Hence, the center frequency of an RF-signal will decrease with increasing depth. Since the center frequency is included in the correlation model that is derived in Chapter 4, the proposed velocity estimators are corrected for the local attenuation of the RF-signals, which makes the performance of them insensitive for attenuation. Furthermore, the proposed unwrapped axial velocity estimator (requiring the calculation of 3 correlation coefficients) is able to measure axial velocities that are much larger than the velocity at which most conventional axial velocity estimators (requiring the calculation of 2 correlation coefficients) start to alias. Since the proposed axial velocity estimator requires only the calculation of 1 extra correlation coefficient compared to the conventional estimators, it should be possible to make color flow mapping free of aliasing, such that turbulent flows will no longer be confused with aliasing (Cape and Yoganathan 1991; Kandath and Nanda 1991; Kandath et al. 1991).

Besides the estimators for the velocity components, the correlation model provides also estimators for the center frequency, the bandwidth and the signal-to-noise ratio of the recorded RF-signals. These estimators might be applied to determine characteristics of the local attenuation of the medium under investigation (some kind of tissue characterization). The potentials of this approach have to be explored.

The signal-to-noise ratio (or the power) of the RF-signals is often used as a threshold to suppress noisy velocity estimates. During blood flow velocity measurements, such noisy velocity estimates occur often in the regions near the vessel wall. The clutter filter removes all signal power in those regions (vessel walls cause clutter signals) such that only noise remains causing a low signal-to-noise ratio and unpredictable velocity estimates. If this is indeed the case, a threshold on the signal-to-noise ratio can be used to suppress these noisy velocity estimates. However, the results of the in-vivo measurements of Chapter 7 show that near the posterior vessel wall a ghost velocity distribution occurs due to the reflection at the

posterior wall (in an other direction) of a part of the acoustic energy. In those situations, the region near the posterior vessel wall will contain some false scatter (blood causes scatter signals) signals aside of noise. Hence, different thresholds on the signal-to-noise ratio will be required for the anterior and posterior vessel wall regions.

The correlation model of Eq. (4-24) is derived for analytic RF-signals, but it can easily be transformed to the model for real RF-signals by taking the real part of it, which results in

$$R(T,Z) = (P_S + P_{N_r}) \exp\left[T^2 C_B(z_t,\varphi) S_{LAT}^2 - \frac{4\pi BW_{EO}^2}{c^2}\left(\frac{Zc}{2f_S} - TS_{AX} \right)^2 \right] \times \cos\left[\frac{4\pi f_C}{c}\left(\frac{Zc}{2f_S} - TS_{AX} \right) \right] \tag{8-1}$$

From the model of Eq. (8-1), it is not possible to derive separate estimators for each of the velocity components in the model. De Jong et al. (de Jong et al. 1990) showed for a similar situation that this problem could be circumvented by assuming a narrow bandwidth in which case the correlation model reduces to

$$R(T,Z) = (P_S + P_{N_r}) \exp\left[T^2 C_B(z_t,\varphi) S_{LAT}^2 \right] \cos\left[\frac{4\pi f_C}{c}\left(\frac{Zc}{2f_S} - TS_{AX} \right) \right] \tag{8-2}$$

From this model, it is possible to derive estimators for both the velocity components. The consequence of the narrow bandwidth assumption for the correlation model of De Jong et al. (de Jong et al. 1990) was that a bias occurred in the axial velocity estimates (Hoeks et al. 1993). The influence of the narrow bandwidth assumption on the velocity estimators derived from the correlation model of Eq. (8-2) has to be examined. The advantage of these estimators would be that the RF-signals would no longer be needed to be made analytic, which would cause a substantial reduction of the computation time.

The proposed absolute velocity estimation technique has two main shortcomings, namely the requirement of a calibration curve for the beam characteristic and the omission of the direction of the lateral velocity component, i.e., the direction in the xy-plane (see Fig. (4-1)). The latter makes true 3-D velocity detection impossible. Both shortcomings can be resolved by combining the RF-signals recorded with two separate identical transducers of which the sound beams are for the greater part overlapping. Such a dual ultrasound beam configuration can, for example, very easily be created with a linear array transducer by activating two groups of transducer elements which are partly overlapping (Fig. 4-1B). Both transducers can be activated alternately or simultaneously (von Ramm et al. 1991). The only consequence of simultaneous activation is a broadened transmit beam width. The receive beam width is not affected. Hence, besides an increase in system complexity, the only penalty for simultaneous activation would be a slightly decreased lateral resolution (Fish et al. 1997). The magnitude and sign of the axial and of the transverse velocity components can be determined from the correlation of the RF-signals from both transducers without the need of a calibration curve for the beam characteristic. If both beams are also circular-shaped, then the magnitude (not the sign) of the velocity component in elevation direction (Fig. 4-1B) can also be determined without the need of a calibration curve. If the beams are not circular-shaped, the magnitude of the elevation velocity can be determined if a calibration curve is available for the beam characteristic in the elevation direction. The magnitude and sign of the elevation velocity component can also be determined if a third transducer is applied of which the ultrasound beam overlaps in the elevation direction with at least one of the other two transducers. This approach can no longer be realized with a linear array transducer, but with a 2.5-D transducer is should be possible. If three beams or two beams with a calibration curve for the beam characteristic in the elevation direction are applied, it is no longer required that the beams are circular-shaped, but also elliptical ultrasound beams (which are transmitted by all transducers) are tolerated. Recently, we developed a model for the correlation of RF-signals acquired with two different transducers (model not presented in the current thesis). This model is an extension of the model presented in Chapter 4. A patent application on this new model and the corresponding absolute velocity estimators is currently pending. A thorough evaluation has still to be performed to examine the potentials of those estimators. The advantage of the multiple beam estimators, which are an extension of the estimators presented in the current thesis, would be that true 3-D velocity measurements are possible. For example, for the measurement of the motion of the heart, which, amongst others, consists of rotation and contraction, true 3-D motion measurement is required.

Phase aberrations, which are caused by irregular interfaces between tissue layers with a different propagation speed (Ledoux et al. 1996; Li 1997), influence the shape of the ultrasound beam. The calibration curve for the beam characteristic can not be corrected for these instantaneous phase aberrations. Hence, severe phase aberrations will influence the accuracy of the velocities estimated with the proposed estimators. With the multiple beam approach, the local instantaneous beam characteristic is also estimated in which case no calibration curves are required and the influence of phase aberrations on the estimated velocities is less. Severe phase aberrations, which only occur at locations where the difference in propagation speed between both media is very extreme, will also affect the performance of the velocity estimation technique based on multiple beams, since the (lateral) shape of the ultrasound beam will no longer be Gaussian as is assumed for the correlation model.

Multiple beam measurements go at the expense of an increased complexity of the echographic system and higher costs, but compared to, for example, MRI systems these echographic systems will still be relatively cheap. Imagine what the capabilities would be of an echographic system of the same cost as an MRI system. Such an echographic scanner would be able to obtain simultaneously M-mode data with a high pulse repetition frequency along a large number (e.g., 128) of lines of observation. The corresponding data could, for example, be used to do real-time true 3-D velocity measurements (based on the proposed velocity estimation technique) that covered the entire B-mode image. This would, for example, be a very interesting instrument for the noninvasive evaluation of the regional myocardial function of the heart. Unfortunately, such an elaborate system has not yet been built, although it would open a new area of clinical research.

References

Bonnefous O, Pesqué P. Time domain formulation of pulse-Doppler ultrasound and blood velocity estimation by cross correlation. Ultrason Imaging. 1986;8:73-85.

Brands PJ, Hoeks APG, Ledoux LAF, Reneman RS. A radio frequency domain complex cross-correlation model to estimate blood flow velocity and tissue motion by means of ultrasound. Ultrasound Med Biol. 1997;23:911-920.

Cape EG, Yoganathan AP. Basic principles of ultrasound. In: Pohost GM, O'Rourke RA, ed. Principles and practice of cardiovascular imaging. Boston: Little, Brown Co, 1991.

de Jong PGM, Arts T, Hoeks APG, Reneman RS. Determination of tissue motion velocity by correlation interpolation of pulsed ultrasonic echo signals. Ultrason Imaging. 1990;12:84-98.

Fish PJ, Hoskins PR, Moran C, McDicken WN. Developments in cardiovascular ultrasound: Part 1: signal processing and instrumentation. Med Biol Eng Comput. 1997;35:561-569.

Hoeks APG, Arts TGJ, Brands PJ, Reneman RS. Comparison of the performance of the RF cross correlation and Doppler autocorrelation technique to estimate the mean velocity of simulated ultrasound signals. Ultrasound Med Biol. 1993;19:727-740.

Kandath D, Nanda NC. Conventional Doppler echocardiography. In: Pohost GM, O'Rourke RA, ed. Principles and practice of cardiovascular imaging. Boston: Little, Brown Co, 1991.

Kandath D, Nanda NC, Fan PH, Cooper J. Color Flow Doppler Mapping. In: Pohost GM, O'Rourke RA, ed. Principles and practice of cardiovascular imaging. Boston: Little, Brown Co, 1991.

Ledoux LAF, Berkhoff AP, Thijssen JM. Ultrasonic wave propagation through aberrating layers: experimental verification of the Conjugate Gradient Rayleigh method. IEEE Trans Ultrason Ferroel Freq Control. 1996;43:158-166.

Li Y. Phase aberration correction using near-field signal redundancy -- Part I: principles. IEEE Trans Ultrason Ferroel Freq Contr. 1997;44:355-371.

Loupas T, Powers JT, Gill RW. An axial velocity estimator for ultrasound blood flow imaging, based on a full evaluation of the Doppler equation by means of a two-dimensional autocorrelation approach. IEEE Trans Ultrason Ferroel Freq Contr. 1995;42:672-688.

Peronneau PA, Bournat J-P, Bugnon A, Barbet A, Xhaard M. Theoretical and practical aspects of pulsed Doppler flowmetry: real-time application to the measure of instantaneous velocity profiles in vitro and in vivo. In: Reneman RS, ed. Cardiovascular applications of ultrasound. Amsterdam: North-Holland publishing company, 1974, 1974.

von Ramm OT, Smith SW, Pavy (Jr.) HG. High-speed ultrasound volumetric imaging system - Part II: Parallel processing and image display. IEEE Trans Ultrason Ferroel Freq Contr. 1991;38:109-115.

Glossary

Glossary

Symbols

$==$	is equal to
$\approx$	approximates
$*$	complex conjugate
$\hat{}$	estimate
$\langle\ \rangle$	expectation
$\bar{}$	mean
$'$	modified
^{T}	transpose
$\propto$	varies directly as; is proportional with
$\|\ \|$	(complex) modulus or magnitude

Abbreviations

2-D	2 dimensional
3-D	3 dimensional
AD	analog digital (conversion)
B-mode	brightness mode
BS	bias
COV	covariance
DEV	deviation
HP	high-pass
LF	low frequency
M-mode	motion mode
MRI	magnetic resonance imaging
RF	radiofrequency
SD	standard deviation
SLR	standard linear regression
SVD	singular value decomposition
VAR	variance

Nomenclature

α	[°]	transducer-to-motion angle
α_I	[°]	angle (with normal to surface) of incident sound wave
α_R	[°]	angle (with normal to surface) of reflected sound wave
α_T	[°]	angle (with normal to surface) of transmitted wave
A	[m]	radius of curvature of acoustic lens (spheric/cylindric)
$A(f)$	[dB]	(analytic) frequency spectrum
β	[°]	angle of rotation of correlation function
B	[N/m^2]	bulk modulus (elasticity)
BW_{dB}	[Hz]	power bandwidth as the power is dB decibels down
BW_{EQ}	[Hz]	equivalent power bandwidth
bp	[-]	begin position
γ	[°]	angle between consecutive singular values
$C_B(z)$	[1/m^2]	depth-dependent beam characteristic
$C_{Bx}(z)$	[1/m^2]	transverse part of beam characteristic
$C_{By}(z)$	[1/m^2]	elevation part of beam characteristic
C_P	[1/m]	characteristic of phase part of sensitivity function
C_X	[1/m^2]	characteristic of transverse part of sensitivity function
C_Y	[1/m^2]	characteristic of elevation part of sensitivity function
C_Z	[1/m^2]	characteristic of axial part of sensitivity function
c	[m/s]	sound velocity
$c_{crystal}$	[m/s]	sound velocity in piezoelectric crystal
$\delta\alpha$	[°]	deviation in transducer-to-motion angle
δC_B	[%]	deviation in beam characteristic
$\delta v/\delta\rho$	[1/s]	wall shear rate
ΔL	[m]	distance between curved and plane wave front
d	[m]	axial distance from transducer to scatterer or reflector
dB	[-]	decibel-level (negative for attenuation)
η	[Pa·s]	blood viscosity

$error_{v_{LAT}}$	[%]	error of estimated lateral velocity
$error_v$	[%]	error of estimated absolute velocity
e	[-]	random number (from uniform probability distribution)
φ	[°]	angle of lateral motion direction with positive x-axis
F	[-]	matrix with characteristics of SVD-clutter filter
f	[Hz]	frequency
f_c	[Hz]	center frequency, i.e., frequency with max. amplitude
f_{dop}	[Hz]	frequency shift due to Doppler effect
f_{res}	[Hz]	resonance frequency of transducer
f_S	[Hz]	sample frequency
$f_t(x, y, z)$	[-]	3-D sensitivity function for RF-sample at time t
$f_t(x)$	[-]	transverse part of sensitivity function
$f_t(y)$	[-]	elevation part of sensitivity function
$f_t(z)$	[-]	axial part of sensitivity function
$g(x, y, z)$	[-]	3-D space distribution of scatterers
I	[-]	unity matrix
IN	[-]	input value
J_1	[-]	Bessel's function of the first kind
λ	[m]	wavelength
L_S	[lags]	spatial width correlation function (lag T =0, certain level)
L_T	[lags]	temporal width correlation function (certain level)
l	[-]	number of singular values
l	[m]	length of piezoelectric element
M	[-]	RF-matrix
M_{SVD1}	[-]	SVD-clutter filtered RF-matrix (1 singular value removed)
M_{ZERO}	[-]	zero (clutter) filtered RF-matrix
N	[-]	number of sample points
N_T	[-]	number of temporal sample points (or RF-segments)
N_z	[-]	number of (spatial or axial) sample points

O	[-]	zero matrix
OUT	[-]	output value
ψ	[rad]	initial phase (of sound waves)
P_N	[-]	normalized noise power
PRF	[Hz]	pulse repetition frequency
P_S	[-]	normalized signal power
$P_X(z)$	[1/m]	characteristic for transverse part of wave front curvature
$P_Y(z)$	[1/m]	characteristic for elevation part of wave front curvature
p	[-]	number of clutter singular values
pc	[%]	percentage change
p_I	[Pa]	pressure of incident sound wave
p_R	[Pa]	pressure of reflected sound wave
p_T	[Pa]	pressure of transmitted sound wave
$p(x, y)$	[Pa]	lateral pressure distribution
$p(z)$	[Pa]	axial pressure distribution
Q	[-]	quality factor (ratio of center frequency and bandwidth)
ρ	[kg/m^3]	density
ρ	[-]	expected correlation
ρ	[m]	radial position
$\Re$	[-]	real value
$\Re^{N_T \times N_Z}$	[-]	real matrix with N_T rows and N_Z columns
R	[-]	correlation (coefficient)
R	[m]	radius of blood vessel
$R(T, Z)$	[-]	correlation with temporal lag T and axial lag Z
$\lvert R(T, Z)\rvert_{MIN}$	[-]	minimal acceptable value for modulus of correlation
$R_X(T, Z)$	[-]	transverse part of correlation function
$R_Y(T, Z)$	[-]	elevation part of correlation function
$R_Z(T, Z)$	[-]	axial part of correlation function
$RF_T(t)$	[-]	T^{th} (continuous) RF-signal

$RF(t)$	[-]	t^{th} (sampled) RF-signal
$RF(t, z)$	[-]	z^{th} sample point of t^{th} RF-signal
r	[m]	radius of transducer element
σ_i	[-]	i^{th} singular value
S	[-]	diagonal matrix containing singular values
S	[m]	step size
$S(f)$	[dB]	frequency spectrum
S_{ACT}	[m]	actual motion between acquisitions
S_{AX}	[m]	axial motion between acquisitions
$\hat{S}_{AX_{ARG}}$	[m]	argument-based axial motion estimate
$\hat{S}_{AX_{ARG\,MAX}}$	[m]	maximal detectable argument-based axial motion
$\hat{S}_{AX_{MOD}}$	[m]	modulus-based axial motion estimate
$\hat{S}_{AX_{MOD\,MAX}}$	[m]	maximal modulus-based axial motion (no search)
$\hat{S}_{AX_{MOD\,MAX\,SEARCH}}$	[m]	maximal modulus-based axial motion (with search)
$\hat{S}_{AX_{UNWRAP}}$	[m]	unwrapped argument-based axial motion estimate
S_{LAT}	[m]	lateral motion between acquisitions
$S_{LAT_{ACT}}$	[m]	lateral motion derived from actual and axial motion
$S_{LAT_{MAX}}$	[m]	maximal detectable lateral motion
SNR	[-]	signal-to-noise ratio
SNR_{dB}	[dB]	signal-to-noise ratio
S_P	[-]	signal space
θ	[°]	angle normal to transducer surface
θ_0	[°]	angle θ at which main lobe of sound beam is reduced to 0
τ	[Pa]	wall shear stress
T	[-]	temporal (correlation) lag
THR	[-]	threshold value
t	[s]	time after emission
t_d	[s]	round trip time for sound wave to reach axial distance d

U	[-]	left singular matrix (orthonormal matrix)
u_i	[-]	i^{th} eigenvector of MM^T
V	[-]	right singular matrix (orthonormal matrix)
v	[m/s]	(actual) velocity
v_{AX}	[m/s], [λPRF]	axial velocity
v_i	[-]	i^{th} eigenvector of M^TM
v_{LAT}	[m/s]	lateral velocity
$v_{observer}$	[m/s]	velocity of observer
v_{source}	[m/s]	velocity of source of sound waves
vw	[λPRF]	width of (rectangular) velocity distribution
$w(t, z)$	[-]	z^{th} sample point of t^{th} RF-segment in data window
$wx_{dB}(z)$	[m]	transverse round-trip dB beam width at depth z
$wy_{dB}(z)$	[m]	elevation round-trip dB beam width at depth z
X	[m]	transverse position
x	[m]	transverse position
Y	[m]	elevation position
y	[m]	elevation position
Z	[kg/m^{2}s], [Rayl]	acoustic impedance
Z	[-]	axial (correlation) lag
z	[m]	axial position
z	[-]	Fisher z-transform
z_{MAX}	[m]	(axial) near field distance
z_t	[m]	axial round-trip distance corrresponding to t seconds

Summary

Summary

In medicine, ultrasonic echography is the most widely used noninvasive imaging technique, because it produces images in real time that provide functional as well as morphological information in a relatively cheap and patient friendly way. Over the past decades, ultrasonic echography has evolved considerably. Nowadays, echographic systems are available that provide, aside of qualitative information, to some degree quantitative information. One of the main quantitative parameters that can be measured is the velocity component of moving blood or tissue in the direction of the ultrasound beam, i.e., in the axial beam direction. Ultrasonic echography is able to measure this velocity component with temporal and spatial resolutions that are better than are possible with other imaging techniques.

For clinical studies, the axial velocity component is less indicative than the absolute velocity. To obtain the absolute velocity, commercially available systems require information about the angle between the ultrasound beam and the direction of the absolute velocity component. Goniometry is applied to derive the absolute velocity from this angle in combination with the assessed axial velocity component. So far, the only medical measurement for which this angle is approximately known is the measurement of the blood flow velocity in a straight vessel. For such a measurement, it is assumed that the direction of the absolute velocity component is the same as the direction of the blood vessel. The angle between the blood vessel and the ultrasound beam is estimated by the user from the corresponding two dimensional echographic image of the longitudinal cross-section of the blood vessel.

This approach to assess the absolute velocity is only applicable for blood flow velocity measurements in straight vessels. For the measurement of, for example, absolute tissue motion, it is not applicable, because the angle between the absolute motion direction and the ultrasound beam can not be extracted from the echographic image and varies from position to position. Noninvasive echographic tissue motion measurements are very interesting, because they provide information about the deformation behavior of organs with high temporal and spatial resolutions without physical interaction of the measurement system.

In the current thesis, a method based on ultrasound is described for the measurement of absolute velocities. The method can be incorporated in conventional echographic scanners, because it is based on data acquired with a single ultrasound beam. The great advantage of the method is that it obtains the absolute velocity without requiring any information about the angle between the

absolute velocity component and the ultrasound beam. The method is able to determine, aside of the axial velocity component, also the local velocity component in the plane perpendicular to the ultrasound beam, i.e., the lateral velocity component. Simple goniometry is sufficient to derive from these two velocity components the absolute velocity at any point within the two dimensional plane of observation.

The axial and lateral velocity components are obtained by means of correlation of the radiofrequency (RF) signals (chapter 3). From literature, it is known that objects passing laterally through the ultrasound beam cause an amplitude modulation of the RF-signals repeatedly observed along the same line of observation. The amplitude modulation causes that the maximally obtainable correlation between subsequent RF-signals decreases with increasing temporal lag. It is experimentally demonstrated that the rate of temporal decorrelation is related to the lateral velocity and local characteristics of the ultrasound beam (beam width and curvature of wave front). A transducer with a circular beam shape is applied to make the rate of temporal decorrelation independent of the direction with which the lateral velocity component passes through the ultrasound beam. Furthermore, it is demonstrated that the correlation behavior of RF-signals is also dependent on the axial velocity, the bandwidth, center frequency, signal-to-noise ratio and sample frequency of the received RF-signals and the sound velocity in the medium under investigation.

The correlation between subsequent RF-signals can be calculated for different time and spatial lags. To establish the link between the value of such a correlation coefficient and the lateral velocity, an analytic model is derived that describes the correlation of the RF-signals considered (chapter 4). The model includes, besides the lateral velocity, also all the above mentioned parameters. Experimental evaluation of the correctness of that correlation model showed a very good resemblance between the correlation coefficients calculated from measured RF-signals and the ones predicted by the model.

From the analytic model for the correlation of RF-signals, estimators are derived for the local axial and lateral velocity components and for the local bandwidth, center frequency and signal-to-noise ratio of the received RF-signals (chapter 5). These estimators require for each local estimate only the calculation of a few correlation coefficients. The estimator for the lateral velocity requires also information about the local beam width and curvature of the wave front. Besides measurement of the entire ultrasound field, the easiest way to obtain this information is to acquire an

RF-data set while a large scattering object moves through the ultrasound beam with an exactly known velocity. From this data set, it is possible (using the estimators mentioned above) to derive a calibration curve that provides for each depth the desired information of the beam characteristics. This calibration curve has to be generated only once.

Experimental verification of the performance of the velocity estimators showed that spatial resolutions are possible on the order of two to four times the wavelength of the applied ultrasound frequency, which is equal to the resolution of the echo system used. For a 5 MHz transducer, the spatial resolution is in the range of 300 μm to 600 μm. Using spatially half-overlapping estimation windows, the gradual transition can be resolved with an even better precision. The temporal resolution depends on the applied pulse repetition frequency, but it is shown that for blood velocity measurements temporal estimation windows of 10 ms are feasible. Again, the application of temporarily half-overlapping estimation windows can resolve the gradual transition with an even better precision.

An advantage of the current axial velocity estimator is that it is not susceptible for aliasing. Its standard deviation is much lower than 1%, while the standard deviation of the lateral velocity estimator is slightly smaller than 10%. As a consequence of these deviations, the standard deviation of the absolute velocity estimates is smaller than 10%. The bias of the absolute velocity estimates is as far has could be observed much smaller than the standard deviation. With this precision, it is possible to determine the angle between the ultrasound beam and the direction of the motion (transducer-to-motion angle) with a standard deviation that is less than 2^{o}.

For the in-vivo validation, the current velocity estimation technique is applied to measure the center stream velocity of the blood in the a. Carotis Communis. Blood flow velocity measurements with ultrasound require the application of a clutter filter to reject the echoes from the slowly moving vessel wall. In the present thesis, a clutter filter is introduced that is based on the Singular Value Decomposition (SVD) of the RF-signals (chapter 6). The concept of this filter is that the strongest common sub-signals in a set of consecutive RF-signals are removed in the entire set of signals, because these sub-signals are very likely to be caused by the slowly moving vessel wall. Some of the advantages of the SVD clutter filter are that it has no settling time and that it is almost independent of the signal-to-noise ratio of the clutter, because it has no roll-off. Furthermore, it adapts its behavior depending on

the velocity of the clutter, which makes the SVD clutter filter an attractive alternative if an adaptive clutter filter is required. Verification of the filter performance with data acquired with a conventional echographic system from the a. Carotis Communis demonstrated (off-line) that the SVD clutter filter indeed can be applied for RF-data acquired in-vivo (chapter 7).

After the RF-signals received from the a. Carotis Communis have been SVD clutter filtered, the data is used as input for the proposed angle-independent velocity estimators to measure the corresponding absolute center stream velocity (chapter 7). The results showed that the estimated center stream velocity waveform was indeed very close to the expected one in those cases that the clutter signals could completely be suppressed. From these results, it is concluded that the proposed method is suited for tissue motion assessments, since tissue motion measurements require no clutter filtering and have normally a much better signal-to-noise ratio. This will, for example, result in echographic systems that are able to evaluate noninvasively the regional myocardial deformation pattern, and hence the functioning of the heart, which would open a new clinical area of research.

Samenvatting

Samenvatting

Echografie met behulp van ultrageluid is tegenwoordig een van de belangrijkste afbeeldingstechnieken in de medische geneeskunde. Een belangrijk pluspunt van de techniek is dat die in staat is om de op patiënt vriendelijke wijze verkregen anatomische informatie direct in beeldvorm te presenteren. Bovendien is echografie ook nog eens relatief goedkoop. Gedurende de afgelopen decennia zijn de mogelijkheden van echografische systeem aanzienlijk uitgebreid. Tegenwoordig zijn er systemen beschikbaar die, naast globale kwalitatieve informatie, ook tot op zekere hoogte kwantitatieve informatie presenteren. Een van de belangrijkste kwantitatieve parameters is de snelheidscomponent waarmee bloed of weefsel beweegt in dezelfde richting als de geluidsbundel, de zogenaamde axiale snelheidscomponent. Echografische systemen zijn in staat om deze snelheids-component te meten met tijd- en diepte resoluties, die veel beter zijn dan die van andere afbeeldingstechnieken.

Voor klinische studies is de axiale snelheidscomponent echter meestal minder indicatief dan de waarde van de absolute snelheid. Commercieel verkrijgbare echo systemen zijn echter (nog) niet in staat om deze absolute snelheid rechtstreeks te meten. Om deze snelheid te bepalen moet men weten hoe groot de hoek is tussen de as van de geluidsbundel en de richting van de absolute snelheidscomponent. Zodra die hoek bekend is kan op basis van goniometrie de absolute snelheid worden bepaald. De enige klinische meting waarbij deze hoek redelijk nauwkeurig kan worden ingeschat is bij de meting van de bloed stroomsnelheid in relatief rechte bloedvaten. Dan mag worden aangenomen dat de bewegingsrichting van het bloed hetzelfde is als de richting van het bloedvat. De hoek tussen het bloedvat en de as van de geluidsbundel moet door de gebruiker worden geschat uit het twee dimensionale echo beeld, dat een longitudinale dwarsdoorsnede van het bloedvat laat zien.

Deze aanpak om de absolute snelheid te meten werkt alleen voor de meting van de bloed stroomsnelheid in rechte bloedvaten. Voor het meten van de absolute waarde van weefselbewegingen bijvoorbeeld kan deze aanpak niet worden gevolgd, omdat de hoek tussen de richting van de bewegingscomponent en de as van de geluidsbundel niet kan worden afgeleid uit het echografische beeld en bovendien ook nog eens varieert van positie tot positie. Het niet invasief meten van weefsel bewegingen zou echter een interessante uitbreiding zijn voor de huidige generatie echo systemen, omdat dan ook informatie met goede tijd- en diepte resolutie kan worden verkregen over het bewegings- en vervormingsgedrag van organen zonder fysische interactie met het te meten object.

In het onderhavige proefschrift wordt een methode beschreven om met behulp van uitrageluid absolute snelheden te meten. Omdat er slechts gebruik wordt gemaakt van een enkele geluidsbundel is de methode zo eenvoudig van opzet dat die kan worden geïmplementeerd in conventionele echo systemen. Het grote voordeel is dat geen informatie meer noodzakelijk is over de hoek tussen de bewegingsrichting en de geluidsbundel. Dit komt doordat de methode in staat is om naast de axiale snelheidscomponent ook de snelheidscomponent in het vlak loodrecht op de geluidsbundel, de zogenaamde laterale snelheidscomponent, te bepalen. Eenvoudige goniometrie is vervolgens voldoende om aan de hand van deze twee snelheidscomponenten de absolute snelheid te bepalen op ieder punt binnen het twee dimensionale vlak van waarneming.

De axiale en laterale snelheidscomponenten worden bepaald met behulp van correlatie van de terugontvangen radiofrequente (RF) signalen (Hoofdstuk 3). Uit de vakliteratuur is het reeds geruime tijd bekend, dat objecten die de geluidsbundel in laterale richting doorkruisen een amplitude modulatie veroorzaken bij de opeenvolgende, langs dezelfde richting van observatie terugontvangen, RF-signalen. Door deze amplitude modulatie neemt met het toenemen van de tijdstap tussen de opeenvolgende RF-signalen het maximaal haalbare niveau van de correlatie af. Het is experimenteel aangetoond dat de mate van correlatie afname gerelateerd is aan de laterale snelheid en lokale eigenschappen van de geluidsbundel (bundel breedte en kromming van het golffront). Verder hebben experimenten aangetoond dat het correlatie gedrag van RF-signalen afhankelijk is van de axiale snelheid, de bandbreedte, draaggolffrequentie, signaal-ruis-verhouding en bemonsteringsfrequentie van de ontvangen RF-signalen en van de geluidssnelheid in het medium waarin gemeten wordt.

De correlatie tussen opeenvolgende RF-signalen kan worden uitgerekend voor verschillende tijd- en diepte stappen tussen de signalen. Om de relatie tussen de waarde van een correlatie coëfficiënt en de laterale snelheid te leggen is een analytisch model afgeleid dat dit correlatie gedrag beschrijft (Hoofdstuk 4). Dit model bevat naast de laterale snelheid alle hierboven genoemde parameters. De juistheid van het model is experimenteel aangetoond. Vergelijking van de aan de hand van gemeten data berekende correlatie coëfficiënten met die voorspeld door het model toont een goede overeenkomst.

Het model voor de correlatie van RF-signalen is gebruikt om schatters af te leiden voor de lokale axiale en laterale snelheden en voor de lokale bandbreedte,

draaggolffrequentie en signaal-ruis-verhouding van de ontvangen RF-signalen (Hoofdstuk 5). Voor iedere lokale schatting hoeven deze schatters slechts enkele correlatie coëfficiënten uit te rekenen. De schatter voor de laterale snelheid heeft bovendien nog enige informatie nodig over de lokale bundelbreedte en kromming van het golffront. Deze informatie kan worden verkregen door het hele geluidsveld van de transducent te meten, maar een eenvoudigere manier om die informatie te verkrijgen is om één keer een RF dataset op te nemen terwijl een object met bekende snelheid door de geluidsbundel passeert. Met behulp van deze dataset en de hierboven genoemde schatters is het mogelijk om een calibratie curve te creëren die voor iedere diepte de gewenste geluidsbundel informatie geeft.

Experimenteel is aangetoond dat met deze schatters een diepte resolutie mogelijk is in de orde van twee tot vier keer de golflengte van de gebruikte ultrageluids-frequentie. Deze resolutie komt overeen met de resolutie van het gebruikte echo systeem en ligt voor een 5 MHz transducent in tussen de 300 μm en 600 μm. Als in de diepte richting ook nog eens halfoverlappende schattingsgebieden worden gebruikt, dan zal de geleidelijke overgang met een nog betere plaats nauwkeurigheid worden bepaald. De tijdsresolutie hangt af van de gebruikte puls herhalings frequentie, maar het is aangetoond dat voor bloedstroomsnelheids-metingen tijdvensters van 10 ms mogelijk zijn. Wederom kan de geleidelijke overgang, maar nu in de tijd richting, met een betere nauwkeurigheid worden bepaald als halfoverlappende tijdvensters worden gebruikt.

Een voordeel van de huidige schatter voor de axiale snelheid is dat deze tot zeer hoge snelheden juist functioneert. De standaard deviatie van de axiale schatter is veel kleiner dan 1%, terwijl de standaard deviatie van de laterale snelheidsschatter iets lager is dan 10%. Als een gevolg van deze deviaties is de standaard deviatie van de absolute snelheidsschatting iets kleiner dan 10%. De bias op de absolute snelheidsschatting is voor zover als kon worden waargenomen veel kleiner dan de standaard deviatie. Met deze nauwkeurigheden van de schattingswaarden kan de hoek tussen de richting van de beweging en de as van de geluidsbundel worden bepaald met een standaard deviatie die kleiner is dan 2^{o}.

Voor de in vivo validatie zijn de nieuwe snelheidsschatters toegepast voor het meten van de snelheid van de bloedstroming in het midden van de halsslagader. Voor het meten van de snelheid van de stroming van bloed is het gebruik van een vaatwand filter vereist om de sterke echo's van de langzaam bewegende vaatwand te onderdrukken. In het onderhavige proefschrift is een vaatwand filter

geïntroduceerd dat is gebaseerd op Singular Value Decomposition (SVD) van de RF-signalen (Hoofdstuk 6). Het concept van het filter is dat de sterkste gemeenschappelijke signalen in een set van RF-signalen worden verwijderd, omdat deze gemeenschappelijke sterke signalen zeer waarschijnlijk worden veroorzaakt door de langzaam bewegende bloedvatwand. Enkele voordelen van dit SVD vaatwand filter zijn, dat het geen inschakeltijd heeft en dat het nagenoeg ongevoelig is voor de signaal-ruis-verhouding van de van de vaatwand afkomstig zijnde echoes omdat het filter geen roll-off heeft. Bovendien past het filter zijn gedrag aan aan de snelheid waarmee de vaatwand beweegt. Dit maakt het SVD filter een aantrekkelijk alternatief als een filter met adaptieve eigenschappen is gewenst. Verificatie van het gedrag van het filter met data ingevangen met een conventioneel echo systeem van de halsslagader toont aan dat het SVD vaatwand filter de verwachte eigenschappen heeft en in de praktijk inderdaad kan worden toegepast (Hoofdstuk 7).

Nadat de RF-signalen zijn gefilterd met het SVD vaatwand filter, zijn ze gebruikt als invoer voor de meethoek onafhankelijke snelheidsschatters voor het meten van het bloed stroom snelheidsprofiel in het midden van de a. Carotis Communis (halsslagader) (Hoofdstuk 7). De resultaten van de evaluatiestudie tonen aan dat, nadat het vaatwand filter alle storende signalen goed heeft onderdrukt, het door de snelheidsschatters berekende bloed stroomsnelheidsprofiel goed overeenkomt met het verwachtte profiel. Uit deze resultaten mag worden geconcludeerd dat de voorgestelde methode voor het meten van de absolute snelheid ook toepasbaar zal zijn voor het meten van weefsel bewegingen, zeker omdat voor het meten van weefsel bewegingen geen filtering nodig is en de signaal-ruis-verhouding veel beter is. Het moet daarom mogelijk zijn om echo systemen te maken die in staat zijn om op niet invasieve wijze het regionale vervormingspatroon van het myocard te bepalen om aan de hand daarvan het functioneren van het hart in kaart te brengen. Een dergelijk systeem zou daarom een nieuwe mogelijkheid bieden voor klinisch onderzoek op dit gebied.

About the Author

About the author

Curriculum Vitae

Léon Armand Franciscus Ledoux was born in Heerlen (The Netherlands) on May 1, 1971.

He attended secondary school at the Benardinuscollege in Heerlen from August 1983 to June 1989 where he received the VWO gymnasium certificate.

He received the M.Sc. degree from the Eindhoven University of Technology, faculty of Electrical Engineering, Eindhoven (The Netherlands), in February 1995. His field of specialization was Medical Electrical Engineering.

He worked, undersupervision of Dr.ir. J.M. Thijssen, at the Biophysics Laboratory of the University of Nijmegen (The Netherlands) from October 1993 until February 1995 on the M.Sc. degree thesis pertaining to ultrasonic wave propagation through aberrating layers.

From April 1995 until April 1999, he worked, undersupervision of Prof.dr.ir. A.P.G. Hoeks, as a Ph.D. degree student at the Maastricht University, department of Biophysics, Maastricht (The Netherlands). Starting on a project dealing with the reduction of the clutter component in Doppler ultrasound signals based on Singular Value Decomposition, he changed in September 1996 to a project, financially supported by the Dutch Department of Economic Affairs, dealing with the detection of absolute velocity based on correlation of ultrasound signals. In 1999, he obtained a grant ("Van Walree Fonds") from the Royal Netherlands Academy of Arts and Sciences (KNAW) for attending an international conference.

Currently, he is still working as a researcher (Post-Doc) at the department of Biophysics of the Maastricht University. The main goal of his research is the implementation of the in the current thesis proposed method for absolute velocity detection for clinical studies. His research interests include ultrasound signal processing for noninvasive quantification of physiological parameters.

He is a member of the Dutch Society for Pattern Recognition and Image Processing (NVPHBV) and of the Dutch Foundation for Ultrasound in Medicine and Biology (SUGB).

Publications

Papers (first author)

Ledoux LAF, Berkhoff AP, Thijssen JM. Ultrasonic wave propagation through aberrating layers: experimental verification of the Conjugate Gradient Rayleigh method. IEEE Trans Ultrason Ferroel Freq Contr. 1996;43:158-166.

Ledoux LAF, Brands PJ, Hoeks APG. Reduction of the clutter component in Doppler ultrasound signals based on singular value decomposition: a simulation study. Ultrason Imaging. 1997;19:1-18.

Ledoux LAF, Willigers JM, Brands PJ, Hoeks APG. Experimental verification of the correlation behavior of analytic ultrasound radio frequency signals received from moving structures. Ultrasound Med Biol. 1998;24:1383-1396.

Ledoux LAF, Willigers JM, Brands PJ, Hoeks APG. Angle-independent motion measurement by correlation of ultrasound signals assessed with a single circular-shaped transducer. Ultrason Imaging. 1999a;(accepted for publication).

Ledoux LAF, Willigers JM, Brands PJ, Hoeks APG. Modeling of the correlation of analytic ultrasound radiofrequency signals for angle-independent motion detection. Ultrason Imaging. 1999b;(accepted for publication).

Patent (pending)

Title:	Detection of vectorial velocity distribution
Inventors:	A.P.G. Hoeks and **L.A.F. Ledoux**
Application number:	1010061
Applicant:	Maastricht University
Country:	The Netherlands
Date of submission:	10 September 1998

Papers (co-author)

Brands PJ, Hoeks APG, **Ledoux LAF**. A single bit RF domain complex cross-correlation velocity estimator for color flow mapping. Ultrason Imag. 1997a;19:180-194.

Brands PJ, Hoeks APG, **Ledoux LAF**, Reneman RS. A radio frequency domain complex cross-correlation model to estimate blood flow velocity and tissue motion by means of ultrasound. Ultrasound Med Biol. 1997b;23:911-920.

Brands PJ, Willigers JM, **Ledoux LAF**, Reneman RS, Hoeks APG. A non-invasive method to estimate pulse wave velocity in arteries locally using the temporal and longitudinal gradient of blood vessel distension. Ultrasound in Med and Biol. 1998;24:1325-1335.

Verbeek XAAM, **Ledoux LAF**, Brands PJ, Hoeks APG. Baseband velocity estimation for second-harmonic signals exploiting the invariance of the Doppler equation. IEEE Trans Biomed Eng. 1998;45:1217-1226.

Verbeek XAAM, Willigers JM, Brands PJ, **Ledoux LAF**, Hoeks APG. Measurement of the contrast agent intrinsic and native harmonic response with single transducer pulse waved ultrasound systems. Annals of Biomedical Engineering. 1999; (submitted).

Abstracts

Berkhoff AP, **Ledoux LAF**, van den Berg PM, Thijssen JM. Pulse-echo ultrasound simulation in 3D aberrating media. 22nd International Symposium on Acoustical Imaging Firenze, Italy september 3-6. 1995;Book of abstracts:11.

Berkhoff AP, **Ledoux LAF**, van den Berg PM, Thijssen JM. Rigorous analysis of propagation through acoustic lens structures. Ultrasonic imaging. 1995;17:59.

Berkhoff AP, **Ledoux LAF**, van den Berg PM, Thijssen JM. Pulse-echo ultrasound simulation in 3D aberrating media. Acoustical Imaging. 1996;22:15-20.

Dankwoord

Dankwoord

De kennis en ideeën die geleidt hebben tot de totstandkoming van dit proefschrift zijn niet het resultaat van de inspanningen van slechts één persoon. Allen die, op welke wijze dan ook, hebben bijgedragen wil ik voor hun inzet bedanken. Toch zijn er enkele personen die een aparte vermelding verdienen.

Op de eerste plaats is dat mijn promotor Arnold Hoeks. Arnold heeft het project uitgeschreven dat uiteindelijk heeft geleidt tot dit proefschrift. De vrijheid die hij mij bij de realisatie hiervan gaf heb ik zeer gewaardeerd. Zijn snelheid van artikelen nakijken is onverstelbaar. Binnen 24 uur na inlevering had ik mijn artikelen altijd gecorrigeerd terug. Verder heb ik veel gebruik kunnen maken van zijn meer dan ruim aanwezige parate kennis op het gebied van ultrageluid en signaalbewerking. Daarnaast heb ik genoten van zijn vaak uitgesproken meningen over de meest uiteenlopende zaken. Speciaal wil ik Arnold bedanken dat hij mij de mogelijkheid geeft om het werk, dat ik zo graag doe, nog even voort te zetten.

Speciale dank verdienen ook mijn paranimfen Jean Willigers en Peter Brands voor hun technische ondersteuning.
Jean was gedurende de afgelopen vier jaar mijn persoonlijke "slavendrijver", die ervoor gezorgd heeft dat dit proefschrift binnen de gestelde tijd is afgerond. Zijn kritisch oordeel en verfrissende kijk op problemen hebben mij vaak op het juiste pad gehouden. Tevens wil ik Jean bedanken voor de vele overuren die hij met aanstekelijk enthousiasme maakte als we weer eens bezig waren met onze experimenten in de waterbak.
Peter is een van de voornaamste initiators geweest van het in ons laboratorium gebruikte data-acquisitie systeem, waarvan ook ik dankbaar gebruik heb kunnen maken. Ondanks de veelzijdige mogelijkheden van dit systeem, waren er voor de experimenten toch steeds weer enige software-aanpassingen nodig. Peter was altijd bereid om deze aanpassingen op korte termijn uit te voeren. Tevens heeft het analytische correlatie model, dat is afgeleid door Peter, gediend als aanzet voor de afleiding van het in het huidige proefschrift gepresenteerde correlatie model.

Een van de moeilijkste onderdelen van de promotietijd is voor CARIM-AiO's met een technische achtergrond het volgen van de klinische CARIM-cursussen. Gelukkig verkeerden de mede-AiO's Frank Aelen en Xander Verbeek in hetzelfde schuitje, zodat we bij elkaar ons beklag konden doen. Tijdens de CARIM-cursus in Amsterdam hebben Frank en ik veel profijt gehad van de aanwezigheid van Steven Samijo. Steven had, als basis-arts, niet alleen de bij ons ontbrekende medische kennis om ons de lesstof te verduidelijken, maar ook wist hij in Amsterdam de

goede eetgelegenheden te vinden. Met name het "Surinaamse eetcafé" is nog door vele ander AiO's tijdens latere cursussen regelmatig bezocht. Omdat Frank gelijktijdig met mij bezig was met de afronding van zijn proefschrift hebben we ook tijdens de afronding van ons promotie-onderzoek veel aan elkaar gehad. Xander wens ik nog veel sterkte toe in de strijd tegen het "onrechtvaardige" AiO-stelsel. Voor mij heeft het in ieder geval niet meer mogen baten.

Zoals alom bekend is een goede secretaresse onontbeerlijk. Lucienne van Haarlem zorgde er niet alleen voor dat mijn brieven en faxen onmiddellijk gemaakt en verstuurd werden, maar ze was ook één van de drijvende krachten achter de gezellige dagjes-uit en de kerstlunches .

Al de overige (ex-)medewerkers van de capaciteitsgroep Biofysica (Anneke, Annette, Dick, Jacqueline, Jan C., Jan M., Jons, Marc, Micheal, Roel, Ruben, Theo, afstudeerders en stagiaires (met name Luc)) wil ik bedanken voor de prettige werksfeer. Hopelijk kunnen we nog genoeg redenen verzinnen om gezamenlijk vlaai te eten.

De stage- en afstudeertijd op het laboratorium van Han Thijssen in Nijmegen heeft ervoor gezorgd dat ik besmet ben geraakt met het "ultrageluids-virus". De begeleiding door Rien Cuypers en Arthur Berkhoff hebben ervoor gezorgd dat die tijd zeer leerzaam is geweest. De kennis die ik daar heb opgedaan heeft mede gezorgd voor de goede start van het project dat heeft geleidt tot dit proefschrift. Ook moet ik Han bedanken dat hij mij in contact heeft gebracht met Arnold.

Tenslotte dank aan mijn familie, die altijd voor mij klaar stond als het nodig was.
Met name Jolanda is tijdens deze periode een grote steun voor mij geweest. Jolanda heeft er nooit een probleem van gemaakt dat ze me door de week meestal niet zag door werk en sportactiviteiten.
Mijn ouders wil ik bedanken voor de mogelijkheden die ze me hebben geboden om te studeren. Hopelijk ervaren zij dit proefschrift als een bekroning op hun inspanningen. (Pap, ik hoop dat je nu niet meer zegt dat ik naar school ga.)
Ook mijn schoonouders wil ik bedanken voor hun luisterende oor en de belangstelling die ze altijd toonden in mijn onderzoek.

Léon

ISBN 90-5681-067-7